High Pressure Hydrogen Storage on Carbon Materials for Mobile Applications

James Michael Blackman, MChem

Thesis submitted to the University of Nottingham
for the degree of Doctor of Philosophy

April 2005

"False facts are highly injurious to the progress of science, for they often endure long; but false views, if supported by some evidence, do little harm, for every one takes a salutary pleasure in proving their falseness."

Charles Darwin

Abstract

Recognising the difficulties encountered in measuring the adsorption of hydrogen at high pressure, a reliable volumetric differential pressure method of high accuracy and good repeatability has been developed for measurement up to *ca* 100 bar. The apparatus used has two identical limbs, a sample and a blank limb, between which a high accuracy differential pressure cell measures changes in pressure. By simultaneously expanding the two limbs and closely controlling the temperature of the entire system, many of the errors due to expansion of the gas can be avoided. In addition, helium blank measurements are used as a base line correction, which substantially reduces the effects caused by the rapid expansion of gas through a small port. Using this method, the hydrogen storage capacities of relatively small samples (1.0-2.5 g) of a selection of carbon materials have been accurately measured to a conservative limit of detection of 0.05 wt% and an accuracy of ±0.02 wt%. The accuracy of the apparatus has been proven using lanthanide nickel ($LaNi_5$), which has a known hydrogen storage capacity of 1.5 wt%, as a standard. The method has also been developed in order to analyse samples at elevated temperatures of up to 270 ˚C. This has been demonstrated using lithium nitride (Li_3N) compounds.

The carbon materials studied include a series of activated carbons, carbon nanofibres (CNF) and carbon nanotubes (CNT). The activated carbons have displayed almost instantaneous hydrogen uptake independent of the degas method used, which indicates that sorption occurs via a physisorption mechanism. The series of powdered activated carbons have displayed direct correlation between the BET surface area and the hydrogen sorption capacity. The largest hydrogen sorption capacity observed for activated carbons was for a chemically activated carbon with a surface area of 3100 m^2 g^{-1}, achieving an uptake of 0.6 wt%.

The preparation of CNF, grown from ethylene over mixed copper, iron and nickel alloy catalysts, has been extensively investigated. Control of the parameters of preparation has allowed the formation of CNF with surface areas of 10 - 500 m^2 g^{-1}, diameters of 100 - 1000 nm, lengths of 1-10s μm, gas conversions of 0-90 % and the formation of herringbone and platelet CNF structures. The CNF studied have been observed to be capable of adsorbing a maximum of 0.5 wt% hydrogen at 100 bar and ambient temperature.

Only one of the materials studied was observed to break by a significant amount the trend of surface area vs hydrogen sorption capacity, observed for the activated carbons. This was a single-walled nanotube (SWNT) sample which achieved *ca* 1.6 wt% after slow carbon dioxide activation at low temperature. This larger sorption is hypothesised to result from the hydrogen slowly diffusing into the SWNT through defects in the structure and between the graphite planes in the CNF.

Affirmation

The work reported in this thesis is solely the work of the author and has not been published elsewhere except for the following publications.

Conference Proceedings
Blackman J. M., Patrick J. W., Snape, C. E., Preprints, Division of Fuel Chemistry, 227th American Chemical Society National Meeting, Anaheim, Volume 49, Issue 1, page 207, 2004

Blackman J. M., Patrick J. W., Snape, C. E., Selected papers from the 227th American Chemical Society National Meeting, Anaheim, 2004

Blackman J. M., Patrick J. W., Snape, C. E., Selected papers from the 4th European Renewable Energy & Environmental Technology Solutions, Birmingham, 2004

Jewell C. M., Blackman J. M., Snape C. E., Gregory D. H., Selected papers from the Materials for Sustainable Energy Technologies, RSC, London, 2004

Refereed Conference Proceedings
Blackman J. M., Patrick J. W., Snape, C. E., Preprints, 3rd International Conference on Sustainable Energy Technologies, Nottingham, Paper POE042, 2004

Blackman J. M., Patrick J. W., Snape, C. E., Selected papers from the 3rd International Conference on Sustainable Energy Technologies, Nottingham, 2004

Submitted Journal Publications
Blackman J. M., Patrick J. W., Snape, C. E., The differential pressure method for the determination of hydrogen storage capacity at high pressures and its application to carbon materials, submitted to Carbon

Blackman J. M., Patrick J. W., Snape, C. E., Activation of carbon nanofibres, submitted to Carbon

Proposed Journal Publications

Blackman J. M., Patrick J. W., Snape, C. E., Carbon, The factors affecting the hydrogen storage capacity of carbon nanofibres, Carbon

Blackman J. M., Patrick J. W., Snape, C. E., Hydrogen production from the preparation of CNF, Fuel

C. Jewel, Blackman J. M., Snape, C. E., Gregory. D, Lithium nitride and lithium nitride nanotubes as a hydrogen storage system

Acknowledgements

I would like to thank my supervisors, Professor Colin Snape and Professor John Patrick, for their unshakable support and guidance throughout my PhD. They kept me on a loose leash and let me break things, which was definitely the best way to learn. Thank you for having faith in me.

I would also like to thank a few of the characters residing in L3. At the heart of the building we have the technicians who keep the place running even with the postgrads and academics best efforts to ruin everything, a special mention must go to Mick and Fred who never tired of my endless queries. Hiding upstairs are Ron, Mick, Trevor, Ana, Will, Paul and the rest of Research Fellows, who were always up for a laugh and listened to my questions no matter how daft. Last but not least in L3, we have the postgrads, thanks to all for putting up with me, especially Karl and Johnny.

I would also like to thank Dave Clift for his help with spectroscopic analysis and microscopy, Dr. J. Parra (INCAR, Spain) for additional surface area adsorption work, John Andresen for his expertise on nanotubes and Janos for help with atomic absorption work and activated carbons. I would also like to acknowledge the work of Katie and Duncan in Chemistry for their preparation of Li_3N for hydrogen sorption analysis.

Thank you Mum and Dad for your support, Em's you get a mention for just being you.

And, of course, thank you Becky

Table of Contents

List of Figures

List of Tables

CHAPTER 1
Introduction

1.1 Introduction to the hydrogen economy

In recent decades there has been intense international interest, discussion and agreements made, such as the Kyoto protocol, which have been directed at developing cleaner sources of energy to meet our ever-increasing demands without sacrificing our environment (United-Nations, 1997). Hydrogen energy systems represent such a means with which to achieve these goals. When hydrogen is combusted or electrochemically oxidised to create heat or electricity, respectively, the only product is water. No pollutants or greenhouse gases are generated or emitted, allowing the potential of zero emission vehicles to become a reality. This clean energy solution is known as the "hydrogen economy" where energy is transported and stored in the form of hydrogen.

However, hydrogen, the most common chemical element on the planet, does not exist in nature in its elemental form. The majority being combined with oxygen in the form of water (Greenwood *et al.*, 1997). Today, fossil fuels are the main source of industrially produced hydrogen. One of the main factors controlling the cost of hydrogen production is the ratio of hydrogen to carbon atoms in the fuel. The cheapest method of producing hydrogen is by the steam reforming of natural gas, which is mainly methane (Jones, 2003). With current efficiencies and capital costs, gas, coal and oil would all be cheaper sources of large-scale hydrogen production than any current renewable source at today's level of development. It is clear, therefore, that fossil fuels offer the most viable source of hydrogen in the short and medium-term, providing there are no drastic global changes in the availability of the world's reserves.

Although the technology for production of hydrogen from renewable sources is well understood, it is currently not utilised for making hydrogen in large quantities. Hydrogen produced from renewable energy sources is currently too expensive for anything other than niche markets, as found in remote regions like Alaska and Iceland (Systemtechnik, 2003). Production of significant quantities of hydrogen

using such methods would take considerable time and investment to develop, to allow capital costs to be reduced to a satisfactory level to allow introduction on a wide-scale. However, in the long term, hydrogen offers a potential route for gaining energy independence from fossil fuels.

Hydrogen energy systems are not a new technology. There are two main systems for mobile applications; the internal combustion engine and the fuel cell invented in 1839 by Sir William Robert Grove (McNicol, 1913). The basic principle behind the production of energy from hydrogen is combination with oxygen, from the air in most cases. Using hydrogen fuel cells, electricity can be produced to power motors to propel zero-emission vehicles, providing a potential solution to the problem of urban pollution (Simonyan *et al.*, 2002). However, for realising hydrogen energy systems in the near future, suitable energy storage and transportation technologies need to be researched and developed. One of the key technologies in this regard, is the development of high performance hydrogen storage systems.

1.2 Hydrogen storage

Hydrogen has very high gravimetric energy content, almost three times larger than petrol (Figure 1-1). However, the volumetric energy content is relatively low, due to the low density of the gaseous state (Figure 1-2). This means that, although the weight of the hydrogen necessary for a given process will be low relative to current energy storage systems, the volume required is larger. For stationary systems, the weight and volume of the system used is not a key factor. However, for mobile applications, such as fuel cell electric vehicles (FCEV) or hydrogen-fuelled internal combustion cars, hydrogen tanks have to be compact, lightweight, safe and affordable in order to make their use practical. In 1996, the International Energy Agency (IEA) established the "hydrogen storage task force" to search for innovative hydrogen storage methods and materials (IEA, 1996). The United States Department of Energy has set the hydrogen storage target to 6.5 wt% for gravimetric, and 62 kg m^{-3} for volumetric, densities to make vehicular fuels cells viable (Hynek *et al.*, 1997). Although, as progress is made with the efficiency of hydrogen powered cars it is inevitable that fuel consumption will be reduced enabling the targets for hydrogen storage to be reduced. However, until then,

applied and fundamental research around the world is focused on finding a method to meet this storage target.
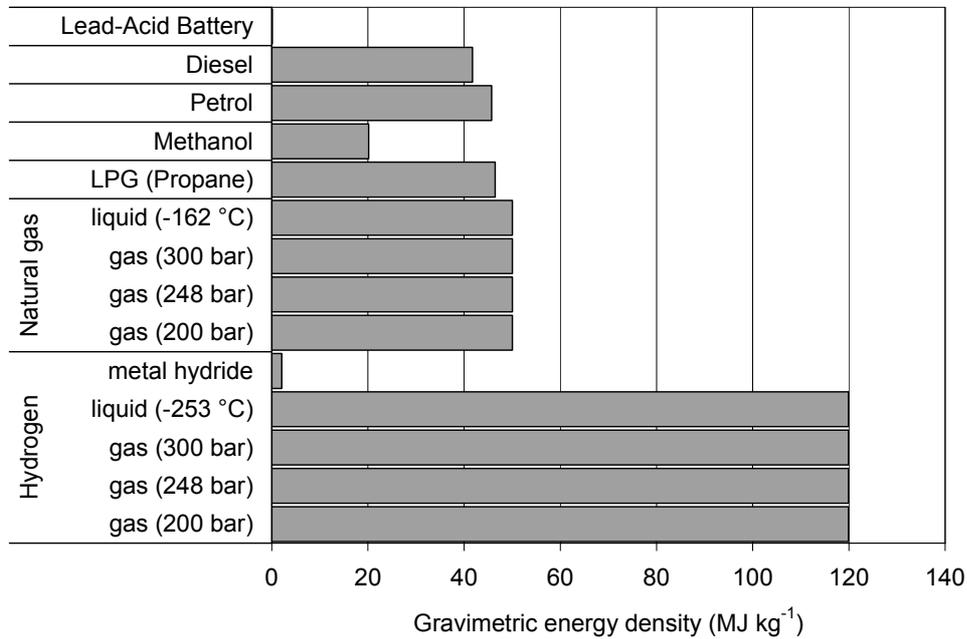
Figure 1-1 Gravimetric energy densities of hydrogen in comparison with other energy carriers (McEnaney, 2003; Systemtechnik, 2003)
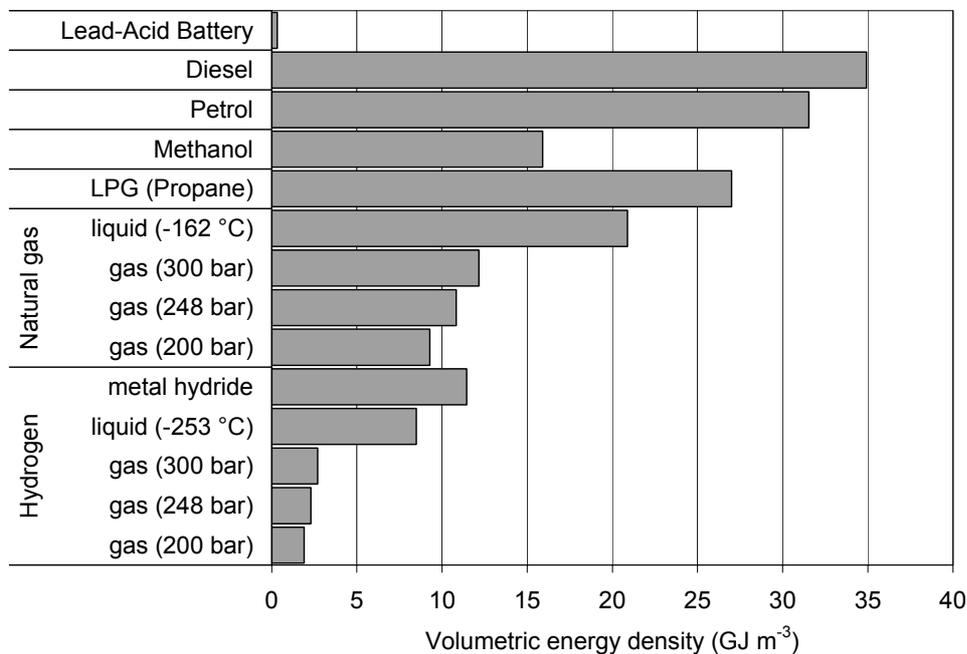
Figure 1-2 Volumetric energy densities of hydrogen in comparison with other energy carriers (McEnaney, 2003; Systemtechnik, 2003)

Hydrogen gas is fourteen times lighter than air, is highly flammable with a very low flash point, and has boiling and melting points of 20.4 K and 14.0 K respectively

(Greenwood *et al.*, 1997). These properties pose difficult challenges for safe mobile storage. Currently being researched as potential hydrogen storage systems are:

- High-pressure hydrogen
- Liquid hydrogen
- Hydrides
- Metal organic structures
- Carbon structures

On-board reforming of hydrogen from methanol or other liquid fuels is also being researched as indirect methods to store hydrogen; however, this is beyond the scope of this thesis.

1.2.1 Compressed hydrogen gas

For more than 100 years hydrogen has been traditionally stored and transported in the gaseous phase in high-pressure vessels. In 1898, hydrogen was shipped for the first time in a steel cylinder with a capacity of 43 litres, holding the gas at a pressure of 140 bar (McAlister, 1999). In 1916, cylinders were pressure tested for the first time and approved for service. In the following years, safety devices such as pressure release valves have been fitted to avoid over pressurisation in order to meet industrial standards.

Traditional steel cylinders are cheap and tough, but very heavy and thus have a low gravimetric energy storage density. Steel cylinders can achieve a gravimetric density of approximately 1.1 wt% of hydrogen stored. To run a compact car for 400 km, approximately 4 kg of hydrogen is required for a current fuel cell electric vehicle (FCEV) or 8 kg for a hydrogen internal combustion engine. To store 4 kg of hydrogen in the gaseous form at 200 bar, a traditional cylinder would have to have an internal volume of 220 litres, which is suitable for buses and lorries but impractical for a modern compact car.

Today, modern storage tanks can be made with carbon fibre composite materials, which are ultra light with a permeation resistant seamless liner and tough impact resistant reinforced shell. This makes them up to ten times stronger than steel, allowing them to store hydrogen at pressures in excess of 350 bar, which can be safely used for over 100,000 refill cycles and withstand surface temperatures over 800 ˚C (Quantum, 2003). However, even at these pressures, to store a commercially acceptable amount of hydrogen the fuel tank required would still be too large in volume for a compact FCEV. Presently, the most advanced prototype tanks can store hydrogen at pressures up to 700 bar for mobile, and 825 bar for stationary, applications and have been safety tested to 2130 bar (Dynetek, 2003). However, the potential risks associated with very high-pressure systems, and the even more risky procedure of compressing hydrogen, raises important practical problems, as there is currently no practical solution to refilling cylinders in a domestic situation to such high pressures rapidly and safely. This, coupled with the fact that the compression of hydrogen to 70 bar requires almost as much energy as liquefaction of an equivalent amount of hydrogen, leaves a lot of problems to be solved before high pressure hydrogen can become viable on a commercial scale.

1.2.2 Liquid hydrogen

Liquid hydrogen has been used as the fuel energy storage system for space travel since the 1960s (Sherif *et al.*, 1997). Liquid hydrogen is light, relative to other liquids, but it has a density over 800 times higher than the gaseous state and does not need the high pressure that is required for compressed gas storage, thus has less potential risks. The disadvantage is that hydrogen has a liquefaction temperature of *ca* 20 K at 0.1 bar. Thus the storage system requires very efficient insulation techniques in order to minimise the unavoidable heat transfer leading to hydrogen loss via boil-off (Greenwood *et al.*, 1997).

The energy required to liquefy hydrogen is approximately 40 mJ kg^{-1}, which is about 28 % of the energy content of hydrogen (Peschka, 1998). This energy requirement is one of the major problems with storing hydrogen as a liquid but expenditure is compensated for by the high volumetric density of 25.9 wt% achieved by liquid hydrogen (Peschka, 1992).

Another problem with this method of storage is caused by the massive thermal gradient between the interior and exterior of the storage vessel requiring advanced insulation techniques in order to maintain the temperature of the liquid (Aceves *et al.*, 2000). Even so, the high thermal gradient results in hydrogen being lost due to boil-off which varies from 0.06 % per day from large static containers to 3 % per day from tanks sized for use in cars (Browning *et al.*, 1997; Ewe *et al.*, 1987). Research is currently trying to find improved insulation and cooling methods. For example, in Germany a new cooling system has been patented that claims to be able to minimise evaporation, allowing the standby time of a car, before the evaporation of hydrogen begins, to be extended from 3 to 12 days (Wolf, 2002).

Hydrogen boil-off, and the high cost of sophisticated insulating techniques required for maintaining the very low temperatures, coupled with the initial energy cost to create liquid hydrogen, makes this method of hydrogen storage impractical for application in hydrogen fuel cell powered vehicles. However, liquid hydrogen has very high volumetric energy density and, by using larger tanks, much better surface to volume ratios are possible reducing boil off. This makes liquid hydrogen better suited for refuelling stations and larger transport tanks, such as in ships and road tankers, which utilise much larger reservoirs of hydrogen.

1.2.3 Hydrogen storage on hydrides

1.2.3.1 Metal hydrides

Hydrogen can be combined with many metals to form hydrides that will release hydrogen on heating (Bentzen *et al.*, 2001). An extremely safe hydrogen storage system can be designed using this type of hydride, because, if the storage vessel is ruptured, the hydride will still not release hydrogen until heated, and in some instances, hydrides can store a greater amount of hydrogen than an equivalent volume of liquid hydrogen (McAlister, 1999). For these reasons, much research has been carried out to determine if hydrides could be used for mobile hydrogen storage. Metal hydrides are composed of metal atoms that consist of a host lattice, and hydrogen atoms that are trapped in interstitial sites (Shriver *et al.*, 1999).

However, metal hydrides only release hydrogen at relatively high temperatures, 100 ˚C and above, currently too high for fuel cell applications. In addition, all current metal hydrides are either too expensive, or too heavy, for commercial application. To overcome this problem, materials using lighter elements have been investigated. One such material is magnesium hydride, which is directly formed from the reaction of hydrogen gas with elemental magnesium, reaching a maximum hydrogen uptake of 7.6 wt% (Zaluska *et al.*, 1999a). However, the reaction is slow and temperatures in excess of 300 ˚C are required to release the hydrogen. To ameliorate the conditions required to invoke hydrogen release, different processes to produce nanostructured magnesium have been investigated. It has been found that forming nanometer sized magnesium hydride crystal structures can significantly improve the thermodynamic and diffusional properties, resulting in enhanced hydrogen storage properties (Zaluska *et al.*, 1999a).

Recently, one magnesium hydride system has been developed that is now approaching large scale production. This is formed from palladium coated nanostructured magnesium films, which are reported to be able to adsorb approximately 5 wt% at 100 ˚C under a hydrogen atmosphere of 1 bar and completely desorb below 100 ˚C under vacuum (Higuchi *et al.*, 2002; Yamamoto *et al.*, 1999). It has also been found that in some metal hydride systems, such as magnesium hydride, the adsorption could be drastically improved by ball milling magnesium with nanometer size catalysts of nickel and iron under a 10 bar argon atmosphere (Zaluska *et al.*, 1999b).

To date, the highest recorded hydrogen capacity for a metal hydride, applicable for fuel-cell electric vehicles is 2.6 wt%. This was recorded for a chromium-titanium-vanadium alloy at 40 ˚C, under ambient pressure, but is well below the US Department of Energy target of 6.5 wt%. However, many metal hydride systems are still being researched and potentially many more remain undiscovered. Thus, with the promising results observed to date, metal hydrides clearly have potential as hydrogen storage systems, with the limits of this potential yet to be fully defined.

1.2.3.2 Complex metal hydrides

Non-transition metal hydrides, also known as complex metal hydrides, have been shown to have a high theoretical hydrogen storage capacity and are relatively inexpensive to produce. Initial reports on some of these materials, such as aluminium hydrides, claimed that the hydrogen was bound irreversibly. However in 1996, it was found that by doping sodium alanate ($NaAlH_4$) with a titanium catalyst hydrogen binding of up to 4 wt% at 200 ˚C could be made reversible with an enhanced kinetic release rate (Bogdanovi *et al.*, 1997). Several research groups are currently working on ways in which to optimise the system by altering the chemistry of the metal catalyst (Gross *et al.*, 2002; Sandrock *et al.*, 2002). Another group have reported that milling, in the presence of carbon, also enhances the reversible hydrogen capacities of the sodium alanates. It was reported that storage capacities of 2.5-3.0 wt% have been achieved at 80-140 ˚C, and 4.5-5 wt% at 150-180 ˚C (Zaluska *et al.*, 2000). The required temperatures and reaction rates for the operation of sodium alanates and variants, are however, still inadequate for use with FCEV applications and the exact mechanism of the catalyst is still unknown. In addition, the hydrogen release of the systems is still not optimised, because the full storage capacity is lost after the first cycle (Sandrock *et al.*, 2002). This leaves researchers working with sodium alanates left with many questions to answer.

1.2.4 Hydrogen storage within metal organic frameworks

A recent study has highlighted a new class of hydrogen storage compound. The material is composed of a metalorganic framework with a cubic, three-dimensional, extended porous structure and can adsorb up to 2 wt% of hydrogen at 10 bar pressure and ambient temperature, and up to 4.5 wt% at sub-ambient temperatures (Rosi *et al.*, 2003). As a potential hydrogen storage material, it is still in its infancy and the work is yet to be independently confirmed. However, the initial reported results are impressive, which will encourage more funding with which to research and develop metal organic frameworks as potential hydrogen storage materials.

1.2.5 Hydrogen storage on carbon materials

In recent decades, many advances have been made in the preparation of microporous and ultra microporous carbonaceous materials (Darkrim *et al.*, 2002). These materials have been found to have good adsorbing properties for most current gases.

1.2.5.1 Activated carbon

Research to evaluate the potential of carbon for hydrogen storage at low temperatures began in the 1980s. The first work started by investigating the potential of hydrogen storage in the capillary passages of activated carbon at low temperatures (McEnaney, 2003). Activated carbons possess very porous structures providing a very large surface area, some in excess of 3000 $m^2 g^{-1}$.

In the early 1990s, Chahine *et al.* reported hydrogen adsorption of *ca* 2 wt% at -196 ˚C and room temperature on AX21 activated carbon, formed from chemical treatment of coke (Chahine *et al.*, 1994). They were the first to comment on the importance of micropore volume relative to the hydrogen capacity of a carbon material.

However, values of hydrogen adsorption of anything less than 6 wt% are not sufficient for application to mobile hydrogen storage. Thus, further research is required to determine the limits of these materials.

1.2.5.2 Carbon nanomaterials

There are two main types of carbon nanomaterials that are of interest to this research, carbon nanofibres (CNF) and carbon nanotubes (CNT). CNF were first reported in the early 1970s, as advances in microscopy allowed these materials to be observed (Oberlin *et al.*, 1976). CNT were first prepared accidentally during the synthesis of fullerenes using the arc-discharge method in the early 1990s (Iijima, 1991). As interest in these materials has increased, a great deal of research has been carried out to determine the potential of these materials to adsorb hydrogen.

In the mid 1990s, Maddox and Gubbins employed Grand Canonical Monte-Carlo simulations in order to evaluate the potential of the adsorption of gas in materials with cylindrical porous structures, which is the basic structure of CNT (Maddox *et al.*, 1994; Maddox *et al.*, 1995). Their studies illustrated that by varying tube diameter and the inter-tube spacing; the thermodynamic conditions of the tubes could be controlled and optimised for the adsorption of gases. These findings further increased the interest in the potential of CNT for hydrogen adsorption.

In recent years, interest in carbon nanomaterials for hydrogen storage applications has escalated, following claims of experimental results, made in 1997 by Dillon *et al.,* that CNT might be capable of 5-10 wt% hydrogen capacity (Dillon *et al.*, 1997). The following year, a report claimed that more than 60 wt% of hydrogen had been observed to adsorb on CNF at room temperature (Chambers *et al.*, 1998). These reported findings received interest from car manufacturers, who invested heavily in further, independent, research. As yet, however, no group has been able to recreate these findings, and against these must be set a number of independent claims, varying from 0-20 wt%, made for both CNF and CNT.

Following this, Liu *et al.* reported that single-walled nanotubes (SWNT) possessed a reproducible hydrogen capacity of 4 wt% at ambient temperature and 100 bar (Liu *et al.*, 1999). Since, then several groups have reported observing hydrogen capacities above 1 wt% for SWNT (Shiraishi *et al.*, 2002; Wang *et al.*, 2002; Zhu *et al.*, 2001).

Chen *et al.* reported that CNT doped with alkali metals could adsorb up to 20 wt% of hydrogen at 380 °C and 10 bar (Chen *et al.*, 1999). However, it was later suggested that the presence of water might have influenced this result. In 2002, it was claimed by a team from Loughborough University that CNF had been observed to adsorb hydrogen up to 6.5 wt% at ambient temperatures and 120 bar (Browning *et al.*, 2002). They proposed that hydrogen chemisorption occurs at a rate controlled by dissociation of hydrogen at graphitic edge sites. This theory is supported by observations made by Yang, who reported that the hydrogen capacity of multi-walled nanotubes (MWNT) decreased with the residual metal oxide catalyst content. They proposed that the mechanism involves hydrogen dissociation at the catalyst particle and spillover to the nanotube (Yang, 2000).

Theoretical work by Yin *et al.* has concluded that the United States Department of Energy target for gravimetric capacity for hydrogen storage in nanotube arrays could be met at ambient temperatures and pressures of 160 bar (Yin *et al.*, 2000). However, the same study reported that the largest volumetric capacity attainable was just over a third of that required to make the use of SWNT feasible for hydrogen storage. All the theoretical work mentioned previously, assumed that the adsorbed hydrogen binds to carbon via physisorption. Using molecular simulation Lee *et al.* reported that chemisorption also occurred, and estimated that a capacity of 14 wt% was possible for SWNT (Lee *et al.*, 2002a; Lee *et al.*, 2002b; Lee *et al.*, 2001b).

1.3 Summary

The hydrogen economy and the field of carbon materials and hydrogen storage have been introduced including a few of the issues that have caused inaccuracies, contradictions and even controversy. This chapter has only a brief synopsis of some of the research that has been conducted on hydrogen storage systems, outlining some of the key papers from literature. The next chapter takes a more in depth look at hydrogen storage on carbon materials, paying particular attention to the methods of production of the carbon nanomaterials and the various methods that have been used to attempt to determine the hydrogen storage capacities.

CHAPTER 2
Literature Review

2.1 Introduction to carbon nanomaterials

CNF and CNT constitute a large part of the group of materials that are referred to in this work as carbon nanomaterials. Simple schematic representations of CNF and CNT are shown in Figure 2-1, which highlights the basic structures. CNF possess the same basic structure as carbon fibres, but on a nanometer scale, and thus display more long range order (Figure 2-1). CNF may exhibit a wide variety of graphitic structures such as platelet and herringbone (Figure 2-1). As the diameter of the fibres decreases, a point is reached where the most energetically favourable structure is the closed cage form of a fullerene and these structures are known as CNT.

Herringbone   Platelet   MWNT   SWNT
            CNF   CNT
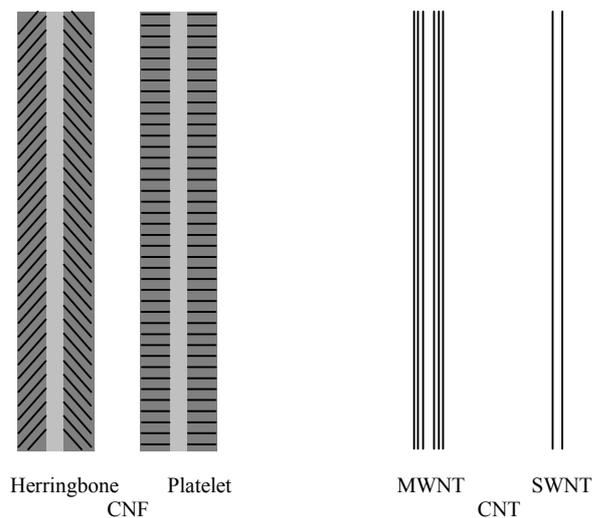
Note: The black lines represent graphitic layer orientation within the structure

Figure 2-1 Schematic representation of examples of CNF and CNT

However, the reality is that it is not easy to differentiate between these materials. In the majority of cases, the CNT and CNF are not aligned or straight, but instead are all interwoven. CNF, and especially CNT, have proved very difficult to produce on a large scale in high purity. Often a mixed product is formed, containing many types of carbon, from SWNT to amorphous material.

In the following study, a selection of the work carried out on CNT and CNF will be discussed. The definitions of a CNT or CNF will not be primarily related to the

dimensions of the material in question, but instead to their crystal structure (Vander Wal *et al.*, 2001):

CNT - A carbon nanofilament, where there are graphitic planes aligned parallel to the axis of the tube.

CNF - A carbon nanofilament, where there are graphitic planes aligned in any orientation relative to the axis of the filament, other than parallel.

The terminology used to describe carbon nanomaterials has not been formally standardised. This has led to different research teams using different names, such as nanofilament, nanowhisker, nanotube and nanofibre, for the same material. This has created a degree of confusion and controversy within the subject as comparisons between studies have been marred by confusing nomenclature.

The term carbon nanofibre was first used in the early seventies to describe observations made of carbon structures grown by chemical vapour deposition (CVD) then studied by scanning electron microscopy (SEM) (Baker *et al.*, 1972). As SEM images do not reveal the graphitic structure of the materials, full classification cannot be achieved. Only transmission electron microscopy (TEM) can examine the graphitic characteristics of these materials and thus determine a more specific classification.

2.2 Carbon nanotubes

The mid 1980s saw the birth of a new class of carbon materials, with the discovery of fullerene carbon nanostructures (Kroto *et al.*, 1985). Fullerenes are hollow geometric cage-like structures of carbon atoms, that are composed of hexagonal and pentagonal faces (Thostenson *et al.*, 2001). The first closed, convex fullerene formed was the C_{60} molecule, named buckminsterfullerene after the architect R. Buckminster Fuller known for designing geodesic domes (Figure 2-2). Buckminsterfullerene possesses a hollow, closed cage molecular structure of sixty carbon atoms, where each side of a pentagon is adjacent to aside of a hexagon, forming a perfect polygonal structure.
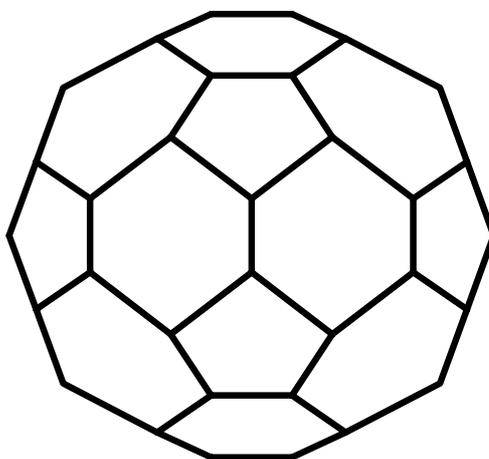
Figure 2-2 Schematic representation the C_{60} molecule (buckminsterfullerene)

The discovery of fullerenes led to research into the properties of these structures and investigations looking at other possible carbon structures. In 1991 Iijima *et al.* reported the discovery of hollow tube analogues to the original fullerenes naming them nanotubules or nanotubes (Iijima, 1991). CNT were discovered accidentally during the synthesis of fullerenes using the arc-discharge method. Each CNT was observed to consist of tubes of graphitic sheets, with the carbon-atom hexagons arranged in a helical fashion about the tube axis. Iijima noted that the diameter of the needles ranged from a few, to tens of nanometers in size, suggesting that the engineering of these carbon macromolecules may be possible on a much larger scale than with previous fullerenes.

It should be noted that CNF research teams observed CNT as early as the 1970s (Baker *et al.*, 1973; Boehm, 1973; Koyama, 1972; Oberlin *et al.*, 1976; Sinfelt *et al.*, 1972). At the time, they were assumed smaller versions of the less ordered vapour-grown CNF. This, to an extent, is true, as both are graphitic tubular carbon on a nanometer scale; however they do differ in structural detail.

2.3 Classifications of carbon nanotubes

CNT occur in two distinct forms, MWNT and SWNT. MWNT consist of multiple concentric graphitic cylinders, whereas SWNT are composed of a graphitic sheet rolled into a cylinder. Compared with MWNT, SWNT are expensive and difficult to obtain in high purity. Within these two broad classifications, there are many different CNF achievable, resulting from a large range of possible diameters, lengths, chiralities and morphologies, also CNT can have open or closed ends.

The CNT first observed by Iijima in 1991 were MWNT (Iijima, 1991). Bethune *et al.* and Iijima *et al.* independently reported the synthesis of SWNT a couple of years later (Bethune *et al.*, 1993; Iijima *et al.*, 1993).

2.3.1 Preparation

Since the discovery of CNT over a decade ago, there have been a number of methods developed for producing them. The primary production techniques for SWNT and MWNT being arc-discharge, laser ablation and CVD from carbon monoxide and various hydrocarbons.

2.3.1.1 Arc-discharge

The first CNT observed were synthesised from the electric-arc technique by Iijima *et al.* in 1991 (Iijima, 1991). The technique involves the use of two high-purity carbon rods as the anode and cathode, with the cathode doped with a transition metal catalyst. The electrodes are brought close together in a helium atmosphere, and then a potential difference is applied until a stable arc is achieved (Figure 2-3). As the anode is consumed, it is moved closer to the cathode in order to maintain the arc. The material deposited on the cathode consists of an outside shell of fused material and a softer fibrous core containing the CNT. To produce SWNT the cathode is

doped with a small amount of metallic catalyst such a nickel or cobalt based alloys (Bethune *et al.*, 1993; Shi *et al.*, 2000). Studies have also indicated that the presence of hydrogen in the atmosphere improves the purity of the CNT produced (Wang *et al.*, 1995).
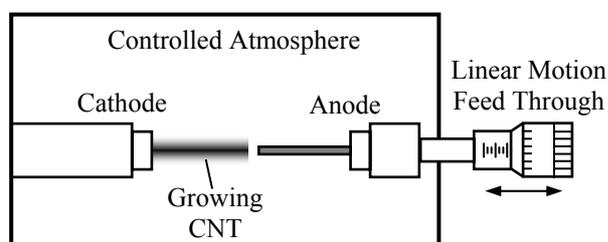
Figure 2-3 Schematic representation of the arc-discharge technique (Journet *et al.*, 1997).

Further work on this method had led to the development of semi-continuous methods, such as semi-continuous hydrogen arc discharge developed by Cheng *et al.* (Cheng *et al.*, 2000). This method is claimed to be capable of creating gram quantities of SWNT per hour.

2.3.1.2 Laser ablation

Laser ablation was developed for the synthesis of fullerenes, and has since been adapted for the production SWNT. The techniques involve utilising a laser to vaporize a graphite target doped with a transition metal catalyst in an inert atmosphere at temperatures of *ca* 1200 ˚C. A continuous flow of inert gas, such as argon, is used to move the product to a water cooled copper collector at the end of the furnace (Rinzler *et al.*, 1998; Thess *et al.*, 1996) (Figure 2-4). To produce SWNT the graphite target needs to be doped with a mixed cobalt and nickel catalyst.

The laser ablation method may be used to produce a more homogeneous product than the arc discharge and thus is more suitable for the study of their growth mechanism (Zhang *et al.*, 1999). However, this comes at a price, as the formation of SWNT by laser ablation requires a much higher temperature than arc discharge.
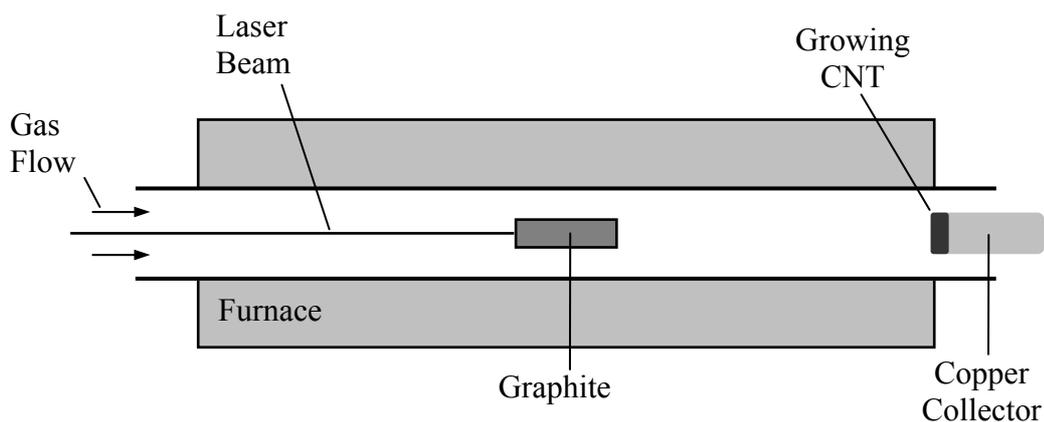
Figure 2-4 Schematic representation of the laser ablation technique (Thostenson *et al.*, 2001).

2.3.1.3 Chemical vapour deposition

The arc discharge and laser ablation techniques are both limited in the amount of sample they can produce by the size of their carbon source; the anode in arc discharge and the carbon target in laser ablation. In addition, further purification steps are required in order to isolate the CNT from the by products that are produced by both techniques.   These limitations have encouraged the development of gas phase techniques, in which CNT are produced from the decomposition of carbon-containing gases.

CVD can be used in the preparation of CNT, CNF and carbon fibres, the product is dependent on the catalyst, reactant gas composition and reaction conditions used. Basic chemical vapour deposition involves flowing a carbon containing gas, such as carbon monoxide or light aliphatic hydrocarbon, over a transition metal catalyst at high temperatures. As such, CVD techniques may be used in a continuous process, allowing much larger quantities of materials to be produced.   In addition, CVD produces carbon nanomaterial with a much higher purity, minimising the need for purification.

2.3.1.3.1 From carbon monoxide

Nikolaev *et al.* reported the production of high purity SWNT using carbon monoxide employing a CVD method with iron as the catalyst, from an iron carbonate catalyst precursor, at a temperature of 1200 °C (Nikolaev *et al.*, 1999). The SWNT produced were very pure, and possessed a diameter of 0.7 nm, believed to be the smallest achievable size.

2.3.1.3.2 From hydrocarbons

SWNT may also be prepared by the CVD of gaseous hydrocarbons, such as ethylene and methane, through to heavier aromatic liquids such as benzene (Sen *et al.*, 1997). Most hydrocarbon vapour deposition techniques used today involve passing a mixture of ethylene-hydrogen over a reduced mixed transition metal catalyst. The CNT produced are generally mixed with amorphous carbon deposits and thus require further purification.

This technique can also be utilised to control the synthesis of different types of CNT. The use of plasma enhanced CVD allows the synthesis of well-aligned, straight CNT directly onto a variety of substrates. By coating a substrate with a nickel catalyst, then using an ammonia and acetylene reactant gas mixture, catalytic and carbon source respectively, straight CNT may be grown (Ren *et al.*, 1998). CNT length may be controlled by varying the temperature and growth time. The use of plasma results in the growth direction being aligned with the plasma.

Conventional hydrocarbon CVD also has the advantage that it may be processed on a large scale with simple equipment using low cost precursors and catalysts. This is essential for the success of large-scale commercial application of the CNT.

2.4 Carbon nanofibres

The discovery of buckminsterfullerene, C_{60}, and the subsequent discovery of CNT, has generated intense research activity with the anticipation that these materials possess unique properties with many potential applications (Iijima, 1991; Kroto *et al.*, 1985). CVD can be utilised to grow analogous nanostructures known as CNF, as the process can be tailored to control the chemical and physical properties of the material for a particular application.

The formation of carbon materials from the interaction of carbon gases with hot metal surfaces was first recorded in 1889 (Hughes *et al.*, 1889). However, it was not until within the last 30 years, with advances in electron microscopy, that the structural and mechanistic details have been studied. Today, most CNF are grown from the CVD of carbon containing gases, over catalysts such as iron, copper and

nickel and alloys of these and other metals. The dimensions of the CNF may vary between 2 and 1000 nm in diameter, and lengths ranging from 5 to 100 μm (De Jong *et al.*, 2000; Oberlin *et al.*, 1976).

CNF have been researched for many diverse reasons. Initially, the growth of carbon deposits on catalyst was viewed as a menace, because in processes such as the conversion of hydrocarbons, the CNF deposits caused problems by blocking the reactor. This led to deactivation of the catalyst systems due to encapsulation of the metallic component (Bartholomew, 1982). However, over the last twenty years, there has been increasing interest in the mechanism of the growth of these materials, and their potential application, due to their unusual properties (Rodriguez, 1993).

2.4.1 Preparation

CNF form from the interaction of simple carbon containing gases (ethylene, acetylene and carbon monoxide) with pure and bi-metallic transition metal catalysts were the first to be observed. Their preparation is simple, involving CVD at temperatures between 550 and 700 ˚C. For these reasons, transition metal catalysed CNF have been the most widely studied, and so have the most literature published about them.

The synthesis of bulk quantities of CNF may be accomplished using a very similar CVD process to that used for the production of CNT (Section 2.3.1.3). In a typical operation, *ca* 50 mg of powered mixed transition metal oxide catalyst is placed in a reaction vessel in a Lindberg horizontal quartz tube furnace (Steigerwalt *et al.*, 2002). The catalyst is then reduced to its active state under a flow of hydrogen at *ca* 500 ˚C (Best *et al.*, 1954). The tube is then brought up to reaction temperature under an inert atmosphere and the reactant gas; typically, a hydrocarbon and hydrogen gas mixture, is introduced for 1-3 hours. Using this approach on a small scale, up to 10 g of solid carbon is readily producible. There is a very wide range of variables that can be adjusted in order to alter the chemical and physical properties of the CNF produced. These factors include:

- **Catalyst**
    - Chemical composition (transition metals, alkali earth metal oxides, ferrocene)
    - State (powdered, supported, foils, gauzes)
- **Reactant Gas**
    - Light aliphatic gases and aromatics
    - Carbon monoxide
    - Hydrogen and hydrogen sulphide presence and content
    - Flow rate
- **Reactor setup**
    - Single reactor
    - Pre-treatment and reactor
- **Post treatment**
    - High temperature annealing under inert atmosphere
    - Removal of catalyst
    - Activation
    - Doping
- **Reaction temperature**
- **Reaction Time**

2.4.2 Mechanism of growth

In 1972, the first model for the proposed growth of CNF from the metal catalysed decomposition of carbon-containing gas was reported (Baker *et al.*, 1972). It was found that initially, the hydrocarbon is adsorbed and decomposed on certain faces of the metal catalyst particle. Some of the carbon species produced in the reaction dissolve in the bulk and diffuse through the metal particle from the front face to the rear faces where carbon is deposited from solution in the form of a CNF (Rodriguez *et al.*, 1995). Provided the reaction conditions are kept constant, the carbon structure will continue to grow in an uninterrupted fashion (Figure 2-5 a). Growth ceases when carbon encapsulation of the leading face of the particle occurs, which can cause the build up of a carbon over-layer and effectively prevent further hydrocarbon decomposition (Figure 2-5 b) (Yoon *et al.*, 2001).

Key for Schematic (a)
1.   Adsorption and decomposition of hydrocarbon gas at the particle-gas interface on the front face of the catalyst particle
2.   Diffusion of carbon through the catalyst particle
3.   Precipitation of carbon at the particle-nanofiber interface on the rear face of the catalyst particle
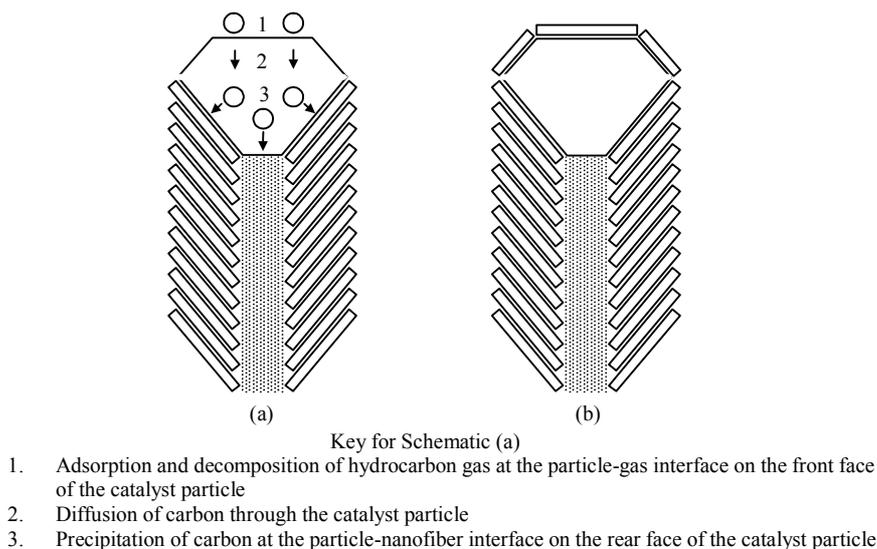
Figure 2-5 (a) Schematic representation showing the key steps in the growth of a carbon CNF. (b) Schematic representation of a carbon CNF that has ceased growth due to a carbon over layer, forming over the leading face. (Rodriguez, 1993)

This model is supported by TEM studies, which show CNF with catalyst particles at the tip of the filament (Figure 2-6). Here, the metal catalyst can clearly be seen as the dark region at the top left of the image, located at the tip of the CNF as the model predicts. The lighter material is the carbon, which is in two distinct forms, distinguishable by the differing shades of grey. The dark grey regions are graphitic platelets formed parallel to the surface of the catalyst particle. The lighter region is the less dense amorphous, or hollow, region of the core of the CNF (Steigerwalt *et al.*, 2002).
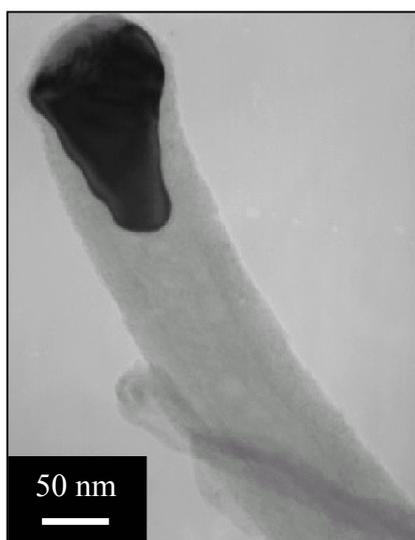
Figure 2-6 TEM showing the appearance of a CNF grown from the interaction of iron with ethylene-hydrogen (1:4) at 600 ˙C (Krishnankutty *et al.*, 1996)

2.4.2.1 Influence of transition metal catalyst on growth mechanism

An examination of catalyst particles, with regard to the mechanism outlined in the previous section (Section 2.4.2), highlights the importance of the nature of the catalyst relative to characteristics of the CNF produced. The nature of the gas-particle interface determines the mode by which the reactant gas bonds to the surface and whether decomposition occurs (step 1, Figure 2-5). The characteristics of the bulk of the catalyst dictate the amount of carbon dissolved and the rate of diffusion, which will affect the rate of CNF growth and the type of structure formed (step 2, Figure 2-5). Finally, the orientation of the particle-CNF interface dictates the structural characteristics of the material (step 3, Figure 2-5), controlling the angle of graphitic planes relative to the CNF axis (Chitrapu *et al.*, 1992; Endo *et al.*, 2002; Toebes *et al.*, 2002a). Thus, there are two possible crystal structures for CNF, "herringbone" and "platelet" (Figure 2-1).

2.4.2.2 Catalyst-gas interface

The initial interaction of the carbon containing gas and the catalyst particle at the gas-particle interface determines if a CNF will be formed. For CNF growth to occur the hydrocarbon must undergo dissociative adsorption on the surface of the catalyst particle before the carbon can begin to diffuse through the particle.

The crystallographic orientation and chemical composition of the catalyst particle are important variables in the interaction of the hydrocarbon molecules and the surface (Koestner *et al.*, 1982). However, although $Cu_{(111)}$ and $Ni_{(111)}$ have identical face arrangements, the interaction of carbon containing gases with the $Cu_{(111)}$ does not lead to carbon-carbon bond cleavage, allowing reversible chemisorption to occur, while with $Ni_{(111)}$ dissociative adsorption occurs (Zhu *et al.*, 1989). Clearly, other variables also control the nature of the adsorption of the hydrocarbon at the catalyst-gas interface.

The site of interaction of ethylene and $Pt_{(111)}$ was originally believed to occupy a position on top of a metal atom in $Pt_{(111)}$. Upon heating, the hydrocarbon undergoes rapid rearrangement to form an "ethylidyne" intermediate ($\equiv C-CH_3$) which is bonded to the surface via a $M\equiv C$ bond (Zhu *et al.*, 1989).

Hydrocarbons, such as ethylene and acetylene, may be adsorbed on a metal surface in two adsorption conformations, "parallel" or "end-on" to the surface of a catalyst particle (Kim *et al.*, 1991)(Figure 2-7).   The parallel conformation favours condensation polymerisation, thus promoting the encapsulation of the catalyst resulting in deactivation. The end-on conformation will favour transformation into the ethylidyne intermediate, providing an alternative pathway of decomposition. This leads to carbon dissolution, through the catalyst particle, forming the carbon nanostructure on the rear face of the particle by subsequent precipitation.

<center>Parallel   End-on</center>
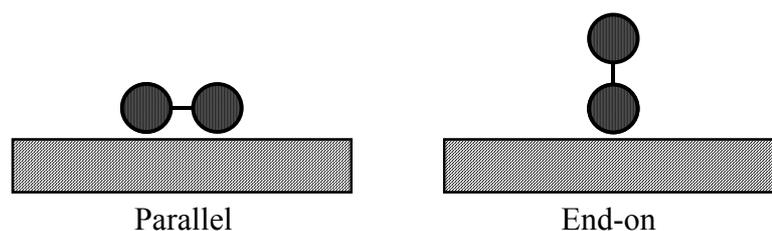
Figure 2-7 Structural arrangements for ethylene bonded to the surface of metal catalyst

2.4.2.2.1 CNF morphology

There are many different structural conformations of CNF possible. In addition to the whisker-like conformation, formed from one-dimensional growth as described in Section 2.4.2 (Figure 2-5 and Figure 2-6), probably the second most common type of growth is bi-directional (Figure 2-8). Kim *et al.* directly observed the formation of this CNF conformation by controlled atmosphere electron microscopy (CEAM) (Kim *et al.*, 1992). Continuous observation showed that growth occurred from two opposite faces of the catalyst particle, which remained located within the body of the CNF throughout the whole process. By using CAEM Kim *et al.* were also able to carry out kinetic studies on this mechanism, and ascertained that both limbs of the structure grew at identical rates (Kim *et al.*, 1992). Audier *et al.* utilised dark field studies to observer the catalyst particles found in CNF formed by the bi-directional mode of growth (Audier *et al.*, 1981). They found that the catalyst particles were polygonal in shape with CNF growing around each vertex. The large flat facets remained free of carbon, allowing the adsorption and decomposition of hydrocarbons to propagate the formation of the CNF.
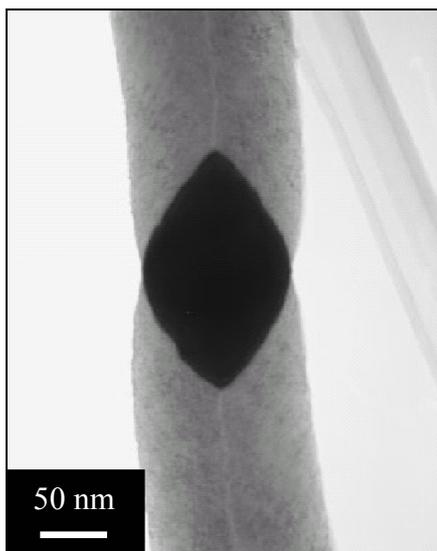
Figure 2-8 TEM of a CNF, produced via the bi-directional mode from a reaction of copper-iron (3:7) catalyst and ethylene-hydrogen (1:4) at 600 ˚C (Krishnankutty *et al.*, 1996)

Another mode of growth, commonly observed, produces helical and spiralled CNF. This conformation is produced when the catalyst particles rotate during the growth of the CNF (Figure 2-9).

Twisted conformation   **Helical conformation**
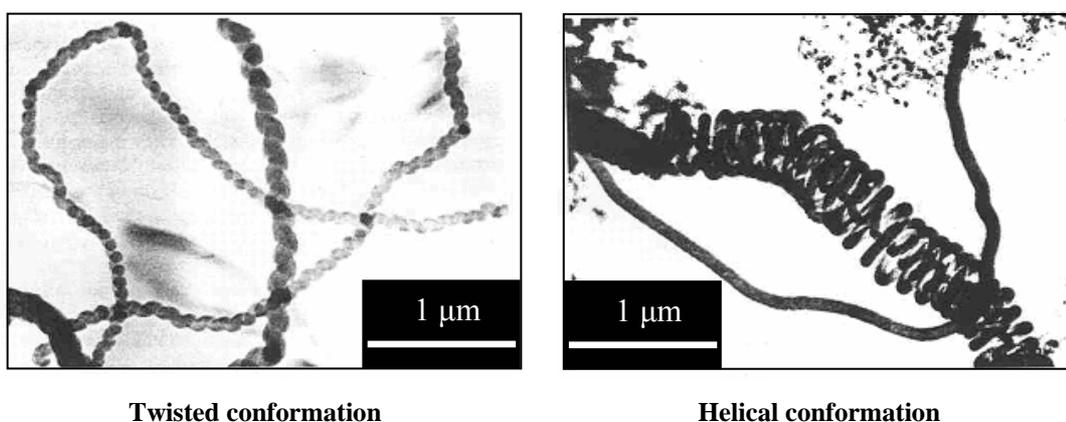
Figure 2-9 TEM images of different CNF conformations produced by the rotation of the catalyst particle during the CNF growth (Kim *et al.*, 1992; Rodriguez, 1993)

Branched CNF may also be produced (Figure 2-10), formed when a catalyst particle producing CNF via the whisker-like growth mechanism "shatters" into numerous smaller particles. These smaller particles then proceed to catalyse the growth of additional, smaller, CNF. This shattering effect was typically observed just after the temperature was raised, or after a given period of growth utilising a bimetallic catalyst, where one component is preferentially lost from the particle owing to gradual dispersion or volatilisation (Baker *et al.*, 1980).
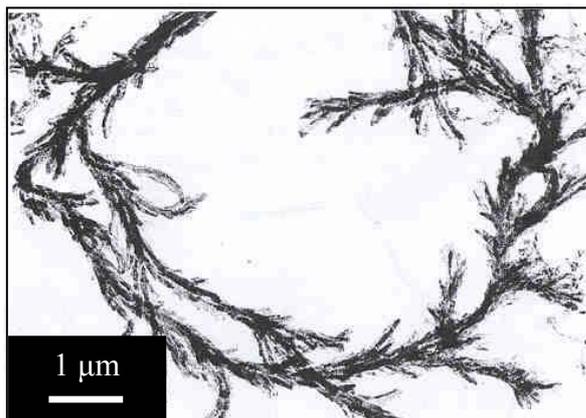
**Figure 2-10 TEM image of branched CNF, grown from a cobalt catalyst and acetylene
(Rodriguez, 1993)**

2.4.2.2.2 Rate determining step

It is generally accepted that diffusion of carbon through the catalyst particle is the
rate-determining step in the growth of CNF (Rodriguez, 1993). This is supported by
experimental findings that the activation energies for the growth of these structures
exhibit a remarkable correlation with those for diffusion of carbon through the
corresponding metals (Baker *et al.*, 1973). A comparison has been carried out of the
activation energies obtained from the direct measurements in the controlled
atmosphere electron microscopy of formation of CNF with those values for diffusion
of carbon through selected metal catalysts (Table 2-1).

Catalyst	Activation energy CNF growth[a] (kJ mol^{-1})	Activation energy diffusion of carbon (kJ mol^{-1})
Nickel	145.28	138.16- 145.7
α-Iron	67.407	43.961- 69.082
γ-Iron	141.93	139.42- 156.59
Nickel iron	140.68	142.35
Cobalt	138.16- 139.42	145.28
Vanadium	115.56	116.39
Molybdenum	162.45	171.66
Chromium	113.46	110.95
Ruthenium	109.69	-
Copper-nickel	130.63	-

[a] Directly measured by *in situ* electron microscopy

**Table 2-1 Measured activation energies for carbon CNF growth from the metal catalysed
decomposition of acetylene (Baker *et al.*, 1973; Rodriguez, 1993)**

The driving force for carbon diffusion through the particle is still unclear. One
theory is that a carbon concentration gradient from the front face of the particle to
the rear face will drive this diffusion step (Rodriguez, 1993). The exact nature of the

thermodynamic parameters that control the process has been the subject of a number of studies (Alstrup, 1988; Boellaard *et al.*, 1985; Chitrapu *et al.*, 1992; Sacco *et al.*, 1984; Yang *et al.*, 1985). In the first proposed mechanism, it was suggested that a temperature gradient from the front face of the particle to the rear face is present, owing to the exothermic decomposition of hydrocarbon at the front face and endothermic precipitation of carbon at the rear face (Baker *et al.*, 1972). Sacco *et al.* put forward a second theory that a metal carbide phase was formed and that the gas-catalyst interface caused the driving force for diffusion of carbon through the catalyst (Sacco *et al.*, 1984). Alstrup reported a refined version of this theory, claiming that a thin carbide layer is generated on the catalyst surface at the catalyst-gas interface. Further decomposition of unstable species then leads to super saturation of carbon at the gas-particle interface, thus creating the concentration gradient required for diffusion. However, Chitrapu *et al.* proposed that it is not necessary to assume that carbide species are present on the front face of the catalyst particle, if the hydrocarbon gas phase activity is the critical parameter (Chitrapu *et al.*, 1992).

Although some mechanistic models propose rational explanations for the formation of straight CNF, they all lack the ability to predict the effect of catalyst composition, which acts to cause the major perturbations in the morphological characteristics of the nanostructures (Section 2.4.3).

2.4.3 Carbon nanofibre engineering

The structure of CNF may be manipulated by changing one or more of the preparation parameters during the CNF growth phase (Section 2.4.1).

2.4.3.1 Catalyst activity

The catalytic activity of pure transition metals with pure ethylene and acetylene is relatively low. In some instances however, their activity may be greatly enhanced by incorporation of an adatom or by inclusion of gas additives to the reactant gas mixture. In addition, the temperature of reaction has been found to have a profound effect on the activity of some catalysts.

2.4.3.1.1 Effect of adatoms

Addition of another metal, such as copper, tin or potassium, or a non-metal, for example sulphur, to a transition metal catalyst can cause a marked increase in activity in the production of CNF, when reacted with ethylene (Benissad *et al.*, 1989; Boehm, 1973; Kim *et al.*, 1991; Krishnankutty *et al.*, 1996). This is thought to be due to the occurrence of different bonding conformations at the gas-particle interface of pure catalysts, and also for catalysts containing adatoms that do not chemisorb the reactant gas (Baker *et al.*, 1980) (Section 2.4.2.2). It has been proposed that for a pure metal catalyst that adsorbs reacting hydrocarbon, such as ethylene, in the absence of any other gas phase reactant, there would be a tendency for molecules to adsorb in such a conformation that the carbon-carbon double bond lay parallel to the solid surface (Krishnankutty *et al.*, 1996).

At saturation coverage, there would exist a high probability that these adsorbed species would interact with each other, and eventually condense to form a graphite over layer. In contrast, when ethylene is adsorbed on a catalyst surface containing adatoms that are incapable of chemisorbing them, it has been proposed that other molecular arrangements might be formed. For the situation where ethylene encounters two unperturbed, adjacent, nickel atoms, adsorption would occur in a similar fashion to that proposed for the pure metal. On the other hand, when adsorption takes place at a nickel atom, where the only unoccupied nearest neighbour was an adatom, then it is probable that ethylene would adsorb though an end-on arrangement. Under these conditions, catalyst deactivation via the encapsulation process would be less likely, and there would be greater potential for carbon species to dissolve and diffuse through the particle and eventually precipitate to form a CNF.

2.4.3.1.2 Reactant gas

The carbon-containing reactant gas should also be considered a variable, since studies have shown that different gases have different reactivities towards different catalyst systems (Kim *et al.*, 1991). Pure methane and carbon monoxide-hydrogen are less reactive than ethylene-hydrogen. This is not, however, always reflected by catalyst activity towards CNF growth (Toebes *et al.*, 2002a). For unsupported

nickel at 550 ˚C, only ethylene-hydrogen will result in the growth of CNF, whereas methane or carbon monoxide-hydrogen result in the successful growth of CNF, when catalysed by supported nickel.

2.4.3.1.3 Addition of additive gases

The addition of additive gases, such as hydrogen or carbon monoxide, may promote the production of carbon nanostructures from hydrocarbon reactant gases with some transition metal catalyst systems. Two possible reasons have been proposed to explain this phenomenon.

First, presence of other chemisorbed gases on the surface of the catalyst prevents the adsorption of the hydrocarbon in a parallel conformation by blocking some of the surface sites on the catalyst particle (Kim *et al.*, 1991; Krishnankutty *et al.*, 1996; Rodriguez *et al.*, 1993b). This effect is very similar to that proposed above for adatoms, as both encourage bonding in an end-on conformation and discourage parallel bonding which is thought to eventually lead to encapsulation and deactivation of the catalyst (Section 2.4.2.2) (Yang *et al.*, 1985).

Secondly to this, additive gases adsorbed on the metals are known to weaken the metal-metal bond, leading to an induced mobility of surface atoms. This phenomenon is know as "faceting" or "reconstruction" (Bonzel *et al.*, 1972). The new particle face induced by chemisorption is less favourable toward encapsulation of the catalyst so CNF production is promoted.

It has also been found that a 7 % addition of hydrogen increases production of the solid carbon by a factor of 40, when carbon monoxide was passed over a powdered iron catalyst at 600 ˚C. This was attributed to the presence of hydrogen facilitating hydrogenation reactions as additional reaction pathways to produce solid carbon (Rodriguez *et al.*, 1993b).

In addition to hydrogen or carbon monoxide, it has also been demonstrated that a small amount of sulphur, often in the form of thiophene, in the carrier gas enhances catalytic conversion of hydrocarbons to CNF (Vander Wal *et al.*, 2000). However, at high concentrations, the presence of sulphur has been found to poison the

transition metal catalyst and then halt CNF production. Sulphur is believed to promote CNF growth via two mechanisms. First, blocking encapsulation in the same manner as hydrogen and carbon monoxide, and second, facilitating the reconstruction of the catalyst surface, thus facilitating continued CNF growth.

2.4.3.1.4 Thermal conductivity of the reactant gas

The effect of the thermal conductivity of the reactant gas has also been studied using inert carrier gases. Helium or argon were found to have no influence on the reaction. Thus, it was concluded that the thermal conductivity of the gas plays no part in the reaction, as argon possesses a significantly lower thermal conductivity than helium (Kim *et al.*, 1991).

2.4.3.1.5 Temperature effect on the bulk state of the catalyst

The temperature at which a reaction is run has also been found to have an effect on activity of the catalyst. By *in situ* diffraction techniques, it has been shown that the state of the active catalyst particles can be determined for a catalyst supported on graphite in the presence of hydrocarbon at reaction temperatures (Oh *et al.*, 1991). This method has been used to study the temperature range over which various catalysts are active. Kim *et al.* first investigated this property for copper-nickel catalysts interacting with ethylene-hydrogen mixtures (Kim *et al.*, 1992). The catalyst was found to have high activity towards CNF production above 550 ˚C, peaking at 600 ˚C, then decreasing sharply above 700 ˚C. However, when the temperature of the system was lowered to below 700 ˚C, CNF production was seen to resume at the previous rate. *In situ* diffraction studies revealed that the loss of activity of the metal catalyst coincided with its separation into the elemental components (Rodriguez *et al.*, 1993a). This deactivation and reactivation process has been found to be complex, as both events occur at the gas-catalyst interface, and changes in the chemistry of the catalyst effect the reaction (Rodriguez *et al.*, 1993a). If hydrogen was added to the ethylene, catalyst deactivation was found to occur at a higher temperature, with the highest yields observed at 600 ˚C and deactivation occurring at 750 ˚C.

2.4.3.2 Control of diameter of CNF

The diameter of the catalyst particle controls the diameter of the carbon CNF produced from the interaction of a transition metal catalyst particle with a suitable carbon-containing gas. The form of catalyst used and the reaction temperature both influence the size of the catalyst particles.

2.4.3.2.1 The form of the catalyst

Transition metal catalysts may be used in several different forms, the main type being supported, powder and foil. Supported catalysts have the most controlled diameter, the size of the support dictating the size of the catalyst particle and hence control of the diameter of the CNF produced (Chang *et al.*, 1990). Foil and powdered catalyst systems provide less control over the CNF produced.

For powder catalysts, the catalyst precursor oxides, *ca* ~1 μm average diameter, have been found to be considerably larger than the active catalyst form, which produces CNF in the range 25-750 nm. This suggests that the particles are fragmented prior to CNF growth (Kim *et al.*, 1991). Fragmentation of the catalyst particles prior to CNF growth was first proposed as an explanation for the relatively high rates of reaction of samples with low specific area (Guinot *et al.*, 1981). Surface fragmentation has also been proposed as a required step for the formation of CNF from foil catalysts (Rodriguez, 1993).

In order to grow CNF in a well controlled size range, the best method is to use a supported catalyst system (Bessel *et al.*, 2001). These systems are produced by depositing a few monolayers of the catalytically active metal onto a support such as carbon, alumina or silica, followed by nucleation to form small particles (Baker *et al.*, 1972; Baker *et al.*, 1973; Lamber *et al.*, 1988). The diameters achievable range from 10 nm and can result in a homogenous product (Table 2-2). This method gives more control over the width of CNF by altering parameters such as the strength of the catalyst-support interaction and the reaction temperature, which have a direct impact on the size of the active catalyst particle.

Catalyst	Support	Majority Diameter Range	Reference
Ni	100 nm Ti coated sodalime glass	50 – 60 nm	(**Lee** *et al.*, **2001a**)
Ni	NaY zeolite	< 20 nm	(**Park** *et al.*, **2001**)
Ni	SiO_2	10 – 30 nm	(**Park** *et al.*, **2001**)
Fe	CaO	70-80 nm	(**Vander Wal** *et al.*, **2001**)
Ni	TiO_2	200-400 nm	(**Vander Wal** *et al.*, **2001**)
Fe	Powdered SiO_2	70-300 nm	(**Vander Wal** *et al.*, **2001**)
Fe	Ferrofluid on fumed SiO_2	60-70 nm	(**Vander Wal** *et al.*, **2001**)
Fe	Fumed SiO_2	700-800nm	(**Vander Wal** *et al.*, **2001**)
Co	Normally oxidised Si wafer	30-40 nm	(**Yoon** *et al.*, **2001**)
Ni	CNT	40-60	(**Pham-Huu** *et al.*, **2002**)

Table 2-2 Summary of CNF produced from a selection of supported catalyst systems

2.4.3.2.2 Temperature of reaction

The temperature of reaction has an adverse effect on the diameter of CNF produced from supported catalysts. The average diameter of CNF has been found to increase as the reaction temperature increases (Oh *et al.*, 1991). This is thought to be due to the rate of reaction increasing, with no appreciable increase in the rate of carbon diffusion through the catalyst particle.

In a study carried out by Arai *et al.*, it was observed that platinum and nickel particles over 10 nm in size displayed internal liquid-like behaviour at temperatures of 600-750 ˚C. This leads to a sintering effect and so a reduction in size of the catalyst particles (Arai *et al.*, 1984). This has the effect of reducing the diameter of the CNF produced from these catalysts as the temperature increases.

2.4.3.3 Crystal structure of CNF

The crystal structure of CNF has been found to depend on several of the variables that effect CNF growth, especially catalyst and reactant gas composition, and reaction temperature (Table 2-3). In addition to the effect of hydrogen, the presence of sulphur in the reactant gas stream has been found to reduce the crystallinity of the CNF produced (Vander Wal *et al.*, 2000). It has also been observed that, as the diameter of the CNF decreases, the crystallinity of the CNF structures increase (Fan *et al.*, 1998).

Catalyst	Type of Crystal Structure[a]	Conditions	Reference
Co	Graphitic, bi-dir	600 ˚C, C_2H_4:H_2 (1:4)	(Chambers *et al.*, 1996a)
Co-Au	Highly graphitic, multi-dir	600 ˚C, C_2H_4:H_2 (1:4)	(Chambers *et al.*, 1996c)
Co-Cu (3:1)	Highly graphitic, multi-dir	600 ˚C, C_2H_4:H_2 (1:4)	(Chambers *et al.*, 1996b)
Cu-Ni (1:9)	Graphitic, bi-dir, spiral	600 ˚C, C_2H_4:H_2 (1:4)	(Kim *et al.*, 1992)
Cu-Ni (2:8)	Highly graphitic, bi-dir	600 ˚C, C_2H_4:H_2 (1:4)	(Kim *et al.*, 1992)
Cu-Ni (7:3)	Amorphous, bi-dir, spiral	600 ˚C, C_2H_4:H_2 (1:4)	(Kim *et al.*, 1992)
Fe	Amorphous, bi-dir	600 ˚C, C_2H_4:H_2 (1:4)	(Rodriguez *et al.*, 1993b)
Fe (Si sup)	Highly graphitic, bi-dir	600 ˚C, CO: H_2 (1:4)	(Rodriguez *et al.*, 1995)
Fe-Cu (3:7)	Amorphous, bi-dir	600 ˚C, C_2H_4:H_2 (4:1)	(Krishnankutty *et al.*, 1997)
Fe-Cu (7:3)	Highly graphitic, bi-dir	600 ˚C, C_2H_4:H_2 (1:4)	(Rodriguez *et al.*, 1994)
Fe-Cu (98:2)	Highly graphitic, bi-dir	600 ˚C, C_2H_4:H_2 (1:4)	(Krishnankutty *et al.*, 1997)
Ni	Highly amorphous, bi-dir	600 ˚C, C_2H_4:H_2 (1:4)	(Kim *et al.*, 1992)
Pt	Amorphous, bi-dir	550 ˚C, C_2H_2:H_2 (1:4)	(Owens *et al.*, 1992)

[a] **multi-dir = multi-directional, uni-dir = uni-directional, bi-dir = bi-directional, sup = supported**
Crystallinity was determined by TPO, CAEM, XRD and TEM studies

Table 2-3 Summary of crystallinity of CNF produced from a selection of transition metal

The observations in Table 2-3 are qualitative, since it is difficult to reliably quantify the crystallinity of these materials. The main methods that are used to assess the graphitic quality of CNF are temperature programmed oxidation (TPO), controlled atmosphere electron microscope (CAEM), x-ray diffraction (XRD) and TEM.

2.4.3.3.1 Temperature programmed oxidation studies

The oxidation profiles of CNF in a controlled carbon dioxide environment have been examined though TPO studies in order to attempt to determine the degree of crystallinity. Small samples (1-15 mg) have been heated to *ca* 1000 °C at a constant rate in a stream of carbon dioxide in a thermo-gravimetric analyser (TGA) (Owens *et al.*, 1992; Park *et al.*, 1998). Weight loss is recorded as a function of both time and temperature. The amorphous carbon is expected to burn off at a much lower temperature than the less reactive, ordered, graphitic plates with the same catalyst loading. In some cases, it is possible to remove the catalyst by acid treatment in order to allow unimpaired analysis. However, if the catalyst is not removed it will catalyse the gasification reaction, potentially leading to erroneous results.

2.4.3.3.2 Controlled atmosphere electron microscope studies

A study carried out by Baker *et al.* on CNF produced from the interaction of acetylene and nickel, iron and cobalt using CAEM (Baker *et al.*, 1973), showed that when heated at 600 °C in a 660 Pa oxygen atmosphere, the inner portions of the CNF oxidise, leaving a much more oxidation resistant outer skin. When the temperature

was raised to 725 °C the remaining carbon was removed, leaving the remains of the active catalyst particles and some much smaller metal particles. Baker *et al.* proposed that these small fragments were the original part of the main catalyst particles that broke off during the CNF growth and become dispersed in the body of the CNF (Baker *et al.*, 1975).

2.4.3.3.3 Transmission electron microscopy and x-ray diffraction studies

The crystal structures of certain CNF have also been examined by TEM, high resolution TEM and XRD in order to provide more information on the crystal structures of the CNF. Using XRD data, the average spacing between the basal planes can be estimated and the alignments studied (Rodriguez, 1993). Many groups have studied CNF, providing information on the dimensions, structural conformations and the arrangement of the graphitic planes with respect to both the CNF axis and orientation around the catalyst particles. From these studies, it has been observed that the crystal structure of CNF can be tailored by careful control of the reaction parameters (Section 2.4.3).

2.4.3.4 Controlling the surface area of CNF

The surface area, characteristics and adsorption properties of CNF have been the focus of many studies and publications over the last decade (Dillon *et al.*, 2001). The focus of this work has primarily been on high pressure hydrogen adsorption, which is covered in a later section of this chapter (Section 2.6).

The surface area and properties of CNF have also been extensively studied by nitrogen adsorption at -192 ˚C using the Brunauer, Emmet and Teller (BET) relation. CNF formed from the passage of aliphatic gases over transition metals have been found to possess a Type II isotherm, which is typical of a nonporous solid with regard to nitrogen (Figure 2-11) (Gregg *et al.*, 1982). The magnitude of the BET nitrogen surface areas of these CNF have been found to vary from 10 to 400 $m^2\,g^{-1}$, depending on the catalyst and preparation conditions (Rodriguez, 1993). This will be covered in a later section of this chapter (Section 2.4.3.4).
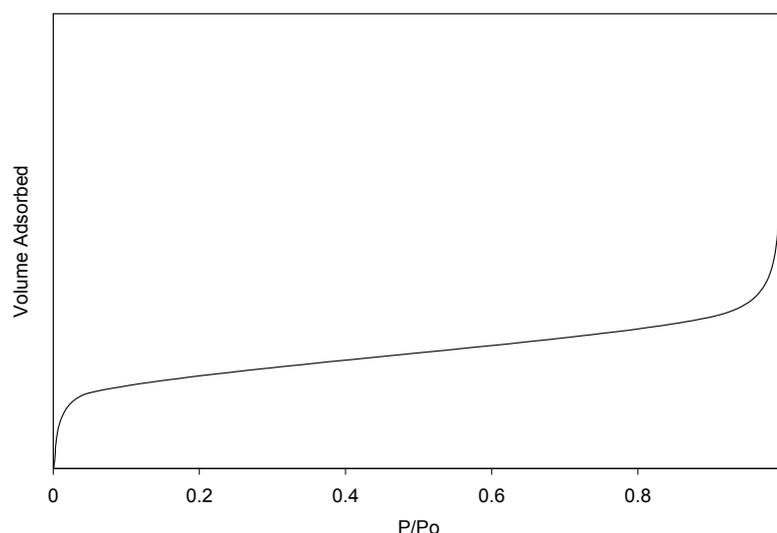
Figure 2-11 Type II BDDT classification of isotherm, typical of CNF from the interaction of aliphatic hydrocarbons and transition metal catalysts (Gregg *et al.*, 1982)

Type II isotherms can be considered to represent unrestricted monolayer-multilayer adsorption on a heterogeneous surface (Attard *et al.*, 1998). Substances that typically display this behaviour towards nitrogen penetration and adsorption at -192 ˚C are nonporous or macroporous (pore diameter > 50 nm) powders. However, this does not mean CNF do not have further porosities accessible to those gases with a smaller kinetic diameter than nitrogen (Rodriguez, 1993).

The surface area of CNF determined by nitrogen BET, has been found to be dependent on catalyst composition, catalyst precursor salt used, reactant gas composition and reaction temperature (Krishnankutty *et al.*, 1996).

2.4.3.4.1 Catalyst composition

The composition of the catalyst employed has been found to have a profound effect on the BET nitrogen surface area of the CNF produced. It has been found that as a general rule bi-metallic catalysts produce CNF with higher surface areas than pure metals (Table 2-4).

Catalyst	Reaction Conditions	BET Surface Area ($m^2 \, g^{-1}$)
Co	600 °C, C_2H_4	60
Co-Cu (1:1)	600 °C, C_2H_4	290
Fe	600 °C, C_2H_4:H_2 (1:4)	32
Fe-Cu (7:3)	600 °C, C_2H_4:H_2 (1:4)	228

Table 2-4 The nitrogen BET surface area of a selection of CNF produced from pure metal and bi-metallic catalysts (Chambers *et al.*, 1996b; Krishnankutty *et al.*, 1997; Rodriguez *et al.*, 1993b)

The nitrogen BET surface area of CNF has also been found to be dependent upon the ratio of transition metals present in the catalyst. The effect on the surface area depends on which metals are in the catalyst (Krishnankutty *et al.*, 1997).

2.4.3.4.2 Temperature

The temperature of preparation at which CNF were prepared has been found to have a strong effect the BET nitrogen surface area. The temperature at which the CNF with the highest surface area are produced depends on the other parameters of growth such as catalyst composition and reactant gas composition, although for most cases the figure is around 600 °C (Chambers *et al.*, 1996b; Krishnankutty *et al.*, 1997).

2.4.3.4.3 Reactant gas composition

The presence of hydrogen in the reactant gas mixture has also been found to affect the nitrogen BET surface area of CNF. The general trend that has emerged from several studies is that the proportion of hydrogen present in the reactant gas mixture is directly related to the surface area of the CNF (Chambers *et al.*, 1996b). In some cases, increasing the amount of hydrogen present has been noted to decrease the nitrogen BET surface area (Krishnankutty *et al.*, 1997).

2.4.4 Carbon nanofibre properties

Like CNT, CNF are light, flexible, thermally stable and chemically inert. They have been found to exhibit exceptional material properties that are variable depending on the type of CNF being studied.

2.4.4.1 Mechanical properties of carbon nanofibres

The mechanical properties of CNF have not been studied in great depth due, to the difficulties associated with working with such minute structures. However, the elastic properties of some relatively large coiled CNF have been explored by Motojima *et al.* (Motojima *et al.*, 1991). Here one end of the coil was attached to a copper mesh, thus fixing it in place; the other end was then manipulated in order to extend the coil. It was found that the structures could be elastically extended up to 3 times their original length and a further 1.5 times inelastically.

2.4.4.2 Electrical properties of CNF

The graphitic platelets that are controlled on the atomic level by the nature of the catalyst particle surface suggest that CNF will have electronic properties that are controllable.

2.4.5 Other carbon nanofibre systems

The CVD of simple aliphatic hydrocarbons and carbon monoxide over transition metal catalysts has been the most widely studied method for the production of CNF. However, other methods for CNF production have also been investigated, such as the floating catalyst method and smaller scale methods like plasma-enhanced CVD, hollow cathode plasma synthesis and radio frequency (RF) magnetron sputtering.

2.4.5.1 Floating catalyst method

The growth of CNF from hydrocarbons, other than simple aliphatic molecules, via CVD has been known for decades (Koyama, 1972). Using benzene as the carbon source and a metallocene, such as ferrocene, as the catalyst precursor, CNF with diameters of 10-200 nm have been prepared without the use of catalyst support (Fan *et al.*, 1998). Benzene and ferrocene vaporize at 81 ˚C and 185 ˚C, respectively, with ferrocene decomposing at 400 ˚C (Lide, 2003). The preparation is carried out at 1100-1200 ˚C with the catalyst exit pathway blocked, allowing collection of the CNF produced (Figure 2-12). Prior to the reaction chamber, ultra fine catalyst particles are vaporized from the ferrocene and then carried into the reaction tube by a carrier gas consisting of hydrogen and benzene vapour.
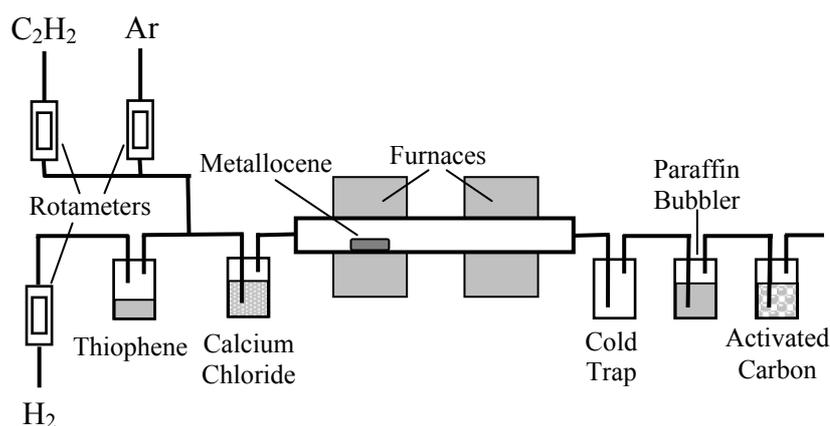
Figure 2-12 Schematic representation the setup of a typical floating catalyst CNF preparation apparatus (Singh *et al.*, 2002)

Further work found that the sulphur content, metallocene identity and temperature of the feedstock fluid to be key parameters to the successful growth of good quality CNF (Ci *et al.*, 2000a; Fan *et al.*, 2000; Singh *et al.*, 2002). In addition to this, the hydrogen content of the feedstock fluid has been found to have a complex effect on the CNF growth, with the primary relationship being a decreased CNF diameter with increased hydrogen content. The CNF vary in alignment depending on the precise reaction conditions, with both straight and "crooked" structures being possible.

The CNF produced from this method have been found by XRD and HRTEM (High Resolution Transmission Electron Microscopy) to possess duplex structures and be highly graphitic in nature studies (Ci *et al.*, 2000a; Endo *et al.*, 2002; Fan *et al.*, 1998). The crystallinity of CNF produced by this method has been found to be enhanced further by graphitisation at 2500 ˚C (Ci *et al.*, 2000b). By further optimisation of this method, it has been found that CNF, MWNT and SWNT can be prepared with diameters as low as 10 nm (Ci *et al.*, 2001; Endo *et al.*, 2001).

Figure 2-13 Typical TEM of CNF with smaller diameter grown by the floating catalyst method (Fan *et al.*, 2000)

2.4.5.2 Plasma-enhanced CVD

This technique has been proposed as a means to allow the direction of thin film CNF growth to be controlled. CNF alignment has been found to be controlled by the direction of the electric field lines during the synthesis process (Merkulov *et al.*, 2001; Merkulov *et al.*, 2002d). A typical plasma-enhanced CVD reaction is carried out in a vacuum chamber at 250 Pa and 700 ˚C, using DC glow-discharge to provide the plasma enhancement with a reactant gas mixture of acetylene, as the carbon source, and ammonia, as an etchant gas (Merkulov *et al.*, 2001). Silicon-supported transition metal thin films and dots are used as catalysts, allowing isolated CNF to be grown and studied (Figure 2-14) (Merkulov *et al.*, 2002a; Merkulov *et al.*, 2002b). Control of the percentage of ammonia present in the reactant gas has been found to have a strong effect on the size of the CNF formed.   Increasing the etchant gas content resulted in increased deformities in the CNF, with significant damage being observed and sometimes resulting in the catalyst particle being lifted from the silicon substrate (Melechko *et al.*, 2002; Merkulov *et al.*, 2002c).
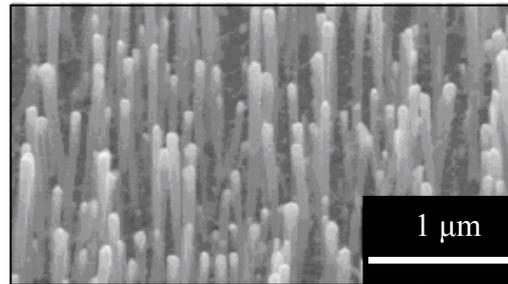
Figure 2-14 SEM image of forests of densely spaced CNF grown by plasma-enhanced CVD (Merkulov *et al.*, 2002c)

A variation on this process has been developed by Ikuno *et al.*, using lower temperatures of around 400 ˚C and iron phthalocyanine as the carbon source (Figure 2-15) (Ikuno *et al.*, 2002). The plasma is generated between an anode plate, which incorporates the substrate holder, and a spiral tungsten wire cathode. In contrast to the CNF produced by Merkulov *et al.* outlined above, the CNF were produced in a random orientation with diameter ranging from 100 nm to 10 μm. However, the CNF produced by this method have been observed to possess excellent field emission characteristics.
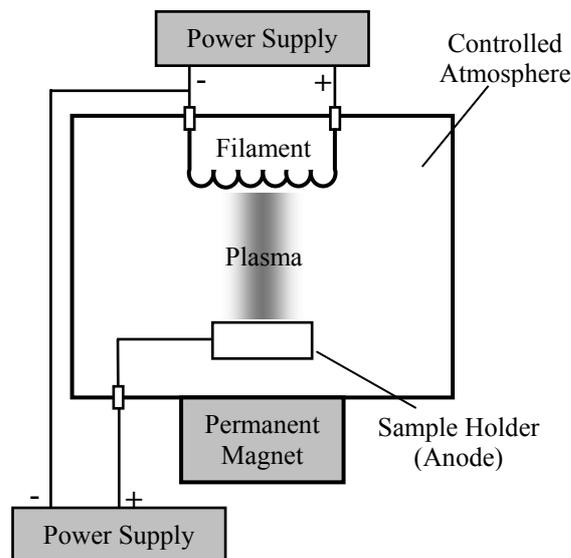
Figure 2-15 Schematic representation of plasma enhanced CVD apparatus (Ikuno *et al.*, 2002)

2.4.5.3 Hollow Cathode Plasma

Hollow cathode plasma CVD involves the plasma pyrolysis of ferrocene in a helium atmosphere at 200 ˚C (Figure 2-16) (Huczko *et al.*, 2002). This method produces aligned amorphous bundles of CNF perpendicular to the anodic aluminium oxide (AAO) membrane, with numerous iron nanoparticles embedded in them. The CNF formed have a diameter of 20-50 nm. Heating them to 3000 ˚C in a high purity argon atmosphere induced graphitisation to generate CNT.
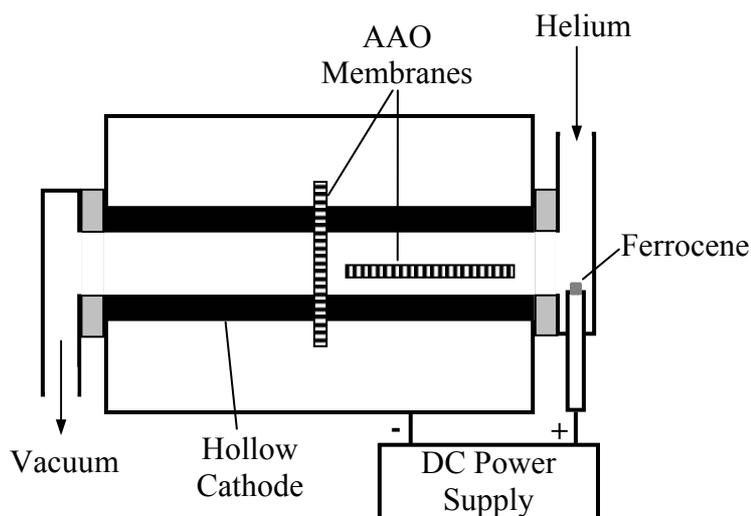
Figure 2-16 Schematic representation of hollow cathode plasma apparatus (Huczko *et al.*, 2002)

2.4.5.4 Radio-frequency magnetron sputtering

This method uses a hot element radio-frequency (RF) magnetron sputtering in order to control the alignment, diameter and density of thin film CNF (Honda *et al.*, 2002). This technique employs a filament heated to 2000 ˚C to facilitate the sputtering and a heating lamp to elevate the silicon substrate temperature to 700 ˚C. The RF magnetron source uses a pure graphite target, operated at 100 W, as the carbon source, and argon or nitrogen discharge gas at a pressure of 1 Pa (Figure 2-17). Prior to the preparation, the silicon substrate is pre-treated by thin film nickel deposition, followed by hydrofluoric acid wet etching.
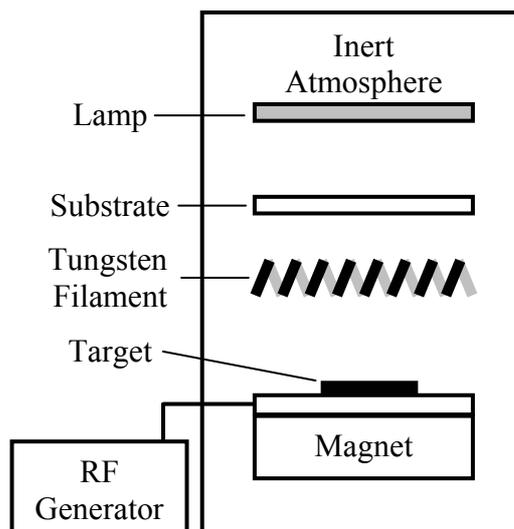
Figure 2-17   Schematic representation of an RF magnetron sputtering experimental setup (Honda *et al.*, 2002)

The nature of the discharge gas, substrate temperature and substrate pre-treatment have all been found to be critical for controlling the growth of thin film CNF. Using this method, isolated, vertically aligned thin film CNF can be prepared (Figure 2-18).

1 μm
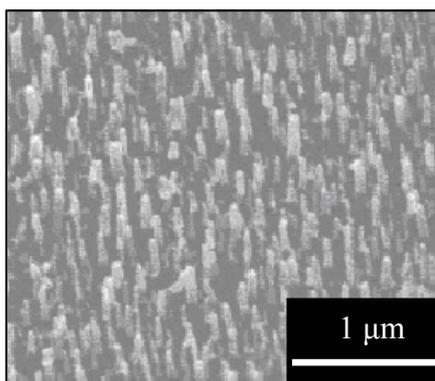
Figure 2-18 SEM of isolated vertically aligned thin film CNF produced by the RF Magnetron Sputtering method (Honda *et al.*, 2002)

2.5 Potential applications

The material properties of CNF and CNT suggest several potential applications that are currently being researched and developed:

- AFM tips (Yasutake *et al.*, 2002)
- Catalyst (Espinola *et al.*, 1986; Meguro *et al.*, 1985; Rodriguez *et al.*, 1987)
- Catalyst support (Kaneko, 1989; Rodriguez *et al.*, 1994; Toebes *et al.*, 2002b)
- Field emission display (Ikuno *et al.*, 2002) (Jin *et al.*, 2002)
- Fuel cell electrode (Bessel *et al.*, 2001; Steigerwalt *et al.*, 2002)
- Lithium ion batteries (Gao *et al.*, 1999)
- Nanoelectronics (Collins *et al.*, 1997)
- Nanotube composite materials (Wei *et al.*, 2002)
- Proton exchange membrane fuel cells (Che *et al.*, 1998)
- Reinforced matrix materials (Pattabiraman *et al.*, 1990; Tibbetts *et al.*, 2002)
- Selective adsorption agent (Jacoby, 1998)
- Super capacitors (Adhyapak *et al.*, 2002; Che *et al.*, 1999; Niu *et al.*, 1997)
- Electrochemical hydrogen storage (Dai *et al.*, 2002; Kibria *et al.*, 2001)
- Hydrogen storage (Darkrim *et al.*, 2002)

2.6 Hydrogen storage in carbon nanomaterials

The true potential of carbon nanomaterials for the application of hydrogen storage by adsorption is still not clear. Over the last decade, much research has been undertaken in to try and quantify these using various methods for both production of carbon nanomaterial and the adsorption measurement equipment, in an attempt to answer this question.

Hydrogen storage capacity is an excess quantity and represents the amount of gas that can occupy a given volume in the presence of any hydrogen storage effect relative to the amount of gas occupying the same volume at constant temperature (Chen *et al.*, 1997). Defined as such, the hydrogen storage capacity of a material is the additional capacity provided by that material, compared to that of compressed gas at the same pressure and temperature.

The literature has many terms that are used to refer to the capacity to adsorb such as hydrogen storage capacity, uptake or adsorption. In order to maintain consistency for this thesis, hydrogen storage capacity will be used to refer to any system where a hydrogen storage effect is observed. The term adsorption will be retained for direct reference to physisorption and chemisorption (Chapter 3).

Hydrogen storage capacity is most commonly expressed as weight percent (wt%), which corresponds to the unit quantity of gas with respect to the sum of the unit quantity of gas and unit quantity of adsorbent. Weight percent, w, is defined in Equation (2-1), where $m_{adsorbate}$ is the mass of the adsorbate and $m_{adsorbent}$ is the mass of the absorbent. Other, less common, units of measurement are mole per gram (mol g^{-1}) or gram per gram (g g^{-1}) and even, less frequently, atom of hydrogen per atom of carbon.

$$w = \frac{m_{adsorbate}}{m_{adsorbent} + m_{adsorbate}} \bullet 100 \qquad \textbf{(2-1)}$$

2.6.1 Methods for hydrogen storage determination

There are two methods for storing hydrogen in carbon materials, physical and chemical adsorption. To determine the hydrogen storage capacity of a carbon material three main methods have been utilised volumetric, gravimetric and temperature programmed desorption (TPD). For electrical storage, only electrical experiments can be used.

2.6.1.1 Volumetric

The basis for the volumetric method is that when a degassed sample of carbon, in a container of known volume, is exposed to a known amount of hydrogen at high pressure the carbon will adsorb some of the hydrogen and cause a reduction in pressure. To achieve this, two volumetric methods have been used by various teams, direct pressure measurement and, more recently, differential pressure measurement. This method of determining hydrogen storage is the nearest to simulating the conditions of a storage tank.

2.6.1.1.1 Direct Pressure Measurement

The direct pressure method was originally employed to determine the hydrogen storage capacity of metal hydrides at pressures between 1 and 40 bar, and is known as Sieverts apparatus (Figure 2-19) (Sandrock *et al.*, 1981; Sivakumar *et al.*, 1999). A known amount of hydrogen is exposed to the potential hydrogen storage material and the resulting pressure drop is monitored using a pressure transducer from which the hydrogen storage capacity of the material can be determined.
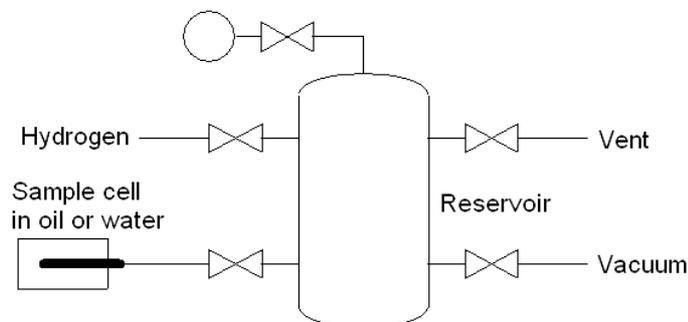
Figure 2-19 Simple Schematic representation of an example of a Sievert's type apparatus (Fan *et al.*, 1999)

In 1998, Rodriguez *et al.* used a Sievert's type apparatus to determine the hydrogen storage of some CVD grown CNF (Chambers *et al.*, 1998). This was one of the first

attempts at using a Sievert's type apparatus for the determination of the hydrogen storage capacity of carbon materials and is the work on which most other direct pressure measurements have been based. This is largely a result of the very high hydrogen storage capacity they reported, which will be discussed later in this section.

The Rodriguez *et al.* apparatus consisted of a conventional high-pressure stainless steel sample cell (*ca* 20 cm^3), connected to a high-pressure hydrogen reservoir container (*ca* 75 cm^3), via a high-pressure bellows valve (Figure 2-20). The system was calibrated with several blank runs in order to take into account the pressure drop on exposing the evacuated sample cell to the reservoir. For each run, *ca* 0.2 g of sample was used. The system was then evacuated to 0.1 Pa while being heated to 150 ˚C, in order to remove all physisorbed species. Hydrogen was then introduced into the reservoir to the desired pre-expansion pressure with the target post-expansion pressure being 120 bar. The bellows valve between the reservoir and the sample cell was then opened, exposing the sample to the hydrogen. The pressure was then monitored for a period of 24 hours. Once the system had reached equilibrium the gas was vented through the regulator allowing the desorbed gas to be measured by water displacement and be analysed by GC-MS to prove that only hydrogen is present.
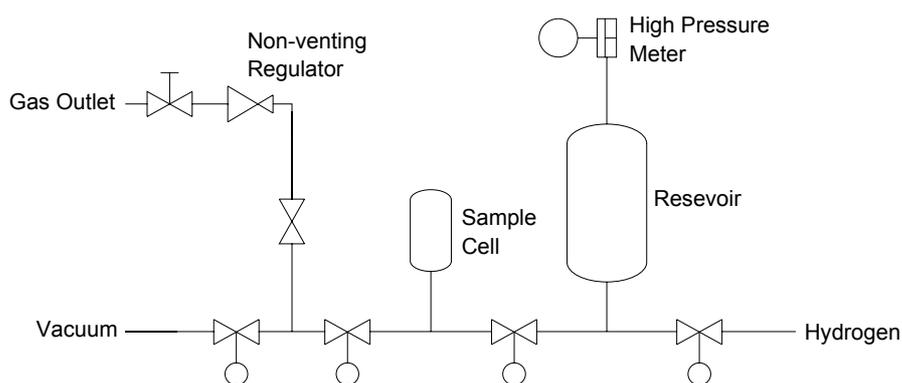
Figure 2-20 Schematic representation of the basic apparatus used for the measurement of hydrogen uptake in various materials (Chambers *et al.*, 1998)

Many different variations of this apparatus have been built and used in order to study the potential for carbons as a hydrogen storage medium. These differences include:

- Temperature control systems

- Scale of apparatus

- Helium free space analysis

- Calibration with metal hydrides

- The type of valves

- Additional desorption monitoring apparatus

2.6.1.1.2 Differential pressure measurement

In 2001, a novel method using differential pressure measurement for the determination of a the potential hydrogen storage capacities of carbon materials was proposed by Mellor *et al.* (Browning *et al.*, 2002).

The hydrogen adsorption capacities of CNF were determined at 120 bar using differential pressure measurements between four volumetrically balanced chambers (Figure 2-21). The hydrogen adsorption was measured as a differential pressure between the sample and reference limbs. Prior to each experiment, the sample (*ca* 50-100 mg) was heated to 150 ˚C at 100 Pa. The lower, linked, valves were closed and the reservoirs were pressurised with hydrogen. The upper linked valves were then closed and the lower linked valves opened in order to expand the hydrogen into the sample limbs to begin the experiment. The differential pressure was recorded at regular time intervals. To prove the rig was leak free, blank runs were carried out. In addition to this, the rig was calibrated using a commercial metal hydride $MmNi_{4.5}Al_{0.5,}$ where Mm denotes mischmetal of lanthanides, which was observed to adsorb 1.3 wt% coinciding well with the manufacturer's data.
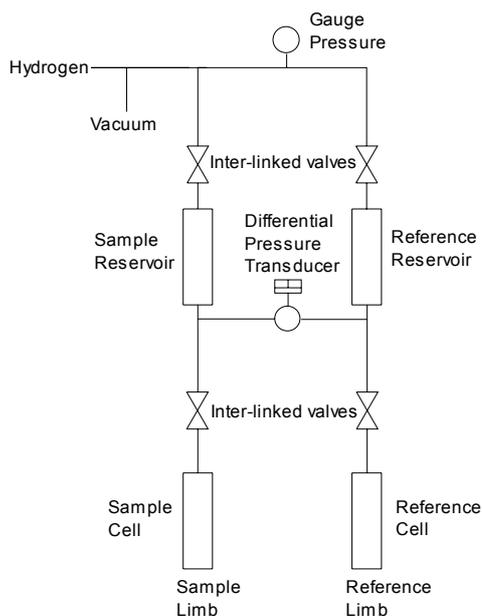
Figure 2-21 Schematic of experimental set-up of differential volumetric hydrogen adsorption apparatus as used by Mellor (Browning *et al.*, 2002).

This technique is claimed to possess several advantages over the traditional direct pressure measurement. Firstly, high pressure transducers are far less precise than differential pressure transducers operating at high pressure, thus the accuracy of the pressure monitoring system is higher. The method also attempts to eradicate many of the problems associated with the expansion of non-ideal hydrogen gas, which can introduce large errors when performing this type of measurement by using simultaneous expansion of the sample and reference cells. The authors claimed that the apparatus is capable of reproducing hydrogen uptakes as low as 0.1 wt% when using 100 mg of material.

2.6.1.2 Gravimetric method

The basis for the gravimetric method is that when a degassed sample of carbon contained in a container of known volume is exposed to hydrogen the carbon will adsorb some of the hydrogen and cause an increase in weight of the sample. To achieve this, two methods have been used by various teams; high pressure and ambient pressure systems. This method is sensitive to all gases sorbed, since it is purely based on weight.

2.6.1.2.1 High pressure isothermal method

The high pressure TGA experiments are usually equilibrium determinations (Chen *et al.*, 2001). The basis for the principle is that a degassed sample is exposed to high pressure hydrogen, and then the weight change is monitored as a function of time. The equilibrium hydrogen storage capacity may then be calculated for that material at that pressure and temperature. Using a series of such measurements an adsorption-desorption isotherm can be constructed.

For taking measurement at pressures of over 100 bar, Strobel *et al.* developed a high pressure system using a Supermicro S3D-P microbalance (Figure 2-22) (Strobel *et al.*, 1999). The balance chamber could be pressurised to 150 bar while operating at ambient temperature. The reference crucible (R) was loaded with quartz and the sample crucible (S) with carbon material. Buoyancy was numerically corrected. Before the high-pressure experiment was started, the chamber was purged with hydrogen and helium. The chamber was then evacuated until the pressure and mass remained stable for 30 minutes. To record a hydrogen adsorption isotherm for each sample the experiment was repeated at pressures from 0 to 130 bar.
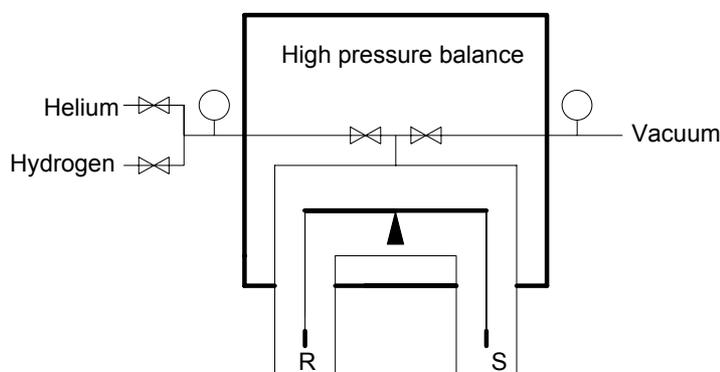
Figure 2-22 Schematic of experimental set-up of gravimetric hydrogen adsorption apparatus as (Strobel *et al.*, 1999).

More recently, high pressure gravimetric experiments have been performed in a direct gravimetric analyser with a high pressure, temperature controlled, balance chamber (Badzian *et al.*, 2001). These systems commonly operate between 1 and 60 bar and at temperatures between -196 and 1000 ˚C (Pradhan *et al.*, 2002). In a typical run a sample of carbon is degassed under high vacuum at 150 and 500 ˚C (de la Casa-Lillo *et al.*, 2002). The sample was then exposed to hydrogen at the desired

pressure and the change in weight was then monitored and used to calculate the hydrogen storage capacity of the material.

2.6.1.2.2 Dynamic temperature / ambient pressure method

Ambient pressure systems use direct TGA analysis and are usually dynamic measurements recording the hydrogen storage capacity of a material as a function of temperature (Lueking *et al.*, 2002). In a typical run, a sample (*ca* 10 mg) is loaded onto the balance, then degassed (Bai *et al.*, 2001).   The adsorption-desorption procedures used varied between groups, Wu *et al.* have published a detailed protocol which was representative of many of the other methods used (Chen *et al.*, 1999). The sample was purged with hydrogen then preheated to 400 ˚C. The adsorption cycle was begun by decreasing the temperature to 200 ˚C then 25 ˚C.   The desorption cycle was then recorded by heating back to 400 ˚C.

Some methods also include a correction for buoyancy to compensate for the difference of taking the measurement in hydrogen rather than air (Badzian *et al.*, 2001). Another feature of this method that some researches include is the use of mass spectrometry in order to identify which gases are being desorbed, in an attempt to prove that only hydrogen is present (Bai *et al.*, 2001).

2.6.1.3 Temperature programmed desorption (TPD)

Temperature programmed desorption, sometimes referred to as temperature desorption spectroscopy, measures hydrogen desorption only in high vacuum, utilising mass spectrometry.

In 1999, Dillon *et al.* reported that they had used TPD to determine the hydrogen storage capacity of SWNT soot (Dillon *et al.*, 1997). Their method was used later by several different groups (Shiraishi *et al.*, 2002). The experiments were carried out in an ultra-high-vacuum chamber equipped with a cryostat and a mass spectrometer. Samples of carbon material (*ca* 1 mg) were contained in platinum foil packets with pinholes for gas diffusion.   The packet's temperature was monitored by a thermocouple and controlled by resistive heating.   Standard hydrogen exposures were carried out at 40 kPa for ten minutes at 0 ˚C, followed by 3 minutes at -140 ˚C. The samples were then cooled to -183 ˚C under high vacuum (1 x 10^{-5} Pa) and were

then heated to 700 ˚C at 1 ˚C s^{-1} under vacuum. Throughout the process the presence of hydrogen was monitored by mass spectrometry. From this, the amount of hydrogen desorbed can be quantitatively calculated. This has been used as a secondary method in order to quantify hydrogen desorbed after a hydrogen adsorption experiment such as isothermal gravimetric (Chen *et al.*, 2001).

An addition to this method is the use of deuterium rather than hydrogen (Hirscher *et al.*, 2002). This greatly enhances the sensitivity as water and other hydrogen containing-molecules provide an additional source of hydrogen, which can impede accurate results.

2.6.1.4 Electrochemical

This method investigates electrochemical charge-discharge cycles of ionic hydrogen (Frackowiak *et al.*, 2002). The carbon to be analysed is ground and mixed with conducting transition metals and polymer binders to create a carbon composite electrode. This electrode and a counter electrode, often a first series transition metal, are submersed in an electrolyte solution separated by a membrane (Figure 2-23). The voltage across the two electrodes is measured as a function of time while a constant current is maintained, until equilibrium is achieved (Dai *et al.*, 2002). The accuracy of this method may be increased by using a reference electrode to take the voltage measurements, which is independent of the charge-discharge circuit. The voltage / time profile can then be used to calculate the hydrogen uptake achieved by the sample materials.
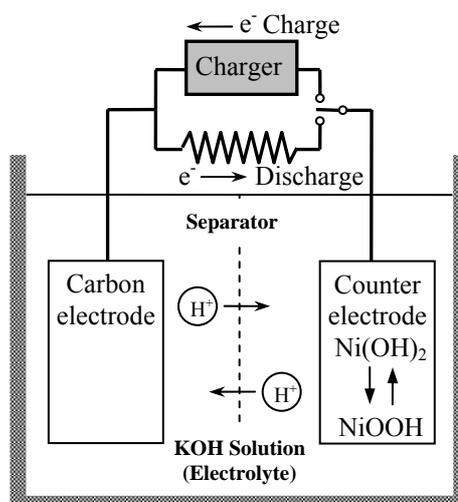
Figure 2-23 Schematic diagram of an example of electrochemical hydrogen storage apparatus (Lee *et al.*, 2000b)

2.6.2 Comparison of experimental findings

The results vary considerably, with no discernable pattern between type of materials or methods used. The results have been grouped by method used for the determination of the hydrogen storage capacity, and ordered chronologically. The largest hydrogen storage capacity reported has been quoted for each class of material analysed from each paper.

2.6.2.1 Gravimetric

The gravimetric method has been used by several teams to determine the hydrogen storage capacity of a selection of carbon nanomaterials (Table 2-5). The results vary from 0.25 wt% for MWNT to 20 wt% for lithium doped CNT, although it was later reported that the presence of water caused an erroneously high result (Pinkerton *et al.*, 2000; Yang, 2000).

Sample			Hydrogen Adsorption Measurement		Reference
Type	**Preparation**	**BET** $(m^2 g^{-1})$	**H_2 Adsorbed (wt%)**[a]	**Measurement Method** **Hydrogen adsorption conditions**	
Isothermal Temperature Gravimetric					
CNF ($\varnothing$ ~100 nm) **AC**	CVD (no further details) Commercial	~200 ~1500	**1.2** **1.6**	Isothermal Gravimetric, <100 mg, 125 bar, 23 ˚C	(Strobel *et al.*, 1999)
CNT ($\varnothing$ 50-100 nm)	Plasma assisted hot filament CVD, tube ends opened, demineralised		**13.8**	Isothermal Gravimetric ~70 mg, ~10 bar, ~20 ˚C (desorption peaks 120-170 ˚C)	(Chen *et al.*, 2001)
N_2 doped graphite nanoparticles	Microwave enhanced plasma CVD of $CH_4/H_2/N_2$, ~1000 ˚C		**0.8**	Isothermal Gravimetric ~100 mg, ~2 bar, ~20 ˚C	(Badzian *et al.*, 2001)
AC	From anthracite	1058	**1**	Isothermal Gravimetric <100 mg, 100 bar, 20 ˚C	(de la Casa-Lillo *et al.*, 2002)
Dynamic Temperature Gravimetric					
CNT Li-doped ($\varnothing$ 25-35 nm) **CNT K-doped** ($\varnothing$ 25-35 nm)	CVD from CH_4, demineralised, doped by solid state reaction using Li and K salts	130 130	**20** **14**	Dynamic temperature Gravimetric, <100 mg, 1 bar, max H_2 adsorbed at 600 ˚C and 27 ˚C for Li and K doped respectively	(Chen *et al.*, 1999)
MWNT ($\varnothing$ 5-25 nm)	CVD from CO or CH_4 and Co-La_2O_3 catalyst, Demineralised with nitric		**0.25**	Dynamic temperature Gravimetric, <100 mg, 1 bar	(Wu *et al.*, 2000)
MWNT	CVD from CH4 and $Ni_{0.4}Mg_{0.6}$ catalyst, demineralised	184	**0.6**	Dynamic temperature Gravimetric, 20 mg, 1 bar	(Lueking *et al.*, 2002)

a bracketed is the equilibrium time for completion of adsorption
b peapods are defined as C_{60} encapsulated SWNT

Table 2-5 Summary of hydrogen storage capacities of a selection of carbon materials recorded by the gravimetric methods

2.6.2.2 Temperature programmed desorption

The TPD method was used by Dillon *et al.* for the determination of a projected 5-10 wt% hydrogen storage capacity of SWNT from soot that contained 0.2 % SWNT. This was one of the results that sparked the international interest in this field (Dillon *et al.*, 1997). Since this initial result was reported, several groups have adopted the method in order to analyse various carbon materials (Table 2-6). The results are split; three teams have reported results above the target of 6.5 wt%. However, three teams have reported results no higher than 1 wt% well below the point of commercial viability.

	Sample		Hydrogen Adsorption Measurement		Reference
Type	**Preparation**	**BET (m² g⁻¹)**	**H₂ Adsorbed (wt%)ᵃ**	**Measurement Method Hydrogen adsorption conditions**	
Soot containing SWNT 0.2 % cobalt 20 %	Co-evaporation of graphite and cobalt in an electric arc		**Projected 5-10 wt%**	TPD, 1 mg, 0.4 bar, 0 ˚C then -140 ˚C (desorption peaks -123 ˚C)	(Dillon *et al.*, 1997)
Carbon nitride nanobells	Microwave plasma CVD of CH_4 /N_2 on a silicon substrate		**8**	TPD, QMS, 10 mg	(Bai *et al.*, 2001)
Nanostructured Graphite	Commercial graphite, ball milled under hydrogen	10	**8**	TPD (desorption peaks 423-727 ˚C)	(Orimo *et al.*, 2001)
CNT bundles and peapodsᵇ	Nd laser ablation, 1200 ˚C, using Ni/Co catalysts purified by H_2O_2 reflux and NaOH washing		**0.01**	TPD, 0.1 and 6 MPa (desorption peaks 77 ˚C)	(Shiraishi *et al.*, 2002)
SWNT	Arc discharge using Ni and Y catalysts (50 %wt) Ball milled under D_2		**1**	D_2 TPD, 0.08 MPa (desorption peaks 427-527 ˚C)	(Hirscher *et al.*, 2002)
CNF	CVD using ferrocene ball milled under D_2		**0.5**		
Graphite	Commercial, ball milled under D_2		**0.3**		
CNF (∅ 50-200 nm)	CVD using ethylene and Co-Fe catalyst		**0.05**	TPD, 20 mg, 45 bar, 25 ˚C	(Ritschel *et al.*, 2002)
MWNT (∅ 10-40 nm)	CVD Floating catalyst using benzene and ferrocene catalyst		**0.18**	TPD, 20 mg, 45 bar, 25 ˚C	
SWNT 90 %	CVD, 1050 ˚C using ethylene and Co-Fe catalyst on MgO thin film		**0.63**	TPD, 20 mg, 45 bar, 25 ˚C	

a bracketed is the equilibrium time for completion of adsorption
b peapods are defined as C_{60} encapsulated by SWNT

Table 2-6 Summary of hydrogen storage capacities of a selection of carbon materials recorded utilising TPD methods

2.6.2.3 Volumetric

The volumetric method was used by Chambers *et al.* for their work on CNF, reporting a hydrogen storage capacity of 67 wt%, a result which fuelled even more interest in the field (Chambers *et al.*, 1998). Since this result was reported, the volumetric method has become the most popular method for the determination of the

hydrogen storage capacity of carbon nanomaterials, the reported results have been found to vary considerably, from 0.22 to 67 wt% (Table 2-7).

Sample			Hydrogen Adsorption Measurement		Reference
Type	Preparation	BET $(m^2 g^{-1})$	H_2 $(wt\%)^a$	Measurement Method	
CNF AC	CVD, 600 ˚C using C_2H_4-H_2	25 3000	0.01 0.005	Volumetric direct, 25 ˚C, 160 bar	(Ahn *et al.*, 1998)
CNF	CVD, 550-750 ˚C using C_2H_4, CO, H_2 with bi-metallic catalysts		67 (20 hrs)	Volumetric direct, 100-300 mg, 25 ˚C, 121 bar	(Chambers *et al.*, 1998)
CNF	CVD, 550-750 ˚C using hydrocarbon, CO, H_2 with bi-metallic transition metal catalysts		40	Volumetric direct, 500-1000 mg, 25 ˚C, 110 bar	(Park *et al.*, 1999)
CNF (Ø ~90 nm) Demineralised	CVD floating catalyst, 1200 ˚C using benzene with ferrocene and sulphur		~13 (4 hrs)	Volumetric direct, 200-600 mg, 25 ˚C, 110 bar	(Fan *et al.*, 1999)
SWNT 50 % (Ø ~1.85 nm)	Semi-continuous arc discharge with Ni, Co and Fe Catalysts, Vacuum treated, 500 ˚C		4.2 (5 hrs)	500 mg, 100 bar	(Cheng *et al.*, 2000; Liu *et al.*, 1999)
MWNT MWNT	CVD, 700 ˚C from C_2H_4 with Ni Annealed to 2200 ˚C under Ar CVD Floating catalyst from benzene with ferrocene Annealed to 2200 ˚C under Ar		0.8 4	Volumetric direct, 100 mg, 25 ˚C, 100 bar	(Jia *et al.*, 1999; Li *et al.*, 2001)
Aligned MWNT	CVD, 800 ˚C from xylene with ferrocene		2.4	Volumetric direct, 100 mg, 17 ˚C, 100 bar	(Cao *et al.*, 2001a; Cao *et al.*, 2001b)
CNF	From Denco treated, 3000 ˚C		0.7	Volumetric direct, <1000 mg, RT, 120 bar	(Tibbetts *et al.*, 2001)
CNF	CVD, 600 ˚C, Ni-Cu (98:2) catalyst, C_2H_4		15	Volumetric direct, ~1g, 120 bar, measurement taken on the desorb	(Gupta *et al.*, 2001)
CNF (Ø 30-260 nm)	CVD, 600 ˚C from ethylene and $Cu_5Fe_{85}Ni_{10}$	23	6.5 (2 hrs)	Volumetric Differential 100 mg, 25 ˚C, 120 bar	(Browning *et al.*, 2002)
CNF (Ø 300 nm)	CVD, 1000 ˚C using ethylene with nickel catalyst		4 (3 hrs	Volumetric direct, <500 mg, 25 ˚C, 30-90 bar	(Zhu *et al.*, 2002)
CNF (Ø ~90 nm) Demineralised	CVD, 650 ˚C using CH_4 with $Ni_{0.4}Mg_{0.6}O$, Heat treated, 1200 ˚C under N_2		1.4 (40 min)	Volumetric direct, 500 mg, 25 ˚C, 120 bar	(Hwang *et al.*, 2002)
CNF Demineralised	CVD, 650 ˚C using C_2H_4/H_2 with Ni-Pd		0.7	Volumetric direct, 500 mg, 25 ˚C, 100 bar	(Lupu *et al.*, 2002)
Hydrogenated carbon nitride MWNT	Microwave enhanced plasma CVD Commercial		0.55 0.22	Volumetric direct, 400 mg, 27 ˚C, 120 bar	(Ohkawara *et al.*, 2002)
CNT (Ø 10-25 nm) CNT film	Arc-discharge CVD from C_2H_2 using silicon support		0.22 (35 hrs) 8.0 (60 hrs)	Volumetric direct with 167 mg, 1.1 bar 9 mg, 1.1 bar	(Wang *et al.*, 2002)
Ball Milled Graphite Rods	Commercial vacuum annealed Graphite rods, Ball milled		0.7	Volumetric direct, 2000 mg, -196 ˚C, 51 bar	(Awasthi *et al.*, 2002)
CNF AC MSC-30	CVD, 600 ˚C using C_2H_4/H_2 (1:1) with Cu-Fe (1:1) Maxorb Commercial	3000	0.27 0.057	Volumetric direct, 500 mg, 35 ± 0.2 ˚C, 100 bar	(Kiyobayashi *et al.*, 2002)
MWNT 70 % (Ø 5 nm) Demineralised	CVD Floating catalyst, 1100 ˚C from benzene with ferrocene annealed at 1000 ˚C under Ar		6.5	Volumetric direct, 300 mg, 23 ˚C, 145 bar	(Hou *et al.*, 2002)
MWNT (Ø ~20-30 nm)	CVD, 750 ˚C, silica supported Co catalyst		3.2	Volumetric direct, 1 g, ~20 ˚C, 120 bar	(Huang *et al.*, 2002)

a bracketed is the equilibrium time for completion of adsorption
b peapods are defined as C60 encapsulated SWNT

Table 2-7 Summary of hydrogen storage capacities of a selection of carbon materials recorded by volumetric methods

2.6.2.4 Electrochemical

The electrochemical method has been used in order to determine the hydrogen storage capacity of a selection of CNT by two groups (Table 2-8). The results are in good agreement relative to those for the other methods, with capacities ranging from 0.1-2.3 wt%, all below the target value.

Sample			Hydrogen Adsorption Measurement		Reference
Type	Preparation	Doped	H$_2$ Adsorbed (wt%)^a	Measurement Method Hydrogen adsorption conditions	
CNT	Arc-discharge in He		0.1	Electrochemical, Ni counter, Ag/AgCl reference, KOH 6M, current 0.4 mA/cm^2, 25 ˚C	(Kibria *et al.*, 2001)
		Li	0.6		
CNT (∅ ~60 nm)	CVD, 600 ˚C, C$_2$H$_2$ using Ni catalyst		0.1		
		Li	0.6		
SWNT 90 %	Laser Ablation		1.6		
	Commercial from Smalley	Li	2.3		
SWNT 65 % (∅ 2 nm)	Arc-discharge in H$_2$/Ar		1.8	Electrochemical, 200 mg carbon, Ni counter, Hg/HgO reference, KOH 6M, current 25 mA/g, 25 ˚C	(Dai *et al.*, 2002)

a bracketed is the equilibrium time for completion of adsorption
b peapods are defined as C60 encapsulated SWNT

Table 2-8 Summary of hydrogen storage capacities of a selection of carbon material recorded utilsing electrochemical methods

2.6.3 Mechanism of storage

It is accepted that the adsorption of a gas in microporous and mesoporous carbon materials can occur via the physisorption mechanism. The carbon atoms exert van der Waals' forces on the molecules. Physisorption is reversible by varying the physical conditions of a system, thus at a given temperature, the amount of hydrogen gas adsorbed is a function of the pressure, and can be desorbed by reduction of the pressure in the system.

A mechanism of hydrogen storage on carbon nanomaterials that explains the much higher than expected reported uptake remains unclear. Chambers *et al.* proposed that the interlayer spacing of CNT and CNF produces an array of nanopores accessible to hydrogen, directly from the edge of the material (Chambers *et al.*, 1998; Park *et al.*, 1999). The hydrogen penetrates the nanopores formed by the layers of CNF and the interior of CNT and, forming an intercalated layer of hydrogen (Cao *et al.*, 2001b; Chen *et al.*, 2001; Dillon *et al.*, 1997; Gadd *et al.*, 1997; Ma *et al.*, 2002; Meregalli *et al.*, 2001). In addition to this, the nanopores

could undergo expansion in order to accommodate hydrogen in a multilayer configuration (Park *et al.*, 1999). A slight variation to this theory was proposed by Browning *et al.*, hypothesising that the exposed edge sites of the graphene sheets, which constitute the bulk of the CNF surface, catalyse the dissociation of hydrogen, followed by intercalation of the graphene layers (Browning *et al.*, 2002). Others have proposed that the hydrogen condenses in the hollow cores of CNT and CNF caused by a capillary effect (Fan *et al.*, 1999; Ma *et al.*, 2001). Another theory is that the hydrogen dissociates on the metal catalyst with the CNF and CNT left from their preparation and spills over in the carbon structure (Lueking *et al.*, 2002). The presence of functional groups has also been attributed with the enhancement of hydrogen storage capacities, by facilitating stronger bonding (Badzian *et al.*, 2001; Bai *et al.*, 2001; Wang *et al.*, 2002; Zhu *et al.*, 2003). Many, less bold, authors attribute the large hydrogen storage capacities of CNT and CNF to a novel, yet undefined, uptake mechanism (Cheng *et al.*, 2000; Hwang *et al.*, 2002; Liu *et al.*, 1999; Strobel *et al.*, 1999). However, until reliable and repeatable results are obtained the question of the mechanism of hydrogen storage cannot be conclusively answered.

2.6.4 Modelling of hydrogen storage

Modelling is a very useful tool for exploring the possibilities of materials physical properties, without expensive expenditure on experimental equipment. In addition to this, many of the problems that have been attributed to the lack of repeatability of results do not affect modelling. The carbon systems are idealised, with no impurities and with uniform dimensions thus, avoiding the problems of preparation. The inaccuracies from the method of determination are also circumvented, as the systems are theoretical.

However, modelling is limited by the level of understanding of the system being modelled. In the case of hydrogen adsorption on carbon nanomaterials, many questions remain unanswered about the mechanism of storage, and for this reason, modelling is limited to the classical approach of adsorption.

2.6.4.1 Physisorption

In order to study physisorption isotherms of hydrogen on CNF and CNT, the most widely used method is the grand canonical Monte Carlo simulation (Meregalli *et al.*, 2001). This method requires the definition of different potentials, such as those of Lennard-Jones for adsorption and of Silvera-Goldman for hydrogen-hydrogen interactions, and of sampling methods. In addition to this, variables can be added in order to account for quantum effects (Darkrim *et al.*, 1998; Gu *et al.*, 2001). There are several different variables that may be considered for CNF such as diameter, temperature, pressure, graphitic plane d-spacings (Table 2-9).

Material	Conditions	d-spacing (nm)	H_2 Adsorbed (wt%)	Reference
CNF	-196 ˚C, 101 bar	0.7	**4.0**	(Rzepka *et al.*, 1998)
		1.0	**7.0**	
CNF	-73 ˚C, 101 bar	0.7	**2.4**	
		1.0	**2.6**	
CNF	27 ˚C, 101 bar	1.0	**1.2**	
CNF	-196 ˚C K, 101 bar	0.6	**3.0**	(Wang *et al.*, 1999a; Wang *et al.*, 1999b; Wang *et al.*, 1999c)
		0.9	**7.5**	
		0.1	**9.0**	
		0.2	**12.5**	
	25 ˚C, 101 bar	0.6	**0.8**	
		0.9	**1.4**	
		0.1	**1.6**	
		0.2	**2.4**	
CNF	25 ˚C, 100 bar	0.3	**1.5**	(Cracknell, 2001)

Table 2-9 Summary of theoretical studies carried out by grand canonical Monte Carlo simulation for the physisorption of hydrogen on CNF

Similar studies have been carried out for CNT, with the effects of changes in geometry studied in some detail. Change in may result from altering the diameter of the CNT, or of the relative geometry of the CNT. The results do not show many encouraging storage capacities (Table 2-10).

Material	Conditions	Hydrogen Adsorbed (wt%)	Reference
SWNT	20 °C, 101 bar	**37**	(Darkrim *et al.*, 1998)
SWNT	-196 °C, 101 bar	**1**	(Rzepka *et al.*, 1998)
		2.5	
	-73 °C, 101 bar	**0.9**	
		1.4	
	27 °C, 101 bar	**0.8**	
		1	
SWNT	42 °C, 608 bar	**1**	(Gordon *et al.*, 1999)
	12 °C, 608 bar	**1.1**	
	-43 °C, 608 bar	**1.3**	
	-183 °C, 608 bar	**1.5**	
	-123 °C, 608 bar	**1.7**	
SWNT ropes (100 CNT)	25 °C, 101 bar	**3.3**	(Simonyan *et al.*, 1999)
	-196 °C, 101 bar	**23**	
SWNT	25 °C, 50.5 bar	**1**	(Wang *et al.*, 1999a; Wang *et al.*, 1999b; Wang *et al.*, 1999c)
	-196 °C, 50.5 bar	**10**	
Open SWNT	-196 °C, 150 bar	**11**	(Darkrim *et al.*, 2000)
SWNT ropes	27 °C, 101 bar	**1**	(Williams *et al.*, 2000)
	140 °C, 101 bar	**3.75-5.75**	
	-196 °C, 101 bar	**5.5-9.5**	
Open SWNT Triangular arrays	25 °C, 100 bar	**4.7**	(Yin *et al.*, 2000)
	-196 °C, 70 bar	**33**	
SWNT	20 °C, 100 bar	**1.1**	(Gu *et al.*, 2001)
		0.9	
		0.7	
SWNT Bundles of 16	20 °C, 200 bar	**1.6**	(Levesque *et al.*, 2002)
SWNT	25 °C, 120 bar	**0.4**	(Cracknell, 2002)

Table 2-10 Summary of theoretical studies carried out by grand canonical Monte Carlo simulation for the physisorption of hydrogen on CNT

The advantage of grand canonical Monte Carlo simulations is that large systems may be examined and modelled, and that the results are temperature dependent. However, only physisorption systems can be studied.

2.6.4.2 Chemisorption

Monte Carlo calculations are not well suited to for chemisorption simulations, as they lack the ability to deal with quantum-mechanical bond formation and breaking (Ma *et al.*, 2001). For this process, *ab-initio* calculations, sometimes called the semi-empirical quantum technique, have been most widely applied, as they are more sophisticated and can study the nature of the chemical interactions between hydrogen and SWNTs.

However, *ab initio* calculations can only look at the molecular level, unlike grand canonical Monte Carlo simulations, which consider the system as a whole. The calculations may represent very precisely, defined, SWNT systems, but the complexity of the definitions limits the model to molecularly scaled systems

(Froudakis, 2001; Lee *et al.*, 2002b). This current scaling limits *ab initio* modelling to examining hydrogen interactions with the carbons of SWNT, rather than much hydrogen can be adsorbed (Lee *et al.*, 2001c; Lee *et al.*, 2000a).

The work carried out to date, with *ab initio* calculations has successfully proved that the model can be applied to this field. However, more work is required to extend this work in order to allow accurate predictions of quantitative hydrogen adsorption (Froudakis, 2002).

2.7 Summary

Thus far, theoretical research has given more consistent results than experimental studies, which have provided varied and even contradictory results (Dagani, 2002). The major reasons for this is that theoretical, and experimental, research have focused on fundamentally different materials and that the experimental determination of the hydrogen storage capacity of materials at higher pressure has proved to be difficult to achieve accurately.

The materials considered in the theoretical simulations have been well-structured open-ended CNT or CNF, with optimised diameter, and inter tube or layer spacing with no impurities for maximum hydrogen adsorption (Darkrim *et al.*, 1998). Conversely, the carbon nanomaterials have proved difficult experimentally to produce and purify. Most researchers have only been able to produce samples of low purity, due to the presence of amorphous carbon and catalyst remnants, which have proved hard to remove. Additional to this, owing to the nature of the various preparations used, samples are only available in small quantities. This makes accurate measurement of hydrogen adsorption difficult, requiring very sensitive equipment and leading to an inevitable loss in accuracy (Darkrim *et al.*, 2002). This leaves the question of how much hydrogen may be adsorbed on carbon nanomaterials very much unanswered.

2.8 Aims and Objectives

Aim

To determine the viability of high pressure hydrogen storage on carbon materials for mobile applications.

Objectives

- To develop the differential pressure method for the high pressure determination of the hydrogen storage capacities of carbon materials

- To extend the differential pressure method to other hydrogen storage systems

- To determine the hydrogen storage capacities of a series of powdered activated carbons and identify any trends with surface area

- To explore other activated carbon systems for hydrogen storage potential

- To prepare CNF from the catalyst $Cu_5Fe_{85}Ni_{10}$ as per Browning *et al.* (2001)

- To prepare and characterise materials from three series of CNF produced with from Cu-Fe, Cu-Ni and Fe-Ni catalyst systems

- To investigate CNF - Metal Hydride hybrid systems and determine their hydrogen storage capacities (Hwang *et al.*, 2002)

- To investigate the hydrogen storage potential of MWNT and SWNT, and compare with that of CNF

CHAPTER 3
Theory of Analytical Techniques

3.1 Adsorption and surface area studies

Adsorption is defined as the process where a molecule, the adsorbate, forms a bond to a surface, the adsorbent (Gregg *et al.*, 1982). The modes by which adsorption can occur may be split into two broad classifications; physisorption and chemisorption.

3.1.1 Physisorption and chemisorption

For physisorption, the bonding interaction between adsorbate and adsorbent is long range and associated with weak "van der Waals" type interactions. Hence, bonding is characterised by a redistribution of electron density, separately, within the adsorbate and adsorbent. This results in only a negligible exchange of electrons, so the value of the enthalpy of physisorption is of the same order as the enthalpy of condensation for the adsorbate.

In practice, the enthalpy of physisorption is often greater owing to the existence of a surface potential at the interface between the two phases, which is most pronounced in solid-gas interfaces. This is caused by an over-spill of electron charge from the solid into the gas phase, which results in an imbalance of electron density on either side of the interface. The resulting surface potential generates an additional bonding interaction (ε), which becomes more significant as the polarisability of the adsorbate increases, and may be calculated using Equation (3-1), where α_p is the polarisability of adsorbate, and E is the electric field strength, which is proportional the surface potential (Attard *et al.*, 1998).

$$\varepsilon = -\frac{1}{2}\alpha_p E^2 \qquad \textbf{(3-1)}$$

Even with the electron over-spill effect physisorption still only binds the adsorbent and adsorbate very weakly. Thus, the bonding in physisorbed systems is weak and tends to be reversible, resulting in molecules from the adsorbate layer and the gas

phase being in a state of constant dynamic equilibrium, with physisorbed species being easily released by changing the physical conditions of the system.

For chemisorption, the bonding interaction between adsorbate and adsorbent is short range. Hence, it may be associated with an exchange of electrons between the adsorbate and the adsorbent, so may be discussed in terms of the traditional notions of covalent, ionic and metallic bonding. Frequently, if the adsorbate is a molecule, dissociation must occur before chemisorption can take place. The enthalpy of chemisorption depends greatly on the surface coverage of the adsorbate, mostly because of adsorbate-adsorbent lateral interactions.

The basics of chemisorption and physisorption of a diatomic molecule, such as hydrogen, may be examined by considering the thermodynamics factors, which affect the kinetics of adsorption.

> Physisorption   - H_2 (g) $\rightarrow$ H_2 (ads)
> Chemisorption   - H_2 (g) $\rightarrow$ H_2 (ads-precursor) $\rightarrow$ 2H (ads)
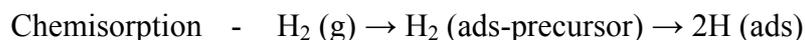
The physisorption of a diatomic molecule requires physical forces only, with no chemical bond-breaking or forming occurring, so the process may be said to be non-activated and associative as no activation barriers need to be over come. Thus, the enthalpy of physisorption of a diatomic molecule is primarily dependent upon the enthalpy of condensation, may be said to be equal to the enthalpy of desorption. This results in a shallow potential energy well at long range from adsorbent surface (Figure 3-1).

The chemisorption of a diatomic molecule requires chemical bonding to occur. Initially, the diatomic molecule adsorbs into a precursor state via a non-activated process, where the enthalpies of adsorption and desorption are equal. However, for the molecule to become chemisorbed it must first dissociate, requiring an activated process. The activation energy barrier of this dissociation (E_{dis}^a) is formed at the intersection of the chemisorption and physisorption potential energy wells. The activation energy requirement, is considerably less than the gas phase dissociation

(D(H-H)), probably due to the adsorbent facilitating dissociation. Consequently, the relative position of the physisorption and chemisorption wells has strong influence over the kinetics of the chemisorption.

The Lennard-Jones potential energy diagram visually illustrates the differences in between chemisorption and physisorption (Figure 3-1). The short-range, and strong, interaction, characteristic of chemisorption, is clearly depicted by the deep and narrow potential energy well at close proximity to the adsorbent. In contrast, the physisorption energy well is shallow, broad and lies at distance from the adsorbent surface, indicating long-range, weaker bonding.
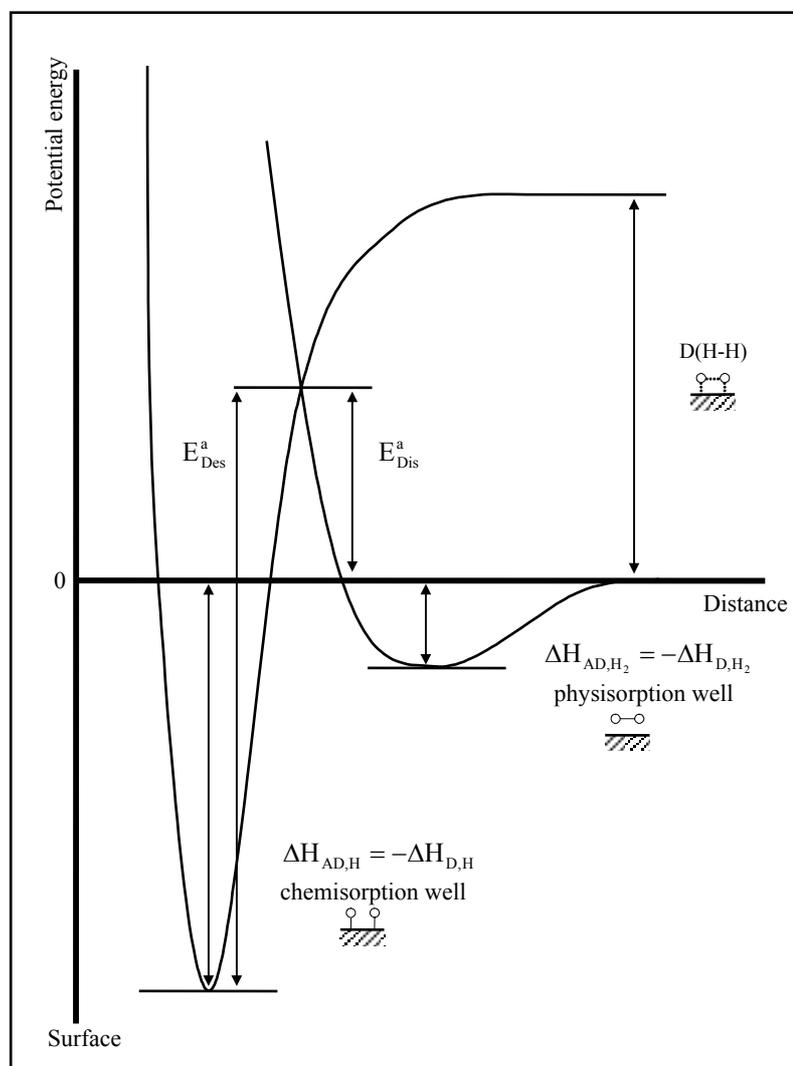
Figure 3-1 Lennard-Jones potential energy diagram for chemisorption and physisorption of a diatomic molecule onto a surface (Attard *et al.*, 1998)

The Lennard-Jones potential energy diagram is a simplification of the real system as the magnitudes of the activation energies are dependent on many parameters, such as the orientation of the incoming adsorbent, rotational and vibrational energies and the characteristics of the surface. However, these factors are beyond the scope of this work and the model qualitatively explains the phenomena of physisorption and chemisorption to an appropriate level of detail. Table 3-1 is a summary of primary characteristics of physisorption and chemisorption that have been discussed.

	Physisorption	**Chemisorption**
Bond type	No electron transfer (van der Waals)	Electron transfer (ionic or covalent)
Nature of adsorption	Associative Reversible	Often Dissociative Sometimes irreversible
Saturation point	Multilayer possible	Limited to one monolayer
Temperature range of adsorption	Near or below the condensation point of adsorbate	No definable limits (molecule dependent)
Kinetics	Non-activated process Fast	Activated process Variable
Adsorption Enthalpy primary dependency	Heat of condensation 5-35 kJ mol^{-1}	Chemical bond 35-800 kJ mol^{-1}

Table 3-1 Summary of comparison between chemisorption and physisorption (Ruthven, 1984)

3.1.2 The adsorption isotherm

Experimentally, when a solid, such as carbon, is exposed in a closed space to a gas at a definite pressure, the solid begins to adsorb the gas, which causes an increase in weight of the solid and a decrease in pressure of the gas (Gregg *et al.*, 1982). The quantity of gas adsorbed is proportional to the mass of the sample and depends on the temperature and pressure of the system, and the nature of the gas and the solid. For a given system at a fixed temperature (T), the amount of gas (n) adsorbed may be defined by Equation (3-2), where p is the pressure of the system.

$$n = f(p)_T \qquad \text{(3-2)}$$

If below the critical temperature of the gas, the formula can be rewritten as Equation (3-3), incorporating the saturation pressure (p_o) of the adsorbate.

$$n = f(p/p_o)_T \qquad \text{(3-3)}$$

The Equations (3-2) and (3-3) are both expressions of the relationship between the amount of gas adsorbed and the pressure of the system at constant temperature; this relationship is known as an adsorption isotherm.

The majority of isotherms that result from physisorption can be divided into five main types, Figure 3-2 as first proposed by Brunauer *et al.* (Brunauer *et al.*, 1940).
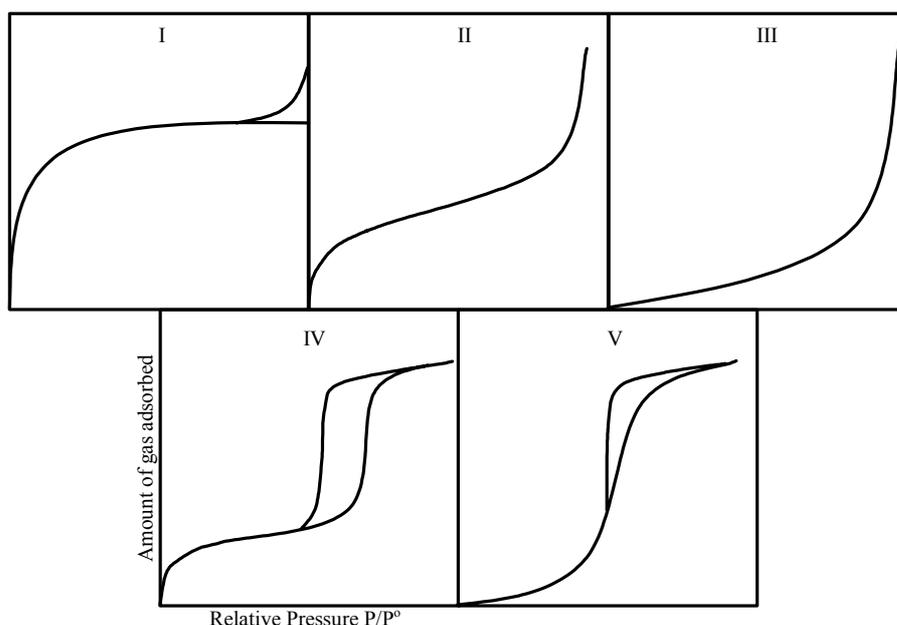
Figure 3-2 The Brunauer, Deming, Deming and Teller (BDDT) classifications of adsorption isotherms

Type	Description	Filling mechanism
I	Microporous 2 nm	Filling of micropores
II	Non porous or macroporous 50 nm	Unrestricted mono-multilayer formation
III	Weak (rare)	Weak interactions, homogenous solid surface
IV	Mesoporous 2-50 nm	Filling of narrow pores that facilitate condensation
V	Mesoporous 2-50 nm	Low energy, homogenous solid surface

Table 3-2 The BDDT classifications of adsorption isotherms

Two of the most widely used models to describe adsorption isotherms are the Langmuir and Brunauer, Emmett, Teller (BET) adsorption isotherms. The Langmuir isotherm is the simplest and was one of the first models to be developed (Langmuir, 1916). From both of these models estimations can be made of the total surface area of a solid.

3.1.2.1 The Langmuir adsorption isotherm

The Langmuir adsorption isotherm model uses the following approximations (Langmuir, 1918):

- The solid surface is uniform and contains a number of equivalent sites, each of which may be occupied by one molecule of adsorbate only.
- A dynamic equilibrium exists between the adsorbate and adsorbent at a given pressure and constant temperature.
- Adsorbate molecules are continually colliding with the surface. If they impact a vacant site they adsorb, if they impact a filled site they are reflected.
- Once adsorbed the molecules are localised

The Langmuir equation (Equation (3-4)) is defined using the pressure of the system (p), the Langmuir constant (b), the amount of adsorbate adsorbed (n), and the monolayer capacity of the adsorbent (n_m).

$$\frac{n}{n_m} = \frac{bp}{1+bp}$$
(3-4)

The Langmuir surface area of the adsorbent (A) may be calculated from Equation (3-5) using Avogadro's constant (L) and the surface area of one molecule of adsorbate (a_m).

$$A = n_m L a_m$$
(3-5)

The major restriction for the use of the Langmuir adsorption isotherm is that it does not consider the multiple layers of adsorbates that may sometimes form on an adsorbent. This can often lead to an over-estimation of the calculated surface area of the adsorbent. By introducing a number of simplifying assumptions, the BET adsorption isotherm provides an extension of the Langmuir monolayer model to multilayer adsorption.

3.1.2.2 The BET adsorption isotherm

The BET adsorption isotherm model uses the following approximations in addition to the Langmuir assumptions (Brunauer *et al.*, 1938):

- Second layer adsorption can only occur on top of the first layer, third on second, fourth on third and can continue to infinity, where the pressure of the system will be equal to the saturated pressure of the adsorbate.

- At equilibrium, the rates of condensation and evaporation are equal for each individual layer.

- When the number of layers is greater than or equal to two, the equilibrium constants and the corresponding values of enthalpy of adsorption (ΔH^{o}_{AD}) and of vaporisation (ΔH^{o}_{VAP}) are equal. For the first adsorbed layer the enthalpy of adsorption is the same as that in the Langmuir case.

The summation of the amount adsorbed in all layers yield the BET equation (Equation (3-6)) (Brunauer *et al.*, 1940). From this, the BET surface area of the adsorbent may be calculated using Equation (3-5), and may be approximated by Equation (3-7) where C is the BET parameter and R the universal gas constant.

$$\frac{p}{n(p_{o}-p)} = \frac{1}{n_{m}C} + \frac{(C-1)}{n_{m}C} \times \frac{p}{p_{o}} \tag{3-6}$$

$$C \approx e^{-(\Delta H^{o}_{AD} + \Delta H^{o}_{VAP})/RT} \tag{3-7}$$

The BET isotherm is the most widely used adsorption isotherm model for surface area studies (Bruch *et al.*, 1997). Current commercial BET machines utilise nitrogen adsorption at -196 ˚C as a standard method. Isotherms are recorded by the stepwise introduction of known amounts of adsorbate and the recording of the equilibrium pressure; from the isotherm produced both Langmuir and BET calculations may be made.

While the concept of an adsorbed layer of gas on the walls of large pores is valid, it becomes unrealistic when the size of the pores is only a little more than one adsorbate molecule wide. Carbon dioxide adsorption experiments at 0 ˚C allows the study of a materials characteristic ultra-microporosity. This is achieved by the

higher temperature of 0 ˚C, relative to -196 ˚C, allowing the activated diffusion of carbon dioxide, and thus facilitating penetration of the ultra-micropores. These structures are invisible to nitrogen adsorption (BET), owing to the relatively low temperature of nitrogen experiments at -196 ˚C, which causes strong adsorption at the mouth of the ultra-micropores blocking them to further adsorption. However, the BET equation cannot be applied to measurements taken with carbon dioxide at 0 ˚C. This has caused the development of additional analysis methods such as the Dubinin-Radushkevich, Dubinin-Astakhov and Density Functional Theory (DFT). DFT analysis is unavailable as an in-house technique, thus is beyond the scope of this thesis.

3.1.2.3 Dubinin-Radushkevich and Dubinin-Astakhov isotherms

The Dubinin-Radushkevich (DR) analysis is an empirical equation, applicable to volume filling in microporous carbons (Webb *et al.*, 1997). The theory uses work by Polanyi by incorporating the adsorption potential (A) described by Equation (3-8). Here ΔG is the change in Gibbs free energy and P/P_o is the reciprocal of the relative pressure.

$$A = RT\ln\left(\frac{p_o}{p}\right) = -\Delta G \qquad \textbf{(3-8)}$$

The DR equation (Equation (3-9)) expresses the volume of gas adsorbed (V) at relative pressure (p/p_o). Here V is the amount of gas adsorbed at the relative pressure p/p_o, V_o is the limiting micropore volume, β is the affinity coefficient and is a variable related to the adsorbate and E_o the characteristic energy of adsorption for the reference vapour (Dubinin *et al.*, 1947).

$$V = V_o\exp\left[-\left(\frac{A}{\beta E_o}\right)^2\right] \qquad \textbf{(3-9)}$$

Substituting Equation (3-8) into (3-9) then extracting the logarithm gives Equation (3-10). The limiting micropore volume being a gas volume must be converted to the liquid volume to effectively characterise the microporosity. The DR method, however, has been found to be limited, often yielding a non-linear result.

$$\ln V = \ln V_o - \left(\frac{RT}{\beta E_o}\right)^2 \times \left(\ln^2 \frac{p_o}{p}\right) \qquad \textbf{(3-10)}$$

A more general equation is the Dubinin-Astakhov (DA) equation (Equation (3-11)) for which the DR equation is a special case. The best linear regression fit may be found by varying n, which usually has a value between 1 and 3, allowing a value for the adsorbent micropore volume to be determined.

$$V = V_o \exp\left[-\left(\frac{A}{\beta E_o}\right)^n\right] \qquad \textbf{(3-11)}$$

3.2 Electron microscopy

Electron microscopes employ a beam of highly energetic electrons in order to examine objects to a very high resolution. Electron microscopes may be used to yield information about the topography, morphology, composition and crystallographic characteristics of nanostructures such as those found in CNF and CNT samples.

Electron microscopes were developed to address the limitations of optical microscopy resulting from the wavelength of light, limiting the resolution to 0.2 μm (Flegler *et al.*, 1993). Looking at the electromagnetic spectrum, ultra violet light has a theoretical resolution of 0.05 μm, but as glass absorbs ultra violet light, it would require quartz lenses making the equipment expensive for only a slight increase in resolution. X-rays are capable of much higher resolution, but cannot be easily refracted to form an image. An alternative to electromagnetic radiation is to utilise sub-atomic particles, which by the wave-particle duality theory, share some of the same properties (Atkins, 1998). Electrons, a charged species, may be refracted easily, using magnetic fields, in order to form an image. In addition, the De Broglie relationship (3-12) where *h* is Planck's constant, m, v and λ are the mass, velocity and wavelength of the molecule respectively, indicates that the stronger the potential, the faster the electron, and so the shorter the wavelength and the better the resolution.

$$\lambda = \frac{h}{mv} \qquad\qquad \textbf{(3-12)}$$

In 1931, the first TEM was developed; this was followed in 1942 with the completion of the first SEM (Flegler *et al.*, 1993). By using a focused beam of electrons instead of a focused beam of light, this barrier was overcome with a resolution of 0.1 nm made possible. Unfortunately, there are problems. As electrons are affected by any atoms they encounter, all electron microscopy must be carried out at high vacuum to avoid the electrons interactions with air molecules.

In operation, a stream of electrons is emitted and accelerated toward the sample to be examined by application of a positive electrical potential. The electrons are focused and confined using metal apertures and magnetic lenses into a thin monochromatic beam. The beam is then centred onto the sample using a magnetic lens. Interactions occur within the irradiated sample, affecting the beam of electrons. These interactions and effects are detected and transformed into an image. The point of detection is the major basic difference between TEM and SEM systems. A typical SEM monitors the reflected electron beam, while a typical TEM monitors the transmitted electron beam. Table 3-3 compares the difference and similarities between typical SEM and TEM systems.

	TEM	**SEM**
Voltage	25~300 kV	0.5~30 kV
Illumination source	Electron	Electron
Observation	Vacuum	Vacuum
Resolution	0.5~0.1 nm	7~0.6 nm
Magnification	10 – 1000 k	100 - 800 k
Depth of field	0.004-0.006 mm	0.003-1 mm
Field of view	Small	Large
Sample size	Small	Large
Sample coating	None	Metal
Image	Transmitted image	Surface image

Table 3-3 Summary of comparison between SEM and TEM (Flegler *et al.*, 1993)

3.2.1 Scanning Electron Microscopy

A typical SEM primarily yields information about a sample's topography and morphology, but with additional equipment can yield information about the composition of the sample in an area as small as 1 μm^2. The highest resolution achievable by a modern SEM is approximately a nanometer.

The basic design of an SEM is illustrated in Figure 3-3. The scanning coils, the feature that SEM takes its name from, scan the beam in a grid-like fashion, dwelling on points for a period of time determined by the scan speed. The objective lens then focuses the scanning beam on the part of the sample to be studied. When the electron beam strikes the sample interactions occur, which are detected by various instruments, such as secondary and backscatter electron detectors. Before the beam moves to its next point these instruments count the number of interactions and a pixel is displayed on a monitor whose intensity is proportional to the number of interactions counted. This process is repeated until the grid scan is complete, creating an SEM image.

Electron gun

First condenser lens

Condenser aperture

Second condenser lens

Electron beam

Objective aperture

Scan coils

Objective lens
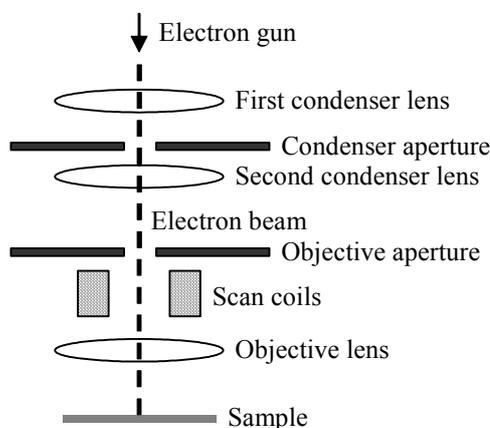
Sample

Figure 3-3   Basic schematic of a typical SEM (Edwards, 1989)

3.2.2 Transmission Electron Microscopy

TEM primarily yields information about a sample's morphology and crystallography information, capable of detecting atomic scale in areas of a few nanometers. The highest resolution of a modern TEM is sub-nanometer.

A basic schematic of a typical modern TEM can be seen in Figure 3-4. The electron gun produces a stream of monochromatic electrons. The condenser lenses focus the beam to a small, thin and coherent beam and the condenser aperture removes high angle electrons. The beam then strikes the sample. The electron beam is affected by the structure of the sample. This results in only part of the electron beam being transmitted through certain parts of the sample. The objective aperture enhances the contrast of the image by blocking diffracted, high angle, electrons and the selected area aperture allows control of the area viewed. The intermediate and projector lenses act to enlarge the image. Finally, the beam hits the phosphor image screen generating light creating an image. The darker regions of the TEM image originate from areas where fewer electrons were transmitted and so represent the denser areas of the sample.
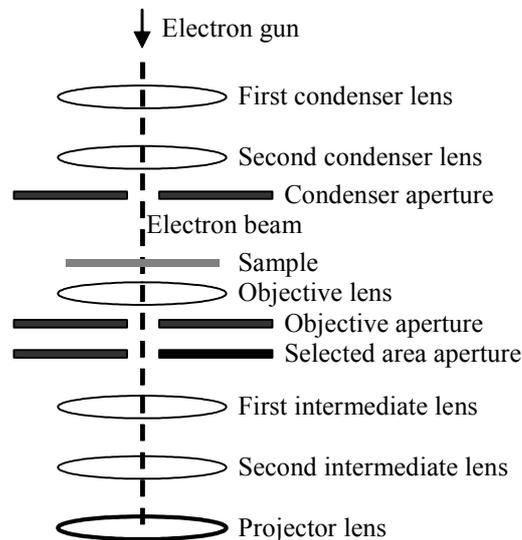
Figure 3-4 Basic schematic of a typical TEM (Edwards, 1989)

Another useful function of TEM analysis is the ability to be able to focus on the diffraction pattern of the electron beam caused by selected areas of the material being studied. The diffraction pattern yields information about the crystalline structure of the material, this is particularly useful for studying CNT and CNF, as the different crystal structures have signature diffraction patterns.

| CNT (MWNT shown) | CNF - Platelet | CNF - Herringbone |
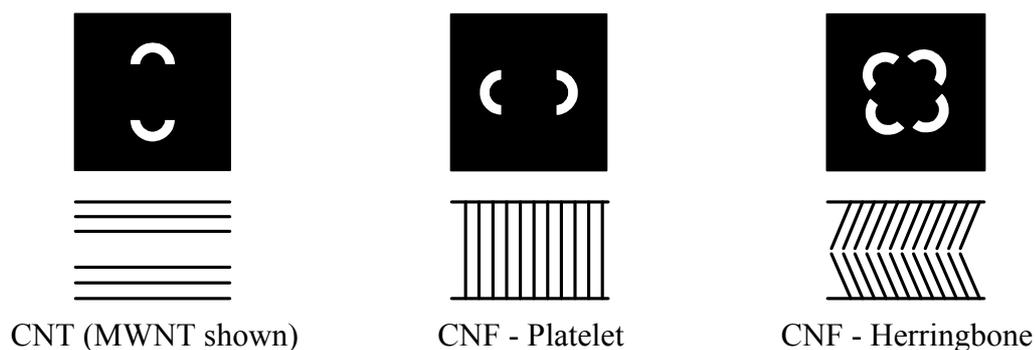
Figure 3-5 Schematic of diffraction patterns indicative of the crystal structures of CNT, platelet CNF and herringbone CNF

3.3 Atomic absorption spectroscopy

Atomic absorption (AA) spectroscopy utilises the absorption of light in order to measure the concentration of gas-phase atoms (Dean *et al.*, 1997). This allows the determination of the concentration of a specific metal in a mixture, as found in the catalyst for CNF preparation which will be discussed later in this thesis (Chapter 7).

All atoms and their components have energy. Unless excited, atoms exist in their most stable state; their ground state. The application of energy, such as thermal or electromagnetic radiation, can change the energy state of an atom, increasing it to an excited state. In theory, there are an infinite number of excited states, however, the higher the excited state the lower the number of atoms from a given population that have a enough energy to reach each level (Welz *et al.*, 1999). These energy states are not continuous but separated by discreet energy gaps known as quantum transitions. The transition from the ground state (E_0) to the first excited state (E_1) requires the atom to absorb energy ($\Delta E_{0 \to 1}$), to relax from the exited state an equivalent amount of energy must be emitted (Figure 3-6). Every element has specific ΔE that they will absorb and emit which correspond to specific wavelengths of the electro-magnetic spectrum.
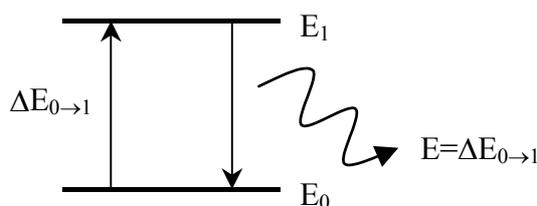
Figure 3-6 Energy diagram of an atom showing excitation to the first excited state followed by relaxation to the ground state by the emission of an electromagnetic wave

The relationship between energy transition and the wavelength (λ) is described by Equation (3-13) where h is Planck's constant (Atkins, 1998).

$$\Delta E = \frac{h}{\lambda}$$
                                                                                    (3-13)

A flame atomic absorption spectrometer consists of a hollow cathode lamp, a nebuliser, the flame, a monochromator and a photomultiplier tube (Figure 3-7) (Ebdon *et al.*, 1998). The hollow lamp uses a cathode made of the element of interest with a low internal pressure of an inert gas. A low electrical current is used to excite the element causing it to emit a few spectral lines of characteristic wavelength, providing a constant and intense analytical light line for the analysis. Samples are introduced into the instrument through a nebuliser and are vaporised in the acetylene flame. The flame destroys any molecules and breaks down complexes creating the atomised form of the elements. The AA utilised for work in this thesis has a slot type flame to increase the path length, and thus to increase the total absorbance as stated in the Beer Lambert law (3-14) where A is the measured absorbance, ε is a wavelength-dependent absorptivity coefficient, b is the path length, and c is the analyte concentration.

$$A = \varepsilon bc$$
                                                                                    (3-14)

The light then passes through a monochromator in order remove scattered light of other wavelengths from the flame and is detected using a photomultiplier tube. The analyte concentration is determined from the amount of absorption. Concentration measurements are usually determined from a working curve after calibrating the instrument with standards of known concentration.
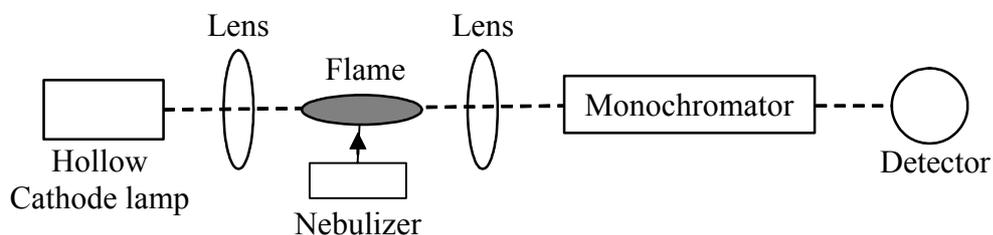
Figure 3-7 Basic schematic of a typical atomic absorption spectrometer

3.4 X-Ray Diffraction

XRD utilises the diffraction of an incident beam of x-rays in order to examine the crystal structure of a material. The x-ray diffraction pattern of a pure substance is unique and thus a fingerprint of the substance. The powder diffraction method is ideally suited for characterisation and identification of crystalline materials, such as graphite, CNF and CNT.

The wavelength range of x-rays is of the same order of magnitude as the distance separating ions or atoms in a crystal, *ca* 100 pm (Warren, 1990). The comparable size of the wavelength and inter-species spacing causes a crystal to diffract an x-ray beam passing through it. The crystal diffracts the beam at signature angles depending on the crystal orientation and structure, and x-ray wavelength (Edwards, 1989). X-ray beams are primarily diffracted by the electron density of a crystal, denoted by peak in the recorded XRD pattern. Analysis of the diffracted beams allows the creation of an electron density map of the crystal, from which information about the crystal structure of the material can be deduced.

A typical x-ray diffractometer utilises an x-ray tube to generate x-rays by bombarding a metal target with high energy electrons, *ca* 10-100 keV, causing emission of core electrons. An electron from the outer shell then fills the vacant hole in the inner shell and emits an x-ray photon. Molybdenum and copper are common targets, as they both produce strong x-ray emissions at 0.071 and 0.154 pm respectively (Cullity *et al.*, 2001). The beam created by the x-ray generator strikes the sample and is diffracted and then detected by either photographic film or a movable proportional counter (Figure 3-8).
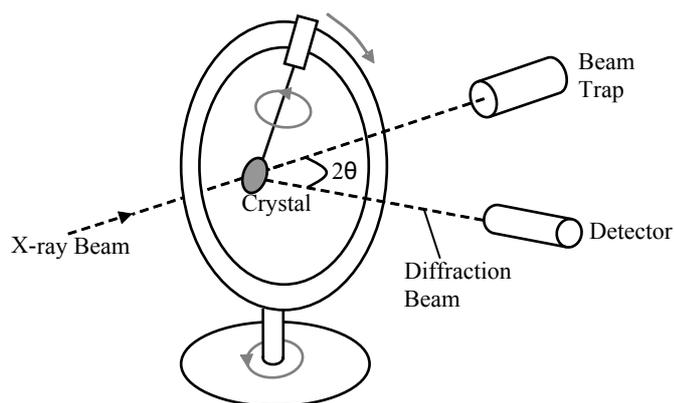
Figure 3-8 Schematic of an x-ray diffractometer (Shriver *et al.*, 1999)

The peaks in an x-ray diffraction pattern are directly related to the atomic distances which can be explained using geometry (Figure 3-9).
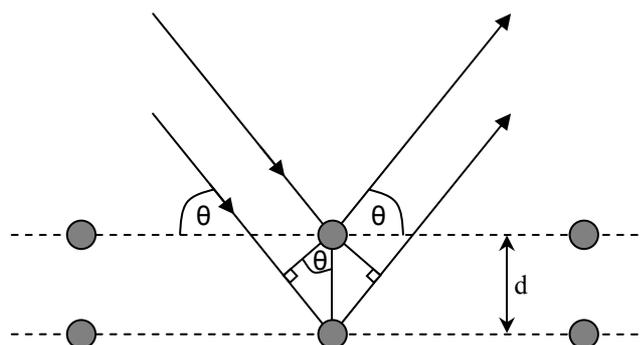
Figure 3-9 Geometrical representation of Bragg's Law

This relationship is described by Bragg's law (3-15) where λ is the wavelength of the x-ray and θ the scattering angle (Atkins, 1998).

$$\lambda = 2d\sin\theta \qquad \textbf{(3-15)}$$

3.5 Gas chromatography

The sample is introduced into the gas chromatograph (GC) inlet through a septum where it is heated (*ca* 150-280 ˚C), and if the sample is a liquid, it is vaporised and swept onto the column by an inert carrier gas such as helium or nitrogen. The sample flows through the column and is separated into its constituent parts, if a mixture, via the chromatographic process (Williams *et al.*, 1995). As the individual sample components emerge from the column, they pass into the detector, which in this study were a mass spectrometer (MS), flame ionisation detector (FID) and thermal conductivity detector (TCD).

3.5.1 Mass-spectrometry

Gas chromatography mass-spectrometry (GC-MS) combines the resolving power of capillary GC with the sensitivity of quadrupole mass spectrometry (Figure 3-10) (Skoog, 2000). This, enables the separation, quantification and identification of many components from an organic mixture, such as the polyaromatic-hydrocarbons (PAH) produced by gasification reactions at higher temperature by certain catalysts, which will be discussed in chapter 7.
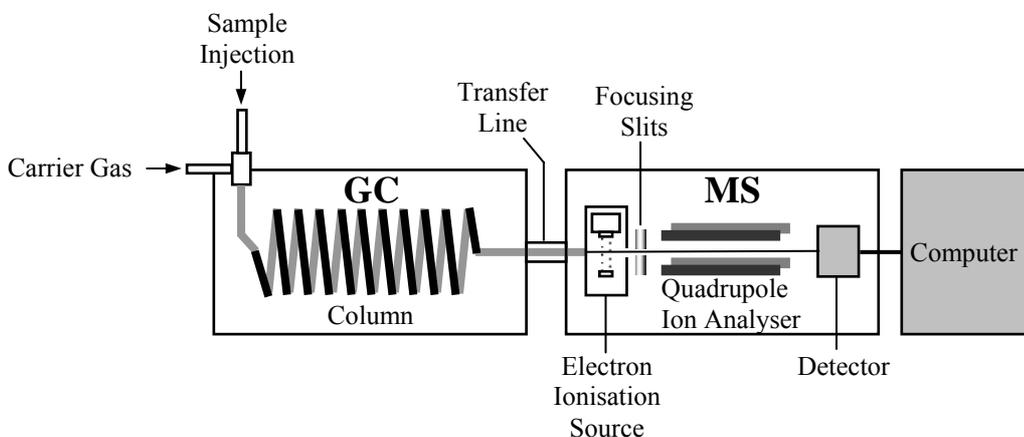
Figure 3-10 Schematic representation of a GC-MS

On entering the mass spectrometer, the separated components are ionised by interaction with a beam of electrons (10 eV), causing the loss of an electron to form a molecular ion. This process produces both positive and negative ions but usually only positive ions are analysed. Once ionised, a small positive potential is used to repel the positive ions out of the ionisation chamber, which are then focussed by a series of slits into a quadrupole mass spectrometer.

The quadrupole mass analyser consists of four parallel cylindrical rods. Opposite rods are electrically connected, with one pair having a positive, and the other a negative voltage applied. Both voltages comprise RF and direct current (DC) components. The RF component between each pair of rods is *ca* 180 ^{o} out of phase, which causes ions of successive *m/z* (mass/charge) values to be transmitted. Ions passing through the mass analyser impinge on an electron multiplier, which amplifies the initially small current by up to six orders of magnitude. The current is converted into a voltage by a preamplifier and recorded ready for manipulation. The entire mass range of *ca* 50 to 550 atomic mass units may be scanned over each gas chromatograph peak, or else data may also be collected for a number of selected *m/z* values. Scanning the complete range facilitates the structural elucidation and identification of unknown compounds, while limiting the scanning range decreases the amount of data but increases sensitivity. The characteristic fragment ion *m/z* values for some important PAH are listed in Appendix 6.

3.5.2 Flame ionisation detection

The FID detector is widely used for the detection of hydrocarbons due to its high sensitivity, large linear response and the low noise levels that are achievable (Skoog, 2000). In the detector, hydrogen is added to the carrier gas and the eluent is mixed with oxygen and combusted in a burner equipped with a pair of electrodes (Figure 3-11). Most organic species, when combusted, produce ionic intermediates, which are collected and detected at the electrodes.
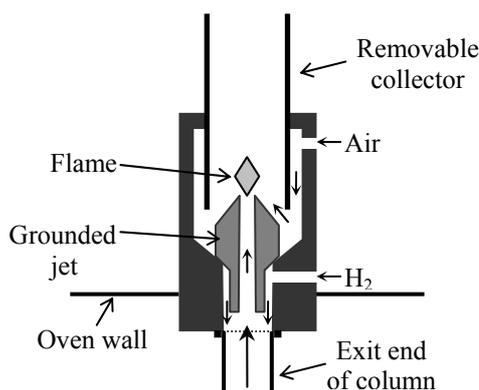
Figure 3-11 Schematic representation of a typical FID

3.5.3 Thermal conductivity detection

The TCD detector was one of the earliest detectors used with GC and is still widely used today. This is mainly due to its simplicity, large linear response range and the general response to organic and inorganic species (Skoog, 2000). The detector consists of an electrically heated source, the temperature of which, at constant electric power depends on the thermal conductivity of the surrounding gas. The heated element may be a fine platinum, gold or tungsten wire (Figure 3-12 a), the electrical resistance of which depends upon the thermal conductivity of the gas. The detectors are incorporated in two arms of a simple bridge circuit (Figure 3-12 b). The bridge circuit cancels the effects of the thermal conductivity of the carrier gas, and minimises the effect of variations in temperature, pressure and electrical power. In this study, TCD is used to detect the concentration of hydrogen in a gas. Helium is usually used as the carrier gas for TCD, however the thermal conductivity of hydrogen very similar to helium but is roughly seven times larger than nitrogen (Laby *et al.*, 1973). Thus even small amounts of hydrogen are readily detectable when using nitrogen as the carrier gas (chapter 7).

(a)   (b)
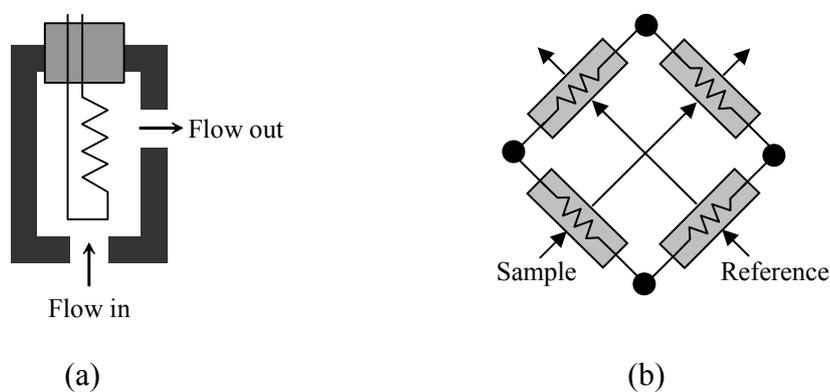
Figure 3-12 Schematic representation of a typical TCD

CHAPTER 4
Methodology

4.1 CNF preparation

4.1.1 Catalyst preparation

4.1.1.1 Transition metal catalyst

Copper nitrate trihydrate ($Cu(NO_3)_2.3H_2O$), nickel nitrate hexahydrate ($Ni(NO_3)_2.6H_2O$) and iron nitrate nonahydrate ($Fe(NO_3)_3.9H_2O$) were mixed in the desired stoichiometric quantities and dissolved in distilled water at a metal oxide concentration of 5 g 100 cm^{-3}. The solution was then stirred at room temperature for ten minutes in order to ensure that all the transition metal salts had completely dissolved. The metals were then precipitated as hydroxides by adding a four equivalent excess of sodium hydroxide, initial experiments employed ammonium bicarbonate as the base. The precipitate was filtered through a glass sinter of porosity 4 and washed several times with warm distilled water. The precipitate was dried for 24 hours at 107 ˚C and then was broken into smaller lumps and calcined for 4 hours in air at 400 ˚C. The resulting product was a stoichiometric, mixed metal oxide.

4.1.1.2 Alkali-earth transition metal catalyst

Magnesium nitrate hexahydrate ($Mg(NO_3)_2.6H_2O$) and nickel nitrate hexahydrate ($Ni(NO_3)_2.6H_2O$) were mixed in stoichiometric quantities. Citric acid was added in a 1.1 equivalent excess to the amount of magnesium nitrate hexahydrate present. Distilled water was then added, 10 ml 8.5 $mmol^{-1}$ metal ions. The solution was sonicated for ten minutes in order to ensure that the reagents had completely dissolved. The solvent was evaporated for 72 hours at 50 ˚C and dried further for 48 hours at 107 ˚C. The resulting solid was then calcined in air at 600 ˚C. The solid product was a stoichiometric, mixed, metal oxide relative to the precursor metal nitrates used.

4.1.2 Chemical vapour deposition

The investigation of CVD utilised a custom built apparatus. Hydrogen, argon and ethylene gases were piped into the apparatus, and the flow rates controlled by needle valves and rotameters (Figure 4-1). The reactor was a quartz tube (100 cm long, 6 cm diameter) in a tube furnace controlled by PID (proportional integral derivative), which was capable of reaching temperatures up to 800 ˚C. The ends of the reactor were sealed with rubber bungs fitted with inlet and outlet gas pipes.

V1	Diaphragm valve
V2	Ball valve
V3	In-line regulator
V4	Needle valve
V5	Needle valve
V6	Needle valve
FBA	Flash back arrester
R1	Ethylene rotameter (0-100 ml min^{-1})
R2	Argon rotameter (0-100 ml min^{-1})
R3	Hydrogen rotameter (0-250 ml min^{-1})
H1	Furnace, PID controlled (1200 W, max 1000 ˚C)
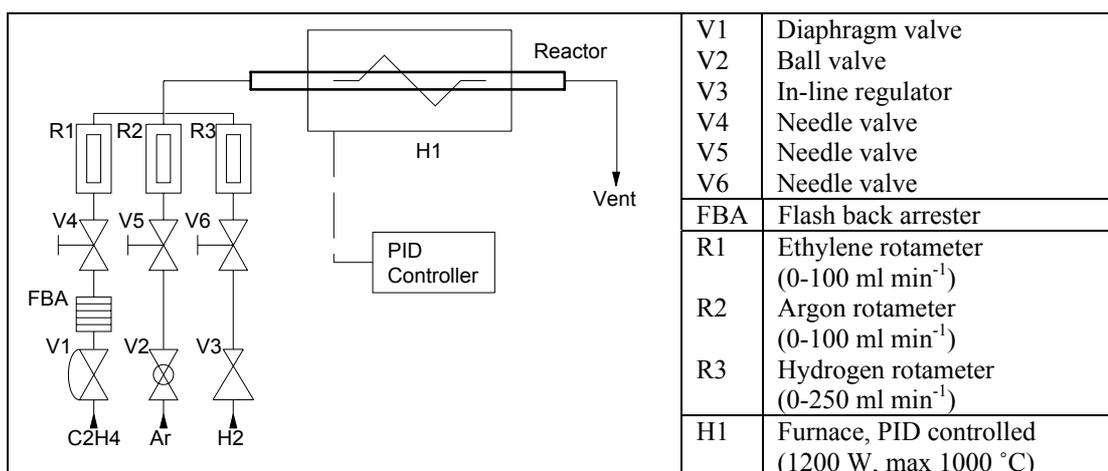
Figure 4-1 Schematic representation of CVD apparatus

The catalyst precursor (50 mg) was crushed in an agate pestle and mortar and placed in a quartz reaction vessel (20 cm long, 4 cm diameter) positioned in the centre of the furnace. The catalyst precursor was then reduced in a stream of hydrogen (100 ml min^{-1}) at 450 ˚C for 16 hours. The temperature profile for a typical CVD run is shown in Figure 4-2. The reaction variables were the time (30-300 min), temperature (450-900 ˚C), catalyst (copper, iron and nickel alloys) and reactant gas composition (ethylene and hydrogen gas mixtures).
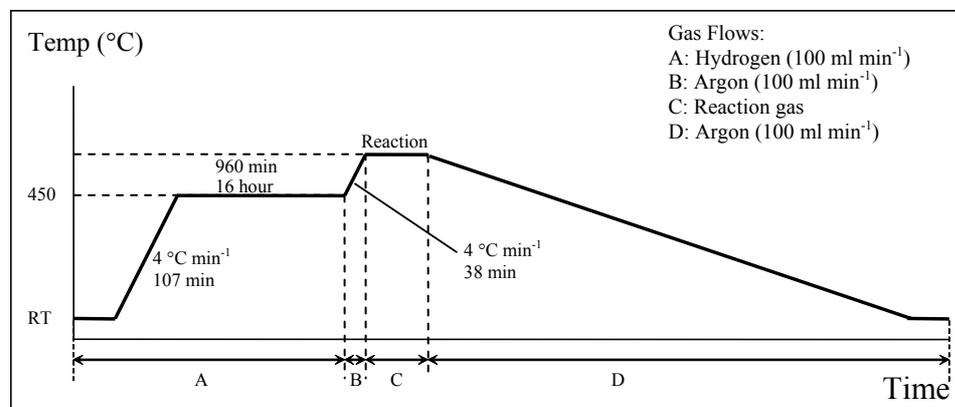
Figure 4-2 Temperature profile of the operating procedure for CNF preparation by CVD

4.1.3 Carbon nanofibre post production treatments

4.1.3.1 Annealing

The annealing procedure utilised a custom built apparatus shown diagrammatically in Figure 4-3. Argon was employed as the inert atmosphere. The reactor was a quartz tube (110 cm long, 5 cm diameter) situated in a tube furnace, capable of reaching temperatures up to 1100 ˚C. The ends of the reactor were sealed with silicon bungs fitted with inlet and outlet gas pipes.
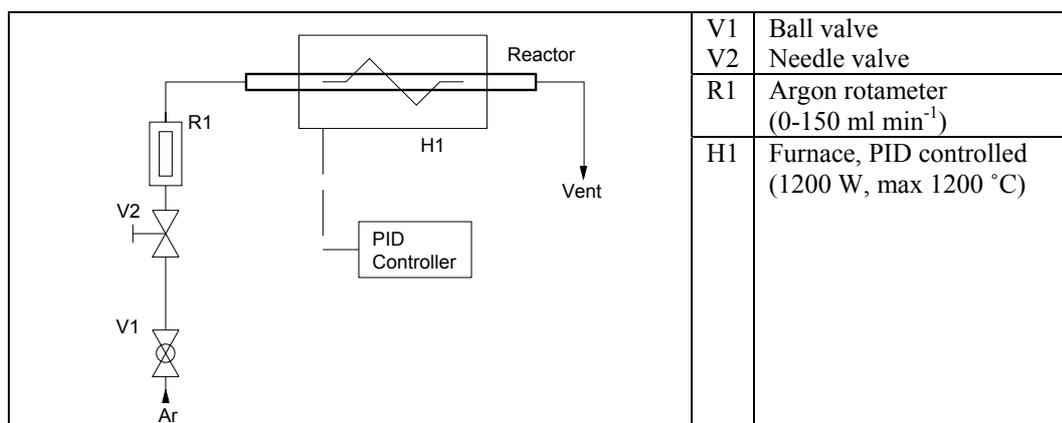
Figure 4-3 Schematic representation of annealing apparatus

A CNF sample (2 g) was placed in quartz reaction vessel (20 cm long, 4 cm diameter) sited in the centre of the quartz tube. The annealing profile for a typical experiment is shown in Figure 4-4.
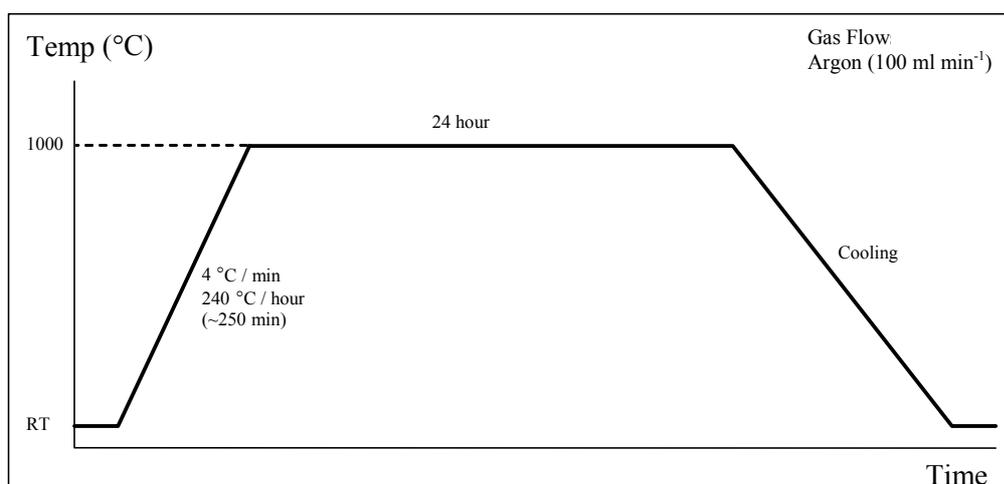
Figure 4-4 Temperature profile for the annealing of CNF

4.1.3.2 Activation

4.1.3.2.1 Carbon dioxide physical activation

The carbon dioxide physical activations were carried using the apparatus shown in Figure 4-5. The reactor was a quartz tube (100 cm long, 6 cm diameter) with its ends sealed with rubber bungs fitted with inlet and outlet gas pipes sited in a tube furnace piped to carbon dioxide and argon.
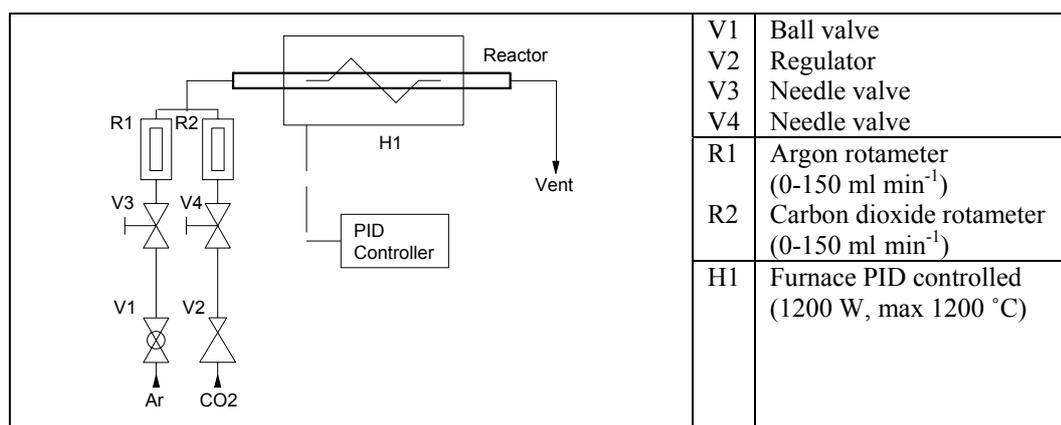
Figure 4-5 Schematic representation of carbon dioxide physical activation apparatus

A CNF sample (2 g) was placed in a quartz reaction vessel (20 cm long, 4 cm diameter) and situated in the centre of the quartz tube. The carbon dioxide physical activation profile for a typical experiment is shown in Figure 4-6. The reaction variables were the activation time (0-45 min) and temperature (900-1000 ˚C).
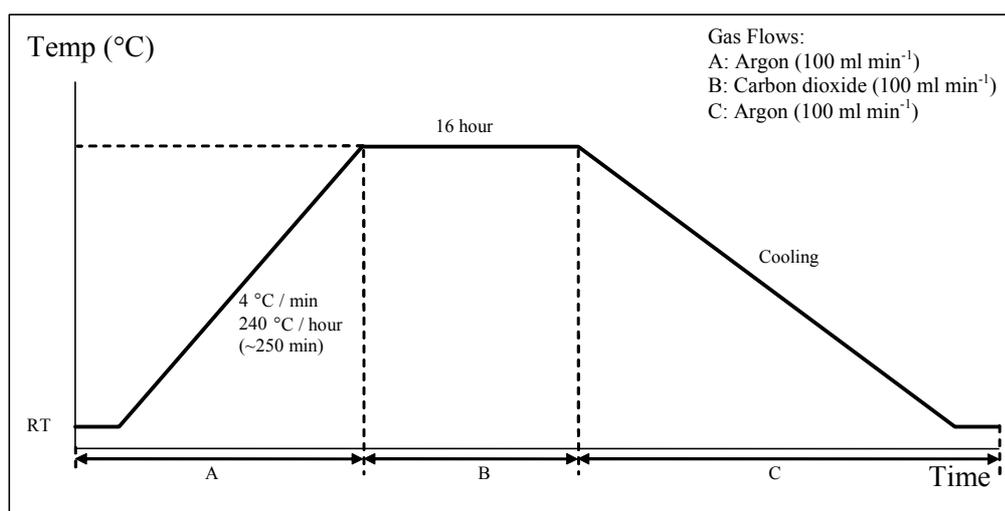
Figure 4-6 Temperature profile for the carbon dioxide physical activation of CNF

4.1.3.2.2 Potassium hydroxide chemical activation

CNF (1 g) were mixed with potassium hydroxide (1 g, 0.02 mol) and distilled water (20 ml). The mixture was heated at 85 ˚C for 4 hours with stirring. The mixture was dried at 107 ˚C for 24 hours. The mixture was then heated (30 ˚C min^{-1}) under nitrogen using the apparatus and procedure described in section 4.1.3.1, with time (15-45 min) and temperature (500-1000 ˚C) used as reaction variables. After cooling, hydrochloric acid (250 ml, 0.5 M) was added to the mixture and heated at 80 ˚C for 30 min. The mixture was then filtered and washed with distilled water until the pH of the filtrate reached pH 6. The CNF were dried at 107 ˚C for 24 hours.

4.1.3.3 Demineralisation

The demineralisation experiments were carried out using 0.3 g of CNF. The variables for the reactions were acid identity (hydrochloric or nitric acid), acid strength (1-6 M), temperature (20-70 ˚C) and time (3 hours - 1 week). After each experiment the CNF were washed repeatedly with distilled water until the pH of the filtrate returned to pH 6. The CNF were dried at 107 ˚C for 24 hours.

4.2 Activated carbon treatments

4.2.1 Palladium doping

Picazine, a commercial activated carbon, (10 g, 28.5 wt% moisture) was mixed with palladium nitrate solution (20 ml, 0.8 M) and distilled water (20 ml), left for 24 hours then dried at 107 ˚C for 24 hours. The palladium was then reduced under hydrogen (100 ml min^{-1}) at 450 ˚C for 2 hours (Figure 4-7) using the apparatus shown in Figure 4-1. The palladium content was confirmed by ashing at 800 ˚C.
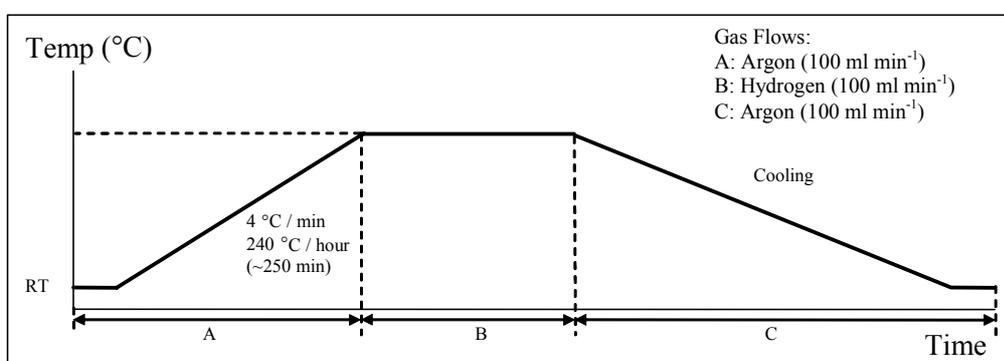
Figure 4-7 Temperature profile for the reduction of palladium doped picazine

4.3 Analysis

4.3.1 Hydrogen storage capacity determination

A full operating procedure for the high-pressure adsorption apparatus (HPAA) is included in Appendix 1 and the design and optimisation of the apparatus will be discussed in Chapter 5. The helium and hydrogen were purified using a liquid nitrogen trap for all procedures.

4.3.1.1 Apparatus

X1	Three way valve
X2	Ball valve
X3	Needle valve
X4	Needle valve
X5	Needle valve
X6	Diaphragm Valve
X7	Remotely controlled inter-linked bellows valves (normally closed)
X8	Remotely controlled inter-linked bellows valves (normally open)
P1	Analogue pressure gauge (0-200 bar)
P2	Vacuum gauges
P3	Pressure transducer (-1-160 bar)
P4	Differential pressure transducer ($\pm$ 5 bar)
R1	Gas reservoir 1
R2	Gas reservoir 2
S1	Sample cell 1
S2	Sample cell 2
H1	Furnace PID controlled (1200 W, max 1200 ˚C)

PID2	PID controller for temperature enclosure
PID1	PID controller for H1
IT1	Independent apparatus temperature indicator
IP3	P3 indicator
IP2	P2 indicator
SP	Main power switch
SH1	H1 isolator switch
SX7	X7 actuator switch
STE	Temperature enclosure control power switch
SH3	Switch to isolate large heaters

Figure 4-8 Schematic of HPAA and the control box

4.3.1.2 Pre-measurement procedure

4.3.1.2.1 Sample loading

A sample container of known mass was filled with the sample (0.5-2 g) for analysis. The exact mass of material was determined. A glass wool plug (0.5 g) was placed above the sample in the container in order to keep the material in place during a run. The sample container was attached to the sample limb, for example S1, and an empty container attached to vacant limb, S2, using the o-ring fitting.

4.3.1.2.2 Free space analysis

The apparatus was carefully evacuated to 10^{-3} torr and the sample cells isolated. The sample limb was isolated from the reference limb by disconnecting the top interlinked valves (X7). The data logger was started. The sample reservoir was then filled with helium (~4 bar) and the sample limb isolated. The sample cell was exposed to the helium in the sample reservoir. From the changes in pressure relative to vacuum, the free space could be determined.

4.3.1.2.3 Degassing methods

Three different degas procedures were mainly used for the preparation of samples, prior to a hydrogen adsorption run.

DG1

The apparatus was carefully evacuated and flushed with helium (~2 bar) three times finishing with the system at vacuum. The vacuum was maintained until a pressure of 10^{-3} torr was achieved.

DG2

The apparatus was carefully evacuated and flushed with helium (~2 bar) three times finishing with the system at vacuum. The furnace was raised into position around the sample cell with heat guards preventing heat from escaping, and a compressed air flow cooling the sample cell feed pipe. The temperature was raised to 150 ˚C (4 ˚C min^{-1}) and maintained until a 10^{-3} torr vacuum was achieved. The furnace was turned off and lowered from the sample cell, which was allowed to cool.

DG3

The apparatus was carefully evacuated and flushed with helium (~2 bar) three times finishing with the system at vacuum. The furnace was raised into position around the sample cell with heat guards preventing heat from escaping and a compressed air flow cooling the sample cell feed pipe. The temperature was raised to 150 ˚C (4 ˚C min^{-1}) and maintained for 30 minutes. The apparatus was then filled with hydrogen (~10 bar). The furnace was then turned off and lowered from the sample cell. This process is repeated twice. The DG2 procedure was then carried out.

4.3.1.3 Analysis procedures

There were two main analysis procedures used with HPAA. The "standard" procedure operated with the entire apparatus at the same temperature (30 ˚C). The "elevated temperature" procedure operates with the sample cell at an elevated temperature.

4.3.1.3.1 Standard procedure

The temperature enclosure was closed and the temperature equilibrated at 30 ˚C using the data logger to monitor the temperature fluctuations. The apparatus was maintained at vacuum following the degas process. The sample cells were isolated from the reservoirs, which were then pressurised with the adsorbate gas (helium or hydrogen) to the required pre-expansion pressure. The reservoirs were isolated from each other and the apparatus isolated from the adsorbate gas supply. The data logger was started, recording temperature, pressure and differential pressure. The reservoir was then expanded to the sample cells. The pressure and temperature fluctuations were monitored for 8 hours. At the end of the experiment, the data logger was turned off and the apparatus was depressurised slowly.

4.3.1.3.2 Elevated temperature procedure

The experiment was started as described in section 4.3.1.3.1. The pressure and temperature fluctuations were monitored until equilibrium was achieved. The furnace was then raised into position around the sample cell and the temperature ramped (4 ˚C min^{-1}) to the desired level, with the remainder of the apparatus

maintained at 35 ˚C. The pressure and temperature fluctuations were monitored until equilibrium was achieved. The furnace was then removed and the system brought to 30 ˚C and the final pressure and temperature measurements were made. At the end of the experiment, the data logger was turned off and the apparatus was slowly depressurised.

4.3.2 Standard adsorption analyses

4.3.2.1 Nitrogen and carbon dioxide studies

Nitrogen and carbon dioxide adsorption studies were carried out using a standard ASAP 2010 (Micromeritrics, USA) at -196 ˚C and 0 ˚C using standard methods. The samples were degassed at 115 ˚C under vacuum. Additional nitrogen analysis was carried out on materials with a surface area over 2000 m^2 g^{-1} in order to enhance the accuracy of the measurement with a modified ASAP 2010 at -196 ˚C. The apparatus utilised a turbo-molecular pump, a long equilibrium time (25 sec), with the low pressure points using a small gas introduction value (5 g cm^{-3}) and samples degassed at 400 ˚C under vacuum. The BET and DA isotherms were required to achieve a correlation coefficient of over 0.999 in order to be considered reportable.

4.3.3 Atomic absorption analysis

The atomic absorption analysis was carried out on a Analyst 100 AA Spectrometer (Perkin Elmer, USA). An oxidative air and acetylene flame was used, with 10 cm burner and 10 mm observation heads. Aqueous solutions of copper nitrate trihydrate, nickel nitrate hexahydrate and iron nitrate nonahydrate (5, 10, 20, 30, 50 mg l^{-1}) were used as standards for calibration.

4.3.4 X-ray diffraction analysis

The XRD studies were carried out on a 1050 XRD (Philips Analytical, Netherlands) attached to a x-ray generator (Hilton Brooks, UK) producing copper Kα radiation at a wavelength of 0.15418 nm. Prior to analysis, samples were placed in a gravity mount ensuring that no preferential orientation of the sample occurred before the measurements were recorded.

4.3.5 Scanning electron microscopy studies

The SEM images were recorded on a SX-30 SEM (ISI, USA), a Quanta 600 SEM (FEI, USA) and a DSM-942 SEM (Zeiss, Germany and UK). Prior to analysis, some samples were dispersed, by sonication, in acetone and dried; the remainder were used as prepared. All samples were mounted on aluminium stubs and coated with gold to ensure good conduction.

4.3.6 Transmission electron microscopy studies

The TEM and HRTEM images were recorded on a 2000 FXII 200 kV analytical TEM (JEOL, Japan) and a 4000 FXII 400 kV analytical TEM (JEOL, Japan) respectively. Prior to analysis, samples were dispersed, by sonication, in isopropyl alcohol and dried. The samples were mounted for analysis on a copper grid coated in a perforated carbon film.

4.3.7 Thermo-gravimetric analysis

The TGA analysis was recorded on a Pyris 1 TGA (Perkin Elmer, USA). Carbon dioxide activation simulation was carried out under carbon dioxide (20 ml min^{-1}) up to 1000 ˚C (25 ˚C min^{-1}). Potassium hydroxide activation simulation was carried out under nitrogen (20 ml min^{-1}) up to 1000 ˚C (25 ˚C min^{-1}).

4.3.8 Gas-chromatography mass-spectrometry analysis

The analysis was carried out on Instruments MD 800 GC-MS (Fisons, UK). Samples were dissolved in dichloromethane and then injected into the GC at 280 ˚C using a helium carrier gas at 100 kPa. The GC used a DB-1 fused silica column (length 50 m, 0.32 mm ID, and 0.25 μm film thickness) for separation. The GC oven temperature program began at 50 ˚C (2 minutes), then it was raised to 300 ˚C (5 ˚C min^{-1}) where it was held for 28 minutes. The transfer line to the MS was maintained at 300 ˚C. The MS (electron voltage 70 eV, source temperature 280 ˚C) scanned over the range of 50-500 Da with scan time of 0.9 sec and with a 0.1 sec interscan delay time.

4.3.9 Gas-chromatograph TCD and FID gas analysis

GC-TCD and GC-FID analysis was carried out on the outlet gas from a selection of CVD experiments that used pure ethylene as the reactant gas. The outlet gas was collected into 1 litre gas bags, over a period of two minutes, at twenty minute intervals. The flow rate was determined by a 25 ml gas bubble meter.

The GC-TCD and GC-FID analysis was carried out on a HRGC 5000 Series (Carlo Erba, Italy) gas chromatograph fitted with FID and TCD detectors using nitrogen as the carrier gas at an inlet pressure of 100 kPa. The GC-FID used a CP-Pora PLOT Q Chrompack capillary column (27.5 m long, 0.32 mm ID, and 0.15 μm film thickness) for separation. The GC-TCD used a stainless steel packed column (2 m long, 4 mm ID), containing Porapak Q, for separation. The GC oven temperature program began at 70 ˚C (3 minutes), and then it was raised to 90 ˚C (40 ˚C min^{-1}) where it was held for 3 minutes. It was then raised to 140 ˚C (40 ˚C min^{-1}) and held for a further 3 minutes. The FID detector was maintained at 240 ˚C and the TCD at 120 ˚C. The TCD filament maintained at 250 ˚C.

CHAPTER 5
Developing the Measurement of High Pressure Hydrogen Adsorption

5.1 Introduction

The measurement of hydrogen adsorption is complicated by many variables that must be considered, understood and controlled in order to ensure accuracy. An objective review of previous work that has been carried out was presented in Chapter 2.

This work carries on from the differential pressure volumetric apparatus that was employed by Mellor (Browning *et al.*, 2002). However, the design and development of the apparatus outlined in the following section was based on knowledge collated in the literature review.

5.2 Differential pressure method

The apparatus developed by Mellor and co-workers was claimed to have several advantages over more traditional volumetric direct pressure measurement apparatus with a single measurement limb (Browning *et al.*, 2002). First, the differential pressure gauge possesses a much higher accuracy than a direct pressure gauge, allowing the accurate monitoring of much smaller fluctuations of pressure. In addition, measurement of the differences in pressure produced between two identical limbs by expanding two reservoirs into two sample cells, it was proposed that the effects of expanding hydrogen, a non-ideal gas, would be cancelled out. This allows only the hydrogen storage properties of the carbon to affect the pressure of the hydrogen. However, Mellor and co-workers found the reproducible production of CNF in amounts greater than 50 mg difficult to achieve.

Using the design by Mellor and co-workers as a starting point, a new hydrogen adsorption apparatus, referred to as the "prototype", was designed and built.

5.3 Prototype high pressure adsorption apparatus

The prototype apparatus was designed on a smaller scale, intended to utilise only 10-15 mg of sample, in order to allow measurements to be made on smaller CNF samples (Figure 5-1). To achieve this, the apparatus only required small limbs in order to achieve a measurable change in pressure caused by a hydrogen storage effect of 1 wt%. This made the use of two reservoirs unnecessary as the sample cells could hold sufficient hydrogen for the experiments. Thus, the prototype apparatus had a single reservoir, which fed two cells, a reference and a sample cell. As both sample cells were expanded at the same time from the same reservoir, the starting pressure in both cells would always be equal.

A	Ball valve	H	Three way valve
B	Ball valve	I	Air tap
C	Check valve	P1	Direct pressure gauge
D	Needle valve	P2	Differential pressure gauge
E	Inter-linked bellows valves	P3	Vacuum gauge
F	Needle valve	H1	Pre-treatment furnace (0-1200 °C)
G	Needle valve	H2	Strip heaters (150 W)
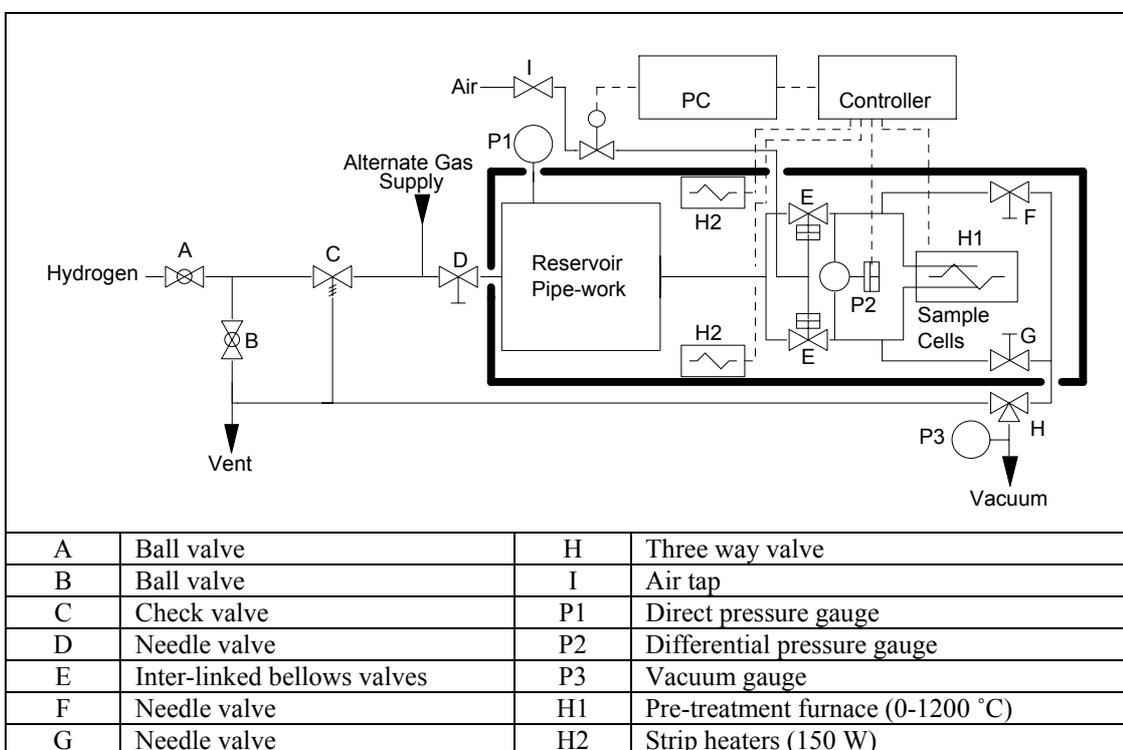
NB The Thick Black line represents the border of the temperature controlled enclosure
   Schematic is in a linear representation, three dimensional information is not included

Figure 5-1 Basic schematic of prototype high pressure adsorption apparatus

The main body of the apparatus was contained within a temperature-controlled enclosure. The enclosure was built out of a stainless steel case using 150 W strip heaters controlled by a PID unit connected to a platinum resistance thermometer (Figure 5-2).   The temperature was monitored by an independent K-type thermocouple, which indicated that the system provided excellent temperature control at 5 °C above ambient with a variance of ± 0.3 °C. The volume of the reservoir was *ca* 90 cm^3 with the sample cells having volumes of 10 and 13 cm^3.

Thus, the pre-expansion pressure for a *ca* 100 bar experiment was required to be *ca* 125 bar.
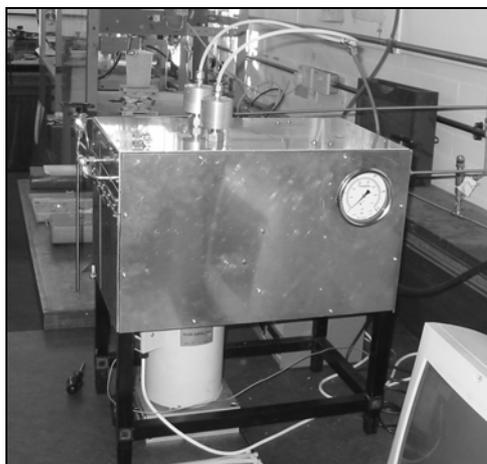
Figure 5-2 Exterior side view of prototype apparatus, showing the outside of the temperature enclosure

5.3.1 Problems encountered

After work began on CNF production, it became apparent that the amount of material that could be reproducibly produced was on a gram rather than a milligram scale (Chapter 7). As the accuracy of any measurements recorded would be higher as a consequence of larger sample size, it was decided to increase the size of the apparatus. In addition, the apparatus had proved difficult to make leak tight due to the three-dimensional compact design and the configuration of the valves and fittings. The cramped working space can clearly be seen in Figure 5-3. Image (a) looks through an inspection hatch at the front end of the apparatus, the two sample limbs may be seen in front of the fans, with the needle valves F and G situated at the top. Due to the design, many of the fittings were difficult to access and could not be adjusted without first removing other fittings and pipe sections. Image (b) looks through an inspection hatch at the side of the apparatus, the sample limbs may be seen to the lower right of the image, with the differential pressure transducer centrally positioned above the fans, and the reservoir pipe work filling the majority of the rest of the box.
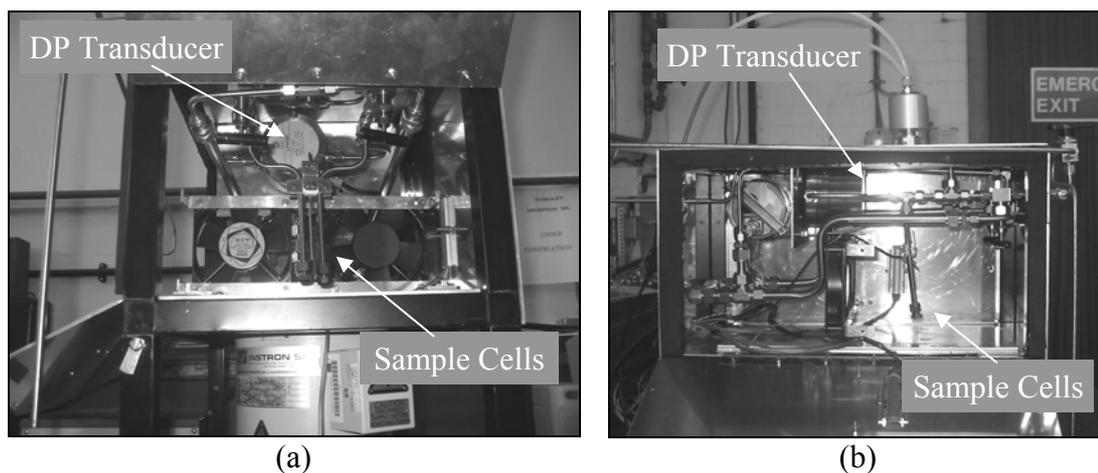
Figure 5-3 Interior views of prototype apparatus (a) Front view of apparatus (b) Side view of the apparatus

The positioning of the key valves also proved to be problematic for leak tight operation, essential for accurate measurements (Figure 5-4). Each sample cell in the prototype apparatus was situated between two valves, a bellows valve (E) and a needle valve (F or G). This created two possible routes for gas to escape through a valve. In addition, valve E was located between the reservoir and sample cells, and during operation the sample cells and the reservoir contained working pressures of 100 bar and *ca* 125 bar respectively. This was found to put strain on the valve, as the pressure differential between the two sides was *ca* 25 bar. However, valve E utilises two bellows values, which have a very low leak rate. Valves F and G were situated between the sample cells and the outlet system and during operation at 100 bar the valves were subjected to a pressure differential of 100 bar. In addition, the needle valves, used for valves F and G, have a maximum leak rate of over seven orders of magnitude larger than that of the bellows valves.
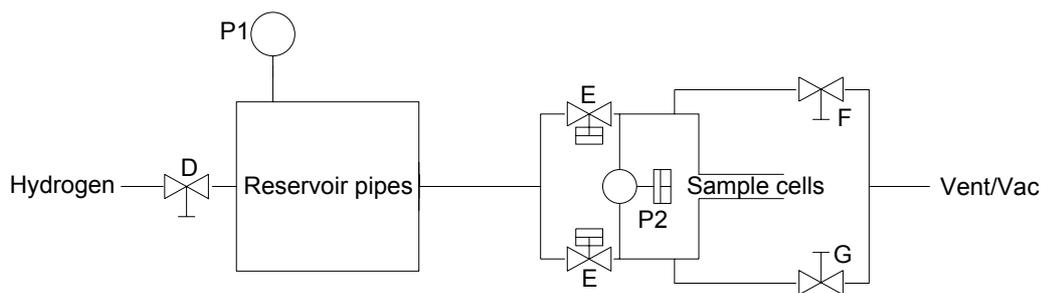
Valve	Type	Position	Maximum Leak Rate $(\text{cm}^3\,\text{s}^{-1})$
D	Swagelok needle valve	Supply to reservoir	0.1
E	Swagelok bellows valve	Reservoir to sample cells	4×10^{-9}
F	Swagelok needle valve	Sample cells to vent/vac	0.1
G	Swagelok needle valve	Sample cells to vent/vac	0.1

Figure 5-4 Schematic showing the analytical section of the prototype apparatus and a summary of each of the key valves (Swagelok, 2004)

These problems led to difficulties in operation such that it was decided to redesign and rebuild the hydrogen adsorption apparatus. However, operation of the prototype apparatus was first evaluated in order to determine the advantages and disadvantages of its design, and to provide the best foundation for the design of the new apparatus.

5.3.2 Evaluation

Below, the advantages of the prototype apparatus are briefly outlined:

1. The overall design:

    a. High precision of the differential pressure cell.

    b. Simplicity of the concept.

2. The linked air actuated valves:

    a. Allowed excellent control.

    b. Protection of the differential pressure transducer, using the differential pressure cell's indicator alarm function to operate the linked pneumatic bellows valves if the pressure difference moved out of the detectable range.

3. Temperature controlled enclosure:

    a. The heaters proved they could easily maintain the temperature in the small enclosure and would be capable of heating a much larger box.

    b. Using PID control, only a very small temperature variation was observed.

Below, the disadvantages of the prototype apparatus are briefly outlined:

1. The apparatus was too compact and three dimensional pipe layout made leak proofing very difficult:

    a. Impossible to reach all joints without first undoing others.

    b. Difficult to work on the apparatus.

    c. Difficult to carry out safety inspections.

    d. Too small a reservoir compared to the sample cells, resulting in a large differential between pre and post expansion pressures.

2. Too many joints, with thirty seven in the analytical section of the apparatus:

    a. Over-complicated.

    b. More potential leaks.

    c. Many joints had been opened and resealed so many times in order to allow access to other joints that the seals were no longer operational.

3. The sample cells had two valves on each:

    a. Not all the valves were designed to possess a low leak rate.

    b. Large strain put on valves due to large differential pressures during operation.

4. All of the gas monitored during an experiment was expanded from the reservoir:

    a. Placed the differential pressure transducer under a lot of strain by the expansion of hydrogen from vacuum to 100 bar gauge pressure instantaneously.

    b. Maximised the unwanted effects of expanding hydrogen.

5. Using a single reservoir setup the sample cells were momentarily linked together at the start of an experiment, this resulted in any instantaneous hydrogen adsorption being undetected.

6. The differential pressure transducer was uni-directional over the range 0-1bar, which was a very limited range considering the maximum working pressure of the apparatus was 100 bar.

7. The absolute pressure gauge was of an analogue type with very low precision.

8. The sample cells were too small and were limited by the size of the pre-treatment furnace.

5.4 High pressure adsorption apparatus

The design of the high-pressure adsorption apparatus was based on that used by Mellor, scaled to accommodate a much larger sample, about 1-2 g, in order to improve accuracy. It was decided to use a dual reservoir configuration, creating two independent limbs, as concerns had been raised that by expanding from a single reservoir not all the errors arising from the expansion of a non-ideal gas were eliminated and that instantaneous hydrogen storage could not be measured. The advantages from the prototype evaluation were also incorporated into the design and attempts were made to eliminate disadvantages.

5.4.1 Design

The final design of HPAA can be seen in Figure 5-5. The pipe-work was laid out in a linear two-dimensional configuration.   The temperature enclosure was approximately three times larger than in the prototype, and had a removable Perspex floor and door.   The following sections will address how the problems with the prototype design were overcome and how other innovations were incorporated into the design.

X1	Three way valve	P1	Analogue pressure gauge (0-200 bar)
X2	Ball valve	P2	Pressure transducer (0-160 bar)
X3	Needle valve	P3	Differential Pressure Transducer (± 5
X4	Needle valve		bar)
X5	Needle valve	R1	Gas reservoir 1
X6	Diaphragm Valve	R2	Gas reservoir 2
X7	Remotely controlled inter-linked Bellows	S1	Sample cell 1
	valves (normally closed)	S2	Sample cell 2
X8	Remotely controlled inter-linked Bellows	T1	Lower logged thermistor
	valves (normally open)	T2	Middle logged thermistor
		T3	Top logged thermistor
AX1	Non-return valve	H1	Furnace PID controlled
AX2	Relief Valve (180 bar)	H2	Electric strip heaters[a]
AX3	Solenoid (control box operated)	H3	Electric strip heaters with fins[a]
AX4	Solenoid (wall switch operated)	F	Fans
AX5	Needle valve	HE	Heat exchanger

[a] H2, H3 and the refrigeration unit are controlled by PID on a heat-cool cycle

Figure 5-5 Full schematic of high pressure adsorption apparatus

5.4.1.1 Accessibility

The linear configuration combined, with the fully removal front door provided easy access to all parts of the apparatus (Figure 5-6). This greatly improved the process of carrying out leak tests and repairs, allowing a helium leak rate at 150 bar of below 0.005 bar over a 24 hour period to be achieved. The Perspex front door allowed the

apparatus to be visible at all times, including during operation. The larger box allowed the sample cells to be separated by a greater distance than in the prototype setup. This meant that the pre-treatment furnace only needed to be able to heat one sample cell, allowing the size of both cells to be increased to accommodate larger samples.
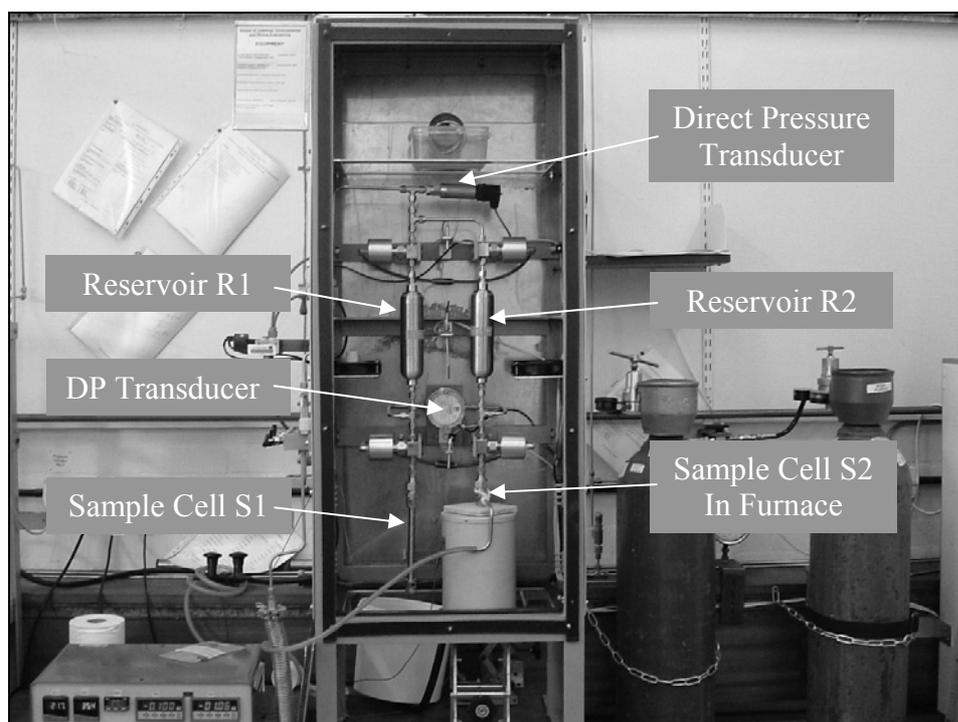
Figure 5-6 View of HPAA with the front door removed

5.4.1.2 Pressure measurement

HPAA employed a differential pressure transducer in order to measure the change in pressure caused by adsorption during an experiment, and a direct pressure transducer to monitor the pre-expansion reservoir pressure.   The prototype apparatus utilised a very sensitive differential pressure transducer, accurate to 0.001 bar. The detection range, however, was found to be too limited and the overpressure range too small (Table 5-1).   For HPAA a differential pressure transducer was used with a much larger detection range (±5 bar) but with reduced accuracy. Even so, the differential pressure transducer in HPAA was still twenty five times more accurate than a typical direct pressure transducer.

	Differential Pressure Transducer	**Differential Pressure Transducer**	**Gauge pressure Transducer**
Apparatus	Prototype	HPAA	HPAA
Model	Druck LPX 9381	Druck LPX 9381	Druck PTX 7517
Detection Range	0-1 bar	±5 bar	Vacuum - 160 bar
Operating range	Vacuum - 200 bar	Vacuum - 200 bar	Vacuum - 160 bar
Operating Temperature	-40 - 100 ˚C	-40 - 100 ˚C	-40 - 100 ˚C
Over pressure	±10 bar & 200 bar	±30 bar & 200 bar	200 bar
Precision	0.001 bar	0.001 bar	0.01 bar
Accuracy	0.001 bar (0.1 %)	0.01 bar (0.1 %)	0.25 bar (0.15 %)
Calibration		British Standards	British Standards

Table 5-1 The specifications of the transducers used on the prototype and HPAA apparatus (Druck, 2004)

In addition to the accuracy benefits of a differential pressure transducer, there are fundamental design differences that made the system better for use with helium and hydrogen. On a very simplistic level, the difference between a differential pressure transducer and one that measures directly is the location and application of the pressure detection membrane (Druck, 2004). In a differential pressure transducer, the membrane is situated between the two gases and acts according to the pressure between them. In a direct pressure gauge, the membrane is situated between the gas being monitored and non-compressible oil. However, current membranes are not totally impermeable to helium atoms and hydrogen molecules due to their small dimensions (Druck, 2004). For differential pressure measurements this has a negligible effect, as a few atoms or molecules moving from one limb to the other are insignificant, relative to the amount of gas present in each limb. The migration is, in any case, very small, due to the very small differential pressures involved. When the molecules or atoms migrate through a direct pressure membrane, however, they dissolve into the oil on the other side. This volume is very limited, and as the pressure across the membrane is *ca* 100 bar, the presence of the additional atoms and molecules becomes significant, causing a detectable pressure increase on the oil side of the membrane. The overall effect is to cause the pressure reading to reduce, due to the effective reduction in the pressure difference between the two sides of the membrane. This effect is cumulative, so is initially negligible, but the longer the timescale of the experiment the more significant this problem becomes. Thus, the

sensitivity and gas diffusion issues makes differential pressure transducers much better suited to hydrogen adsorption measurements.

5.4.1.3 Valve configuration

In order to reduce the risk of potential leaks from the analytical section of the apparatus, only bellows type valves were used (Figure 5-7). The use of pneumatic bellows valves also allowed the valves to be directly linked, this having proved to be so successful in the prototype design. Thus, the valves could be relied upon to operate completely synchronously, removing human error. The pneumatic system also meant the valves could be housed in the centre of the temperature-controlled enclosure but still be operated when the enclosure was sealed.   A major problem encountered with the prototype apparatus was that the sample cells each had two valves (F & G) with large differential pressures across them, greatly increasing the chance of a leak. HPAA operated with valves X8 open, so the only closed valves connected to the measurement limbs were the interlinked bellows valves, X7. Due to the scaling of the reservoirs to the sample cells (8:1) in HPAA the pre-expansion pressure was *ca* 112.6 bar in order to achieve a working pressure of *ca* 100 bar. During a run, the diaphragm valve, X6, was kept closed in order to maintain the pre-expansion pressure in the feed pipe. Thus, the valves X7 only had a differential pressure of *ca* 12.6 bar across them, much less than the 25 bar for the equivalent position on the prototype apparatus. As an additional safety feature, the control of valves X7 could be overridden by the differential pressure transducer indicator if the differential pressure moved out of the range ±5 bar. This instantly acted to equalise the pressure in both limbs, protecting the transducer from over pressure and potential rupture.
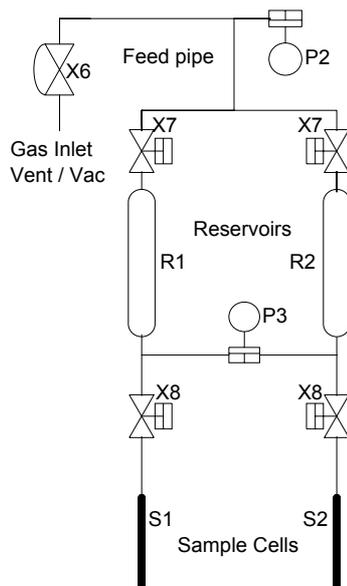
Valve	Type	Position	Maximum Leak Rate (cm^3 s^{-1})
X6	Swagelok diaphragm valve	Supply/vent/vac to feed pipe	4×10^{-9}
X7	Swagelok bellows valve	Feed pipe to reservoir	4×10^{-9}
X8	Swagelok bellows valve	Reservoir to sample cells	4×10^{-9}

Figure 5-7 Schematic showing the analytical section of the prototype apparatus and a summary of each of the key valves (Swagelok, 2004)

5.4.1.4 Data logging

The timescale of hydrogen adsorption on carbon materials is still not fully known. It would be expected for physisorption to happen almost instantaneously, but some researchers have reported much longer equilibration times (Browning *et al.*, 2002). For these reasons, it was decided to record the differential pressure each second for eight hours for each experiment in order to ensure all changes were recorded and to ensure that equilibration had been achieved. Temperature control was also crucial for an accurate measurement, which will be discussed in detail later in this chapter (Section 5.4.2.3). Thus, temperature was also logged in order to allow related effects to be identified in the data. The temperature was recorded at three points in HPAA, T1, T2 and T3 (Figure 5-5).   The direct pressure transducer reading was also logged in order to monitor changes in pressure in the feed pipe. The data converter used for logging the differential pressure and direct pressure transducer measurements was a ADC 16 (Pico, UK) and the data converter used for temperature was a TH-03 (Pico, UK) fitted with thermistor thermocouples (Table 5-2). The accuracy and precision

of the data loggers used were all equal to, or higher than, the sensor that they were monitoring in order to ensure that no data was lost.

Converter	ADC 16		TH-03
Measured	**Differential Pressure**	**Direct Pressure**	**Temperature**
Symbol	P3	P2	T1,T2,T3
Channel	1	2	1,2,3
Resolution	0.001 bar	0.01 bar	0.003 ˚C
Accuracy	0.002 bar	0.01 bar	0.3 ˚C
Max Sampling rate	1.5 Hz	1.5 Hz	1 Hz

Table 5-2 Summary of data logging apparatus used with HPAA (Pico, 2004)

5.4.1.5 Degassing samples

The HPAA used a two stage pump (Edwards High Vacuum, UK) connected via a large volume vacuum pipe. The system was monitored using an Pre 10 K gauge (Edwards High Vacuum, UK) and was found to achieve a vacuum of 0.14 Pa. The sample cells could be independently heated by a PID controlled furnace (H3) up to 300 ˚C. The preferred maximum degas temperature was 150 ˚C, in order to avoid causing damage to the sample cell fittings. Three main degassing methods were used for this study (Table 5-3).

Method	Procedure
DG1	Maintain sample at vacuum
DG2	Maintain sample at vacuum at 150 ˚C
DG3	Maintain sample at vacuum at 150 ˚C
	Cool to ambient temperature under hydrogen (*ca* 10 bar)
	Maintain sample at vacuum at 150 ˚C
	Cool to ambient temperature under hydrogen (*ca* 10 bar)
	Maintain sample at vacuum at 150 ˚C

Table 5-3 Summary of the main degas procedures used to prepare sample for hydrogen adsorption experiments

The DG1 method was intended purely as a preparation for a hydrogen adsorption measurement, as the sample cells needed to be fully evacuated prior to expansion in order to ensure that only the intended gas was present for an experiment. In addition

to this, by starting all experiments from vacuum, ensures that no inaccuracies were present due to inconsistencies at the start of an experiment. The DG2 method was the most common degas procedure used in the literature for carbon materials (Browning *et al.*, 2002; Chambers *et al.*, 1998). By heating to 150 ˚C under vacuum, it was proposed that all physisorbed species would be removed, leaving a clean surface to allow maximum adsorption. The DG3 procedure was used to prepare metal hydride samples. This long procedure was required, due to the air-sensitive nature of metal hydrides and was required to re-activate them for hydrogen adsorption reactions. However, once a metal hydride had been activated it was necessary to use DG2 degas procedure in order to desorb all the hydrogen and allow another experiment to be carried out.

5.4.1.6 Gas purity

The purity of gases used for hydrogen adsorption measurements varied in previously reported studies from standard grade (99.9 %) through to high purity (99.999 %), sometimes with additional liquid nitrogen purification steps (Browning *et al.*, 2002; Poirier *et al.*, 2001). For this study, standard gases were selected as it is not commercially viable for fuel grade hydrogen to be of very high purity, thus it was considered that a standard grade would best represent the quality of hydrogen that would be available as a fuel from a hydrogen economy. However, questions have been raised over the preferential adsorption of moisture from the gases, so causing measurements to be inaccurate. Thus, a liquid nitrogen trap was used inline, directly after the gas cylinders, in order to ensure the gas was dry and so improve the accuracy of the measurement.

5.4.2 Accuracy evaluation

The accuracy of HPAA can be described in two ways. First, the accuracy of the measurement in wt% was required in order to allow meaningful comparison of results with independent studies. In addition to this, the accuracy and repeatability of the measurement was required for comparison between samples, rather than relative to a defined unit. Several factors can affect the measurement including the effects of expansion, temperature, degassing, equipment sensitivity and the ideality of the gas being used.

5.4.2.1 Maximising the accuracy of pressure measurement

The differential pressure measurements have been shown to be preferential for hydrogen adsorption measurements due to the nature of the transducers available (5.4.1.2). In order to maximise the accuracy of the hydrogen adsorption calculation, Equation (5-1) has been derived (Appendix 3) using change in amount of hydrogen (Δn), differential pressure (Δp), volume (V), temperature (T) and the gas constant (R). This derivation proves that the hydrogen adsorption uptake, determined via the differential pressure method calculation, is independent of the measurement made by the less accurate direct pressure gauge. However, the direct pressure gauge is still essential for the determination of working pressure of the apparatus.

$$\Delta n = \frac{\Delta pV}{RT} \qquad \textbf{(5-1)}$$

The equation utilises the differential pressure measurement in order to calculate the amount of hydrogen adsorbed, independently from the direct pressure measurement. Thus, the direct pressure transducer was used solely to determine the pre-expansion pressure from which the operating pressure of the apparatus could be determined. This removes inaccuracy due to use of direct pressure transducers.

5.4.2.2 Minimising inaccuracy due to expansion

The differential pressure volumetric system was intended to totally eradicate the effect of expanding a gas from a reservoir to a sample cell. However, in reality the two limbs of HPAA would never be exactly equal, due to minor variations in fittings and the unequal volume of the two sides of the differential pressure transducer. Any effects caused by expansion could then be reduced by minimising the amount of gas thus expanded. This could be achieved by making the reservoirs as large as possible and the sample cells as small as possible. In the prototype apparatus, the sample limbs were isolated from the reservoir during a run. Thus, 100 % of the gas monitored during an experiment had been expanded, maximising any expansion effects, in addition to this the differential pressure transducer was put under intense strain by going, instantaneously, from a working pressure of vacuum to 100 bar. HPAA employs two seamless cylinders, each of volume 150 cm^3, which combined with the connecting pipes give a reservoir volume 168.1 cm^3 and 165.9 cm^3 for the

left and right reservoirs respectively, which were combined with the sample cells, *ca* 24 cm^3, on expansion to create the sample limbs. Thus only *ca* 14 % of the monitored gas was expanded and only experienced a *ca* 12.6 bar drop in pressure in order to achieve a working pressure of 100 bar, greatly minimising effect of expansion on the behaviour of the gas. In addition to this, as the differential pressure transducer was positioned between the two reservoirs, rather than between the sample cells, it was put under much less stress by the expansion, resulting in a *ca* 12.6 bar change in working pressure compared to the *ca* 100 bar change experienced in the prototype apparatus.

These improvements to the design greatly minimised the fluctuations caused by the expansion of gas from the reservoir to the sample cells. The expansion, however, was an essential part of the experiment and so the fluctuations could never be fully eliminated. This created a problem, as when the experiment was started, the differential pressure instantly started to change. Effectively the system had been through an instant change in volume, and in addition to this adsorption may be occurring. This made defining the differential pressure starting point very difficult. Previous work had assumed that the highest recorded pressure could be taken as the starting point and that all further pressure changes were solely the result of adsorption (Browning *et al.*, 2002). Using steel ball bearings in order to equalise the volume of the two limbs of HPAA at *ca* 190 cm^3, a blank hydrogen run was carried out (Figure 5-8).
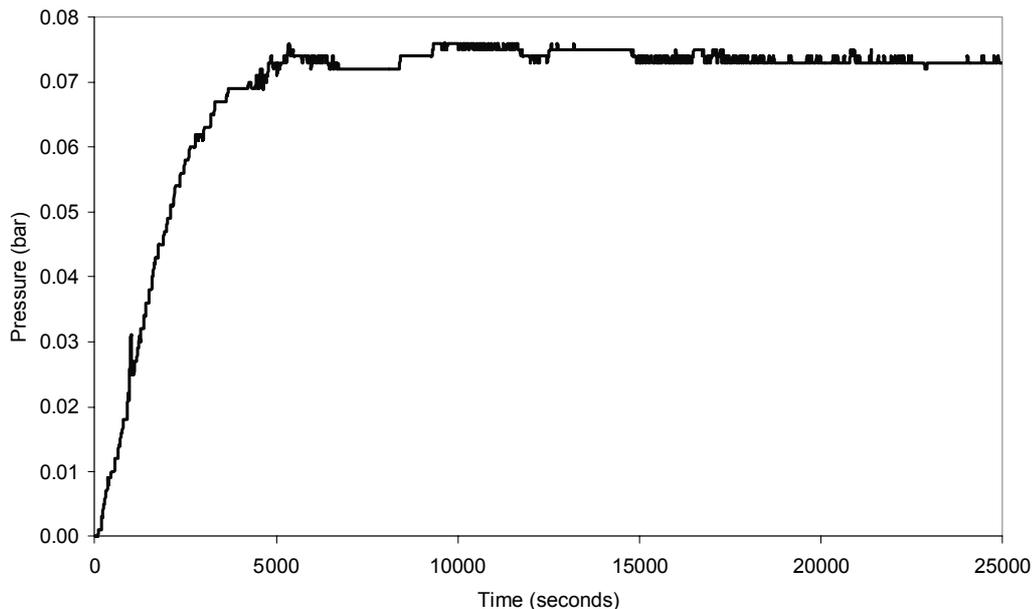
Figure 5-8 Blank run from HPAA using ball bearings to equalise limb volumes at 190 cm^3

If the pressure changes were translated into a hydrogen adsorption profile with a fictional carbon presence of 50 mg, as an average representation of previous work, a hydrogen adsorption of *ca* 2 wt% would be the result (Figure 5-9). The shape of the resulting curve would be consistent, but the origin would vary from run to run.
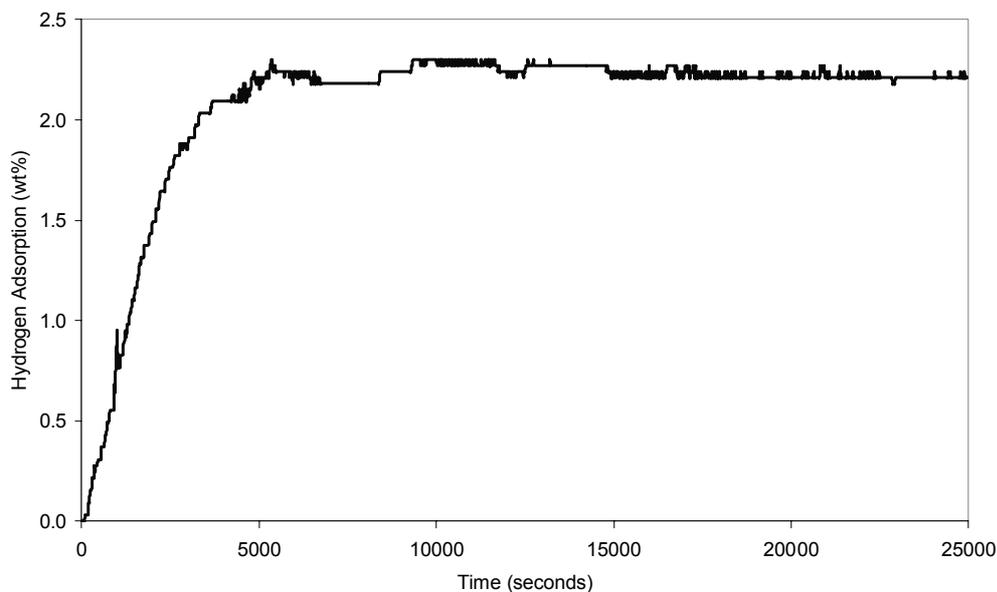
Figure 5-9 Hydrogen sorption profile of a fictional 50 mg carbon sample with only ball bearing present in the sample cell

Helium has been reported not to adsorb so will only undergo the effects due to non-sorption phenomena (Greenwood *et al.*, 1997). Thus, by using a helium run as a baseline correction, it was hoped that most of the fluctuations of expansion would be cancelled out. In addition to this, a fictional sample of 1 g was used, rather than the original 50 mg, to improve the sensitivity of the apparatus. This gave a hydrogen adsorption value of approximately 0 wt% (Figure 5-10), which is what would be expected for an experiment carried out using only inert ball bearings.
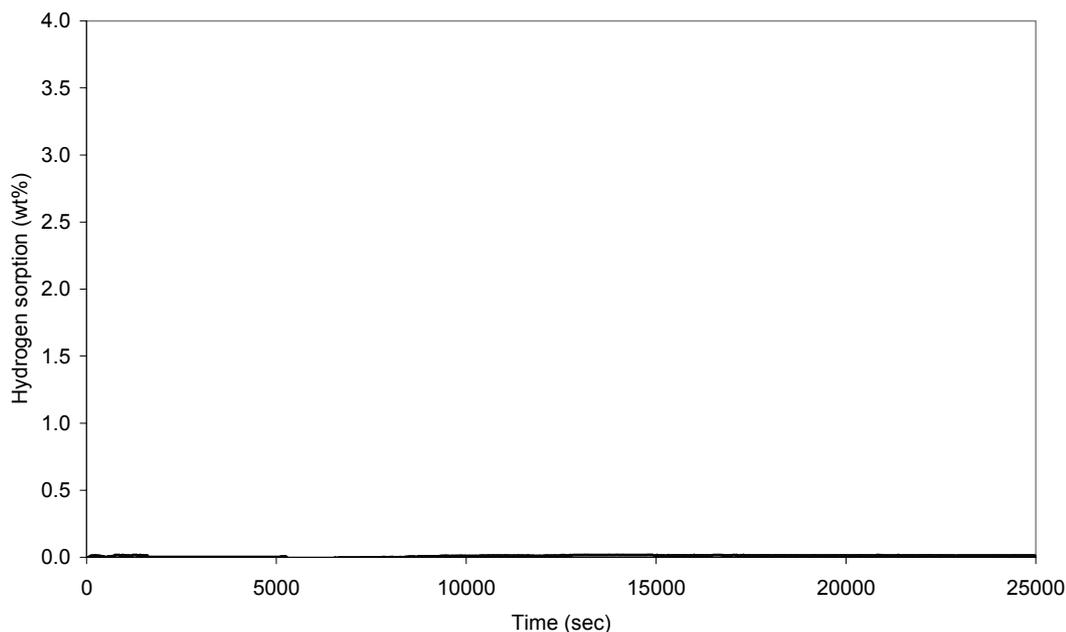
Figure 5-10 Hydrogen sorption profile of a fictional 1 g carbon sample using a helium correction run with only ball bearings present in the sample cell

5.4.2.3 Minimising the effect of temperature

The volumetric measurement of the hydrogen storage capacity of a material is temperature dependent. This is due to the temperature being directly proportional to pressure for a closed system as given by the perfect gas equation of state (Equation (5-2)).

Thus, if the temperature of the whole apparatus was not kept constant during a hydrogen storage capacity measurement, errors would have been present in the result. In addition to this, as the working pressure was increased, the error due to poor temperature control similarly increases. Figure 5-11 shows the change in pressure to a closed constant volume system caused by a 0.5 °C variation in

temperature from 30 ˚C to 30.5 ˚C, as the operating pressure was increased, using the perfect gas equation of state. Due to the accuracy of current temperature control systems, maintaining a constant temperature with a variation of less 0.5 ˚C (±0.25 ˚C) was considered acceptable (Controls, 2003).
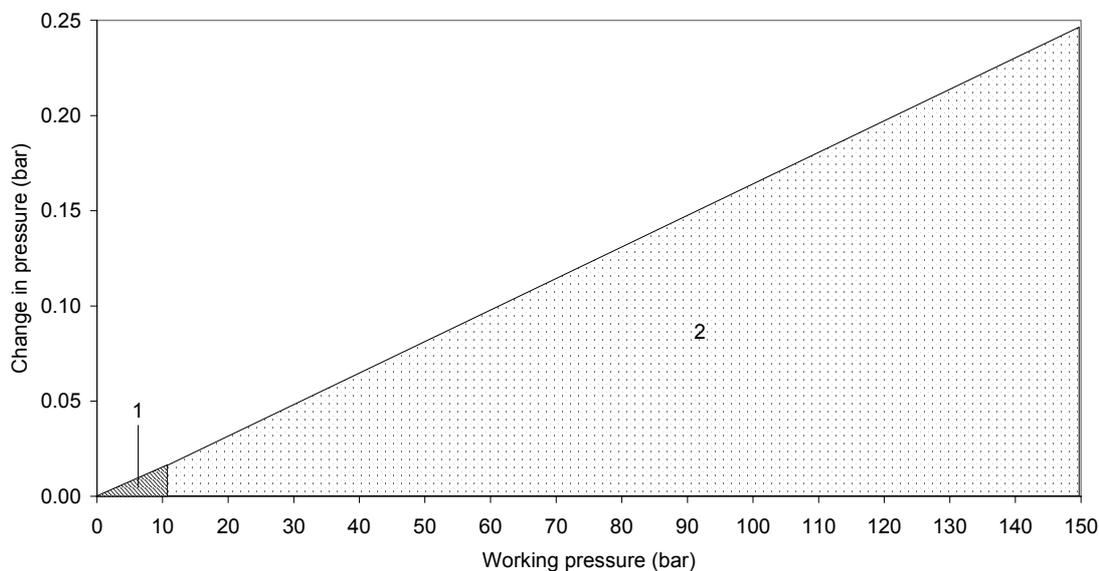
Key
1 - The pressure range required for hydrogen storage capacity determination of metal hydrides
2 - The pressure range required for hydrogen storage capacity determination of carbon nanomaterials

Figure 5-11 Graph showing the change in pressure of sealed system resulting from a change in temperature of 0.5 ˚C as the working pressure of the system is increased

The temperature of the system was also affected by the expansion of the hydrogen from the reservoir to the sample limb. The Joule-Thompson effect states that, as a gas is expanded, it cools due to the energy required to allow the molecules to move further apart against the attractive forces between the molecules. In addition to this, if rapid adsorption is occurring the latent heat of adsorption will also contribute to errors.

The apparatus for determining the hydrogen storage capacity of metal hydrides by the volumetric method utilises direct pressure measurement (Chapter 2). This involved expanding a reservoir of a known amount hydrogen gas into a sample cell containing the metal hydride, and then monitoring pressure change. The resultant pressure drop could then be used to determine the hydrogen storage capacity of the metal hydride. Many metal hydride system require less than 10 bar to reach the

hydrogen adsorption saturation level. At this pressure, a 0.5 ˚C temperature change makes less than a 0.025 bar change to the overall pressure of the system. Thus, the pressure drop caused by the sorption of hydrogen is 1 bar the error in the result is potentially 2 % due to temperature fluctuation, which is acceptable.

CNF hydrogen storage systems require pressures of 100 bar and above to facilitate the sorption of hydrogen.   At this pressure a temperature change of 0.5 ˚C makes almost a 0.25 bar change to the overall pressure of the system. If the system is operating at 100 bar and the pressure drop caused by the sorption of hydrogen is 1 bar the error in the result is potentially over 15 %, this rises to almost 25 % at an operating pressure of 150 bar, both errors being unacceptably large. Thus, the direct pressure measurement is less suitable for volumetric determination of hydrogen storage of carbon nanomaterials.

Using a differential pressure system these errors are predicted to be greatly reduced. By having both reservoirs and sample cells in the same controlled atmosphere most fluctuations in temperature in the system affect both limbs to the same degree. This causes the cancelling out of most of the pressure change due to temperature. The differential pressure gauge measures the difference in pressure between the two limbs and if both undergo the same pressure change the differential pressure reading will not change.

A 9300 PID unit (CAL Control, UK) controls the temperature of the enclosure of HPAA by a heat-cool cycle. Four ceramic insulated strip heaters, two finned strip 400 W heaters (H3) and two flat 150 W heaters (H2) provided the heat, with the cooling provided by a Techne Dip Cooler RU-200 refrigeration system. Two fans were used to ensure the temperature is evenly maintained.   The operating temperature of the apparatus was selected to be 30 ˚C as this 10 ˚C above the average room temperature and was thought to be representative of the operating temperature of mobile hydrogen storage unit. Also, the accuracy of the 9300 PID controller increases with the temperature difference between the operating and room temperature (Controls, 2003).   However, a 10 ˚C temperature differential is still easily achievable for the strip heaters without exceeding the recommended maximum output of 80 %.

HPAA can demonstrate the reduction in error due to temperature effects by employing a differential rather than a direct pressure apparatus. The pressure of the feed pipe of HPAA was monitored by a high accuracy direct pressure gauge and was a closed system when the apparatus was in operation. This section of the apparatus may be used to represent a direct pressure monitoring apparatus, as the volume and amount of gas present are kept constant throughout a run. Figure 5-12 illustrates the observed temperature and direct and differential pressure changes when operating HPAA with no sample at 100 bar and a target operating temperature of 30 ˚C. The efficiency of the temperature control system of HPAA was also evident with the maximum temperature fluctuation from 30 ˚C being 0.1 ˚C.
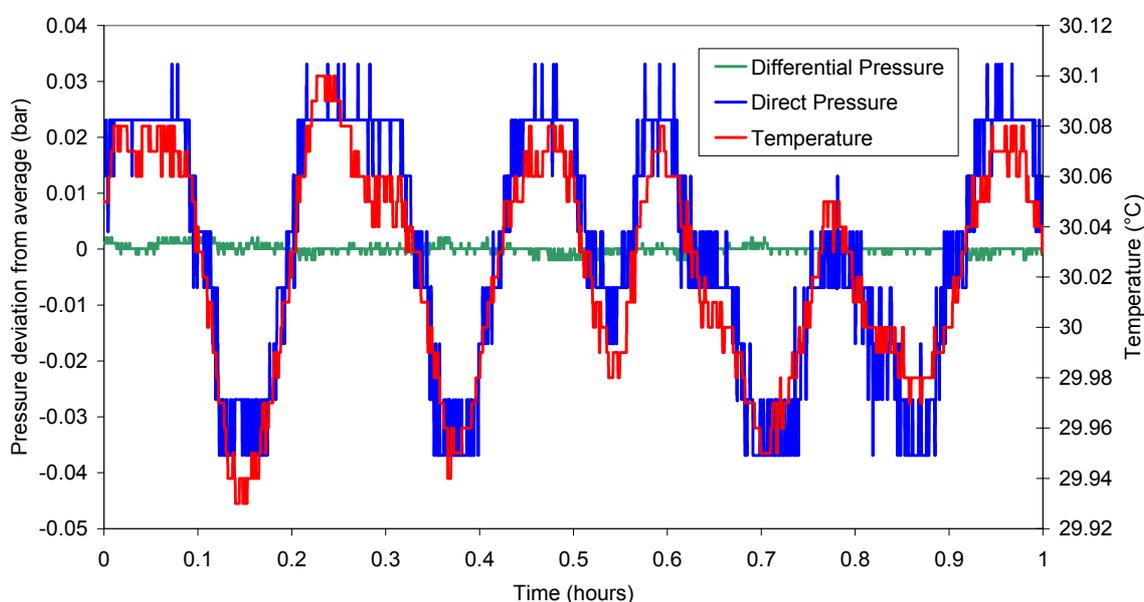
Figure 5-12 Graph showing the deviation from the average direct and differential pressure measurements made by HPAA at 100 bar with a target operating temperature of 30 ˙C.

The relationship between the direct pressure measurement and temperature of the system is clearly visible in Figure 5-12. As the temperature rises, the pressure increases and conversely as the temperature drops the pressure decreases. However, the differential pressure measurement was unaffected by these slight fluctuations of temperature. Thus, by using a differential pressure system to determine the hydrogen storage capacity of a material the effects of small fluctuations of the operating temperature of the apparatus can be assumed to be negligible.

5.4.2.4 Inaccuracy from degassing samples

The degassing procedure was found to cause an unavoidable error in the hydrogen adsorption measurement when using HPAA. This error resulted from the calculations being based on pre-degas sample masses. However, on degassing the sample mass was found to be reduced due to the removal of adsorbed species could be as high as 30 % for an activated carbon (Chapter 7). During this study there was no suitable method for removing a degassed sample from the apparatus to re-weigh it without exposure to air, thus the hydrogen adsorption calculations are quoted relative to their pre-degas weights.

5.4.3 Issues raised due to the ideality of gases

The classical model to describe the physical state of a gas is the equation of state, which is defined using the pressure (p), volume (V), amount (n) and temperature (T) of the gas (Atkins, 1998). The most commonly used example of the equation of state is for a perfect gas (5-2).

$$pV = nRT \qquad \text{(5-2)}$$

However, because the isotherms of real gases often do not correlate with the equation of state for a perfect gas, the van der Waals equation (Equation (5-3)), was introduced in 1873. This is an approximate equation of state for all gases (van der Waals, 1873). The van der Waals equation introduced two constants (a and b), which are specific to the gas being studied (Table 5-4).

$$p = \frac{nRT}{V - nb} - a\left(\frac{n}{V}\right)^2 \qquad \text{(5-3)}$$

	a	b
	(Pa m^{6}mol^{-2})	(m^{3}mol^{-1})
Hydrogen	0.02452	0.0000265
Helium	0.00346	0.0000238

Table 5-4 The van der Waals constants of helium and hydrogen (Lide, 2003)

The equation of state for a perfect gas, and the van der Waals equation, are both models to describe the physical state of a gas. The physical state of a real gas can also be described using experimentally determined compressibility factors (Z) in conjunction with the equation of state for a perfect gas (Equation (5-4)) (Perry *et al.*, 1997). The use of compressibility factors avoids the inaccuracy of model systems; however, the compressibility factor for a given gas varies as a function of pressure complicating any required calculation.

$$pV = ZnRT \qquad\qquad \textbf{(5-4)}$$

The effect of using the different methods of describing the physical state of hydrogen and helium can clearly be seen in Figure 5-13, with a pronounced difference between the methods being clearly visible at a pressure of 100 bar, which is the working pressure of HPAA.
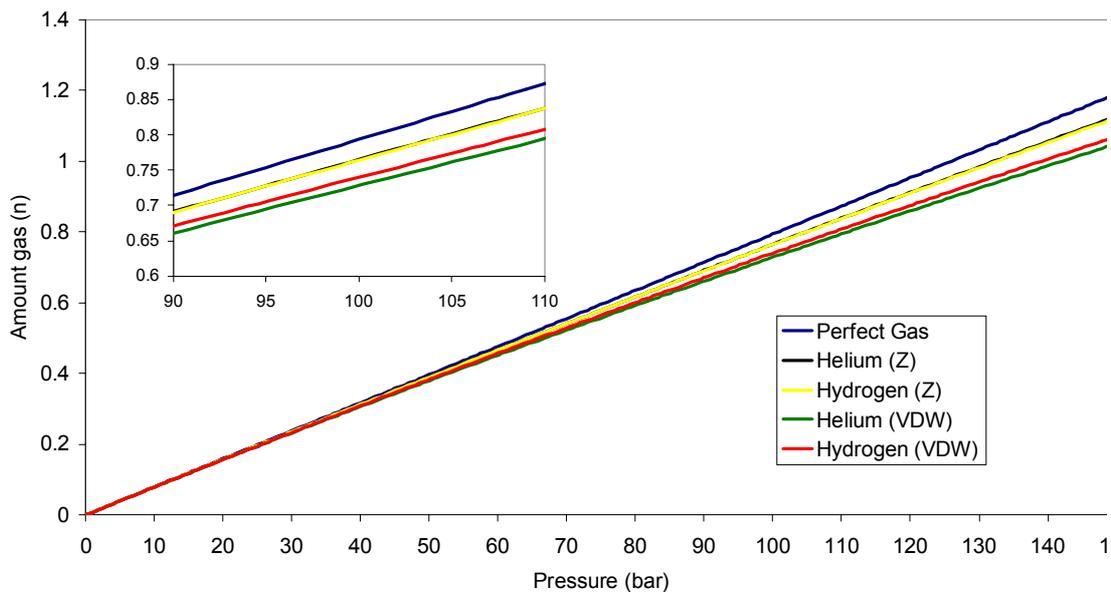
Figure 5-13 The relationship between amount of gas relative to pressure for a system of fixed volume and temperature, 200 cm³ at 30 ˚C respectively, of helium and hydrogen using the perfect gas equation of state, van der Waals equation (VDW) and compressibility factor (Z)

HPAA was capable of measuring small changes in pressure at high working pressure and from this the amount of hydrogen adsorbed may be calculated using (5-1). This method was selected as it allows for simple calculations and is the preferential method used in previous studies (Browning *et al.*, 2002; Tibbetts *et al.*, 2001). The potential error caused by using the different methods of describing the physical state of a gas can be assessed by considering a theoretical HPAA system. Using a volume

of 200 cm^3 and a temperature of 30 ˚C the theoretical hydrogen adsorption capacity can calculated for a 1 g sample caused by a differential pressure in the range 0 to 2 bar (Figure 5-14).
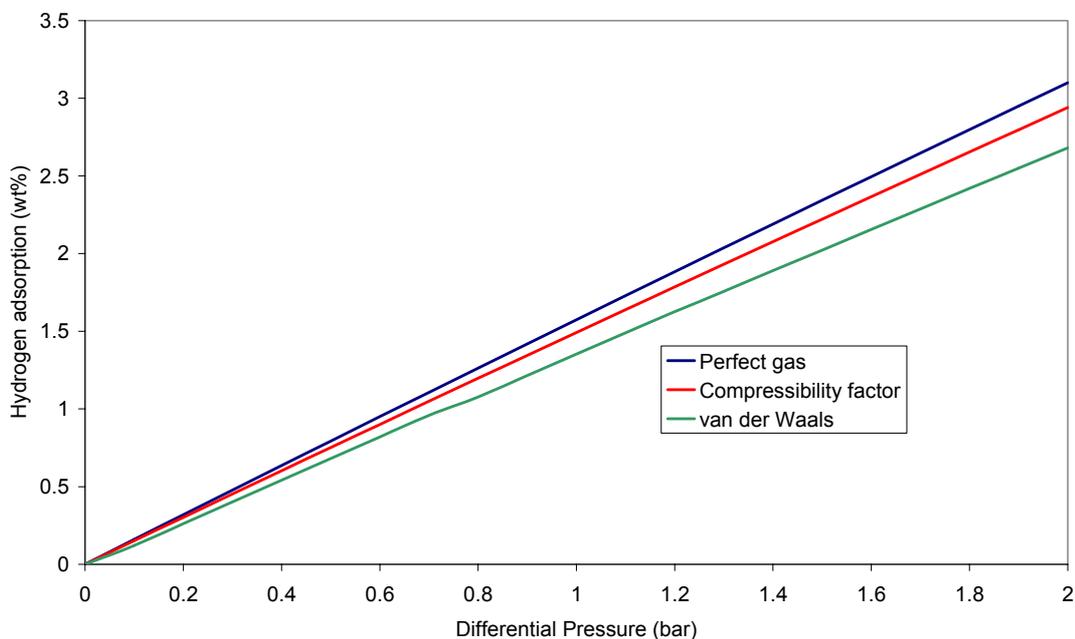
Figure 5-14 The effect of using different modelling systems for the calculation of hydrogen adsorption capacities for a theoretical system using 1 g of sample, 200 cm^3 volume with a 100 bar initial working pressure at 30 ˚C

Figure 5-14 shows that, as the differential pressure increases, the potential error due to the method of calculation also increases. This would imply that, in order to minimise the error, the differential pressure change caused by adsorption should be kept to a minimum. However, to minimise the error caused by expanding the gas, the differential pressure is required to be high in order to make any pressure change due to adsorption more pronounced. This creates a trade off situation to achieve the best accuracy. For the operation of HPAA, the target differential pressure caused by adsorption by sample was selected to be 0.2-1 bar, to minimise inaccuracy caused by the calculation method, but still be of a larger enough magnitude to ensure that the differential caused by adsorption is much larger than pressure changes caused by other phenomena, such as expansion. The differential pressure change caused by adsorption could be scaled by modifying the amount of sample used for an analysis. For example, for a 1 g sample that adsorbs 1 wt% of hydrogen a pressure change of *ca* 0.7 bar would occur (Figure 5-14). However, if a 1 g sample adsorbed 4 wt% the resulting change in pressure would be *ca* 2.6 bar, which would reduce the accuracy

of the measurement, due to the calculation method used. In this situation, the experiment would need to be repeated with *ca* 0.4 g of adsorbent material. By scaling the amount of material present in this manner, the accuracy of HPAA can be maintained.

5.4.4 Accurate volume calibration

The volume of the sample limbs of HPAA needed to be accurately determined, as it was a required variable for the calculation of hydrogen adsorption uptake (Equation (5-1)). Thus, any inaccuracy in volumetric detail of the apparatus will be transferred to the hydrogen adsorption calculation. Thus, the volume of the sample and the glass wool plug needed to be considered. In order to achieve this, a free space analysis was undertaken as part of each experiment, to calculate the free volume within the sample limb (Lueking *et al.*, 2004). For the purpose of the following section, the analytical section of the apparatus is discussed as six parts (Figure 5-15).
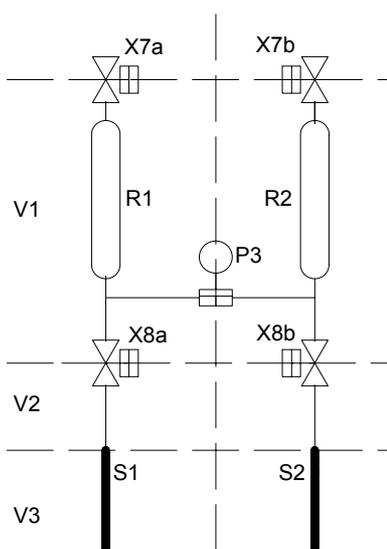
	Reservoir	Sample Section	
	V_1	V_2	V_3
Left Limb (1)	Reservoir (R1)	Connecting pipe	Sample Cell (S1)
Right Limb (2)	Reservoir (R2)	Connecting pipe	Sample Cell (S2)

Figure 5-15 Schematic defining the sections of the limbs of HPAA required for the volumetric calibration

5.4.4.1 Free space analysis

The free space analysis involved the expansion of *ca* 4 bar of helium from the reservoir into the evacuated connecting pipe and sample cell through valve X8, with the differential pressure transducer monitoring the pressure changes relative to vacuum. Helium was selected for this purpose for two reasons, firstly it is the most perfect real gas, so at low pressures its behaviour may be approximated using the equation of state for a perfect gas (Atkins, 1998). In addition to this, helium is a very poor adsorbate due to its small molecular size and non-polarisable nature (Greenwood *et al.*, 1997).   By applying the equation of state for a perfect gas (Equation (5-2)) an expression (Equation (5-5)) was derived to describe the expansion of gas in the sample limb, where p_1 and p_2 are the pre- and post-expansion pressures respectively.

$$V_1 + V_2 + V_3 = \frac{p_1 V_1}{p_2}$$

(5-5)

5.4.4.2 Determination of the reservoir volumes

In order to carry out the free space analysis, the volume of the reservoirs needs to be accurately known. This was achieved by using a series of expansion experiments, in conjunction with a simultaneous equation method (Lueking *et al.*, 2004).   An equation was derived to relate the ratio of the pre- and post-expansion pressures, p_1 and p_2 respectively, with the volumes of the three parts of one limb (Appendix 4).

$$\frac{p_1}{p_2} - 1 = \frac{V_2 + V_3}{V_1}$$

(5-6)

The volume of each sample cell (V_3) was directly measured by water capacity. The experiments were again carried out with helium and the reservoirs filled to the desired pre-expansion pressure. The post-expansion pressure was determined using the differential pressure transducer. Thus, only the volumes of the reservoir (V_1) and sample section (V_2+V_3) remained as unknowns, which were then calculated using a method employing simultaneous equations (Lueking *et al.*, 2004). From a series of expansions using different sized limbs, a plot of pre-expansion pressure against post-expansion pressure was plotted (Figure 5-16).
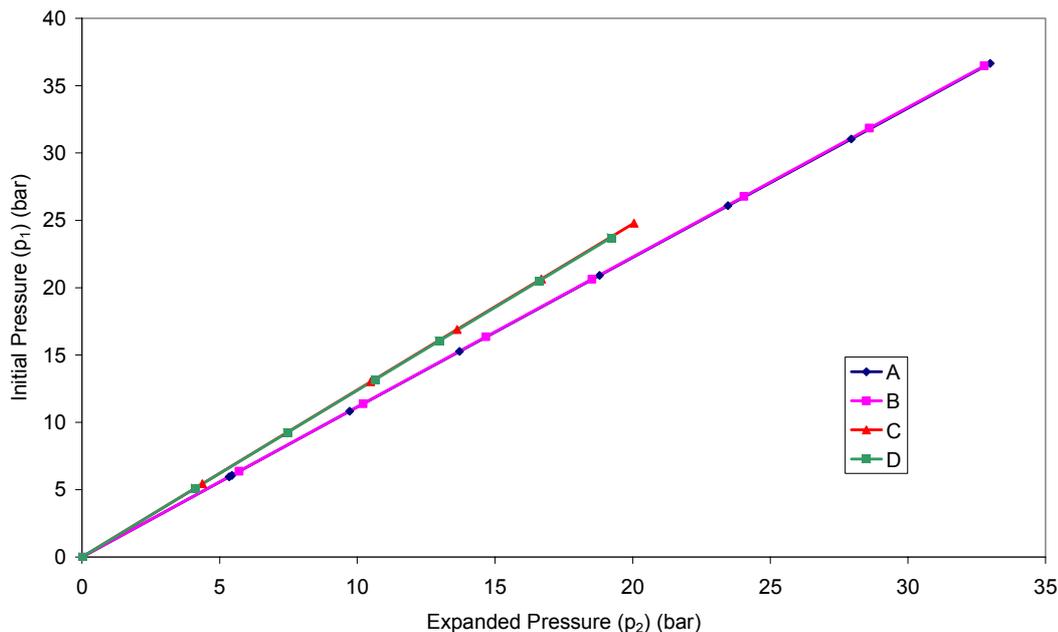
	V_3 Volume (cm³)	Expansion details			
		Left Limb	Right Limb	X8a	X8b
A	12.47	Reference	Expand	Open	Open/Close
B	12.51	Expand	Reference	Open/Close	Open
C	32.85	Reference	Expand	Open	Open/Close
D	32.95	Expand	Reference	Open/Close	Open

Figure 5-16 The relationship between P1 and P2 for different sized sample cells

The gradient of these graphs is the ratio p_1/p_2 that can be directly substituted into (5-6). Two unknowns then remained, the reservoir volume and the sample section volume, which were again calculated using simultaneous equations.

Reservoir	Volume (cm³)
Left Reservoir (RV$_1$)	168.1
Right Reservoir (RV$_2$)	165.9

Table 5-5 Calculated reservoir volumes

These values are approximately as expected as the reservoirs, R1 and R2, are known to possess volumes of approximately 150 cm³ (Swagelok, 2004), with the actual value being slightly higher due to the void space in pipes, fittings and valves.

5.5 Safety

The maximum stated operating pressure for HPAA was 150 bar, although for the majority of experiments this did not exceed 100 bar. For this reason all fittings and pipes used were rated for use to a minimum specification of 200 bar in order to allow for a safety margin. The loading system was equipped with an analogue gauge (P1) to monitor the pressure independently of the regulators. The pressurised pipe work was fully housed in the temperature enclosure, which was constructed from steel with high-impact safety Perspex as the door. This allowed easy and full inspection, combined with protection in case of catastrophic leakage or rupture.

A problem encountered was that the flash back arresters required for flammable gases could only handle pressures below 10 bar, well below the maximum operating pressure of 150 bar. Thus, a non-return valve (AX1) was fitted before the hydrogen regulator in order to minmise risk. In addition to this, the gas bottles supplying the network were situated adjacent to the apparatus in order to allow full access to them and ensure that they were only operational for the minimum period required.

At all times, signs were placed around the apparatus to inform other workers that the apparatus was in operation.

5.6 Accuracy assessment using metal hydrides

In order to assess the accuracy of the hydrogen adsorption measurement made by HPAA the metal hydride lanthanide nickel, which is known to have a hydrogen storage capacity of 1.5 wt%, was used as a standard (Figure 5-17)(Steigerwalt *et al.*, 2001).

$$2LaNi_5 \text{ (s)} + 6.7H_2 \text{ (g)} \leftrightarrows 2LaNi_5H_{6.7} \text{ (s)}$$
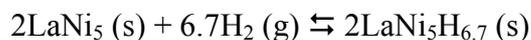
Figure 5-17 The reversible reaction between lanthanide nickel and hydrogen

As metal hydrides utilise a chemisorption system, they require much lower pressures to adsorb hydrogen, with most reaching equilibrium with hydrogen pressure below 10 bar, making hydrogen adsorption capacities much easier to determine. (Verbetsky *et al.*, 1998). Metal hydrides are more advanced as a hydrogen storage technology than carbon materials, thus many more studies have been carried out on their

hydrogen storage potential with consistent results being obtained independently (Bowman *et al.*, 1997; Luo *et al.*, 1998; Witham *et al.*, 1997).

The first calibration was carried out at 10 bar, as this was known to be well above the hydrogen saturation pressure, and was expected to yield an adsorption capacity of 1.4-1.5 wt% (Bowman *et al.*, 1997; Luo *et al.*, 1998; Witham *et al.*, 1997).   The amount of sample used was 1.4 g, as this was the approximate amount of material of carbon to be used for each experiment. The sample was initially degassed using the DG3 procedure in order to ensure that the metal hydride was fully activated for adsorption, and then repeated using a DG2 procedure to show repeatability, without the continued need for the longer DG3 method. This was repeated using both limbs in turn as the sample limb, in order to prove the repeatability and reversibility of the apparatus, and the accuracy of the bi-directional differential pressure transducer (Figure 5-18).
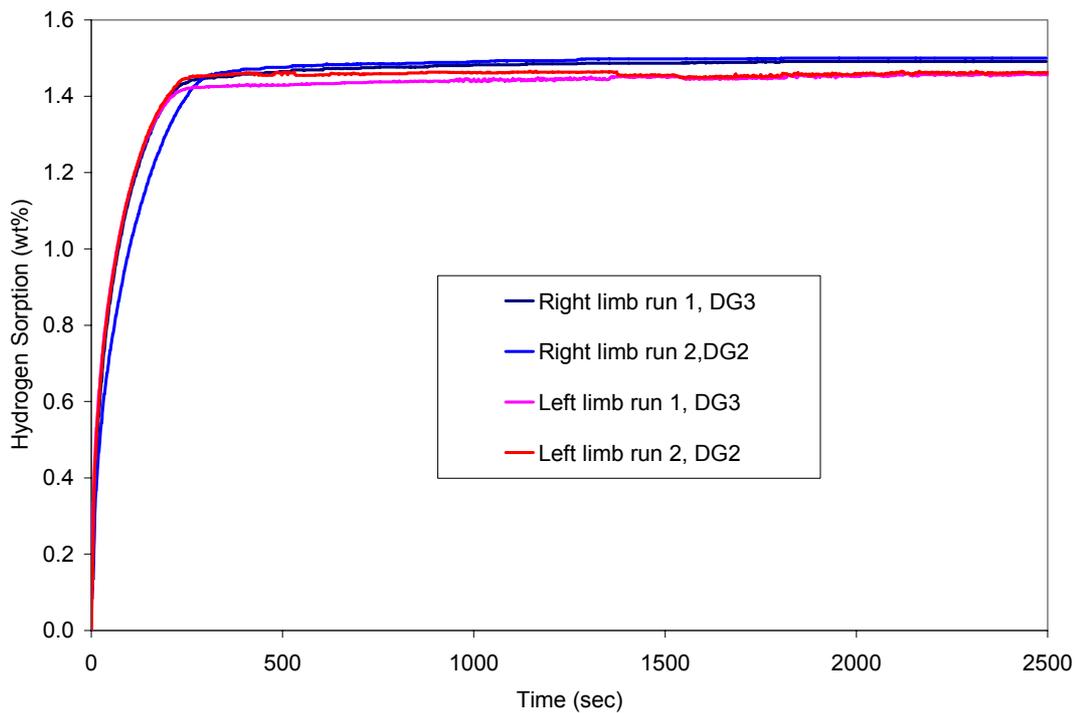
Figure 5-18 Hydrogen adsorption profile of lanthanide nickel at 10 bar

The hydrogen adsorption capacity of the lanthanide nickel consistently was found to be 1.46 wt% and 1.49 wt% on the left and right limbs respectively, with equilibrium being achieved after 300 seconds.

The second calibration was carried out at 100 bar, using the left limb as the sample limb containing 1.4 g of lanthanide nickel (Figure 5-19). The degassing procedure was the same as that used for the experiments carried out at 10 bar.
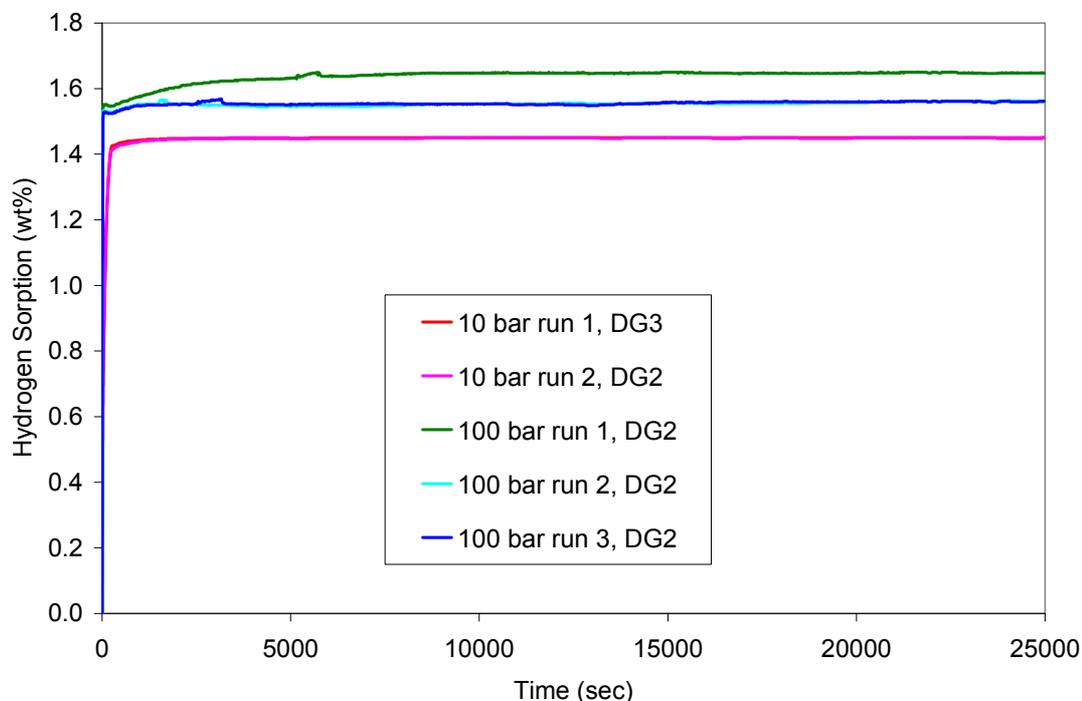
Figure 5-19 Hydrogen adsorption profile of lanthanide nickel at 100 bar

For lanthanide nickel, hydrogen adsorption saturation is thought to be achieved below 10 bar and it would be expected that no additional adsorption would occur at 100 bar relative to 10 bar. However, Figure 5-19 illustrates the hydrogen adsorption capacity for the first run at high pressure being 1.65 wt%, with further runs being consistently 1.55 wt%. This result suggests that, at high pressure, some of the hydrogen is very strongly adsorbed or sealed deep within the structure, and can not be removed by heating to 150 ˚C under vacuum alone, hence the first run produced a higher result at 100 bar relative to consequent runs. The equilibrium time for the first high pressure run was also much larger, 1000 sec, than the other results, suggesting that the hydrogen was slowly penetrating deep into the metallic structure. Even so, the subsequent high pressure runs still gave a 0.1 wt% higher hydrogen adsorption capacity than analogous runs carried out at lower pressures. This can be explained by the following phenomena. Firstly, the hydrogen simply penetrates deeper into the material, finding more adsorption sites due the higher pressure.

Secondly, the occurrence of multilayer hydrogen adsorption made possible by the high pressure of gas present creating more capacity for more adsorption. Although the multi-layer hydrogen adsorption is less likely, due to the low polarisability of hydrogen molecules and the critical temperature of hydrogen being -240 ˚C, making interlayer bonding likely to be weak. The rate of adsorption is also of interest for the high pressure hydrogen experiments, as the majority of the adsorption, 1.53 wt%, occurs almost instantaneously, with the remainder occurring within 300 seconds. This observation would be expected as the higher pressure drives the adsorption reaction to completion at a higher rate. These results compare well with previous studies, with Tibbetts *et al.* finding lanthanide nickel to have a hydrogen adsorption capacity of *ca* 2 wt% at 110 bar and 1.5 wt% at 36 bar (Tibbetts *et al.*, 2001).

5.7 Application to lithium nitrides

The possible rewards of finding a suitable method of hydrogen storage has resulted in new materials constantly being reported as potential candidates for hydrogen storage by adsorption (Chapter 1). During the course of this study, lithium nitride has been proposed as one such candidate utilising chemisorption (Chen *et al.*, 2002).

In order to achieve reversible hydrogen storage, the lithium nitride initially required to be hydrogenated at 270 ˚C, to produce a mixed lithium imide (Figure 5-20, Initiation step). The lithium nitride then released hydrogen when heated to 270 ˚C under vacuum and adsorbs hydrogen under a hydrogen atmosphere above ambient pressure at 270 ˚C (Figure 5-20, Adsorption/desorption cycle).

$$\text{Initiation step} \quad Li_3N \text{ (s)} + 2H_2 \text{ (g)} \rightarrow LiNH_2 \text{ (s)} + 2LiH \text{ (s)}$$
$$\text{Adsorption/desorption cycle} \quad Li_2NH \text{ (s)} + LiH \text{ (s)} + H_2 \text{ (g)} \leftrightarrows LiNH_2 \text{ (s)} + 2LiH \text{ (s)}$$
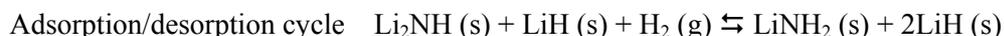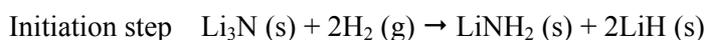
Figure 5-20 The preparation of Li_3NH_4 from Li_3N, then the cycling between Li_3NH_4 and Li_3NH_2 (Chen *et al.*, 2002)

Chen *et al.* reported the initiation step to have an uptake of 9.3 wt% recorded by IGA, with the adsorption and desorption cycling at a repeatable 6.5 wt% (Chen *et al.*, 2002). The theoretical uptakes have been calculated to be 11.5 wt% for the initiation step and 7 wt% for the adsorption and desorption cycling (Chen *et al.*, 2002). However, elsewhere these values have been reported as 10.4 and 5 wt% respectively (Hu *et al.*, 2003; Ichikawa *et al.*, 2004).

5.7.1 Challenges of lithium nitride analysis

Lithium nitride posed two problems for successful analysis on HPAA. Firstly, lithium nitride is highly air sensitive and swiftly oxidises if not stored under an inert atmosphere. Secondly, lithium nitride requires elevated temperature to adsorb hydrogen.

In order to overcome the problem of air sensitivity, a known amount of sample was loaded into the sample tubes in a nitrogen filled glove box and sealed using lab film. HPAA was first purged with helium and then a low positive pressure was maintained as the sample tube was fitted. This prevented any air gaining access to the material and also broke the lab film when the sample was in place in the apparatus. Although lithium nitride required elevated temperatures to chemisorb hydrogen, it is also required it to desorb the hydrogen. This property of the material allowed an accurate determination of the hydrogen sorption to be possible (Hu *et al.*, 2003; Ichikawa *et al.*, 2004). The material was exposed to hydrogen at a known pressure at 30 ˚C and allowed to equilibrate; this provided a zero point differential pressure reading. The sample temperature was then elevated to facilitate adsorption. While the sample was at temperature the differential pressure was monitored in order to observe the kinetics of the reaction. Once equilibration had been achieved, the system was returned to 30 ˚C and the post-adsorption differential pressure reading was recorded. From this the total amount of hydrogen adsorbed could be calculated.

5.7.2 Hydrogen sorption determination of lithium nitride

Lithium nitride and lithium nitride nanotubes were prepared by Dr Katherine Jewel (Chemistry, University of Nottingham) as part of a collaborative study on the hydrogen storage properties of lithium nitride. Four sets of experiments were carried out in order to examine the hydrogen storage potential of both materials (Table 5-6).

The hydrogen sorption capacity of the lithium nitride was found to be consistently *ca* 10.5 wt% for the preparation step, which was in good agreement with the predicted uptakes. On cycling the lithium nitride was found to achieve 3-4 wt% hydrogen capacity which was below the expected figure, this was thought to be caused by not

all of the hydrogen desorbing after the preparation step.   The lithium nitride nanotubes were found to have a lower uptake for the preparation step of 8.8 wt%, this was thought to be caused by sample being combined from several runs and thus being of lower purity. However, on cycling *ca* 5 wt% was achieved, this higher level of capacity was attributed to the nanotubes have a more developed pore structure thus facilitating desorption.

Conditions **Results**	**Li₃N** **A**	**Li₃N** **B**	**Li₃N** **Nanotubes**
Sample (g)	*0.218*	*0.213*	*0.107*
Degas temp (˚C)	*270*	*320*	*270*
Operating pressure (bar)	*10*	*30*	*10*
Run 1 (wt%)	10.5	10.9	8.8
Run 2 (wt%)	3.2	2.9	4.4
Run 3 (wt%)	3.7	4.0	5.3
Run 4 (wt%)	-	-	5.2

Table 5-6 Equilibrated hydrogen sorption results of lithium nitride and the lithium nitride nanotubes recorded at 30 ˚C after equilibrium being achieved at sample temperature of 270 ˚C

The high temperature of adsorption and desorption is the first major barrier for lithium nitride if it is to become a suitable candidate for mobile applications. The second barrier is long period required to achieve equilibrium. To analyse this problem the kinetic data from the experiments was analysed (Figure 5-21). The lithium nitride run recorded at 10 bar requires 140 hours for the equilibration of the first run. This was reduced to 110 hours when the experiment was repeated at 30 bar. The additional adsorption on cycling was minimal indicating that the higher temperature did not facilitate any further desorption. However, using the higher temperature severely reduced the kinetics of the cycling runs; this was attributed to the increased temperature destroying some of the pore structure of the lithium nitride.
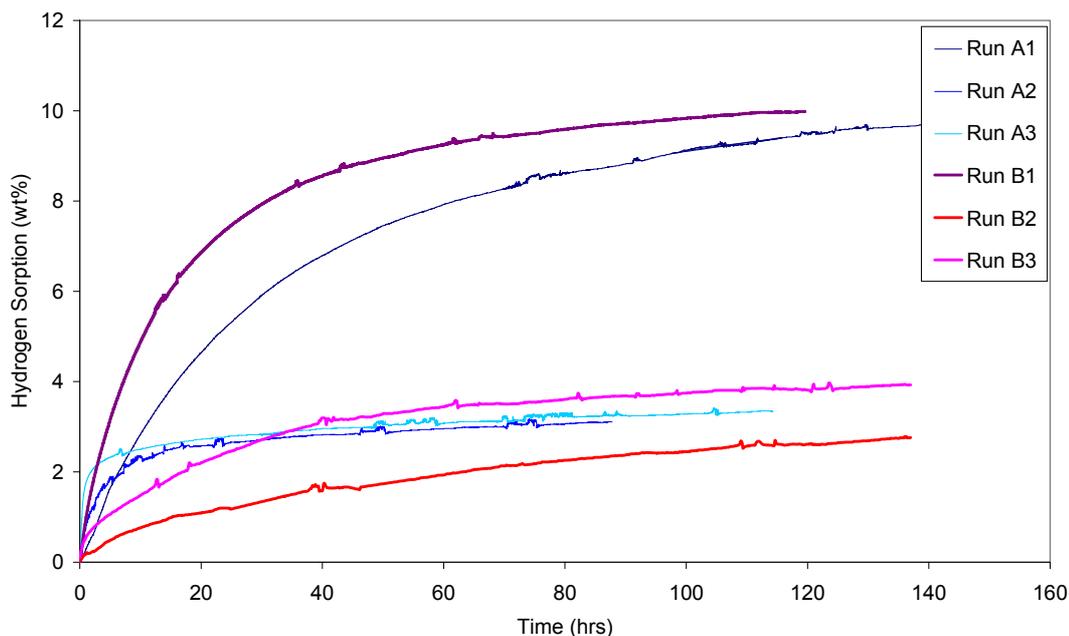
Figure 5-21 Hydrogen adsorption profiles of lithium nitride recorded at a sample temperature of 270 ˙C (Run A) and (Run B) 30 bar using a degas temperature of 270 ˙C

The nanotubes with their more developed pore structure achieved equilibrium after about 60 hours at 10 bar, almost half the analogous lithium nitride time (Figure 5-22). A similar increase in rate was observed for the cycling runs using the lithium nitride nanotubes.
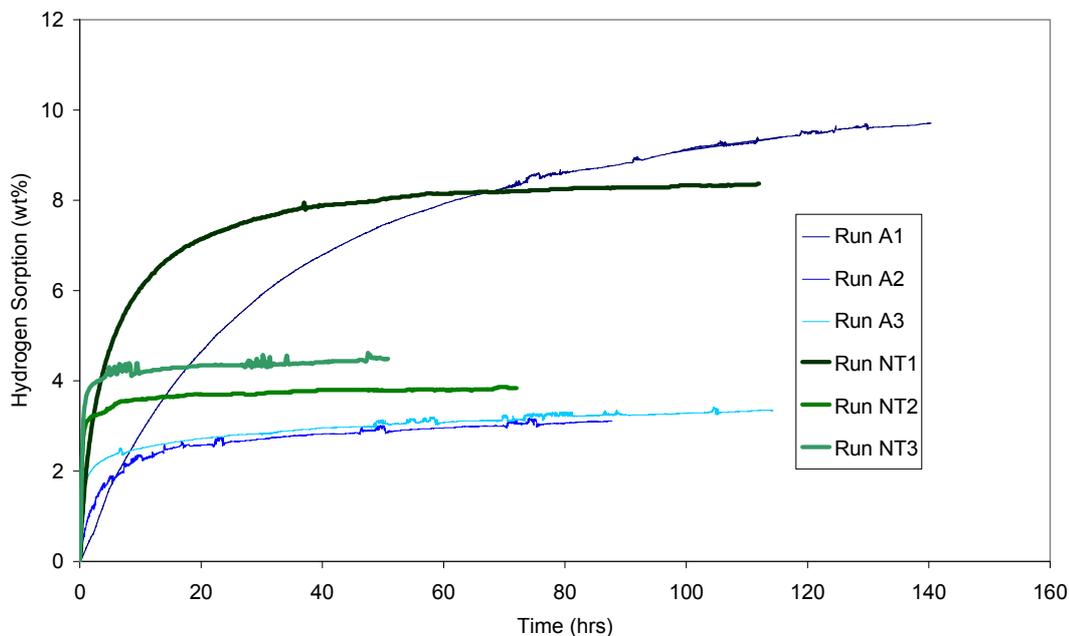
Figure 5-22 Hydrogen adsorption profiles of lithium nitride (Run A) and lithium nitride nanotubes (Run NT) recorded at sample temperature of 270 ˙C and 10 bar using a degas temperature of 270 ˙C

5.8 Summary

A differential pressure method has been developed for the determination of the hydrogen sorption capacity of a material. The procedures and apparatus have been evaluated and optimised in order to facilitate the highest degree of accuracy of the measurement. A helium correction was introduced in order to provide a baseline for experiments, avoiding errors resulting from non-sorption related pressure effects. The effect of temperature was investigated and found to be greatly diminished when using the differential pressure system in comparison to a direct pressure system.

The measurement primarily uses three approximations.

- Helium achieves negligible adsorption on the surface of a material
- Helium and hydrogen behave as ideal gases
- The Pre-degas mass of material is used for the calculation of hydrogen adsorption

The apparatus was calibrated using lanthanide nickel and was found to give a repeatable result, in good agreement with the literature. From this evaluation, HPAA is believed to have a conservative accuracy of 0.1 wt%.

The HPAA has been proven to be a versatile piece of apparatus, capable of operating with the whole system at a controlled temperature near to ambient, or with the adsorbent at an elevated temperature. The apparatus has been demonstrated to be operational at elevated temperature using lithium nitride as the adsorbent. In the following chapters the application of HPAA to activated carbons, CNF and CNTs will be discussed.

CHAPTER 6
Studies of Activated Carbons

6.1 Introduction

Activated carbons are broadly defined as porous, non-graphitisable, and manufactured to exhibit a high degree of porosity and surface area (McEnaney, 2002). The first industrial production of activated carbon was reported in 1909 in Germany by Ostrejko. Although the development of decolourising charcoals was carried out during previous two centuries, and charcoals are known to have been utilised as far back as 2000 BC by the ancient Egyptians for water purification (Byrne *et al.*, 1995; Marksberry, 2004).

The main factor that makes activated carbons excellent adsorbents is their porous structure, created by pores of various dimensions broadly classified as macropores, mesopores and micropores (Figure 6-1). The different pore sizes allow access by a large range of molecules. The majority of the surface area of conventional activated carbons consists of micropores, with macropores and mesopores creating "access points" to the micropores. It should be noted that the microporosity of activated carbons has been hypothesised to be slit-shaped, which has been supported by TEM studies (Rodriguez-Reinoso, 2002).
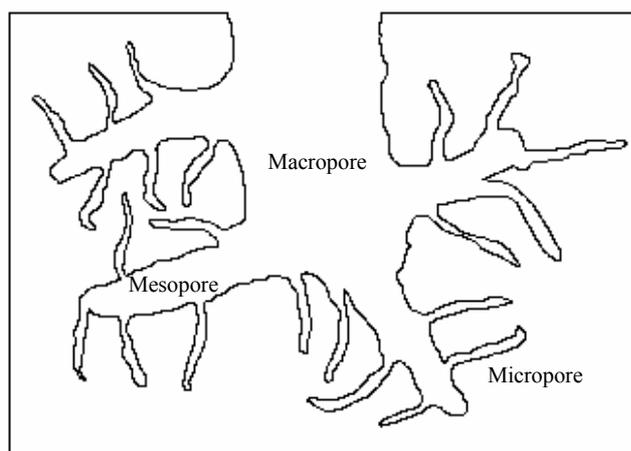
Figure 6-1 Two dimensional representation of the pore structure of granular activated carbon (Rodriguez-Reinoso, 2002)

6.1.1 Production

Activated carbons may be produced from almost any organic non-graphitisable material. Crystalline carbon, however, cannot be activated due to its stronger, more ordered, bond structure. There are two main methods currently used to produce activated carbons; chemical and physical (Figure 6-2). The latter sometimes referred to as thermal activation. Although the two processes are described separately in the following sections, often a combination of chemical and physical activation is required to obtain the desired pore structure.

Physical Activation

Precursor → Carbonisation → Char → Activation → Activated carbon

Chemical Activation

Precursor → Chemical Impregnation → Impregnated Precursor → Heat Treatment Washing → Activated carbon
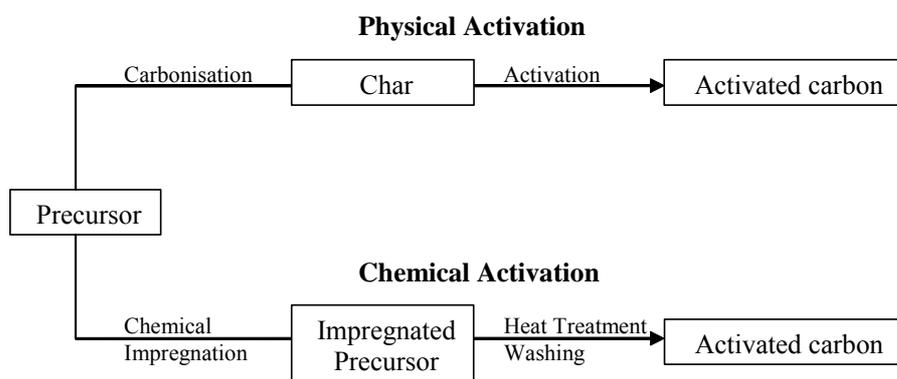
Figure 6-2 The main methods for activated carbon preparation (Rodriguez-Reinoso, 2002)

6.1.1.1 Chemical activation

Chemical activation involves the use of an inorganic agent such as zinc chloride, phosphoric acid or potassium hydroxide in order to chemically activate a carbon precursor, by modifying the chemical reactions which occur in the subsequent heat treatment (McEnaney, 2002). The most common precursors for chemical activation are cellulose-based materials, such as wood or nutshells, since chemical activation affords large pore volumes from these materials.   The heat treatment utilises comparatively low temperatures, usually below 600 ˚C, during which activation of the material occurs. The carbon is then washed repeatedly in order to remove the chemicals. This method creates highly porous, activated, carbons and, when using potassium hydroxide as an activating agent, super activated carbons can be produced with surface areas in excess of 3000 $m^2 \, g^{-1}$ (Rodriguez-Reinoso, 2002). Currently, phosphoric acid remains the most common reagent for chemical activation on an industrial scale, with surface areas of up to 1500 $m^2 \, g^{-1}$ being commercially achieved. Activation by potassium hydroxide is primarily confined to laboratory scale production (McEnaney, 2002).

6.1.1.2 Physical activation

Physical activation usually involves two stages; the carbonisation of the precursor to obtain a char and then activation of the char. The most common precursors for physical activation are lignite and bituminous materials such as peat and certain types of coal. These possess low inorganic content, producing activated carbons with low ash, in good yield, at comparatively low costs (Rodriguez-Reinoso, 2002). The carbonisation process involves the heating of the material to high temperatures (600-1000 ˚C) in an inert atmosphere, thus removing any volatiles present (Derbyshire et al., 1995). For this stage it is important that the precursor is non-graphitisable by the action of heat alone, as this ensures that a non-graphitisable char is produced. The char is then activated at high temperatures, 600-1000 ˚C, using a gaseous oxidising agent such as steam or carbon dioxide. The yield of carbon product after physical activation can be as low as 10 wt%, much lower than possible utilising chemical activation which can be as high as 40 wt% (Rodriguez-Reinoso, 2002). Even so, physical activation remains the most common process of activation, owing to its ease of operation and cost of production relative to chemical activation.

6.1.2 Activated carbon fibres

Activated carbon fibres (ACF) constitute a different type of activated carbon, and have received a lot of attention since they entered the market in the 1960s (Rodriguez-Reinoso, 2002). They are prepared as conventional carbon fibres, by carbonisation from a precursor, but then, instead of being graphitised, they are activated by physical activation. They differ from other activated carbons in both their pore structure and physical form. Owing to the small diameter of the fibres, the activation produces almost an entirely microporous structure, with very little macro or mesoporosity present (Figure 6-3). In addition to this, the pores are directly accessible from the surface of the fibre facilitating fast adsorption. The activated carbons previously discussed come in two main forms; powdered and granular. Owing to the fibrous nature of ACF, however it may be woven in the form of cloth or felt, allowing easier handling, but ACF remains 10-100 times more expensive than conventional activated carbons making it less attractive for many applications.

Fibre Axis
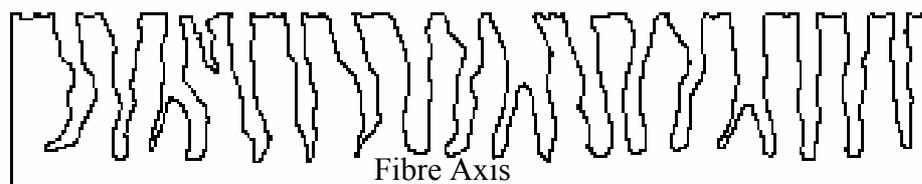
Figure 6-3 Two dimensional representation of the pore structure of activated carbon fibres (Rodriguez-Reinoso, 2002)

6.2 Investigation into powdered activated carbons

6.2.1 Selection

The BET nitrogen surface area is representative of the microporosity of a structure (Chapter 3). Even though nitrogen molecules are much bigger than hydrogen, it is logical to assume that as the BET nitrogen surface increases, a similar increase in hydrogen adsorption capacity would be observed. Thus, activated carbons were selected primarily on their BET nitrogen surface area in order to afford a broad range of adsorbents for study. To ensure that the physical form of the activated carbon was not a variable, the comparative study was confined to activated carbons in powdered form.

Activated Carbons Used for Comparison Study	Source	Quoted Surface area $(m^2 \, g^{-1})$
Norit FGD (Commercial)	Lignite coal	500
Speakman (Commercial)	Coconut	800-900
Fisher Charcoal FGA (Commercial)	Charcoal	1000
Fisher FDC (Commercial)	Charcoal	1500
1523-r-98 (Bath University)	Wood	1650
1526-r-98 (Bath University)	Wood	2200
AC3000 (Chinese Academy of Sciences)	Coke	3200
Other Activated Carbons Studied		
PAN activated carbon fibres (Chinese Academy of Sciences)	PAN Carbon Fibres	300
Granular Picazine (Commercial)	Charcoal	1500

Table 6-1 Activated carbons studied

6.2.2 Nitrogen adsorption studies

In order to ensure that unbiased and accurate comparisons could be made between the activated carbons, the BET nitrogen surface area was determined for each sample, using the method described in Chapter 4. In addition to the BET surface area measurement, full isotherms were also recorded in order to provide adsorbent classification for each of the samples (Table 6-2). The percentage weight loss observed during degas has also been included.

Activated Carbon	Quoted Surface Area $(m^2 g^{-1})$	Measured BET Nitrogen Surface Area $(m^2 g^{-1})$	Isotherm Type	Degas Weight Loss (%)
Norit FGD	600	595	Type I	8.7
Speakman	900-1000	984	Type I	16.1
Fisher FGA	1000	988	Type I	15.0
Fisher FDC	1500	1525	Type I	16.0
1523-r-98	1650	1657	Type I	13.3
1526-r-98	2200	2228	Type I	15.7
AC3000	3200	3101	Type I	22.9
PAN	300	334	Type I	32.1
Picazine	1500	1451	Type I	15.8

Table 6-2   Activated carbons and PAN activated carbon fibre nitrogen BET study

The isotherm type for all the activated carbons was determined to be of type I (Chapter 3), which classifies the materials as microporous materials. The quoted and measured BET surface areas exhibited good correlation for all the samples, with a variance of less than 30 m^2 g^{-1}, except for AC3000. For this sample, the measurement was carried out twice, yielding similar results both times, 3090 and 3109 m^2 g^{-1}, the average being *ca* 100 m^2 g^{-1} lower than the quoted value. In order to check this measurement, enhanced nitrogen BET surface area analysis was carried out on AC3000 using a modified BET apparatus designed to enhance the accuracy of the high surface area measurements. The modified apparatus utilised a turbo-molecular pump, a long equilibrium time (25 sec), utilising a small gas introduction value (5 g cm^{-3}) and the sample was degassed at 400 ˚C under vacuum. These modifications resulted in an increase in accuracy of the initial isotherm points, which are used for the BET calculation, but had the disadvantage that a single experiment

could take as long as five days. The enhanced measurement reported a surface area of 3201 m^2 g^{-1}, which is in good agreement with the quoted value. For the purpose of comparison the measured BET surface areas will be used ain this study.

The degas weight loss has been included, since a good correlation with the nitrogen BET surface area was observed. This needs to be considered due to the effects of degas weight loss on the hydrogen adsorption measurement (Figure 6-4). This will result in the hydrogen adsorption measurement made on HPAA being reduced relative to the true value as materials increase in surface area (Chapter 6).
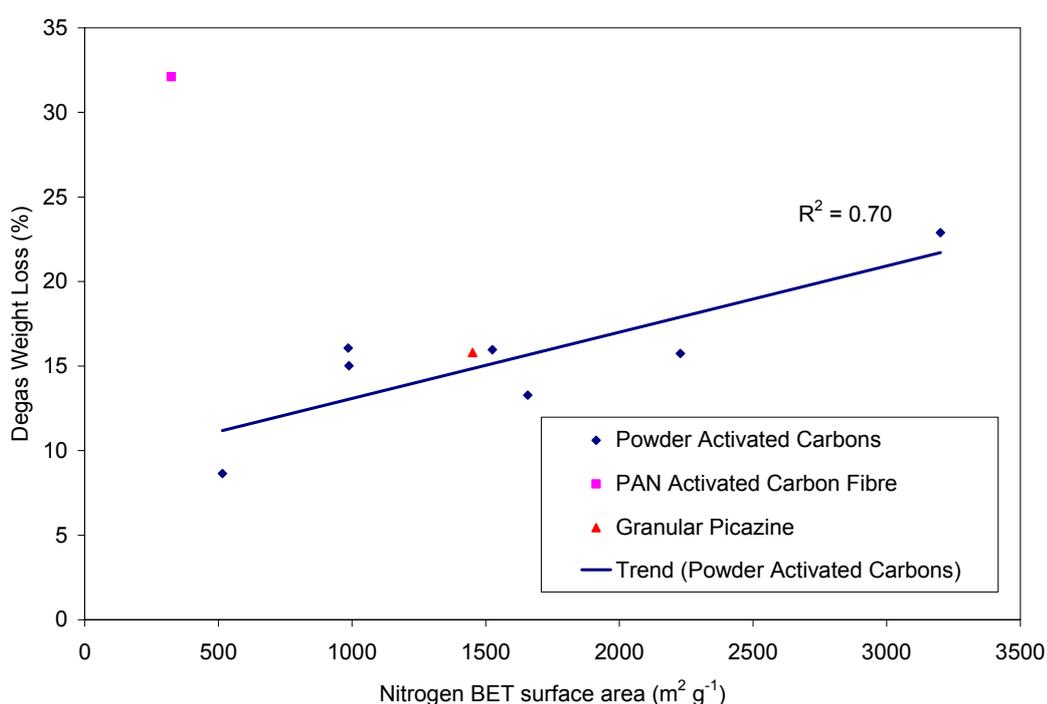
Figure 6-4 The relationship between degas weight loss and nitrogen BET surface area for the comparative study of activated carbons

6.2.3 Hydrogen adsorption studies

The hydrogen adsorption profiles of all the activated carbons listed in Table 6-1 were recorded at 100 bar. The degas procedure employed for pretreatment of each sample was DG2, as this method was favoured by the majority of previous investigations (Chapter 2). For all the samples similar-shaped hydrogen adsorption profiles, were observed, with the primary difference being the final hydrogen storage capacity (Figure 6-5).
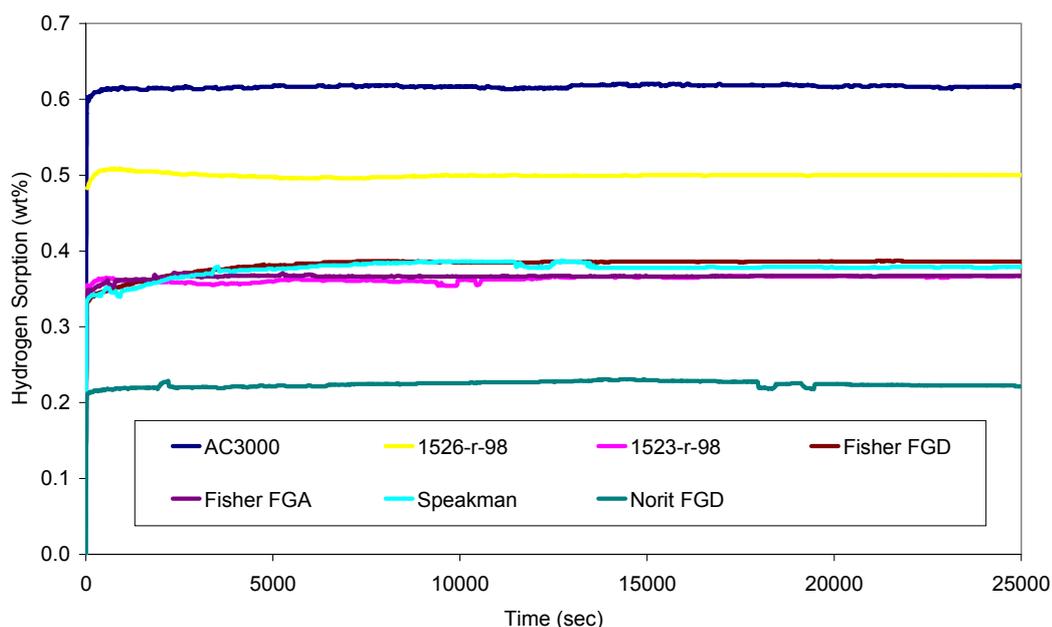
Figure 6-5 Hydrogen adsorption profiles for powder activated carbons using DG2 recorded at 100 bar and 30 °C

In all the experiments, over 90 % of the adsorption occurred almost instantaneously subsequent to expansion. This timescale was consistent with physisorption, which had been hypothesised to be the likely mechanism of interaction between hydrogen and activated carbon.

The materials studied, AC3000, 1526-r-98, Fisher FGA, 1523-r-98 and Norit FGD, all possess very similarly shaped adsorption profiles, with only a very slight apparent increase in adsorption after the initial, instantaneous, uptake. This final, slower increase could have been the result of a number of factors. One possibility was that it was difficult for hydrogen to penetrate regions of the carbon structure, causing a change from physisorption to penetration as the rate determining step, slowing the final stages of the adsorption. Another possible cause was that a rise in temperature caused by the heat of adsorption resulted in a temperature-induced pressure rise in the sample limb, which did not occur in the reference limb. As this heat dissipated, the pressure reduced causing the apparent slow, final stages of adsorption. This phenomenon would not have affected the accuracy of the final result but would have masked the rate of adsorption. Other temperature-related pressure effects, caused by the expansion of the gas, were cancelled out by using the differential pressure

system. In order to prove this theory, a thermocouple would need to have been located in both cells, and the temperature monitored to determine if the sample cell underwent a larger temperature rise than the reference cell. However, this has yet to be achieved as no suitable method has yet been developed for allowing access for the thermocouple, but keeping the system sealed against leaks.

The Fisher FDC and Speakman samples exhibited slightly different behaviour to the other activated carbon samples studied. Again, over 90 % of the adsorption appeared to occur almost instantaneously. However, approximately the final 10 % of the adsorption occurred over a much longer timescale, of approximately one hundred minutes. Similar theories could be applied to this phenomenon as for the other activated carbons, since although the apparent adsorption occurred over a much longer time scale, it is likely that different effects were dominant. Another possibility was that some trace metals were present, which formed hydrides with the hydrogen via a chemisorption process, which occurred over a longer period.

Fisher FGA was repeated under identical conditions in order to prove the repeatability of the method (Figure 6-6). For both runs the degas method DG2 was employed and the results exhibited good repeatability.
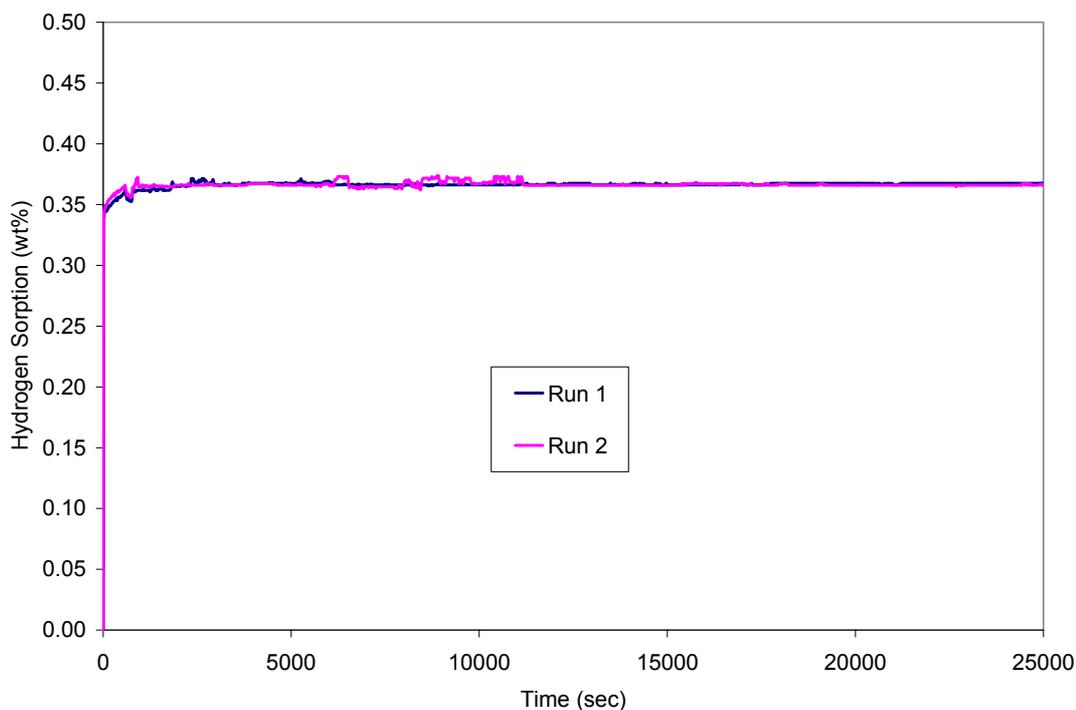
**Figure 6-6 Hydrogen sorption profiles for Fisher FGA using DG2
recorded at 100 bar and 30 ˚C**

6.2.4 Effect of varying the method of degas

In order to study the effect of varying the degas method employed prior to each run, the AC3000 was selected as a sample, as it demonstrated a typical adsorption profile and achieved the highest hydrogen adsorption uptake. Different degas processes were utilised for a series of analysis, in order to determine what effect they made on the hydrogen adsorption capacity of AC3000 (Figure 6-7).
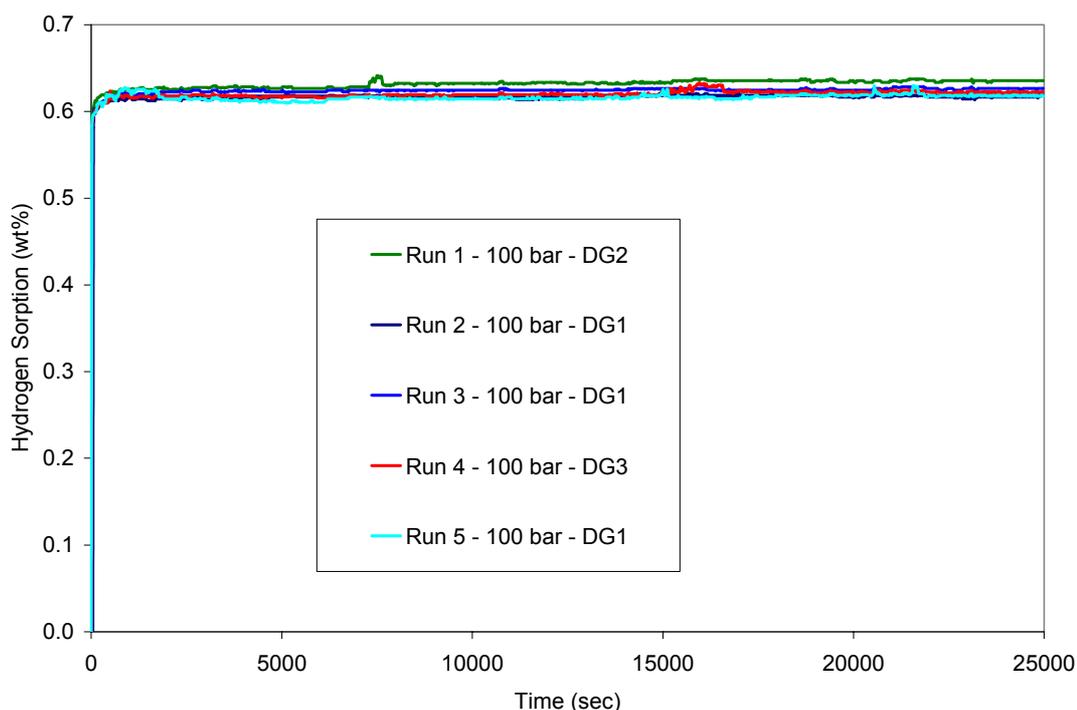
Figure 6-7 Hydrogen adsorption profiles for AC3000 using various degas methods, recorded at 100 bar at 30 ˙C

The first procedure employed was DG2, as this was the standard method used in previous work (Chapter 2). DG1 degas was then utilised for two runs in order to demonstrate that adsorption-desorption cycling had no effect on the level of adsorption. HPAA had no method for measuring the desorption of hydrogen from the carbon, however, it was logical to assume that if the same amount of hydrogen was adsorbed on the second cycle, all the hydrogen from the first cycle must have been desorbed. The DG3 procedure was then utilised in order to determine whether a more severe degas method would facilitate an increased hydrogen uptake. Finally, DG1 was employed in order to display repeatability. All the runs yielded very similar results; this clearly showed that all that was required to desorb all the hydrogen from an activated carbon was to remove the pressure. This was indicative of physisorption, since chemisorption usually requires the input of energy in order to

break the bonds between the adsorbate and adsorbent. On adsorption-desorption cycling AC3000, exhibited no loss of capacity and displayed excellent repeatability, independent of degas procedure employed.

6.2.5 Surface area and hydrogen adsorption

The relationship between surface area and hydrogen adsorption for the seven activated carbons compared (Table 6-1) was investigated by plotting hydrogen adsorption against nitrogen BET surface area (Figure 6-8). The general trend observed was that as the nitrogen BET surface area of the activated carbons increased, the hydrogen adsorption uptake of the also increased. The nitrogen BET surface area measurement indicated an approximation to the relative amount of nitrogen adsorption sites there were available on an adsorbent. If there were more available sites for nitrogen adsorption, it was to be expected that the same sites would have been available for hydrogen adsorption. Diatomic hydrogen, however, has a much smaller diameter than diatomic nitrogen, *ca* 148 and *ca* 220 pm respectively (Atkins, 1998). Thus, the activated carbons may have possessed sites for adsorption that were accessible for hydrogen, but not for nitrogen, creating additional sites undetectable to the nitrogen BET surface area measurement. This was the probable explanation as to why there was only a general trend between nitrogen BET surface area and hydrogen adsorption capacity of the materials.
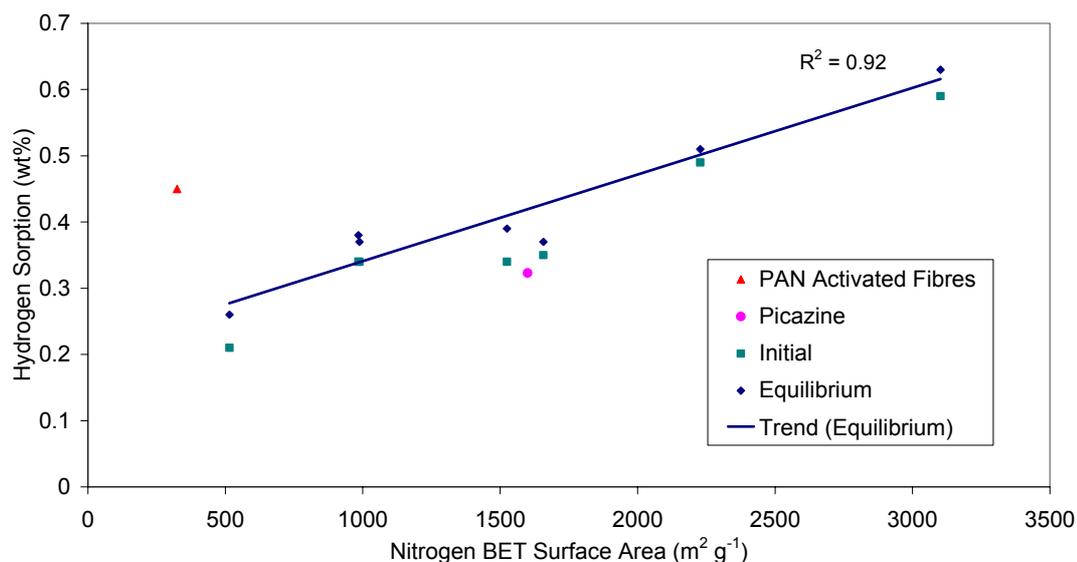
Figure 6-8 Hydrogen adsorption uptake vs nitrogen BET surface area for the series of activated carbon listed in Table 6-1 employing DG2, at 100 bar and 30 ˚C

In order to get an approximate estimate of the surface area required to achieve the US Department of Energy hydrogen storage target of 6.5 wt%, the maximum and minimum linear regression of the equilibrium values were extrapolated. The results of this showed that to achieve the target value at 100 bar, an activated carbon would need to possess a surface area of between 27000 and 50000 m^2 g^{-1}. These surface areas are currently impossible to achieve, as *ca* 3000 m^2 g^{-1} is believed to be close to the accepted physical surface area limit for a carbon material. This can be demonstrated by considering a single layer of graphite (Figure 6-9). The theoretical maximum surface area for this material is 2609 m^2 g^{-1}, this indicates that to exceed the *ca* 3000 m^2 g^{-1} barrier the breaking down of the atoms would be required.
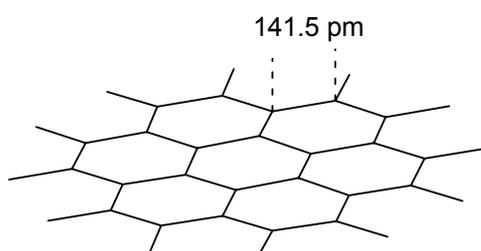
Figure 6-9 Diagram of a section of a graphite plane displaying the carbon-carbon bond length (Greenwood *et al.*, 1997)

6.2.6 Hydrogen adsorption isotherm of AC3000

In order to study an isotherm for an activated carbon, AC3000 was again selected. The hydrogen storage uptake of this activated carbon was recorded at 20, 40, 60, 80 and 100 bar (Figure 6-10).

The equal steps in increasing pressure resulted in the concurrent increase in hydrogen adsorption. With increasing pressure, the relative pressure increase in adsorption was noted to decrease slightly. The slower, final, stage of adsorption, as discussed earlier in this chapter, also became more pronounced as the pressure increased (Section 6.2.3). This was consistent with both theories proposed to explain this phenomenon. If deeper penetration into the structure of the adsorbent was the cause of the apparent slower adsorption, then it would be expected that higher pressures would facilitate this. However, the increase in the amount of this slower adsorption was proportional to hydrogen pressure, which was more indicative of a phenomenon mediated by the heat of adsorption, because, as the amount of hydrogen adsorbed increases, so would the heat of adsorption causing a systematically larger

rise in temperature. Thus, this was strong indication that heat of adsorption causes the final, slower, rate of adsorption. Using the equilibrium hydrogen adsorption uptake onto AC3000 at each of the pressure steps, an isotherm may be created (Figure 6-11).
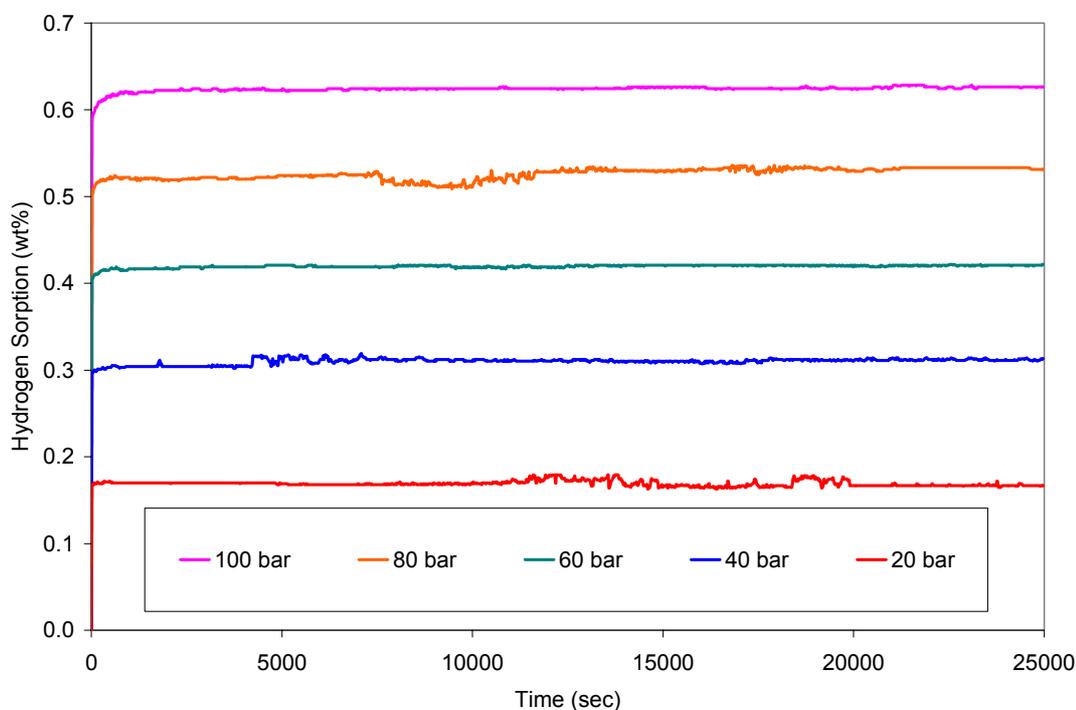
Figure 6-10   Hydrogen adsorption profiles for AC3000 at a series of 20 bar pressure steps recorded at 30 ˚C utilising DG2
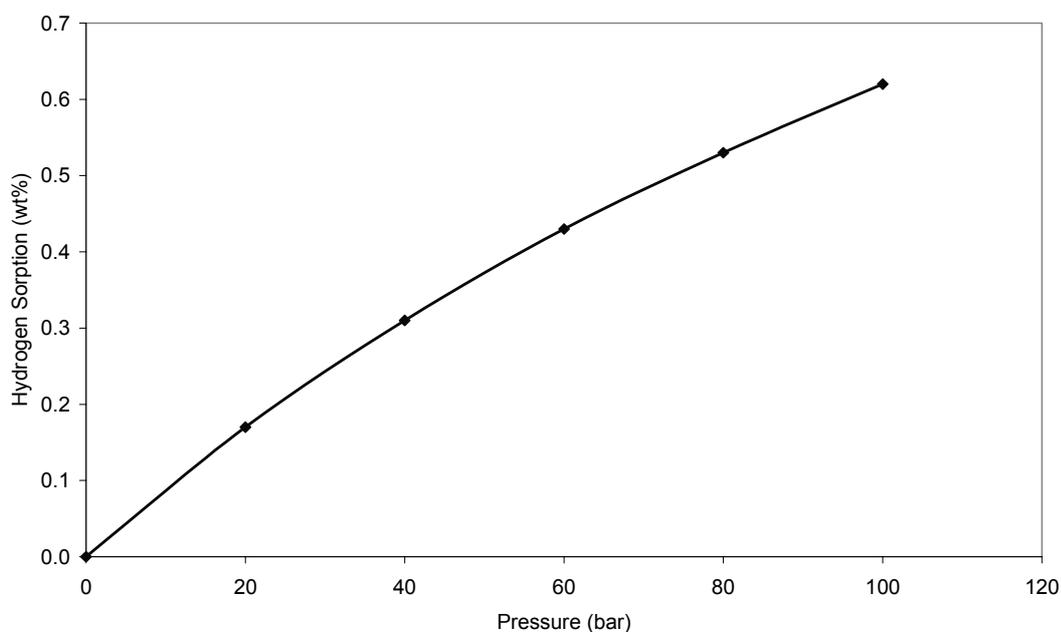
Figure 6-11   Hydrogen adsorption isotherm for AC3000 recorded at 30 ˚C using DG1

This isotherm illustrates the correlation between increasing pressure and increasing hydrogen adsorption capacity. The trend did not achieve equilibrium before the maximum working pressure of the apparatus was reached. Further investigation using apparatus capable of working at higher pressures would be required to determine the plateau pressure for the isotherm.

The beginning of the isotherm for this material fitted the type I BDDT classification of adsorption isotherm (Chapter 3). This indicated that the adsorption was occurring via the filling of micropores and this highlights the largest barrier for hydrogen storage in carbon materials at room temperature. Room temperature is over 250 ˚C above the critical temperature of hydrogen (-240 ˚C), which implies that via physisorption alone, only mono-layer adsorption of hydrogen is possible at room temperature via the action of pressure (Greenwood *et al.*, 1997) (Figure 6-12). If a method cannot be found to over come this problem, physisorption of hydrogen at room temperature above 1 wt% on carbon materials appears unlikely.

(a)   (b)
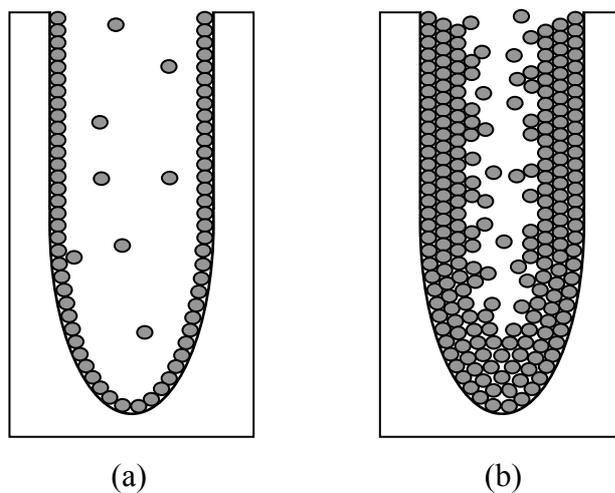
Figure 6-12 Pictorial representation of hydrogen filling a carbon micropore via the action of pressure at a temperature (a) above the hydrogen critical point and (b) below the hydrogen critical point

6.3 Enhancing carbon materials

In order to achieve higher uptake of hydrogen on carbon materials, via adsorption, several methods have been proposed.

- The doping of carbon materials with
  - o heteroatoms such as nitrogen
  - o metal atoms by impregnation
  - o metal atoms by intercalation
- Capillary effect in MWNT and SWNT

6.3.1 Nitrogen containing activated carbon fibres

A sample of activated PAN carbon fibres was obtained from the Chinese Academy of Sciences. The sample was in the form of a felt, and known to have a nitrogen content of 5 wt%. The sample was analysed by enhanced nitrogen BET and found to be an ultra-microporous material, with a non-developed porosity. This implied that it was a char which had not been activated properly, which explains why the surface area was only 334 m^2 g^{-1} (Table 6-2). In addition to this, the isotherm was irreversible, implying that nitrogen was chemisorbing to the material (Figure 6-13).
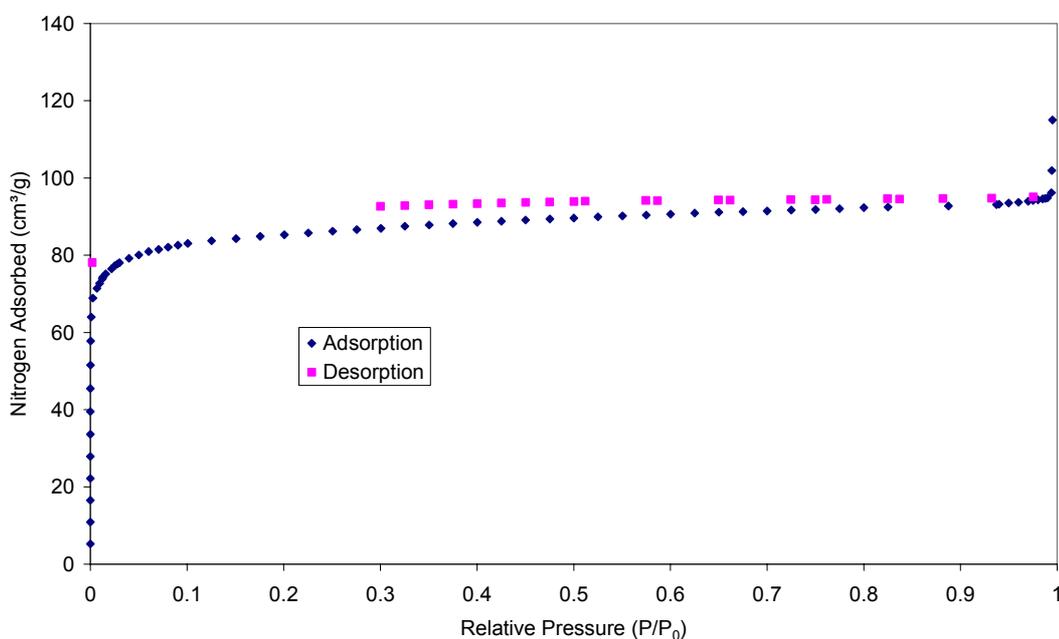
Figure 6-13   Nitrogen BET isotherm of PAN activated carbon

The hydrogen adsorption profiles for the activated carbon PAN were recorded at 100 bar (Figure 6-14). The first run, degassed using the DG2 method, achieved an

uptake of 0.45 wt%, followed by a run using DG1 in order to assess how much of the uptake was physisorption. For this, an uptake of *ca* 0.15 wt% was determined, which was higher than would be expected for a sample with a surface area of only 334 m^2 g^{-1}, relative to the trend observed in Figure 6-8. DG1 was repeated after the other runs had been conducted, in order to assess the repeatability, and was found to vary between 0.13-0.17 wt%. DG3 was found to result in a decreased hydrogen adsorption capacity, relative to DG2. This was thought to be due to the hydrogen not being fully released in this process, so blocking sites for further adsorption during the run. On carrying out a DG2, 0.38 wt% of hydrogen adsorption repeatably observed, lower than the 0.45 wt% achieved initially. This difference was thought to be caused by the initial 0.07 wt% being irreversibly bound to the activated carbon PAN.
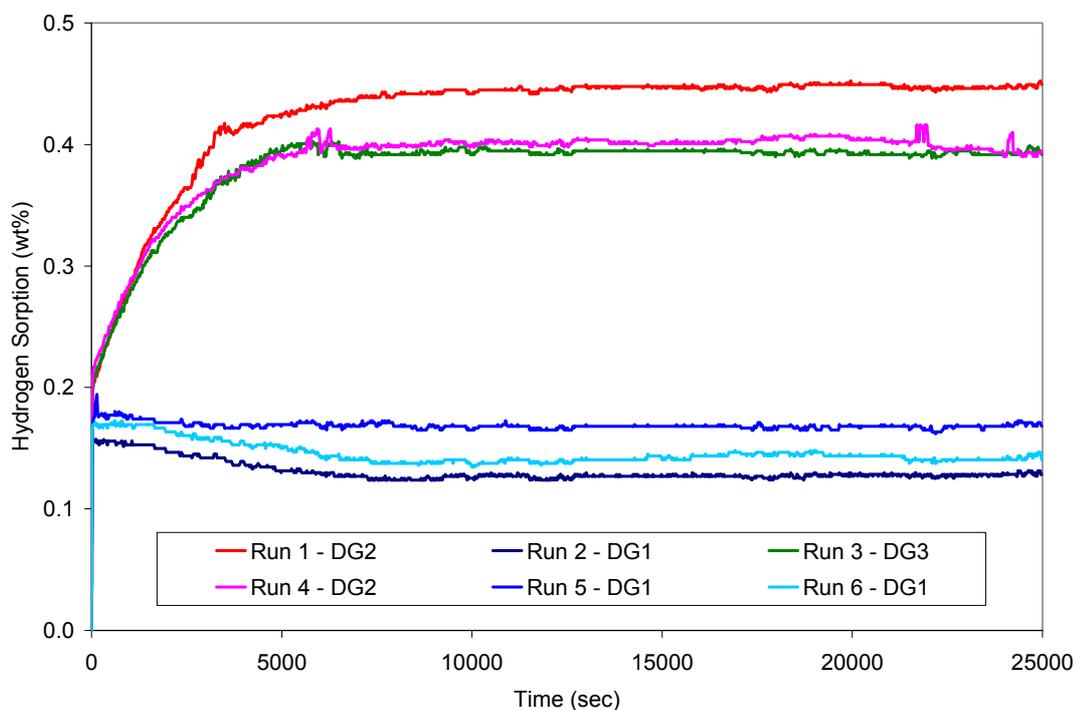
Figure 6-14   Hydrogen sorption profiles of activated carbon PAN at 100 bar and 30 ˙C

The degas procedure utilised on the activated carbon PAN had a large effect on the amount of hydrogen adsorbed, causing up to a three fold increase in the amount of hydrogen adsorbed. This was in marked contrast to the powder activated carbons described earlier in this chapter (Section 6.2.4).

6.3.2 Doped activated carbons

Palladium has been found to be capable of adsorbing up to 935 times its own volume of hydrogen, forming a the hydride $PdH_{0.5}$ (Greenwood *et al.*, 1997). A sample of picazine granular activated carbon was selected as the support for the palladium, as it possessed a high surface area, and had been found to be a suitable support in other work. For this investigation, 10 g of picazine was employed, which was doped with palladium nitrate using a wet method (Chapter 4). The dry picazine-palladium nitrate mixture was of mass of 11.14 g. After the reduction process, however, the mass was reduced to 6.1 g. This was less than the original mass of picazine used, and included a predicted loading of 0.41 g of palladium. This was hypothesised to be caused by the carbon acting as a reducing agent for the palladium in the reduction step (Figure 6-15).

$$C\ (s) + PdO_2\ (s) \rightarrow CO_2\ (g) + Pd\ (s)$$

Figure 6-15   The reduction of palladium dioxide by carbon

The surface area of the doped picazine, $410\ \mathrm{m^2\ g^{-1}}$, was reduced by 70 % relative to that of the undoped material, which possessed a surface area of $1452\ \mathrm{m^2\ g^{-1}}$. This reduction in surface area was supposed to be caused by a combination of the blocking of the pores by palladium, and by the destruction of the porous structure during the reduction step. SEM images of the picazine, prior to and post palladium doping, were recorded (Figure 6-16). The images clearly show that the honeycomb cellulose structure of the picazine (Figure 6-16 (a)) had been heavily clogged by the palladium doping (Figure 6-16 (b)). The blocking of the macro-structure implied that the much smaller porous structure of the material would also be blocked.
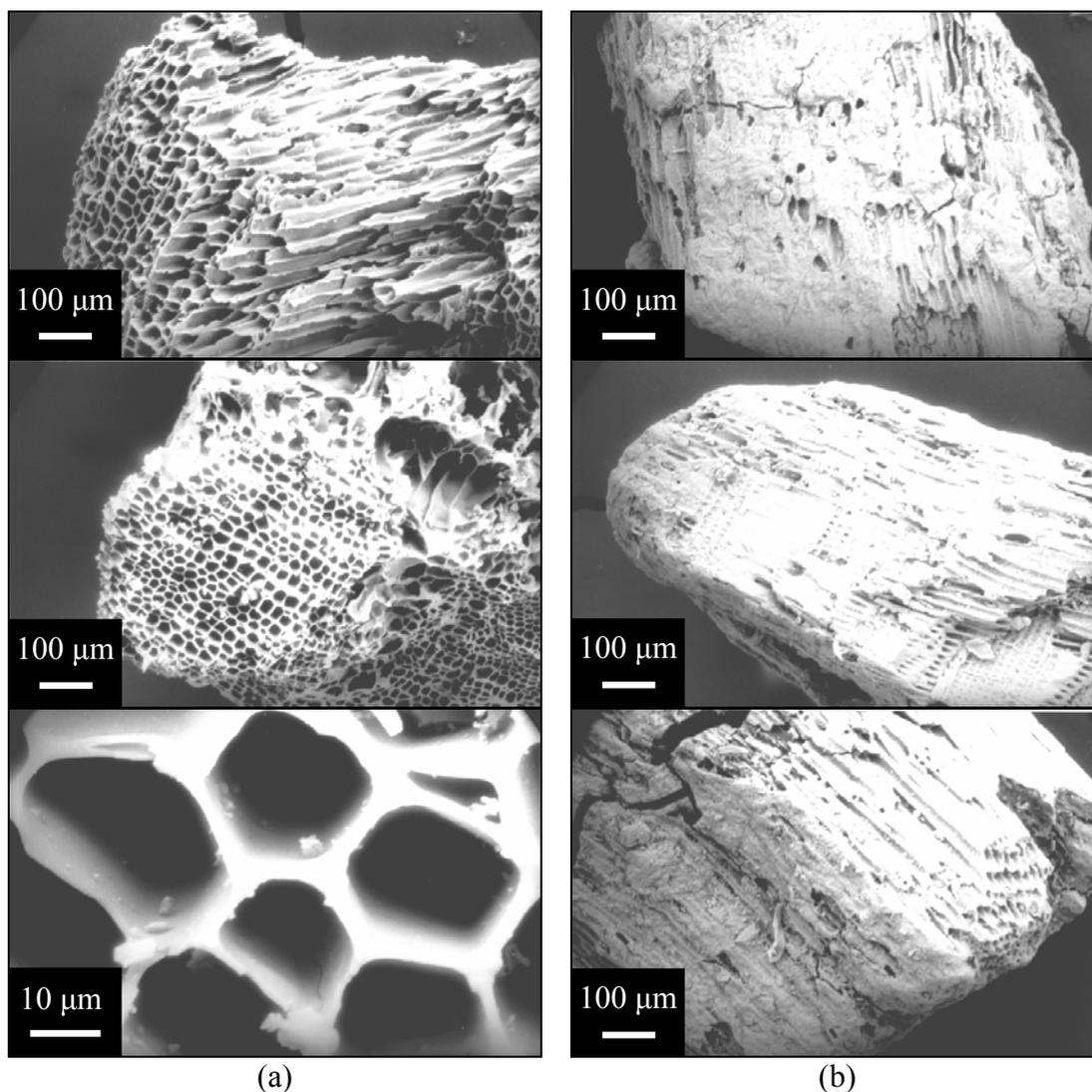
Figure 6-16   SEM images of (a) picazine showing the open macro-structure (b) palladium doped picazine showing the blocked macro-structure

The hydrogen adsorption capacity of the Picazine was also found be to reduced after doping by palladium. The hydrogen sorption capacity was found to decline by 60 %, which correlated well with the reduction in surface area, implying that the loss of sorption was caused by a decrease in surface area (Figure 6-17). This was as expected, since over 90 % of hydrogen sorption capacity was found to be approximately instantaneous in both cases, which has been found to correspond to physisorption. However, hydrogen sorption by palladium would be expected to proceed via a chemisorption method, which would occur over a longer period. This implies that the palladium was contributing a neglible amount to hydrogen sorption.
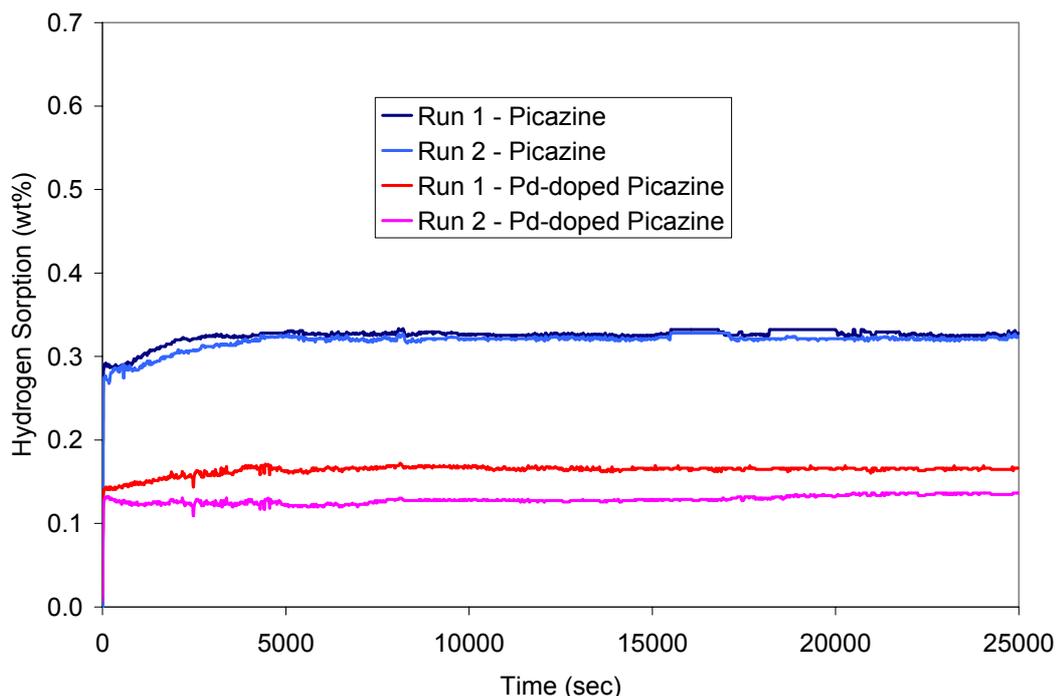
Figure 6-17   Hydrogen sorption profiles of picazine and palladium doped picazine recorded at 100 bar and 30 ˙C, after DG2

6.4 Summary

The highest surface area of activated carbons available today have surface areas of maximum *ca* 3000 m^2 g^{-1}, well below the predicted required amount to achieve the hydrogen sorption of 6.5 wt% utilising surface area alone. Thus, a number of possibilities for this application of activated carbons exist. One being that the pressure of the system could be increased. The isotherm of AC3000, however, the highest adsorbing carbon was at the limit of attainable surface area only achieves a 0.6 wt% uptake at 100 bar, where the isotherm begins to plateau, far short of the hydrogen sorption target.

The initial study on PAN activated carbon fibres indicated could further research could be beneficial, as the sample studied deviated significantly from the surface area *vs* hydrogen sorption trend. However, over an order of magnitude improvement in the uptake would be required to meet the DOE target.

CHAPTER 7
Preparation and Investigation of Carbon Nanomaterials

7.1 Introduction

The volumetric method determines the storage capacity of a material by measuring the pressure drop resulting from adsorption after exposing a sample to hydrogen at constant volume (Chapter 2). The majority of the volumetric work reported using CNF has been carried out employing direct pressure measurement in custom built apparatus based on the Sieverts type apparatus (Fan et al., 1999). However, at high pressures, the Sieverts type apparatus is very sensitive to temperature instability, leaks and additional pressure and temperature effects, caused by the expansion of the hydrogen from the reservoir to the sample cell (Chapter 5). This, combined with a possible inconsistencies of the materials studied, has led to a wide range of results being reported (Awasthi *et al.*, 2002; Bacsa *et al.*, 2004; Browning *et al.*, 2002; Cao *et al.*, 2001a; Cao *et al.*, 2001b; Chambers *et al.*, 1998; Cheng *et al.*, 2000; Ci *et al.*, 2003; Fan *et al.*, 1999; Gundiah *et al.*, 2003; Gupta *et al.*, 2000; Gupta *et al.*, 2001; Hou *et al.*, 2003; Hou *et al.*, 2002; Huang *et al.*, 2002; Hwang *et al.*, 2002; Jia *et al.*, 1999; Kiyobayashi *et al.*, 2002; Li *et al.*, 2001; Liu *et al.*, 1999; Lueking *et al.*, 2003; Lueking *et al.*, 2004; Lupu *et al.*, 2002; Luxembourg *et al.*, 2004; Ohkawara *et al.*, 2002; Park *et al.*, 1999; Poirier *et al.*, 2001; Tibbetts *et al.*, 2001; Wang *et al.*, 2002; Zhou *et al.*, 2004; Zhu *et al.*, 2002; Zhu *et al.*, 2003) (Figure 7-1).
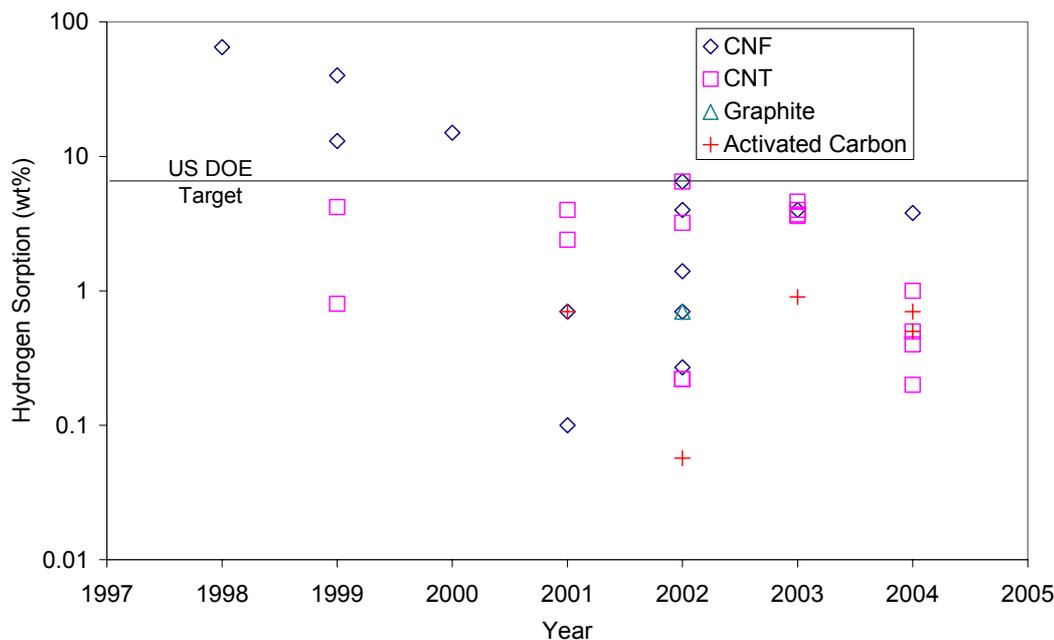
Figure 7-1 The history of hydrogen sorption measurements made using the volumetric method

7.2 Investigating tri-metallic catalyst systems

7.2.1 Controlling the catalyst

The first stage of this work was to prepare the catalysts, originally used by Mellor utilising the same method. The catalyst reported as producing the CNF that adsorbed the most hydrogen was $Cu_5Fe_{85}Ni_{10}$. On the first attempt to repeat this preparation, it was observed that when the precipitate was removed by filtration, the filtrate was a blue solution. This suggested that not all of the transition metals had been precipitated, since ammonium nitrate forms a colourless aqueous solution and transition metal nitrates dissolve in water to form coloured solutions. This was supported by the yield of the catalyst precursor being at most 90 %. In addition, the filtrate solution was blue and the copper content was 5 %, thus it was hypothesised that it was mainly copper that was not precipitating. In contrast, attempts to precipitate solutions of pure iron nitrate gave consistent results, all at approximately 100 %, with a colourless filtrate and almost complete precipitation of the metal being observed. However, inconsistent results were observed for the precipitation from aqueous solutions of copper nitrate and nickel nitrate with coloured filtrate solutions being observed and yields varying from 21 to 98 %. From these

observations, it was concluded that the base utilised in this method, ammonium bicarbonate, was not strong enough to take the required precipitation to completion.

This technique, however, has been employed for the preparation of mixed oxide transition metal catalysts for almost fifty years, and has been used by many different groups with none having reported any comparable observations (Best *et al.*, 1954; Browning *et al.*, 2002; Rodriguez, 1993). There are two possible explanations for this; the first was that owing to the experimental setup used in the laboratory, an unexpected variable was affecting the precipitation. The second was that the phenomena reported above was observed by other groups, but dismissed as unimportant. From the literature, it was difficult to tell which answer was correct as no characterisation of the catalyst, or observations from the preparation can be found.

It was decided to use some of the ammonium bicarbonate prepared catalysts in order to attempt to produce CNF from ethylene (300 ml min^{-1}) at 600 ˚C for 3 hours, the same method used by Mellor. On the first attempt, *ca* 60 mg of carbon was produced much less than the expected 2 g. Initial doubts were that the furnace was not reaching a sufficient temperature to facilitate the decomposition of the ethylene or the reduction of the catalyst. The run was repeated a further two times, first increasing the reduction temperature of the catalyst, then increasing the reaction temperature, while keeping all other variables constant. Both preparations failed to produce a significant amount of carbon. It was decided to try different catalysts batches that had been prepared by identical procedures to check the consistency of the result. The second catalyst produced an identical result to the previous findings. However, the third catalyst ($Cu_5Fe_{85}Ni_{10}c$) produced 1.9 g of solid carbon, which was within the 1-2 g yield reported by Mellor for the same procedure (Browning *et al.*, 2002). The sample was analysed by nitrogen BET and by SEM in order to confirm that CNF had been produced. The nitrogen BET surface area was found to be 20 m^2 g^{-1}, which is again comparable to that reported by Mellor. SEM microscopy proved conclusively that the material produced possessed a fibrous structure with the majority of the CNF having diameters ranging of 100 to 400 nm (Figure 7-2).

Figure 7-2 SEM image of CNF grown from pure ethylene using catalyst $Cu_5Fe_{85}Ni_{10}c$

The procedure was repeated with catalyst $Cu_5Fe_{85}Ni_{10}c$ in order to prove reproducibility. One batch of CNF was also annealed at 1000 ˚C, using the procedure outlined in the methodology (Chapter 5). The annealing of the CNF at 1000 ˚C for 24 hours was carried out, since it was reported to enhance the hydrogen adsorption properties of CNF (Browning *et al.*, 2002). During the process, no appreciable weight loss was observed and analysis by nitrogen BET and SEM revealed no obvious structural changes were made.

The preparation of the CNF was repeated using further batches of $Cu_5Fe_{85}Ni_{10}$ in order to try to prove the repeatability of the catalyst preparation. However, this preparation only produced a very small amount of carbon (*ca* 60 mg), as did the next four attempts, using a different batch of catalyst each time. The small amount of solid carbon produced each time also varied between each batch with a variation factor of two observed. This was a possible indication that the supposedly identical catalysts were subtly different. The process was repeated several more times, with slight variations made to the apparatus, with still little solid carbon being produced. Finally, the CVD apparatus was dismantled and rebuilt to check that no errors had been made in the initial assembly, two more runs were conducted and still little solid carbon was produced. Thus, out of nine supposedly identical catalyst batches, only one produced CNF. Since no changes were implemented in either the procedure or the apparatus it was concluded that the different batches of catalyst were not homogenous.

7.2.1.1 Atomic absorption studies of catalyst

It was hypothesised earlier in this section that the ammonium bicarbonate may not be a strong enough base to achieve full precipitation of all the transitional metal nitrates, especially copper nitrate, in the catalyst preparation. In order, to solve this reproducibility problem, sodium hydroxide a much stronger base, was selected to replace ammonium bicarbonate. It was also decided to add sodium hydroxide to the transition metal nitrate solution as an aqueous solution, rather than as a solid, as had been done with ammonium bicarbonate. This allows the pH of the transition metal nitrate solution to rise from approximately pH 4 to pH 14 quickly. These modifications were intended to force crash precipitation of all the transition metal salts and to stop any preferential grouping of the metals in the final product.

The observations made during the preparation of the catalyst precursors, using the sodium hydroxide catalyst method, were as expected. The transition metal salts precipitated instantly on adding the sodium hydroxide and it was found unnecessary to leave the solution overnight to settle. The yields of the batches made were consistently between 100-110 %. The yields of over 100 % were thought to result from not all of the transition metals being in consistent oxidation states (Table 7-1).

AA Ref	Sample (*Production Method*)	Target Yield (g)	Dry Mass (g)	Calcined Mass (g)	Yield (%)	Appearance of solid
			Ammonium Bicarbonate			
1	$Cu_5Fe_{85}Ni_{10}a$	0.5	0.463	0.4357	87.1	Shiny, Hard
2	$Cu_5Fe_{85}Ni_{10}b$	1.5	1.568	1.3828	92.2	Shiny, Hard
3	$Cu_5Fe_{85}Ni_{10}c$	0.5	0.484	0.4380	87.6	Shiny, Hard
	$Cu_5Fe_{85}Ni_{10}d$	2	0.489	0.3949	19.8	Shiny, Hard
4	$Cu_5Fe_{85}Ni_{10}e$	4	4.346	3.6428	91.1	Shiny, Hard
5	$Cu_5Fe_{85}Ni_{10}f$	2	2.2872	1.6517	82.6	Shiny, Hard
6	$Cu_5Fe_{85}Ni_{10}g$	2	2.0076	1.8263	91.3	Shiny, Hard
7	$Cu_5Fe_{85}Ni_{10}h$	2	2.1078	1.8501	92.5	Shiny, Hard
	$Fe_{100}a$	2	2.259	1.9515	97.6	Shiny, Hard
	$Ni_{100}a$	2	0.610	0.4296	21.5	Matt, Brittle
	$Cu_{100}a$	2	1.383	0.9939	49.7	Matt, Brittle
			Sodium Hydroxide			
	$Cu_{100}b$	0.5	0.5677	0.4988	99.8	Matt, Brittle
	$Ni_{100}c$	0.5	0.5377	0.501	100.2	Matt, Brittle
	$Fe_{100}b$	0.5	0.5740	0.5132	102.6	Shiny, Hard
8	$Cu_5Fe_{85}Ni_{10}i$	1	1.0897	1.0179	101.8	Shiny, Hard
9	$Cu_5Fe_{85}Ni_{10}j$	1	1.1025	1.0192	102.0	Shiny, Hard
10	$Cu_{10}Fe_{80}Ni_{10}a$	0.5	0.5720	0.5137	102.4	Shiny, Hard
11	$Cu_{20}Fe_{70}Ni_{10}a$	0.5	0.5740	0.5316	106.3	Shiny, Hard
12	$Cu_{30}Fe_{60}Ni_{10}a$	0.5	0.6169	0.5541	110.8	Matt, Brittle
13	$Cu_{10}Fe_{80.5}Ni_{9.5}$	0.5	0.5704	0.5104	102.0	Matt, Brittle
14	$Cu_{20}Fe_{71.8}Ni_{8.2}$	0.5	0.5812	0.5221	104.4	Matt, Brittle
15	$Cu_{30}Fe_{62.6}Ni_{7.4}$	0.5	0.6162	0.5292	105.8	Matt, Brittle
16	$Cu_{40}Fe_{53.7}Ni_{6.3}$	0.5	0.5753	0.5381	107.6	Matt, Brittle
17	$Cu_{50}Fe_{44.7}Ni_{5.6}$	0.5	0.5469	0.5052	101.0	Matt, Brittle
18	$Cu_{60}Fe_{35.8}Ni_{4.2}$	0.5	0.5950	0.5539	110.7	Matt, Brittle
19	$Cu_{70}Fe_{26.8}Ni_{3.2}$	0.5	0.5701	0.5231	104.62	Matt, Brittle
20	$Cu_{80}Fe_{17.9}Ni_{4.2}$	0.5	0.331	0.2738	54.76	Matt, Brittle
21	$Cu_{90}Fe_{9.0}Ni_{1.1}$	0.5	0.542	0.5129	102.58	Matt, Brittle

Table 7-1 Table of catalysts prepared, prior to AA work being carried out

In order to confirm that the ammonium bicarbonate was not precipitating the transition metals homogenously, the catalysts listed in Table 7-1 were analysed using atomic absorption spectroscopy to determine the percentage of each metal present in the oxide precursors (Table 7-2). It was not possible to analyse $Cu_5Ni_{10}Fe_{85}d$, as all of the material had been utilised for attempted CNF preparation experiments. The initial preparation of $Cu_{80}Ni_{4.2}Fe_{17.8}$ was in error, so a lower yield of the product was recovered; this result has been included as a check on the operation of the AA.

AA Ref	Sample	Cu at%	Fe at%	Ni at%
Ammonium Bicarbonate				
1	$Cu_5Ni_{10}Fe_{85}a$	2.6	90.0	7.4
2	$Cu_5Ni_{10}Fe_{85}b$	2.6	89.1	8.3
3	$Cu_5Ni_{10}Fe_{85}c$	2.6	89.2	8.3
4	$Cu_5Ni_{10}Fe_{85}e$	2.3	89.2	8.5
5	$Cu_5Ni_{10}Fe_{85}f$	4.5	86.2	9.2
6	$Cu_5Ni_{10}Fe_{85}g$	4.3	86.4	9.3
7	$Cu_5Ni_{10}Fe_{85}h$	1.8	91.0	7.3
Sodium Hydroxide				
8	$Cu_5Ni_{10}Fe_{85}i$	5.2	85.6	9.2
9	$Cu_5Ni_{10}Fe_{85}j$	4.9	85.1	10.0
10	$Cu_{10}Ni_{10}Fe_{80}$	9.6	81.1	9.3
11	$Cu_{20}Ni_{10}Fe_{70}$	20.0	70.0	10.0
12	$Cu_{30}Ni_{10}Fe_{60}$	29.8	60.3	9.9
13	$Cu_{10}Ni_{9.5}Fe_{80.5}$	10.5	80.5	9.0
14	$Cu_{20}Ni_{8.2}Fe_{71.8}$	19.5	72.5	8.0
15	$Cu_{30}Ni_{7.4}Fe_{62.6}$	30.5	62.6	6.9
16	$Cu_{40}Ni_{6.3}Fe_{53.7}$	40.0	51.2	8.8
17	$Cu_{50}Ni_{5.6}Fe_{44.4}$	51.7	43.2	5.1
18	$Cu_{60}Ni_{4.2}Fe_{35.8}$	61.3	34.7	4.0
19	$Cu_{70}Ni_{3.2}Fe_{26.8}$	71.2	26.1	2.7
20	$Cu_{80}Ni_{4.2}Fe_{17.8}$	91.0	8.1	0.8
21	$Cu_{90}Ni_{1.1}Fe_{8.9}$	91.4	7.8	0.8

Table 7-2 Table of results of AA work carried out on catalysts (at% - atomic percentage)

The catalyst precursors produced utilising the ammonium bicarbonate method all contained lower percentages of copper and nickel than the target, composition proving the hypothesis that the copper and nickel were not precipitating fully. Those precursors prepared using sodium hydroxide exhibited good correlation between target and observed compositions. The AA operation check, using the "failed" $Cu_{80}Ni_{4.21}Fe_{17.89}$ sample yielded a lower iron signal proving the technique to be accurate. Sodium hydroxide was then used exclusively in the production of the catalyst precursors.

7.2.1.2 Catalyst precursors prepared using sodium hydroxide

The preparation of CNF was then retried using catalyst prepared using sodium hydroxide. The product yield was again very low, *ca* 50 mg of solid carbon. The preparation was repeated twice more, utilising different batches of catalyst and gave consistently small amounts of carbon. The issue of repeatability with the catalyst appeared to be solved; however, the catalyst precursor produced utilising sodium hydroxide $Cu_5Fe_{85}Ni_{10}$ failed to produce a significant amount of carbon.

It has been reported that without the presence of hydrogen for hydrogenation, catalysts rich in iron, and poor in copper, will be encapsulated with carbon, blocking the production of CNF (Krishnankutty *et al.*, 1997). Some samples of the carbon produced were analysed by SEM which, revealed that the majority of catalyst particles had been encapsulated, with very few areas of CNF growth occurring (Figure 7-3).

(a)   **(b)**
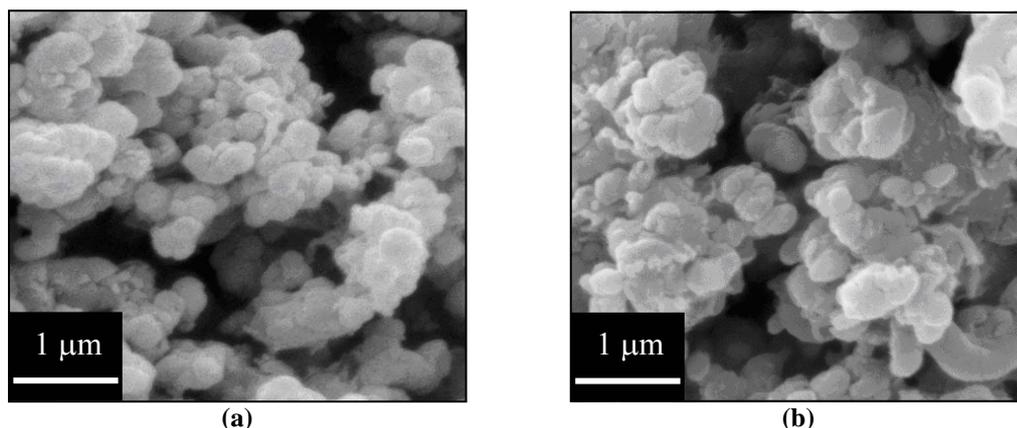
Figure 7-3 SEM image of the encapsulation by carbon of (a) $Cu_5Fe_{85}Ni_{10}$ from ammonia bicarbonate and (b) $Cu_5Fe_{85}Ni_{10}$ from sodium hydroxide from the CVD of pure ethylene

This observation raised one question. What was different about the $Cu_5Fe_{85}Ni_{10}c$ batch and the catalysts described by Mellor that were successful at CNF production, in contrast to the production of carbon encapsulated catalyst for all the other batches, when the method used had been identical? The change caused by the use of sodium hydroxide rather than ammonium bicarbonate in the catalyst preparation was only subtle, in order to ensure the consistency of the catalyst composition. In addition, catalyst batches from both preparations produced comparable results when CNF production was attempted in all cases except one. When contacted, Mellor said that the procedure was "Very unreliable. Some catalysts worked, others didn't" (Mellor, 2003). Further correspondence and in-depth scrutiny of the previously reported work exposed no obvious differences in the methods used. Several methods have been proposed as possible ways of encouraging CNF growth from copper, iron and nickel alloy catalyst systems. These methods include using hydrogen as an additive gas and by increasing the copper content of the catalyst (Chapter 2).

7.2.2 Ethylene-hydrogen reactant gas mixtures

Other preparations of CNF by CVD, reported in the literature, employ a hydrocarbon-hydrogen reactant gas mixture, hydrogen being required for hydrogenation of the CNF growth (Rodriguez, 1993). This was attempted using a $Cu_5Fe_{85}Ni_{10}$ catalyst, under the same reaction conditions as the previous CVD procedure, except that an ethylene-hydrogen mixture (60-240 ml min^{-1}) was used as the reactant gas. The result was that the ceramic boat was buried under solid carbon. The procedure was repeated with catalysts both from the same batch and a different one, and was found to give good reproducibility.

7.2.2.1 Purity of the carbon nanofibres

On visual inspection, the material produced was observed not to be uniform. The material from inside the boat was noted to be dense and rubbery. However, the material produced above the boat possessed a very low bulk density and appeared interwoven as it retained its shape; in addition to this, the material was statically charged. The boat was noted to be covered all over with soot. The carbon conversion from ethylene to solid carbon was calculated to be 60 %. The combined sample was found to have a nitrogen BET surface area of 160 m^2 g^{-1}, which compared well with similar work in the literature (Krishnankutty *et al.*, 1997). SEM analysis revealed that the material from the bottom of the boat contained helical CNF but there was also a lot of what appeared to be amorphous carbon. However, the CNF that grew further from the boat appeared to be mostly free from this amorphous material (Figure 7-4).

<div align="center">(a)   (b)</div>
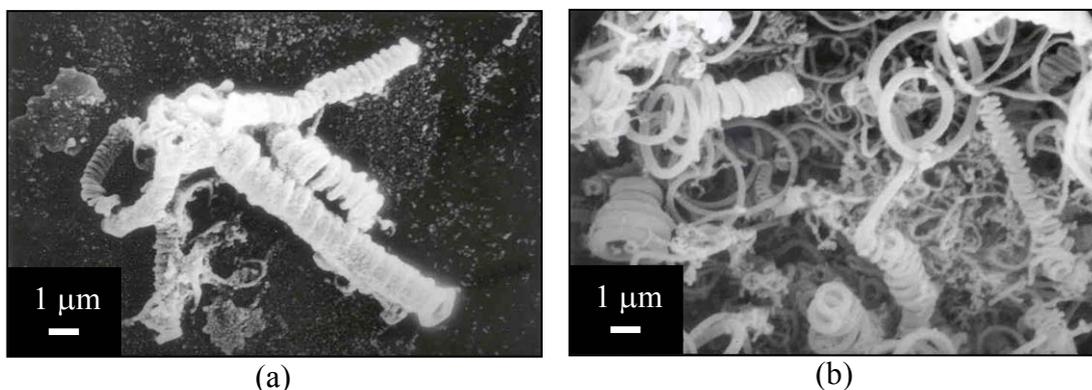
Figure 7-4 SEM images of CNF from catalyst $Cu_5Fe_{85}Ni_{10}$i that were grown (a) in and (b) above a ceramic boat

The images illustrates that show the experimental technique used did not facilitate production of a uniform product. In order to avoid this problem, it was decided that the ceramic boat should not be used, as it appeared to catalyse the formation of soot on its surface. The quartz tube however, was not covered in a layer of soot during the preparation. Thus, a quartz tube was selected as the reaction vessel, because this would provide the maximum uniform volume in which the CNF could grow. In addition, this would make removal of the sample from the apparatus much easier, as static would no longer be able to cause the product stick to the walls of the apparatus tube. The quartz reaction tubes were 20 cm long, 8 cm longer than the heating zone of the furnace; the intention being, to stop CNF growth before it out grew the vessel. The preparation was repeated exactly as previously discussed, the only difference was use of the quartz reaction vessel. After the run it was noted that the quartz reaction vessel was filled with carbon material (*ca* 60 % carbon conversion), with growth just stopping before the ends of the reaction tube. On visual inspection, the product appeared to be similar to the material that grew above the boat in previous runs (Figure 7-5). The nitrogen BET surface area of the material was found to be 290 m^2 g^{-1}, 130 m^2 g^{-1} in excess of the surface area of the sample grown in the ceramic boat.
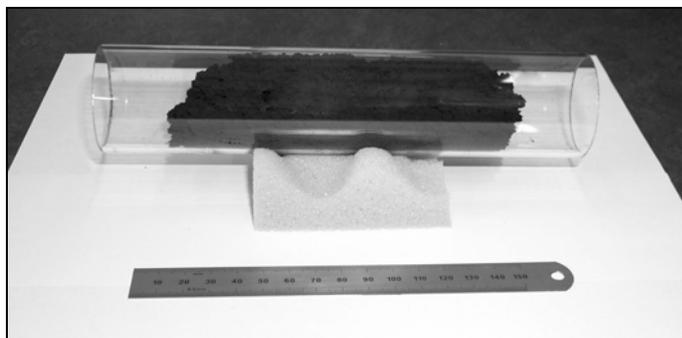
Figure 7-5 The CNF produced from $Cu_5Fe_{85}Ni_{10}i$ in a quartz reaction vessel

7.2.2.2 Microscopy study

CNF from throughout the sample were analysed by SEM in order to identify the sample, and to prove its uniform composition. The images recorded confirmed the sample to be CNF with no evidence of the presence of amorphous material (Figure 7-6). The finer background material appeared to be fibrous; the SEM, however, was not powerful enough to look any closer at this material without severe loss of resolution.

Figure 7-6 SEM images of CNF catalyst $Cu_5Fe_{85}Ni_{10}i$ grown in a quartz reaction vessel

The CNF were then analysed by TEM and found to be of uniform width, approximately 300 nm, with the majority of the CNF being over 10 μm in length. All CNF studied possessing a platelet crystal structure (Figure 7-7). The CNF present were observed in both straight and coiled morphologies. The different structures are thought to result from two slightly different platelet crystal structures. The coiled CNF caused by a skewed platelet structure, the skew causing one side of the CNF to grow faster than the other (Figure 7-7 (b)). The straight CNF possessed an even platelet crystal structure, resulting in the straight growth (Figure 7-7 (c)). A number of catalyst particles were observed located at the tips of individual CNF; this indicated that the CNF grew in a uni-directional mode (Figure 7-7 (d)).

(a)   (b)

(c)   (d)
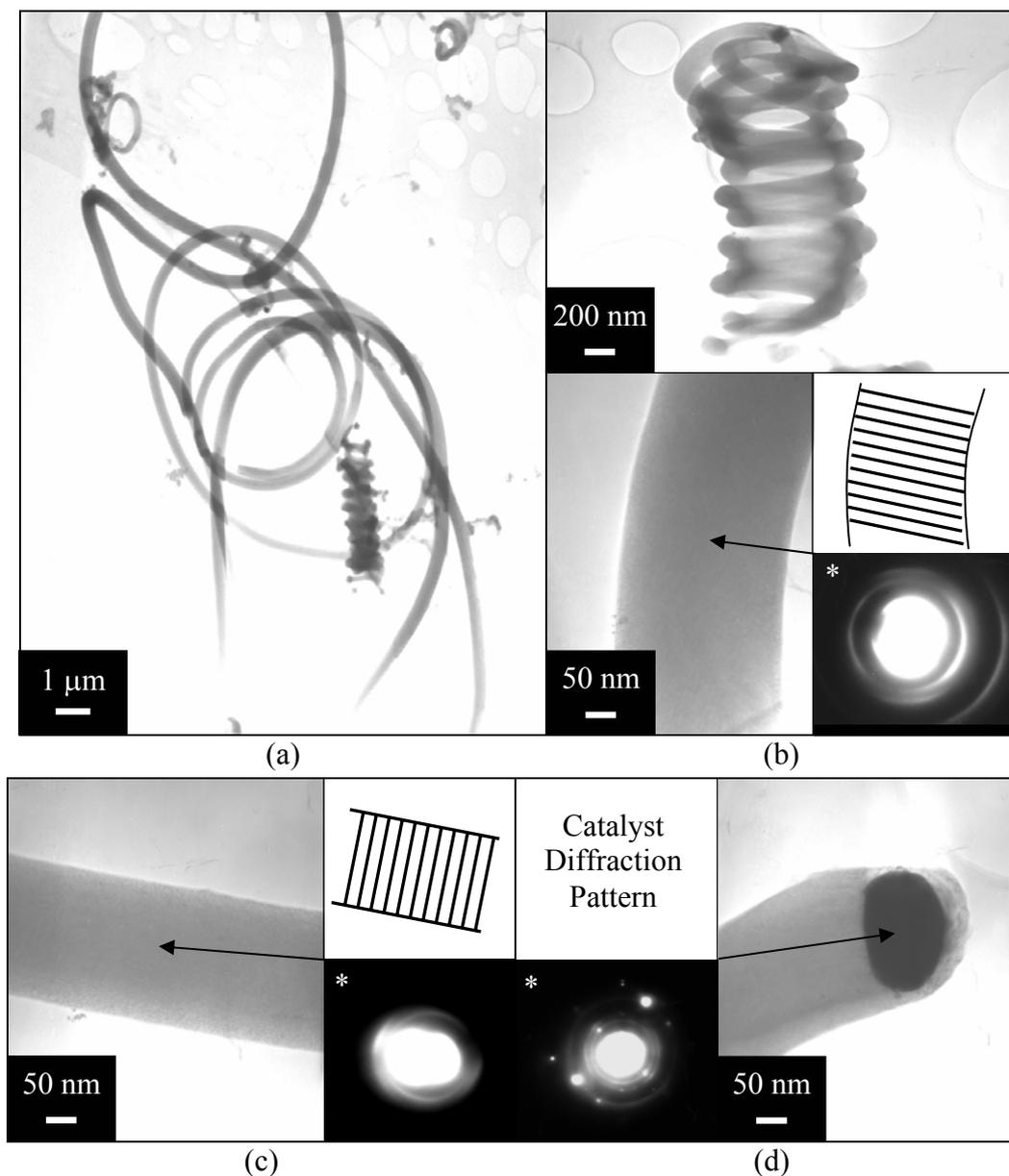
*The negative was over exposed, partially whiting out diffraction pattern

Figure 7-7   TEM images of CNF grown from ethylene-hydrogen (60-240 ml min^{-1}) over Cu$_5$Fe$_{85}$Ni$_{10}$ catalyst in a quartz reaction vessel at 600 ˚C; (a) low magnification image (b) image of a coil, with a high magnification and diffraction pattern of a CNF prior to a coil (c) high magnification image and diffraction pattern of a straight section of CNF (d) high magnification image and diffraction pattern of a section of CNF containing a catalyst particle

7.2.2.3 X-ray diffraction study

A portion of the sample was annealed at 1000 ˚C for 24 hrs in order to determine if any changes to the crystallinity of the material took place.   XRD was used to determine the degree of crystallinity of both the non-annealed and annealed samples. The XRD patterns of graphite, Fisher FDC activated carbon, and catalyst with equal Cu-Fe-Ni content were also recorded for comparison (Figure 7-8).
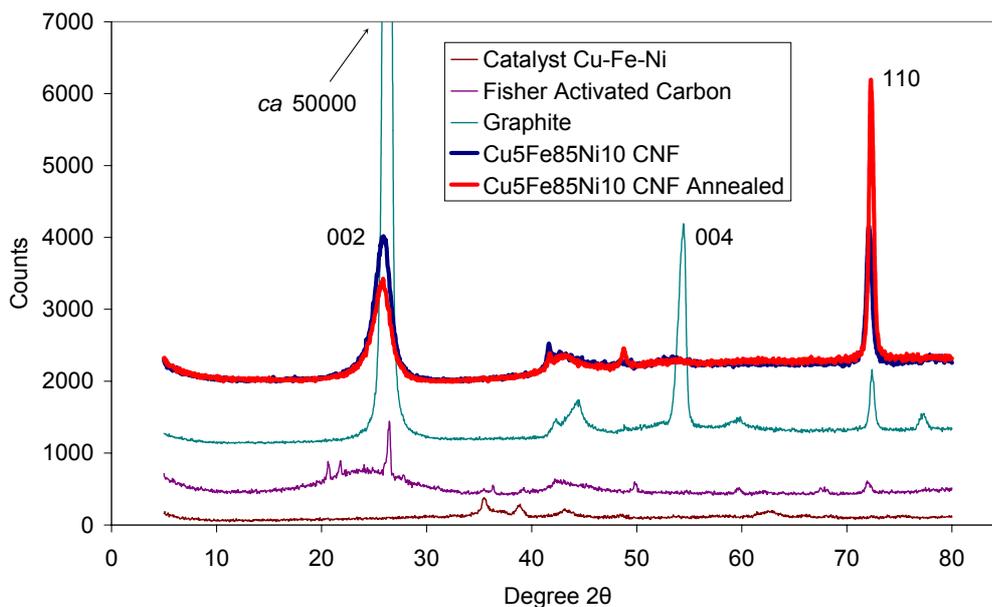
Figure 7-8 XRD patterns of Cu$_5$Fe$_{85}$Ni$_{10}$ (non-annealed and annealed at 1000 ˚C for 24 hrs), a graphite sample, Fisher FDC activated carbon and catalyst (equal Cu-Fe-Ni content)

The CNF and graphite sample both yielded strong, characteristic, peaks at 26˚ and 72˚, 2θ, (Miller indices 002 and 110 respectively) indicating similar crystalline structures, these corresponded to interlayer spacings of 0.334 and 0.123 pm respectively, which compares well to previously reported values (Rodriguez, 1993; Rodriguez *et al.*, 1995). The activated carbon was observed to have a broad "bump" with a small peak at 26˚, 2θ, and almost no signal at 72˚, 2θ, which was consistent with it being predominantly amorphous carbon (Chapter 6). The catalyst showed no sharp peaks, so no interference with the CNF, containing trace catalyst particles, was observed. The annealed CNF peak was observed to produce a slight decrease in the intensity of the 26˚, 2θ, peak and a slight increase in the 72˚, 2θ, peak, indicating a small shift towards narrower interlayer spacings.

7.2.2.4 Hydrogen adsorption study

The hydrogen adsorption profile of CNF was recorded at 100 bar (Figure 7-9). Different degas procedures were found to have an effect on the amount of hydrogen adsorption observed. The DG3, DG2 and DG1 procedures were found to facilitate up to 0.25 wt%, 0.13 wt% and 0.1 wt% respectively. All profiles showed an instantaneous adsorption of approximately 0.1 wt%, which is believed to be due to

physisorption. This was supported by 0.1 wt% adsorption-desorption cycling with only the removal of pressure using DG1. In addition to this, the proposed physisorption uptake of 0.1 wt% fitted with the general trend of surface area observed for activated carbons. The additional slower adsorption however, did not fit into this pattern (Chapter 6). The additional, slower, adsorption facilitated by DG3 and DG2 degas procedures were believed to result from either the interaction of hydrogen with trace quantities of catalyst present, or else by penetration into the crystalline structure of the CNF. These values of adsorption obtained were in contradiction to those reported by Mellor *et al*., they are, however, in strong agreement with those reported by Tibbetts *et al.* (Browning *et al.*, 2002; Tibbetts *et al.*, 2001). The explanation for these differences was believed to lie in the method of measurement, rather than the materials (Chapter 5). The annealed CNF were also analysed for hydrogen adsorption, but were found to achieve a maximum of only 0.2 wt% using a DG3 degas procedure.
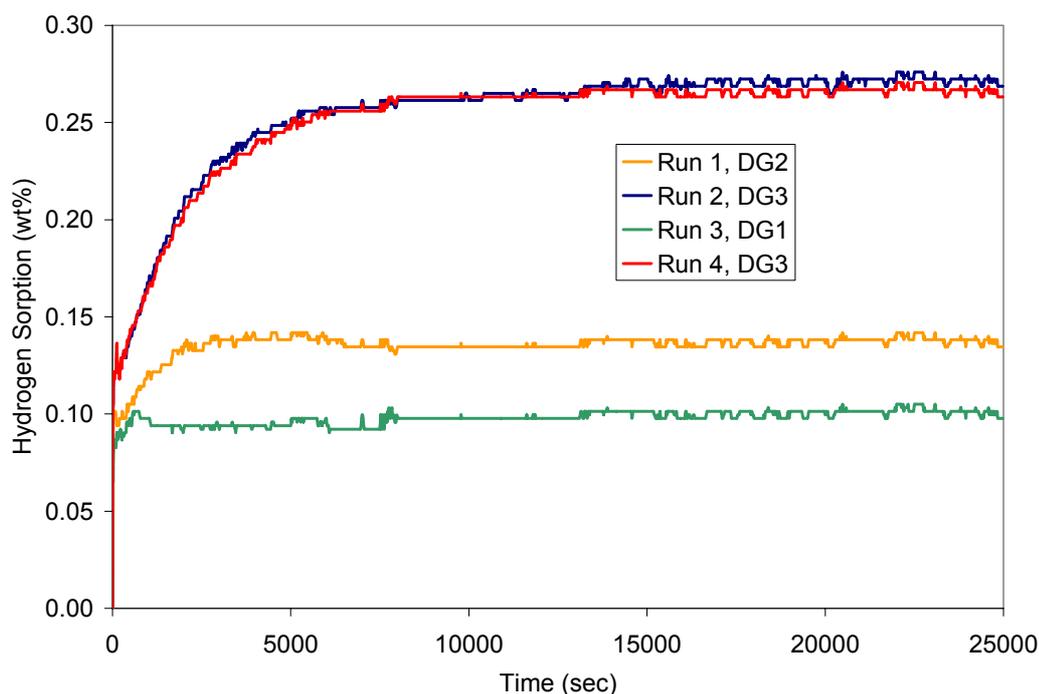
Figure 7-9 The hydrogen adsorption profile of CNF, grown from Cu$_5$Fe$_{85}$Ni$_{10}$ catalyst using ethylene-hydrogen (60-240 ml min^{-1}) at 600 ˙C. Recorded at 100 bar and 30 ˙C

7.2.2.5 Demineralisation

Various authors have reported differing degrees of success using a range of acids and conditions for the demineralisation of CNF (Krishnankutty *et al.*, 1996). A sample of CNF prepared utilising $Cu_5Fe_{85}Ni_{10}$ was selected for a feasibility study of demineralisation. The sample possessed a catalyst concentration of 0.008 g g^{-1} (catalyst/CNF) and was used in 0.3 g portions for a series of demineralisation experiments under increasingly severe conditions (Table 7-3).

No.	Acid	Time (hrs)	Vol acid (ml)	Temp (˚C)	Filtrate Colour	Ash Mass$^◊$ (mg)	Ash AA^Δ *(wash)*
1	1M HCl	3	100	20	Colourless	2.0	Cu Fe Ni
2	1M HCl	168	100	20	Colourless	1.2	Cu Fe Ni
3	2M HCl	3	100	20	Colourless	1.4	Cu Fe Ni
4	2M HCl	168	100	20	Colourless	2.2	Cu Fe Ni
5	2M HCl	6	100	70	Colourless	1.4	Cu Fe Ni
6	2M HCl	24	100	70	Colourless	1.5	Cu Fe Ni
7	2M HNO$_3$	24	100	20	Colourless		*(none)*
	2M HCl	wash	3*50	20	Colourless	1.5	Cu Fe Ni
8	6M HNO$_3$	24	100	20	Colourless		*(none)*
	2M HCl	wash	3*50	20	Colourless	1.9	Cu Fe Ni
9	6M HNO$_3$	24	100	reflux	Yellow		*(Fe)*
	2M HCl	wash	3*50	20	Yellow	0.8	Cu Fe Ni
10	6M HNO$_3$	24	100	reflux	Yellow		*(Fe)*
	2M HCl	wash	3*50	20	Yellow	0.7	Cu Fe Ni
11	6M HNO$_3$	24	100	reflux	Yellow		*(Fe)*
	2M HCl	wash	3*50	20	Yellow		*(Fe)*
	2M HCl	wash	3*50	20	Colourless	0.5	Cu Fe Ni

$^◊$The predicted ash mass was 1.2 mg if no catalyst was removed
^{Δ}The ash was dissolved in 2M hydrochloric acid and analysed by AA to determine which metals were present

Table 7-3 Summary of the attempted demineralisation with CNF grown from $Cu_5Fe_{85}Ni_{10}$

The experiments using hydrochloric and nitric acid at room temperature (experiments 1-8) did not appear to remove any of the catalyst; with the filtrate remaining colourless, indicating that there were no transition metal ions present in solution. This was supported by the presence of all three metals being detected by AA in the ash, the mass of which was noted to be above the predicted value for all the experiments, the excess resulting from the catalyst being oxidised during the ashing process. The failure of the demineralisation was believed to be caused by catalyst particles being trapped within the structure of the CNF rendering them inaccessible to the acids. This was supported by the TEM study, where the catalyst particles were observed to be encased in carbon at the tip of the CNF (Figure 7-7

(d)). Refluxing with nitric acid (experiments 9-11) resulted in the formation of a yellow filtrate solution, which suggested that iron was removed, which was confirmed using AA. However, a reduced amount of ash was still formed and AA revealed that all three metals were still present. Nitric acid is an oxidising agent as well as an acid so it is believed that the CNF structure was partly oxidised, opening pores in the structure allowing access to some of the catalyst particles, with iron being the most abundant. This was confirmed by looking at CNF portions from demineralisation experiments 6 and 7 by SEM (Figure 7-10). Experiment 6, which uses hydrochloric acid only, was observed not to cause significant damage to the structure of the CNF. However, experiment 7 uses nitric acid and the product was observed to lose its fibrous structure.

| (a) | (b) |
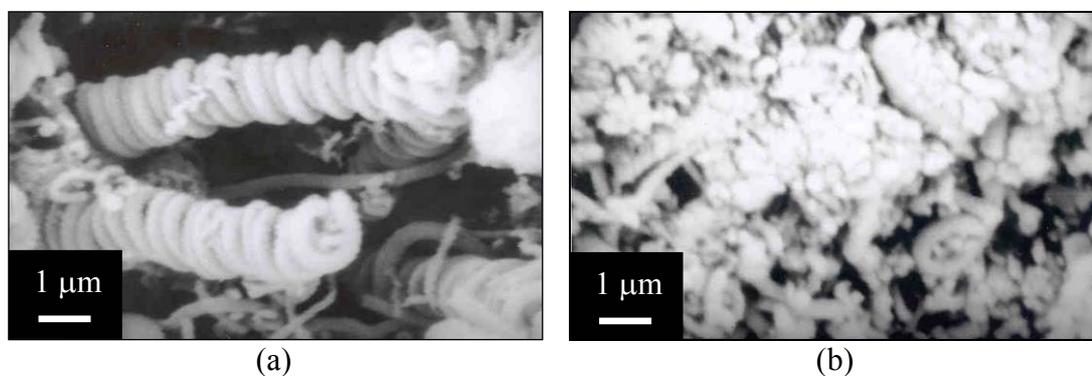
Figure 7-10   SEM images of CNF after demineralisation (a) experiment 6 and (b) experiment 7

This study has shown that complete removal of the catalyst from the CNF is difficult to achieve without the destruction of the nanofibre structure prior to complete removal. In addition to this, typical catalyst concentrations were less than 0.01 g g^{-1} (catalyst/CNF), and it was thus concluded that demineralisation was not feasible.

7.2.3 Influence of copper content

Krishnankutty *et al.* reported that by increasing the copper content in predominately iron catalysts facilitated the growth of CNF from pure ethylene (Krishnankutty *et al.*, 1996). In order to test this, a series of catalysts were prepared, based on $Cu_5Fe_{85}Ni_{10}$ with a range of copper content but constant iron to nickel ratio (Table 7-1, AA numbers 13-21). Each catalyst was used to attempt preparation of CNF, using pure ethylene (60 ml min^{-1}) as the reactant gas (Figure 7-11).
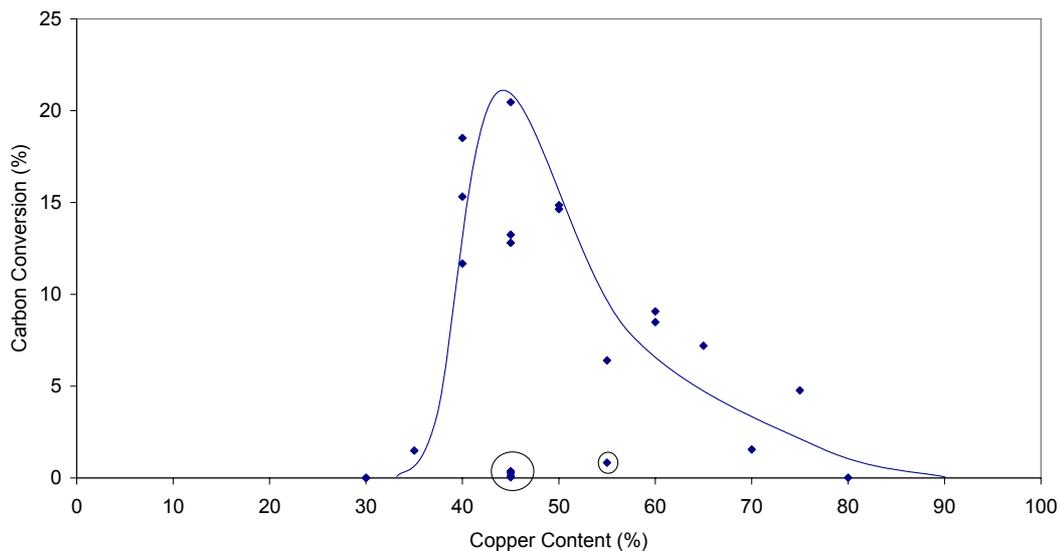
Figure 7-11 Comparison of CVD using pure ethylene (60 ml min^{-1}) varying the ratio of copper content of the catalyst, keeping the iron-nickel content constant

A broad trend was observed between the copper content of the catalyst and the carbon conversion to CNF. At copper content of less than 35 % copper, encapsulation of the catalyst was observed. At contents of 35-40 % the onset of CNF production occurred. The carbon conversion peaked at copper contents between 40-50 % producing at *ca* 20 % carbon conversion. The carbon conversion was then observed to decrease with increasing copper content until *ca* 90 %, where CNF production ceased. The trend loosely correlates with that reported by (Krishnankutty *et al.*, 1996), who observed a similar pattern for a copper-iron catalyst system with pure ethylene (Chapter 2). The hypothesised explanation for this phenomenon is that carbon will encapsulate the catalyst if ethylene is allowed to uniformly adsorb to the surface. However, copper is a very poor adsorbent for hydrocarbons, providing negligible adsorption sites for ethylene, which breaks up the homogeneity of the ethylene surface coverage. Thus, up to a copper content of 35 %, it is thought that there is not enough copper present on the surface of the catalyst particles to stop the encapsulation. At greater copper content the ethylene coverage becomes too low to facilitate hydrogenation allowing the hydrogenation, of the ethylene and the formation of CNF. The carbon conversion then began to decrease; this was believed to be caused by increasing copper content of the catalyst which acted to decrease the number of active sites on the particle surfaces for carbon diffusion leading to CNF growth. At copper content of *ca* 90 % conversion ceases

completely, probably because the ethylene cannot hydrogenate or the carbide cannot dissolve through the particle.

There were problems with the repeatability of this work. The circled points on the plot indicate runs that were carried out under identical conditions as the corresponding successful runs with the same catalyst batches, but instead resulted in encapsulation. The catalyst appeared either to produce CNF at yield or else encapsulated the catalyst with no CNF production. This is hypothesised to be due to the start of the reaction requiring an essential initiation step, which, if not met, the reaction will not propagate, resulting in encapsulation of the catalyst. The initiation step is thought to be the hydrogenation of ethylene facilitating the cleavage of the carbon-carbon bond. The points in question were repeated up to ten times to see if this effect could be controlled but slight variations in reaction and reduction temperature had no beneficial effects.

7.2.3.1 Microscopy study

A sample of CNF prepared using $Cu_{45}Fe_{49.2}Ni_{5.8}$ was studied by TEM. This sample was selected since the preparation yielded the highest conversion rate, and the CNF possessed the highest surface area and hydrogen storage capacity (Figure 7-12). The CNF were found to be of homogenous form with widths in the range of approximately 150-200 nm, varying in length between *ca* 1-10 μm in length. All the CNF studied had a herringbone crystal structure (Figure 7-12 (b) and (c)). Two morphologies of CNF were observed to be present, twisted and straight. The former morphology was thought to be caused by uneven herringbone growth, producing a twisted structure.

(a)   (b)

(c)
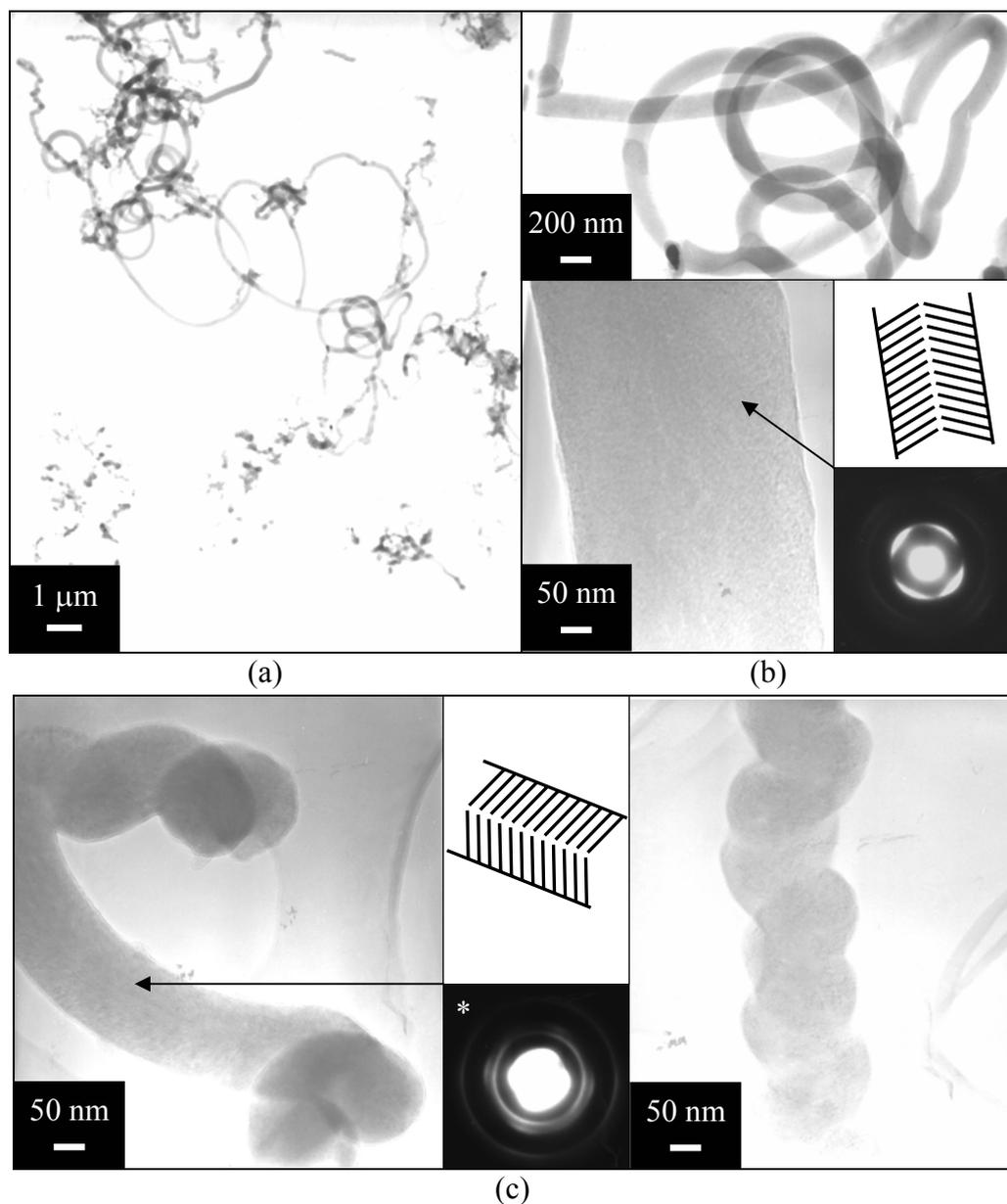
*The negative was over exposed, partially whiting out diffraction pattern

Figure 7-12   TEM images of CNF from ethylene (60 ml min^{-1}) over Cu$_{45}$Fe$_{49.2}$Ni$_{5.8}$, grown in a quartz reaction vessel at 600 $^{\cdot}$C; (a) low magnification image (b) image of a CNF, with a high magnification image and diffraction pattern of a CNF (c) high magnification image and diffraction pattern of a twisted section of CNF

7.2.3.2 Hydrogen adsorption study

The batches of CNF that achieved over 10 % conversion were analysed by nitrogen adsorption using the BET equation and for hydrogen sorption capacity (Table 7-2). The BET surface areas of all the samples were similar; ranging from 38 to 62 m^2 g^{-1}. The maximum hydrogen sorption capacity recorded for these materials was found to be 0.04 wt%, which is on the lower limit of sensitivity for HPAA due to the

maximum sample size of 2 g resulting from the low bulk density of the CNF (Table 7-4). A sample of CNF prepared by $Cu_{45}Ni_{5.8}Fe_{49.2}$ was annealed at 1000 ˚C, but this resulted in no increase in either hydrogen adsorption capacity or nitrogen BET surface area.

CNF	BET surface area $(m^2 g^{-1})$	Hydrogen sorption (wt%)
$Cu_{40}Fe_{53.7}Ni_{6.3}$	62	<0.02
$Cu_{45}Fe_{49.2}Ni_{5.8}$	43	0.04
$Cu_{50}Fe_{44.7}Ni_{5.3}$	38	0.04
$Cu_{60}Fe_{35.8}Ni_{4.2}$	40	<0.02
Annealed $Cu_{45}Fe_{49.2}Ni_{5.8}$	39	0.03-0.04

Table 7-4 Hydrogen sorption capacities recorded at 100 bar and 30 ˚C after DG2 and BET surface areas of a selection of CNF samples prepared from Cu-Fe-Ni catalyst at 600 ˚C from pure ethylene (60 ml min⁻¹)

The catalyst appears to be the key to producing CNF from pure ethylene. The replacement of ammonium bicarbonate with sodium hydroxide in the catalyst preparation has been shown to solve the problem of irreproducibility of the catalyst composition. However, for these reaction parameters, repeatability has been found to be a major issue and, of the CNF produced, negligible hydrogen adsorption activity has been observed, so it was decided to investigate other systems.

7.3 Investigating bi-metallic catalyst systems

To reduce the number of variables involved it was decided to look at copper, iron and nickel bi-metallic catalyst systems (Cu-Fe, Fe-Ni and Cu-Ni) in order to try to control the characteristics of the CNF grown (Table 7-5). The reaction parameters selected for the experiments were a reactant gas mixture of ethylene-hydrogen (60-240 ml min⁻¹) at 600 ˚C for 3 hours, as this had proved successful and repeatable with the tri-metallic catalyst $Cu_5Ni_{10}Fe_{85}$ (Section 7.2.2).

Cu-Fe	Cu-Ni	Fe-Ni
$Cu_{10}Fe_{90}$	$Cu_{10}Ni_{90}$	$Fe_{10}Ni_{90}$
$Cu_{20}Fe_{80}$	$Cu_{20}Ni_{80}$	$Fe_{20}Ni_{80}$
$Cu_{30}Fe_{70}$	$Cu_{30}Ni_{70}$	$Fe_{30}Ni_{70}$
$Cu_{40}Fe_{60}$	$Cu_{40}Ni_{60}$	$Fe_{40}Ni_{60}$
$Cu_{50}Fe_{50}$	$Cu_{50}Ni_{50}$	$Fe_{50}Ni_{50}$
$Cu_{60}Fe_{40}$	$Cu_{60}Ni_{40}$	$Fe_{60}Ni_{40}$
$Cu_{70}Fe_{30}$	$Cu_{70}Ni_{30}$	$Fe_{70}Ni_{30}$
$Cu_{80}Fe_{20}$	$Cu_{80}Ni_{20}$	$Fe_{80}Ni_{20}$
$Cu_{90}Fe_{10}$	$Cu_{90}Ni_{10}$	$Fe_{90}Ni_{10}$

Table 7-5 Catalysts prepared for bi-metallic experiments

7.3.1 Investigating copper-iron catalyst systems

For the Cu-Fe catalyst series, a general trend was observed between increasing copper content and carbon conversion observed (Figure 7-13). Initially, encapsulation of the catalyst was observed at 10 % copper content. At 20 % copper content, CNF formation was observed to commence which peaked when the catalyst contained 40 % yielding *ca* 30 % carbon conversion. The conversion then decreased, with the catalyst becoming inactive at a content of 90 % copper. The Cu-Fe system was found to be very unreliable, with inconsistent results being obtained. This was particularly evident for the catalysts with 20, 30 and 50 % copper content (circled results in Figure 7-13). The experiments were repeated several times using identical conditions and with fresh catalyst batches in order to ensure that no errors had been made. As observed previously, when varying the copper content of the tri-metallic catalyst, no obvious reason for the failure of CNF preparation could be determined. The cause of this is thought to be similar to that outlined for the tri-metallic system (Section 7.2.3).
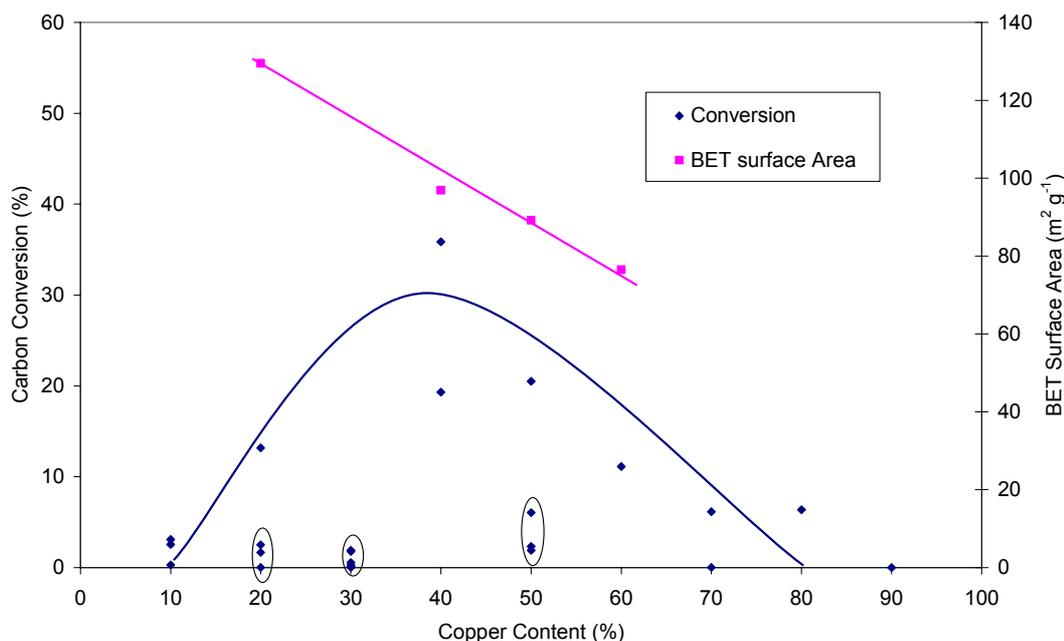
Figure 7-13   **Carbon conversion and nitrogen BET surface area of CNF prepared from the Cu-Fe catalyst series at 600 ˚C for 3 hours using ethylene-hydrogen (60-240 ml min^{-1}) as the reactant gas**

7.3.1.1 Hydrogen adsorption study

A selection of CNF samples, produced in quantities larger than 0.5 g, were analysed by nitrogen BET. The surface areas were found to decrease with increasing copper content of the catalyst, and range from 77 to 130 m^2 g^{-1}, which is lower than that recorded for CNF grown under the same conditions using $Cu_5Fe_{85}Ni_{10}$ (Section 7.2.2). The hydrogen storage capacity was also determined of the CNF samples prepared in quantities larger than 1 g (Table 7-4).

CNF	BET surface area (m^2 g^{-1})	Hydrogen Sorption (wt%)
$Cu_{20}Fe_{80}$	130	<0.05
$Cu_{40}Fe_{60}$	92	0.07
$Cu_{50}Fe_{50}$	89	<0.05
$Cu_{60}Fe_{40}$	77	<0.05

Table 7-6   **Hydrogen sorption capacities and BET surface areas of a selection of CNF samples prepared from ethylene-hydrogen (60-240 ml/min) with Cu-Fe catalysts at 600 ˚C, recorded at 100 bar and 30 ˚C after DG2**

These hydrogen sorption capacities are very low, and on the limit of detection for HPAA (Figure 7-14). The CNF grown from the copper-nickel catalyst system have proved to be difficult to produce repeatably, only achieving low yields with a

maximum of just over 50 % carbon conversion. In addition to this, the CNF have been found to have comparatively low surface areas of 130 m^2 g^{-1} with correspondingly low hydrogen sorption capacities of less than 0.1 wt%.
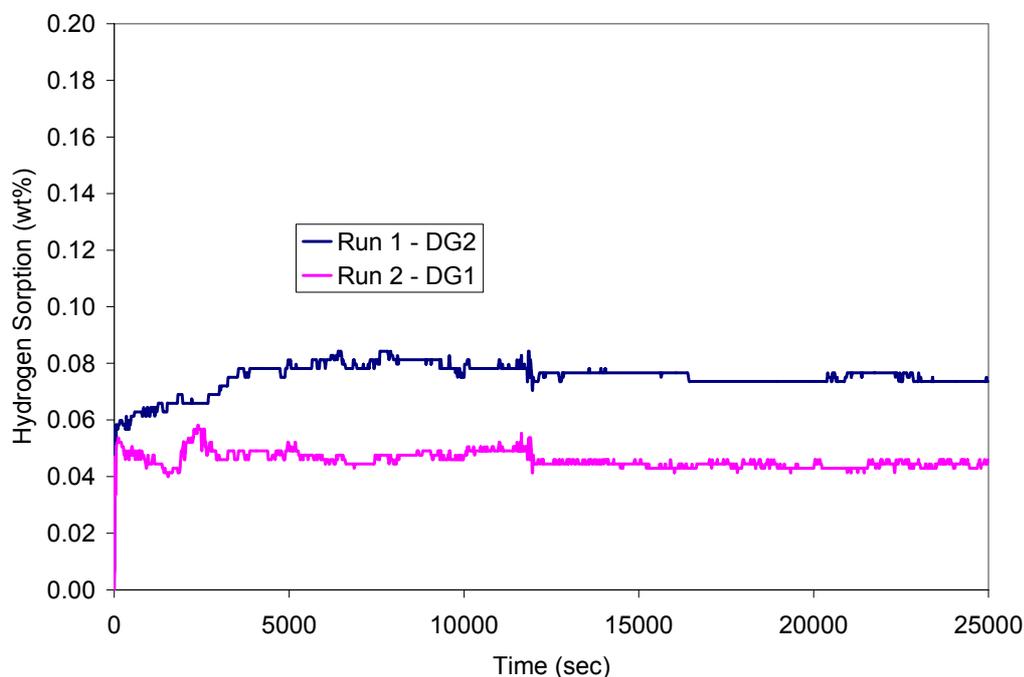
Figure 7-14 Hydrogen sorption profile of CNF prepared from $Cu_{20}Fe_{80}$ at 600 ˙C from ethylene-hydrogen (60-240 ml min^{-1}) recorded at 100 bar and 30 ˙C

7.3.1.2 Microscopy study

A sample of CNF prepared using $Cu_{40}Fe_{60}$ was studied using TEM as the sample had the highest surface area and hydrogen storage capacity of the Cu-Fe CNF studied (Figure 7-15). The CNF were found to be of homogenous form with widths in the range of approximately 150-200 nm. However, all through the sample, large dark areas were observed. All the CNF studied possessed a herringbone structure (Figure 7-15 (b)). Several catalyst particles were observed buried within the structure, rather than at the tips. This is indicative of CNF grown via the bi-directional mechanism (Figure 7-15 (c)).
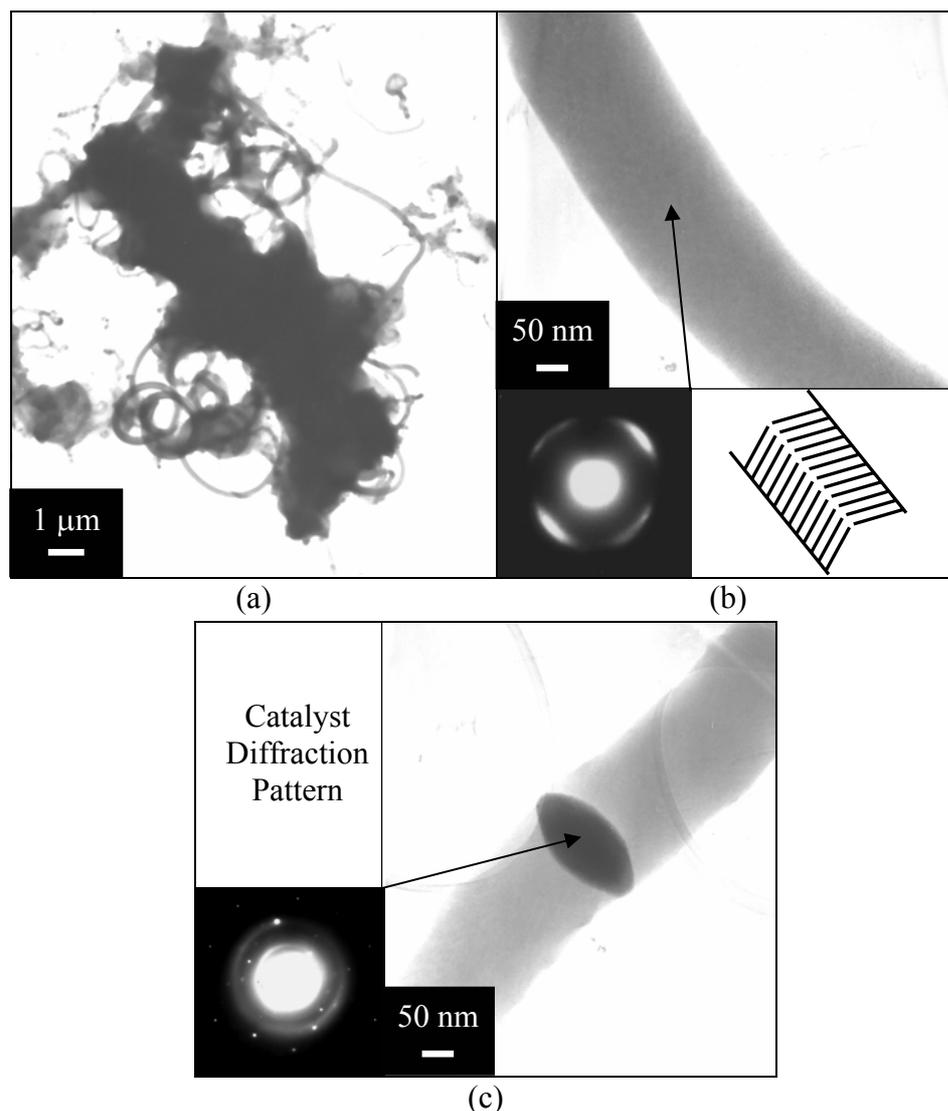
Figure 7-15   **TEM images of CNF from ethylene-hydrogen (60-240 ml min^{-1}) over Cu$_{40}$Fe$_{60}$ at 600 ˚C; (a) low magnification image (b) high magnification image and diffraction pattern of a CNF (c) high magnification image and diffraction pattern of catalyst**

7.3.2 Investigating iron-nickel catalyst systems

The iron-nickel catalyst system exhibit clear trends in both carbon conversion and BET surface area with increasing iron content (Figure 7-16). The conversion of carbon to CNF was observed to be *ca* 55 % for iron content from 10-40 %, beyond which the conversion rate swiftly decreases, approaching complete encapsulation of the catalyst by 90 % iron content. This rate of conversion is much higher than that observed for the Cu-Fe system, which peaked at *ca* 30 % conversion. The BET surface area of the resulting CNF is inversely proportional to this trend with the surface area being *ca* 135 m^2 g^{-1} at low iron concentrations, but increasing beyond

50 % iron content, to *ca* 250 m^2 g^{-1} at 70 % iron content. The preparation of CNF using $Fe_{20}Ni_{80}$ was repeated five times to check reproducibility and because the CNF were required for activation which will be discussed later in this chapter. The repeatability of the Fe-Ni system was observed to be much better than the Cu-Fe system, with none of the catalysts failing to prepare CNF.
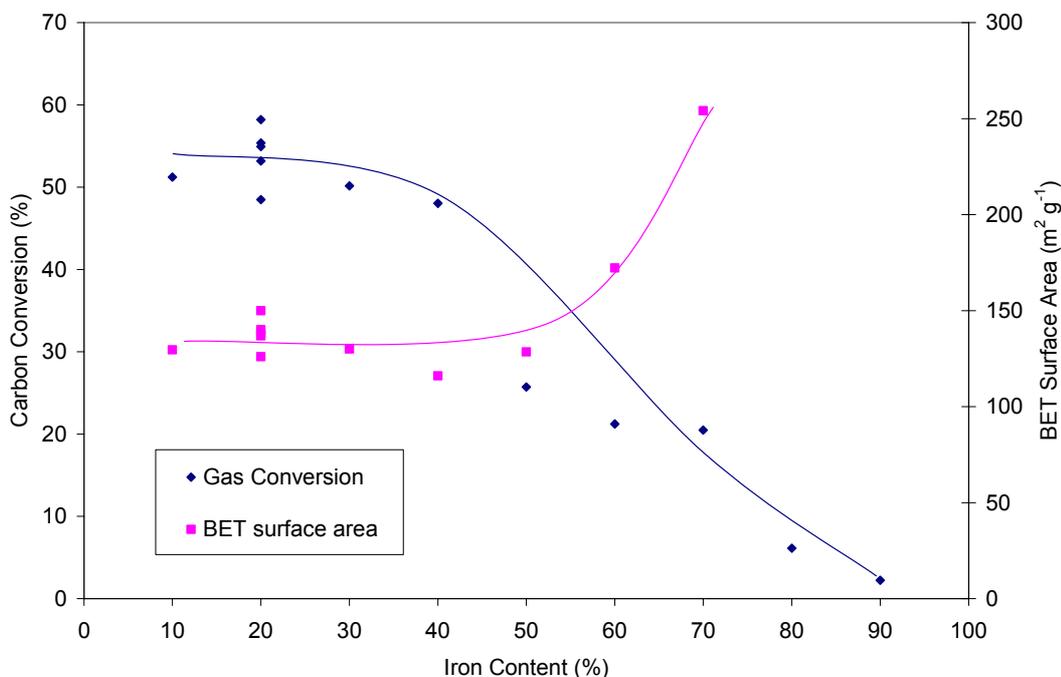

Figure 7-16 Carbon conversion and nitrogen BET surface area of CNF prepared from the Fe-Ni catalyst series at 600 ˚C for 3 hours using ethylene-hydrogen (60-240 ml min^{-1}) as the reactant gas

7.3.2.1 Hydrogen adsorption study

The hydrogen adsorption profiles for the CNF prepared with Fe-Ni were recorded for samples that were obtained in quantities over 1 g (Figure 7-17). CNF produced using $Fe_{10}Ni_{90}$ displayed the lowest uptake with little more than *ca* 0.03 wt% being achieved with a very poorly defined adsorption profile, this was repeated but a similar result was obtained. The profiles for the CNF prepared from the Fe-Ni catalysts with an iron content between 10-50 % all displayed an instantaneous uptake of *ca* 0.05 wt%. The sample produced from a catalyst with iron content of 70 %, achieved a higher instantaneous sorption of 0.08 wt%. This correlates with the relationship between instantaneous hydrogen sorption and surface area discussed in Chapter 6. All the CNF prepared from Fe-Ni displayed a period of slower

adsorption after the initial instantaneous sorption, except CNF prepared using $Fe_{10}Ni_{90}$, with the maximum uptake of 0.15 wt% being observed for $Fe_{50}Ni_{50}$ prepared CNF. CNF prepared with $Fe_{60}Ni_{40}$ failed to display any recordable uptake, the CNF preparation and adsorption experiment were repeated, but the same result was obtained.
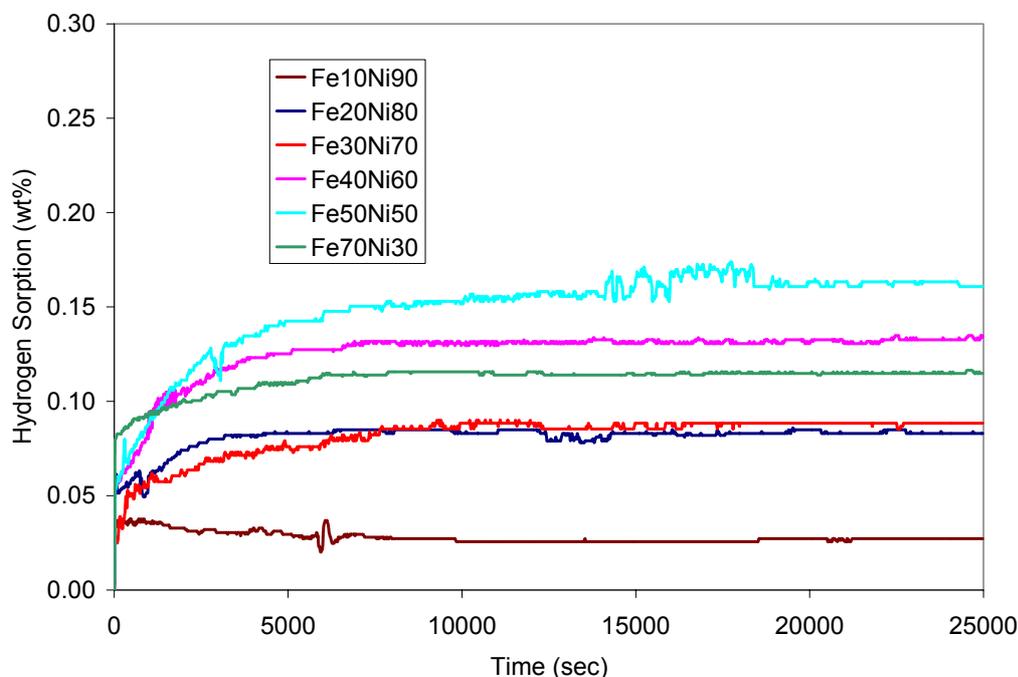
Figure 7-17 Hydrogen sorption profiles of CNF prepared from Fe-Ni catalysts from ethylene-hydrogen (60-240 ml min^{-1}) at 600 °C, recorded at 100 bar and 30 °C after DG2

The instantaneous, final hydrogen sorption and nitrogen BET surface area of the CNF prepared using Fe-Ni are compared in Figure 7-18. Initially, increasing iron content was observed to be directly proportional to the final sorption of hydrogen, peaking for the CNF prepared from catalyst with 50 % iron content, and then decreases with further increasing iron concentration. The final hydrogen sorption displayed no clear correlation with instantaneous hydrogen sorption or with BET surface area of the CNF samples.

The CNF prepared using Fe-Ni proved less problematic to prepare than those produced with Cu-Fe catalysts (Section 7.3.1). Higher carbon conversion rates, BET surface areas and hydrogen sorption levels were achieved. However, the CNF produced from Fe-Ni failed to perform significantly better than CNF prepared from

the tri-metallic catalyst, $Cu_5Fe_{85}Ni_{10}$, in conversion, hydrogen sorption or nitrogen BET surface area (Section 7.2.2).
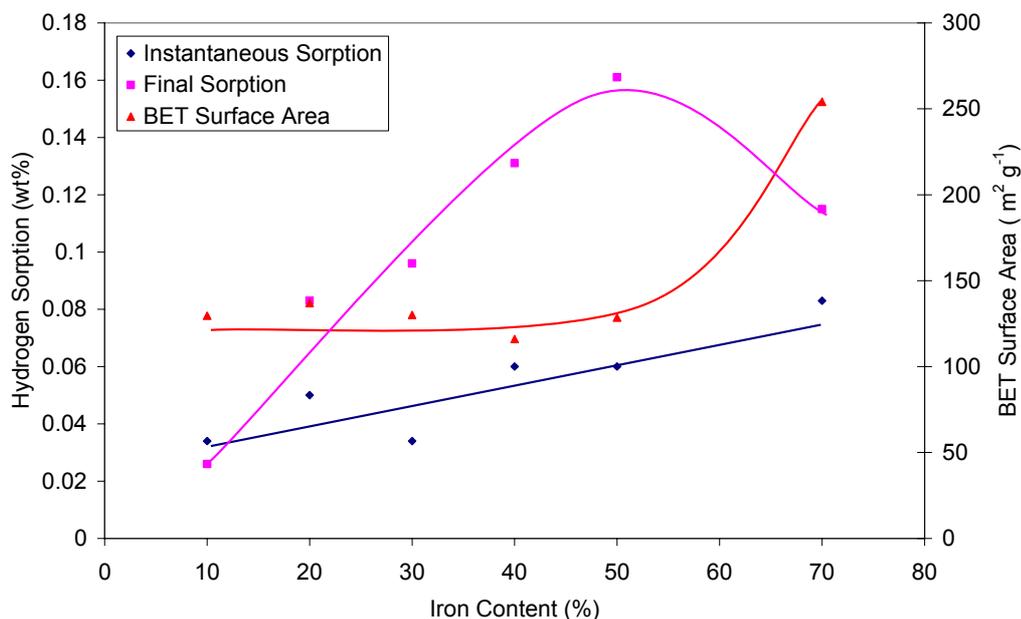
Figure 7-18   Comparison of hydrogen sorption values and BET surface area of CNF prepared from Fe-Ni catalysts from ethylene-hydrogen (60-240 ml min^{-1}) at 600 $^\bullet$C

7.3.2.2 Microscopy study

A sample of CNF prepared from $Fe_{20}Ni_{80}$ was selected for analysis by TEM because the sample possessed a high carbon conversion rate but low hydrogen storage capacity relative to the CNF prepared with Cu-Ni with the same nickel concentration, which will be discussed later in this chapter. The CNF were observed to possess fibre widths in the range of 100-400 nm, with lengths of up to 5 μm. All CNF studied were of a platelet crystal structure. The CNF had a segmented platelet structure, which was visible even at low magnification. This segmented formation was clearly evident at high magnification, with further confirmation arising from the diffraction pattern of a nanofibre being observed indicative of a platelet crystal structure (Figure 7-19 (c)).

(a)   (b)

(c)

*The negative was over exposed, partially whiting out diffraction pattern
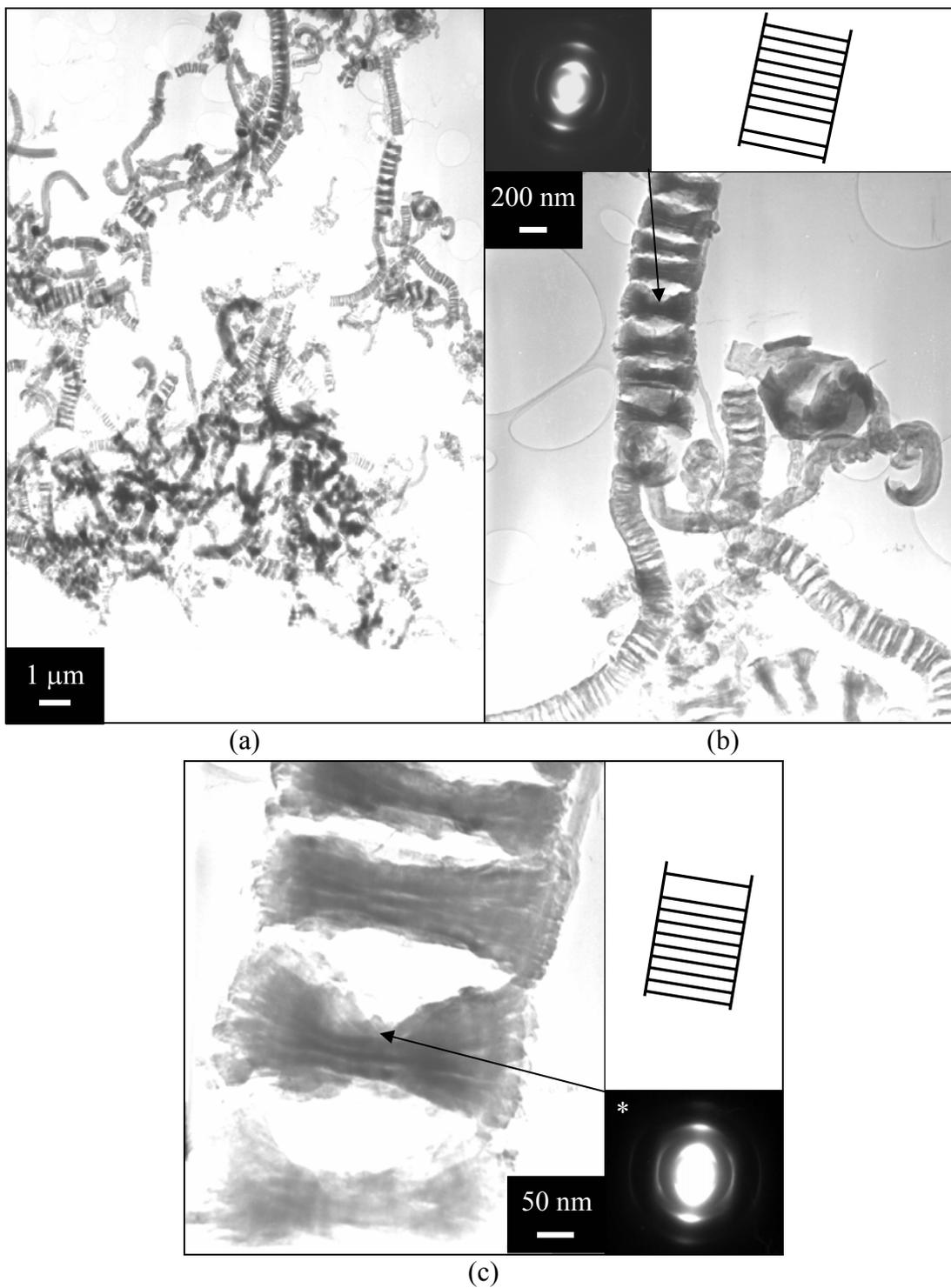
Figure 7-19   TEM images of CNF prepared from ethylene-hydrogen (60-240 ml min^{-1}) over a Fe$_{20}$Ni$_{80}$ catalyst, grown in a quartz reaction vessel at 600 ˚C; (a) low magnification image (b) image of a coil, with a diffraction pattern of a CNF (c) high magnification image and diffraction pattern of a section of CNF

To confirm the morphology of the CNF prepared from $Fe_{20}Ni_{80}$, some SEM images were taken of the material (Figure 7-20). As observed by TEM, the CNF were found to have a diameter in the range of 100-400 nm with lengths of up to 5 μm.
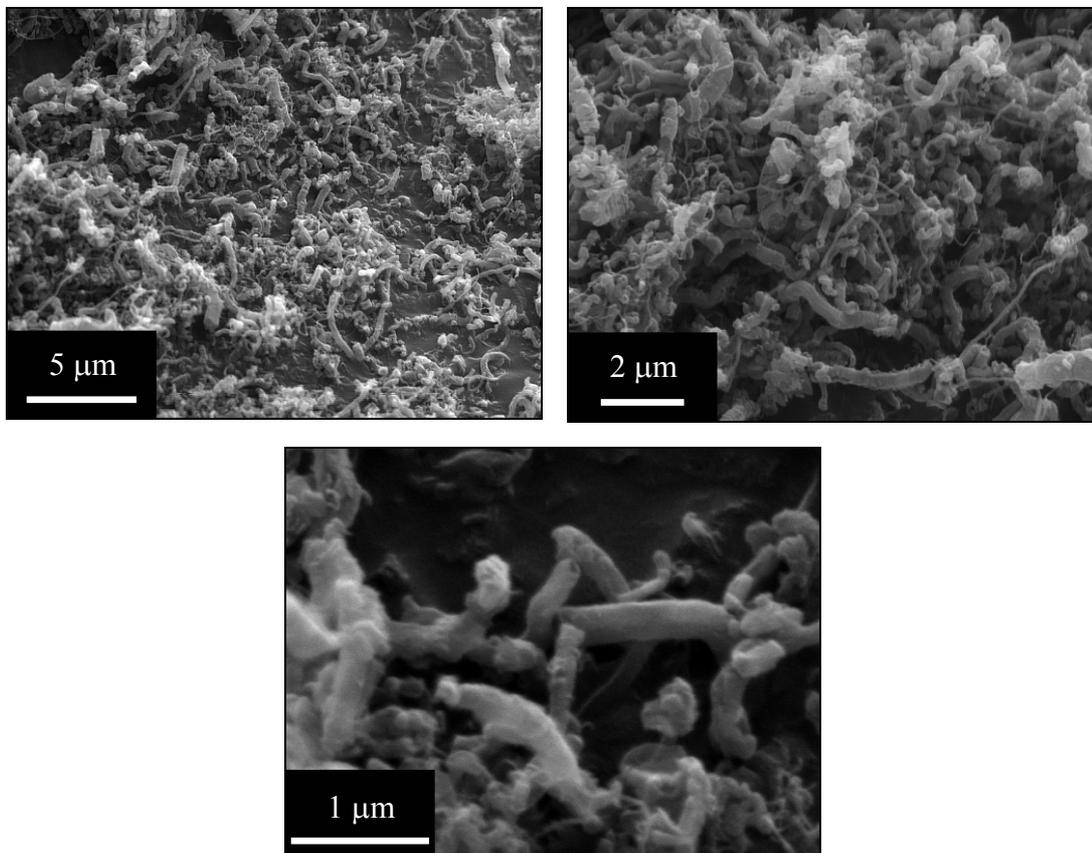
Figure 7-20   SEM images of CNF prepared from ethylene-hydrogen (60-240 ml min^{-1}) and $Fe_{20}Ni_{80}$ at 600 ˙C

7.3.3 Investigating copper-nickel catalyst systems

The copper-nickel catalyst system exhibits clear trends in both carbon conversion and BET surface area with increasing copper content (Figure 7-21). The carbon conversion was *ca* 50 % when copper content in the range 10-50 %, the conversion then swiftly decreases at 60 % copper content to 40 % carbon conversion, finally catalysts containing 70 % of copper and above resulted in encapsulation. The BET surface area of the CNF followed a concurrent trend, with *ca* 500 m^2 g^{-1} achieved by CNF prepared from catalysts with 10-40 % copper content, and then swiftly dropping with increasing copper content.
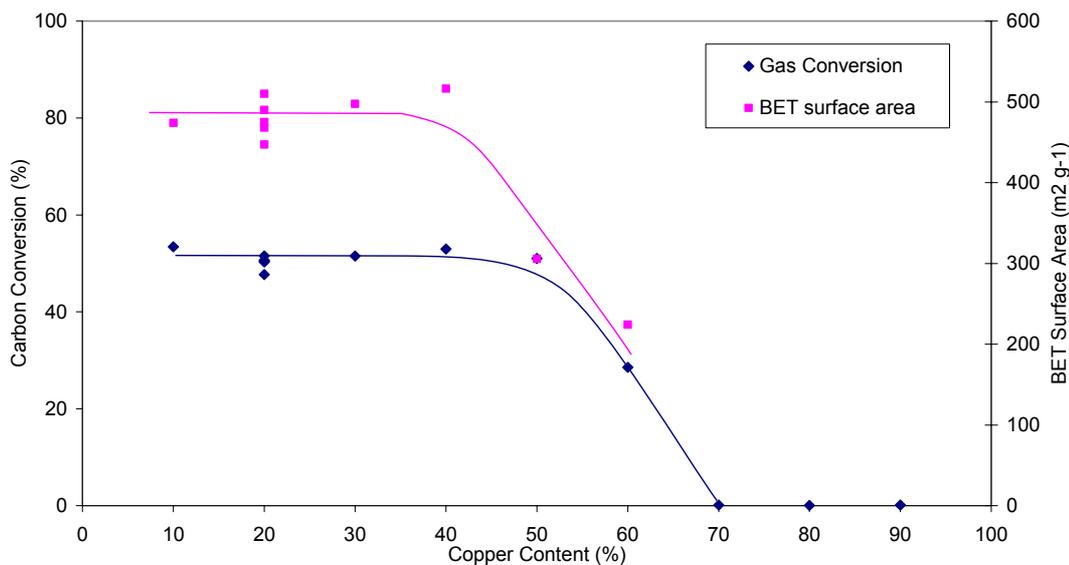
Figure 7-21   Carbon conversion and nitrogen BET surface area of CNF prepared from Cu-Ni catalyst series at 600 ˙C for 3 hours using ethylene-hydrogen (60-240 ml min^{-1})

7.3.3.1 Hydrogen adsorption studies

The hydrogen adsorption profiles for the CNF prepared from Cu-Ni catalysts were recorded for samples that were obtained in quantities over 1 g (Figure 7-22). CNF produced from $Cu_{10}Ni_{90}$ displayed the lowest uptake, with little more than the instantaneous uptake being achieved, resulting in a final hydrogen sorption of 0.14 wt%. As the result is in such sharp contrast to the pattern of the other results for CNF produced from the Cu-Ni series, the $Cu_{10}Ni_{90}$ measurement was repeated. However, the final sorption value was found to be even lower at 0.12 wt%. The total sorption then reached a maximum of *ca* 0.40 wt% for CNF produced from $Cu_{20}Ni_{80}$ then decreases to 0.15 wt% for CNF produced from $Cu_{60}Ni_{40}$.

The hydrogen sorption profiles produced by the Cu-Ni series CNF possess the highest capacities of the three series studied. The majority of the hydrogen sorption profiles for CNF recorded at 100 bar after DG2 in this study fitted a similar pattern. The profiles begin with instantaneous adsorption, thought to be due to physisorption, the magnitude of which is proportional to the surface area of the CNF (Chapter 7). This relationship is supported by the high surface area CNF from the Cu-Ni series possessing the highest instantaneous hydrogen sorption. Beyond the instantaneous adsorption, there was a slower period of adsorption, that for most

samples equilibrated at *ca* 100 min. The slower adsorption could be caused by a number of processes, such as chemisorption to trace catalyst presence or by slow penetration of the graphite layers within the CNF structure.
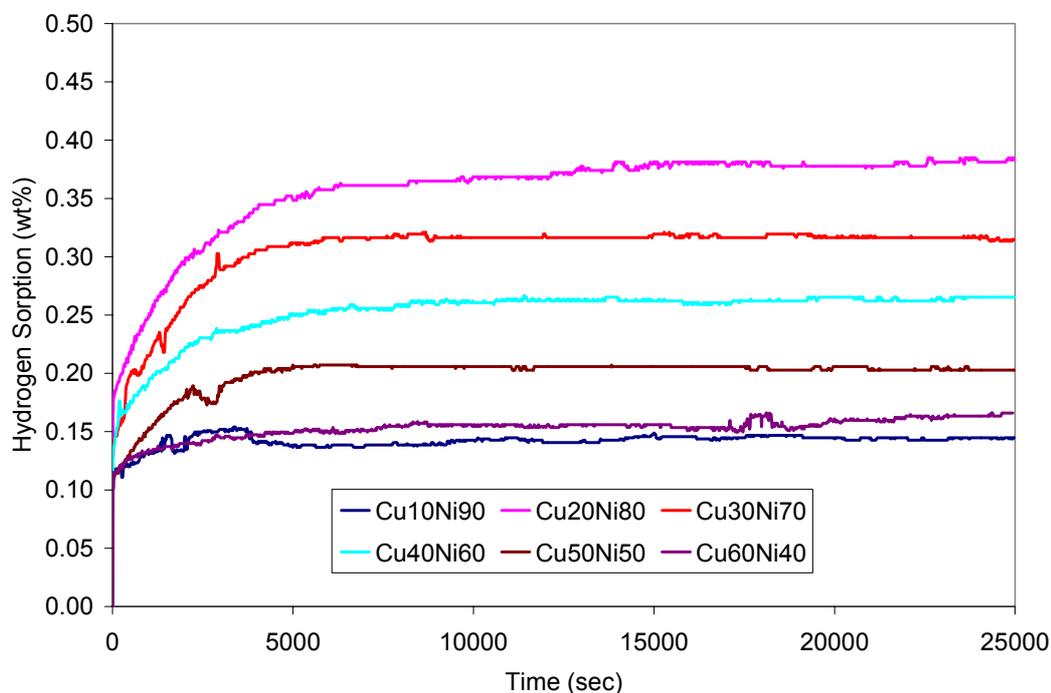
Figure 7-22   Hydrogen sorption profiles of CNF prepared from Cu-Ni catalysts from ethylene-hydrogen (60-240 ml min^{-1}) at 600 ˚C, recorded at 100 bar and 30 ˚C after DG2

The relationship between instantaneous adsorption and surface area is not clearly defined for the Cu-Ni series of CNF (Figure 7-23); this can be explained by the CNF from the Cu-Ni series possessing the larger amount of slower sorption relative to the other series, which may mask the true value of instantaneous hydrogen sorption. The surface area of the Cu-Ni CNF displayed no obvious correlation with the final hydrogen sorption. This indicates that the slower sorption is not a surface area related phenomena, and so not a physisorption effect; this is supported by the longer timescale of this sorption, which is more characteristic of chemisorption or of a penetration effect.
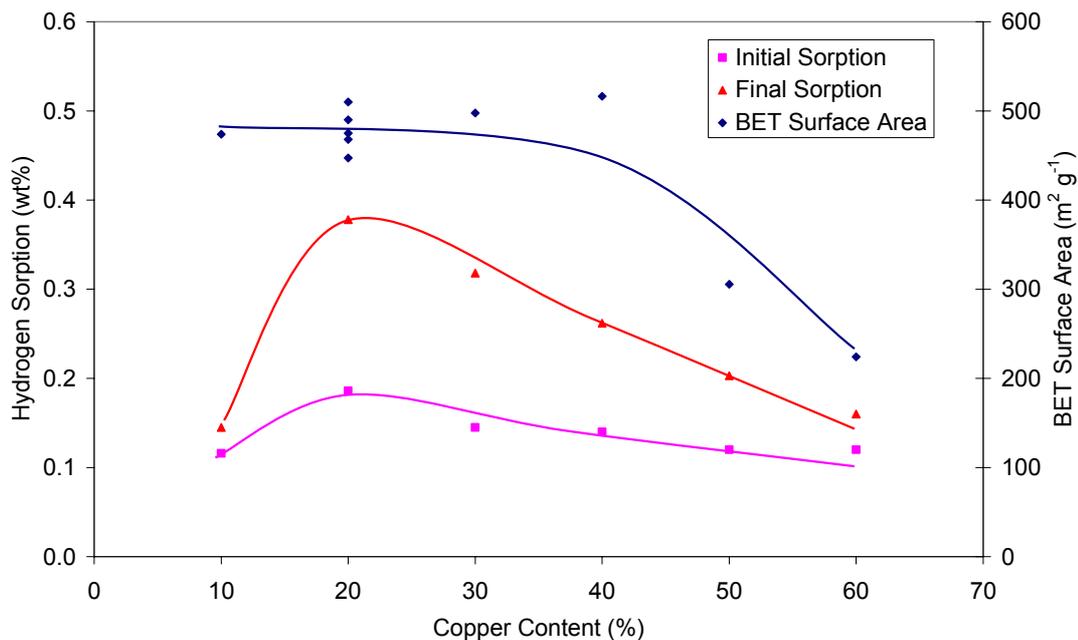
Figure 7-23   Comparison of hydrogen sorption values and BET surface area of CNF prepared from Cu-Ni catalysts from ethylene-hydrogen (60-240 ml min^{-1}) at 600 $^{\bullet}$C

7.3.3.2 Microscopy study

A sample of CNF produced using catalyst $Cu_{20}Ni_{80}$ was analysed by TEM as it had been found to possess a high conversion rate and hydrogen sorption capacity. The CNF produced by $Cu_{20}Ni_{80}$ were observed to be of homogenous form with widths of approximately 250 nm, with the majority of the CNF being 1-10 μm in length (Figure 7-24). All the CNF studied possessed a platelet crystal structure (Figure 7-24 (a) and (b)). A number of catalyst particles were observed located in the body of individual CNF; this indicates that the CNF grew in the bi-directional mode (Figure 7-24 (c) and (d)).

(a)   (b)

(c)   (d)
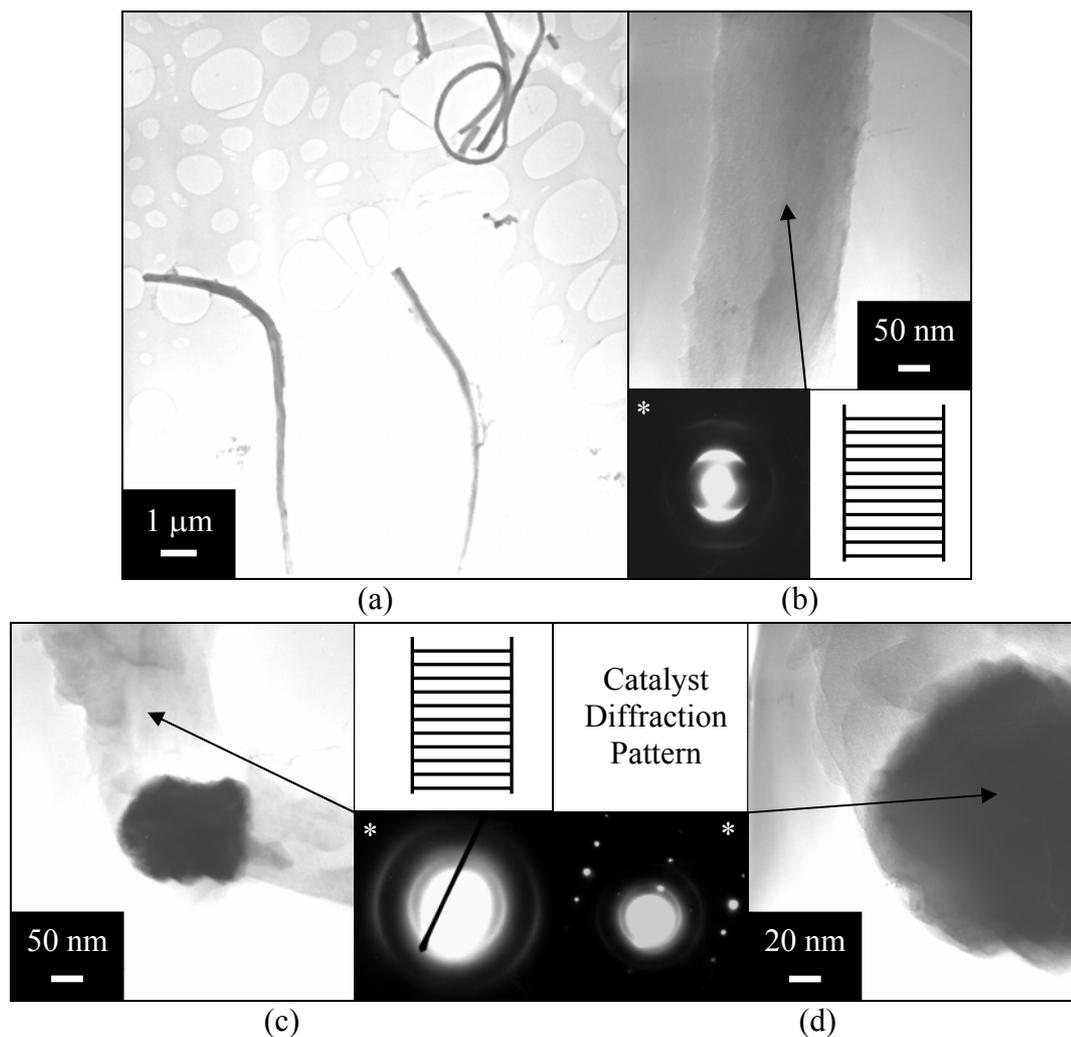
*The negative was over exposed, partially whiting out diffraction pattern

Figure 7-24   TEM images of CNF produced by passing ethylene-hydrogen (60-240 ml min^{-1}) over Cu$_{20}$Ni$_{80}$ catalyst in a quartz reaction vessel at 600 °C; (a) low magnification image (b) image of a CNF, with a diffraction pattern of a CNF (c) image of a CNF containing a catalyst particle, with a diffraction pattern of a CNF (d) high magnification image of a CNF containing a catalyst particle and diffraction pattern of a catalyst particle

In order to confirm the morphology of the Cu$_{20}$Ni$_{80}$ CNF, SEM analysis was also carried out on the material (Figure 7-25).
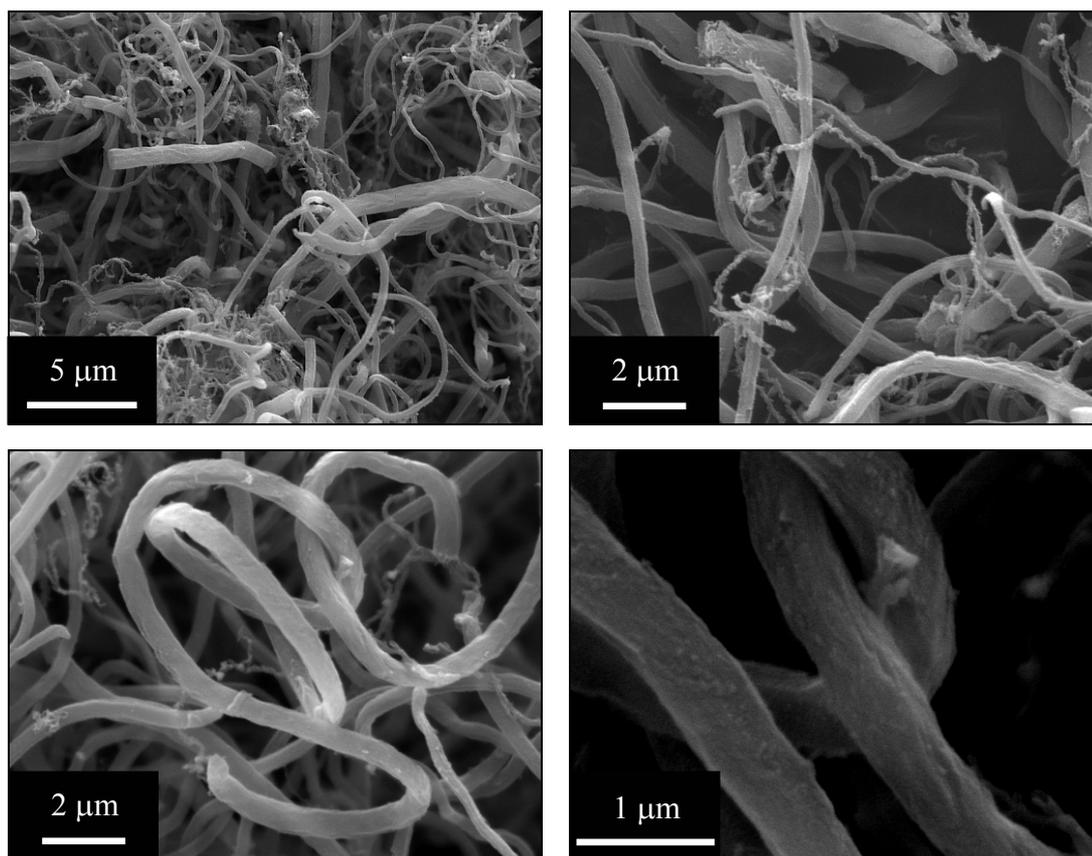
Figure 7-25   **SEM images of CNF prepared at 600 $^{\bullet}$C from a $Cu_{20}Ni_{80}$ catalyst and ethylene-hydrogen (60-240 ml min^{-1})**

As the CNF prepared using $Cu_{30}Ni_{70}$ was found to possess a similar conversion ratio to, but a much lower hydrogen sorption capacity than, CNF prepared with $Cu_{20}Ni_{80}$, both samples were analysed by TEM. The $Cu_{30}Ni_{70}$ CNF were found to be of heterogeneous form, with widths varying from 35 to 800 nm (Figure 7-26 (a)). Twisted, branched and straight CNF were present in the sample (Figure 7-26 (b)). Many CNF diffraction patterns were observed all of which were indicative of a platelet structure.

(a)   (b)
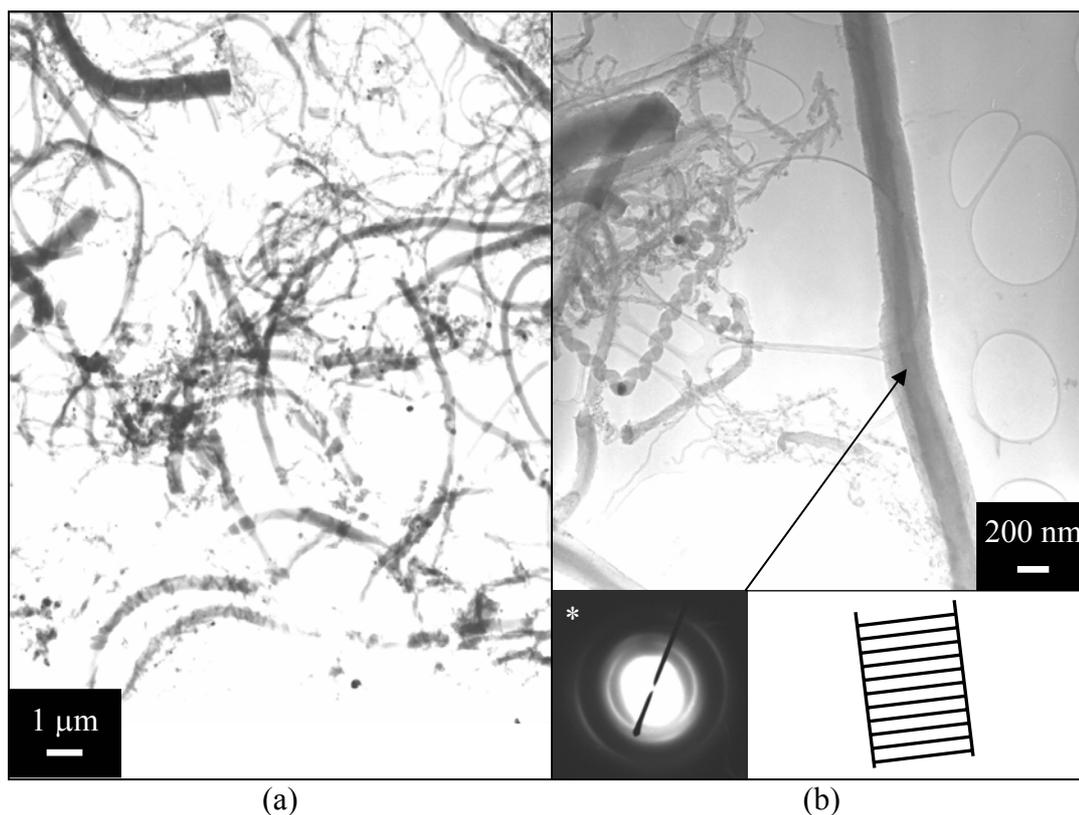
*The negative was over exposed, partially whiting out diffraction pattern

Figure 7-26   **TEM images of CNF from ethylene-hydrogen (60-240 ml min^{-1}) over Cu$_{30}$Ni$_{70}$ catalyst grown in a quartz reaction vessel at 600 ˙C; (a) low magnification image (b) image of a CNF, with a diffraction pattern of a CNF**

7.3.4 Investigating carbon nanofibres prepared with Cu$_{20}$Ni$_{80}$

The CNF produced using Cu$_{20}$Ni$_{80}$ had displayed the most promising hydrogen sorption uptake of all the CNF studied, achieving *ca* 0.4 wt%. In addition to this, the Cu$_{20}$Ni$_{80}$ catalyst system displayed one of the highest activities of the catalysts studied achieving consistently *ca* 50 % carbon conversion, with the CNF having a consistent surface area of *ca* 500 m^2 g^{-1}. For these reasons CNF prepared from Cu$_{20}$Ni$_{80}$ was selected to study effects in variation of preparation and degas in order to optimise the hydrogen sorption capacity of the CNF.

7.3.4.1 Hydrogen adsorption studies

The hydrogen sorption profile of CNF prepared from Cu$_{20}$Ni$_{80}$ using different degas procedures can be seen in Figure 7-27. The profiles recorded were very similar to those seen for CNF prepared from Cu$_5$Fe$_{85}$Ni$_{10}$ differing only in magnitude (Section 7.2.2.4). The degas procedure used prior to a run had a large effect on the hydrogen

sorption capacity of the CNF prepared with $Cu_{20}Ni_{80}$. DG1 was found to achieve an instantaneous hydrogen sorption uptake of *ca* 0.15 wt% with no additional, slower, sorption being observed.   Both DG2 and DG3 runs start with *ca* 0.2 wt% instantaneous hydrogen sorption, which was then followed by a period of slower adsorption.   The explanation for the observed instantaneous and slower sorption is believed to be the same as discussed for CNF prepared with $Cu_5Fe_{85}Ni_{10}$ (Section 7.2.2.4).   DG2 runs were found to achieve an uptake of 0.38 wt%, showing good repeatability, with the second run achieving 0.36 wt%.   The DG3 run was observed to achieve the highest hydrogen sorption of any CNF run, with an uptake of 0.5 wt% being observed.   After run 3 was recorded, runs 4 and 5 were recorded using DG1 and DG2, respectively, in order to ascertain if the uptake of 0.5 wt% could be achieved subsequent to a DG3 run but using a softer degas procedure.   Both DG1 and DG2 runs, however, achieved their previous level of uptake.   Finally, in order to prove the repeatability of the preparation and of the measurement, preparation of the catalyst and CNF was repeated, and the hydrogen sorption capacity was then determined to be 0.48 wt% following DG3.
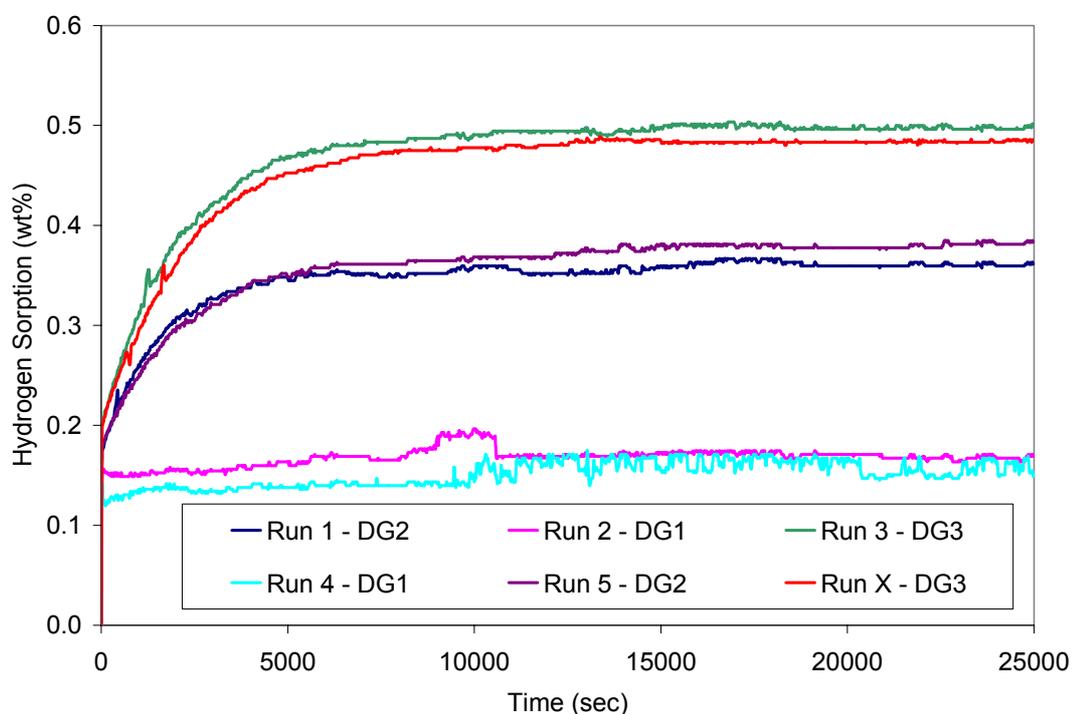
Figure 7-27 The hydrogen adsorption profile of CNF grown from $Cu_{20}Ni_{80}$ catalyst using ethylene-hydrogen (60-240 ml min^{-1}) at 600 ˙C, recorded at 100 bar and 30 ˙C, Runs 1-5 were recorded using the same sample, Run X was recorded using a different sample prepared from a different catalyst batch

7.3.4.2 Study of the effects of annealing

Two samples of CNF produced using $Cu_{20}Ni_{80}$ were annealed at 1000 ˚C for 24 hours. The nitrogen BET surface area of both samples remained constant before and after the annealing process at *ca* 475 m^2 g^{-1}. The hydrogen storage capacities of the samples were analysed and found to have a reduced uptake capacity relative to the precursor material (Figure 7-28). One sample was analysed to determine the effect of the degas procedure used and was found to fit a similar pattern to the as prepared CNF produced by $Cu_{20}Ni_{80}$.
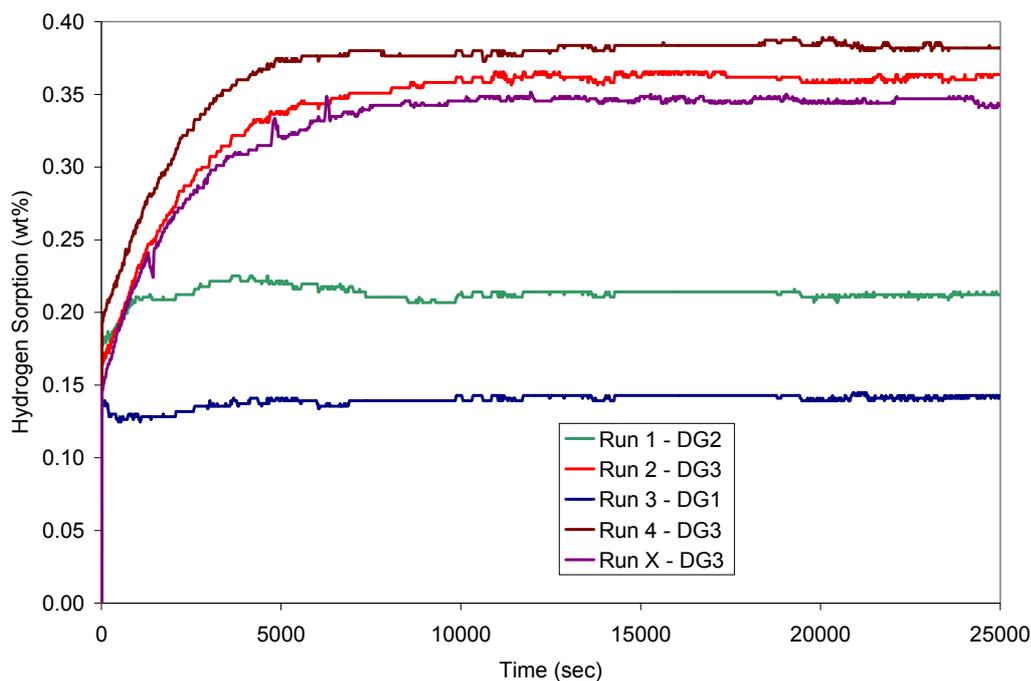
Figure 7-28 The hydrogen adsorption profile of 1000 ˚C annealed CNF grown from $Cu_{20}Ni_{80}$ catalyst using ethylene-hydrogen (60-240 ml min^{-1}) at 600 ˚C recorded at 100 bar and 30 ˚C, Runs 1-4 are recorded using the same sample, Run X is recorded using the second annealed sample

The XRD patterns of the $Cu_{20}Ni_{80}$ CNF and the 1000 ˚C annealed were found to be almost identical, implying that no changes had taken place to the crystal structure of the CNF. To confirm this, one of the 1000 ˚C annealed samples of CNF produced by $Cu_{20}Ni_{80}$ was analysed by TEM (Figure 7-29). The average CNF diameter was slightly more variable than the precursor sample (Figure 7-24); however, this could result from it being a different part of the sample.

(a)   (b)
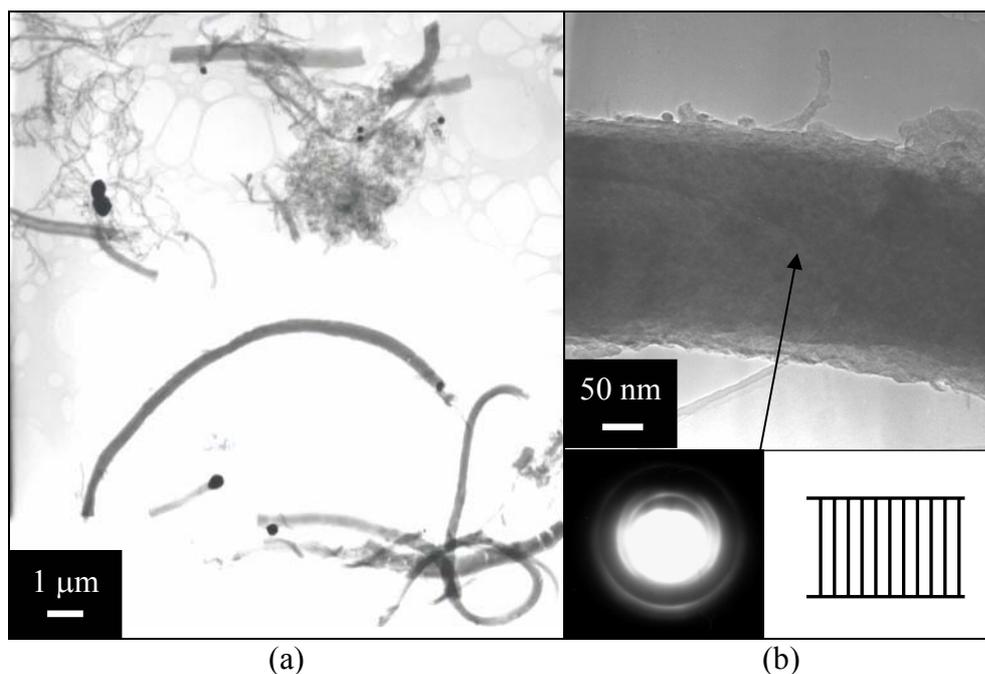
Figure 7-29   TEM images of 1000 ˚C annealed CNF grown from $Cu_{20}Ni_{80}$ catalyst using ethylene-hydrogen (60-240 ml min^{-1}) at 600 ˚C; (a) low magnification image (b) image of a CNF, with a diffraction pattern up of a CNF

7.3.5 Preparation study of CNF from $Cu_{20}Ni_{80}$

The $Cu_{20}Ni_{80}$ prepared CNF studied were prepared at 600 ˚C using ethylene-hydrogen (60-240 ml min^{-1}). In order to optimise the preparation of the CNF, the effect of varying the temperature and gas composition were studied.

7.3.5.1 The effect of preparation temperature

The onset of soot formation began at 650 ˚C, when the reactor tube was given a black coating, and analysis by SEM revealed amorphous material present in the CNF produced. The surface area achieved a maximum of *ca* 500 m^2 g^{-1} at 600 ˚C, just prior to the onset of soot formation (Figure 7-30). Thus, 600 ˚C is the optimal growth temperature for this system, achieving maximum surface area with a 50 % carbon conversion rate, but avoiding soot formation.
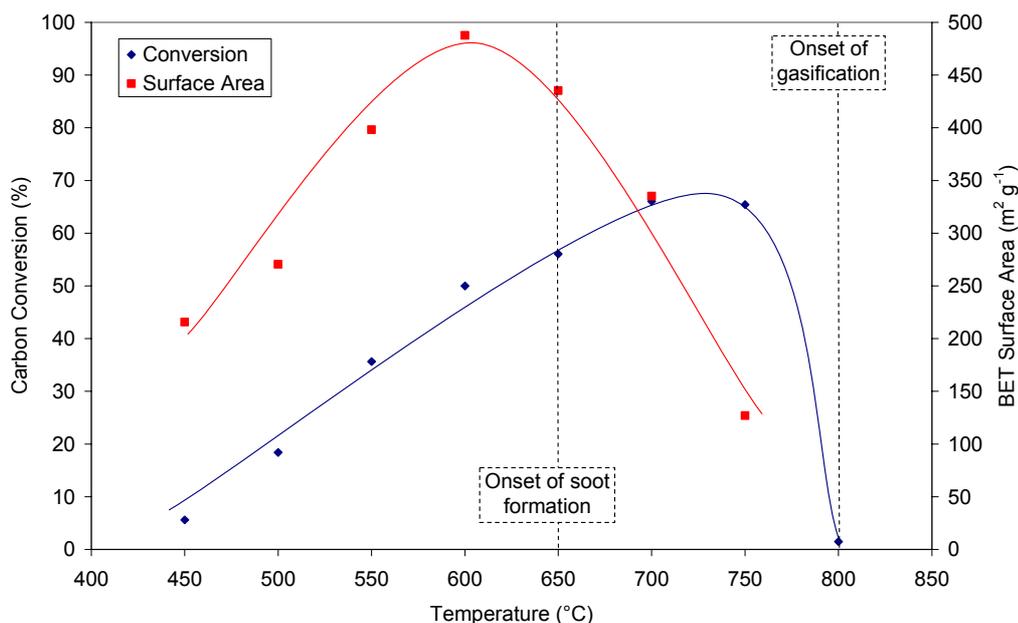
Figure 7-30   The effect of temperature on Cu$_{20}$Ni$_{80}$ preparation of CNF using ethylene-hydrogen (60-240 ml min^{-1}) for 3 hours

The hydrogen sorption capacities of CNF produced at a selection of temperatures were determined (Table 7-7), and was found to be optimal at 600 °C.

Catalyst	CVD Temperature (°C)	Nitrogen BET surface area (m^2 g^{-1})	Hydrogen Sorption (wt%)
Cu$_{20}$Ni$_{80}$	500	271	0.14
Cu$_{20}$Ni$_{80}$	600	475	0.38
Cu$_{20}$Ni$_{80}$	700	335	0.13

Table 7-7 Hydrogen sorption capacities and nitrogen BET surface areas of a selection of CNF samples prepared from Cu$_{20}$Ni$_{80}$ catalyst from ethylene-hydrogen (60-240 ml min^{-1}) recorded at 100 bar and 30 °C after DG2

At 800 °C, the conversion of ethylene to CNF ceases, and colourless crystals form on the wall of the main quartz tube near the gas outlet, with a yellow oil collecting below (Figure 7-31).
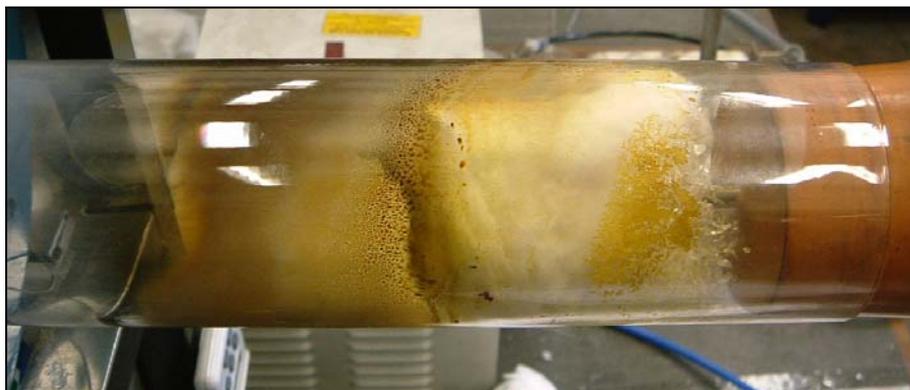
Figure 7-31   Picture of the crystals and oil formed at 800 ˙C from ethylene-hydrogen (60-240 ml min^{-1}) for three hours over a Cu$_{20}$Ni$_{80}$ catalyst

In order to identify the crystals and oil, small samples were dissolved in dichloromethane and analysed by GC-MS which yielded the mass spectrum illustrated in (Figure 7-32). The crystals were found to chromatograph to one peak with mass 128 m/z. The signal at 128 m/z is indicative of the presence of naphthalene (Appendix 6).
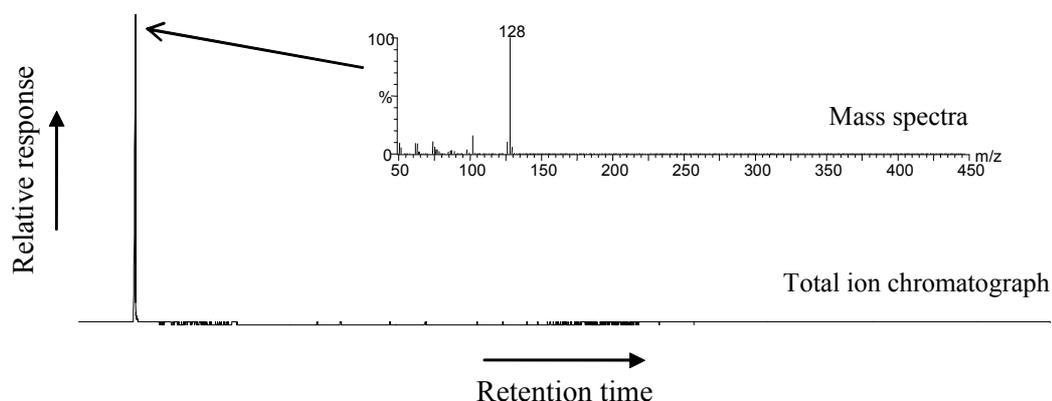
Figure 7-32   GC-MS trace of crystals formed at 800 ˙C from ethylene-hydrogen (60-240 ml min^{-1}) for three hours over a Cu$_{20}$Ni$_{80}$ catalyst

The oil chromatographed to four major peaks which yielded mass spectra indicating the presence of a mixture of PAHs (Figure 7-33). The major peaks, in order of elution, were found to have masses 178, 189, 202 and 202 m/z, which are indicative of anthracene, phenanthrene, fluoranthene and pyrene respectively (Appendix 6).
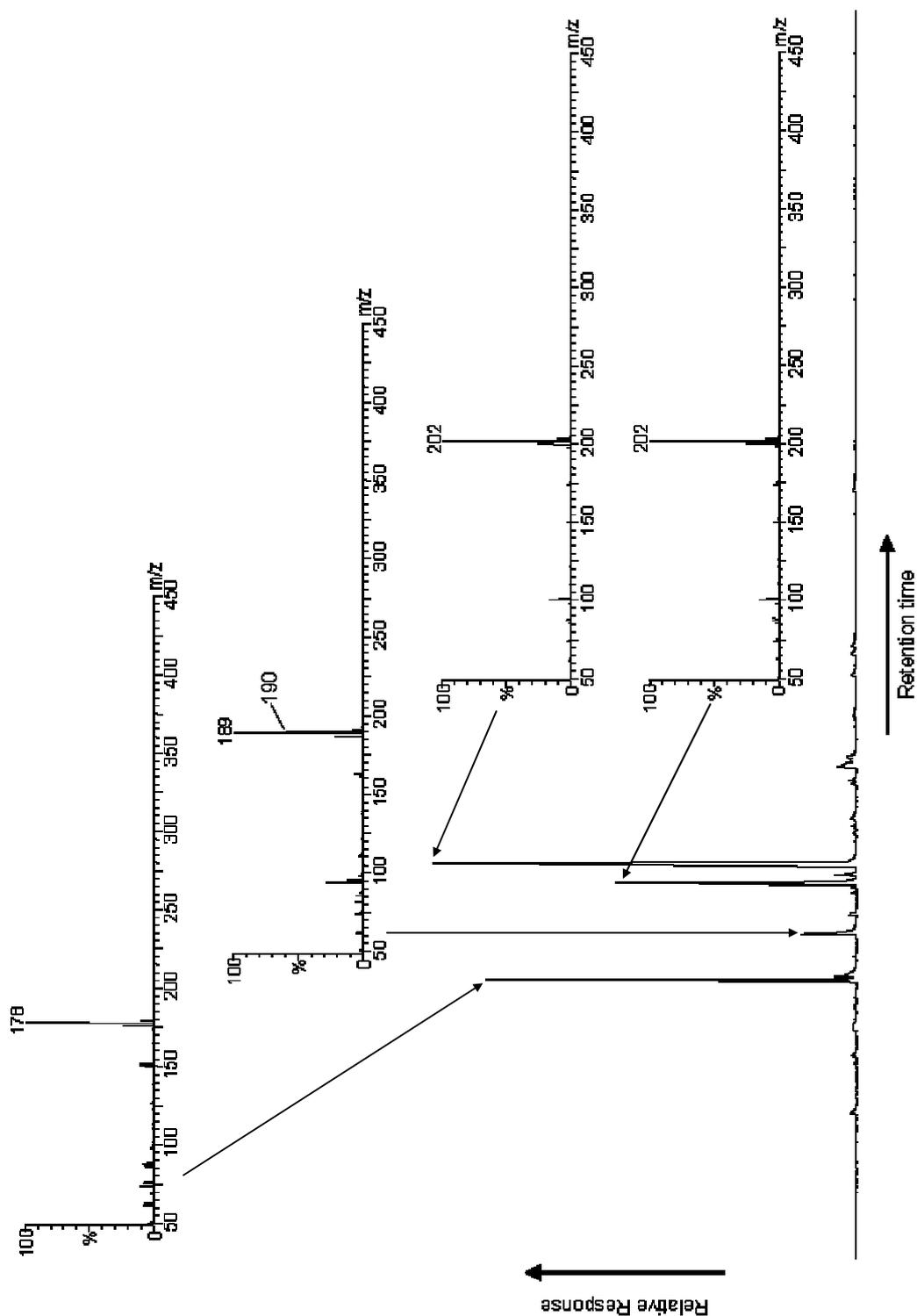
Figure 7-33   GC-MS trace of the oil formed at 800 ˚C from CVD using gas mixture ethylene-hydrogen (60-240 ml min^{-1}) for 3 hours over a $Cu_{20}Ni_{80}$ catalyst. Mass spectra of individual components are also illustrated.

7.3.5.2 The effect of gas composition

The effect of changing the ethylene-hydrogen ratio of the reactant gas was investigated by keeping the ethylene flow rate constant (60 ml min^{-1}), changing the hydrogen flow rate and using argon as an inert gas to maintain a constant flow rate of 300 ml min^{-1}. The ethylene-hydrogen ratio of the reactant gas was found to have only a minor effect on the gas conversion rates, and the BET surface area of the CNF formed (Figure 7-34). The conversion rate dropped from *ca* 80 % to *ca* 50 % as the hydrogen concentration increased, conversely BET surface area increased from 425 to 475 m^2 g^{-1}.
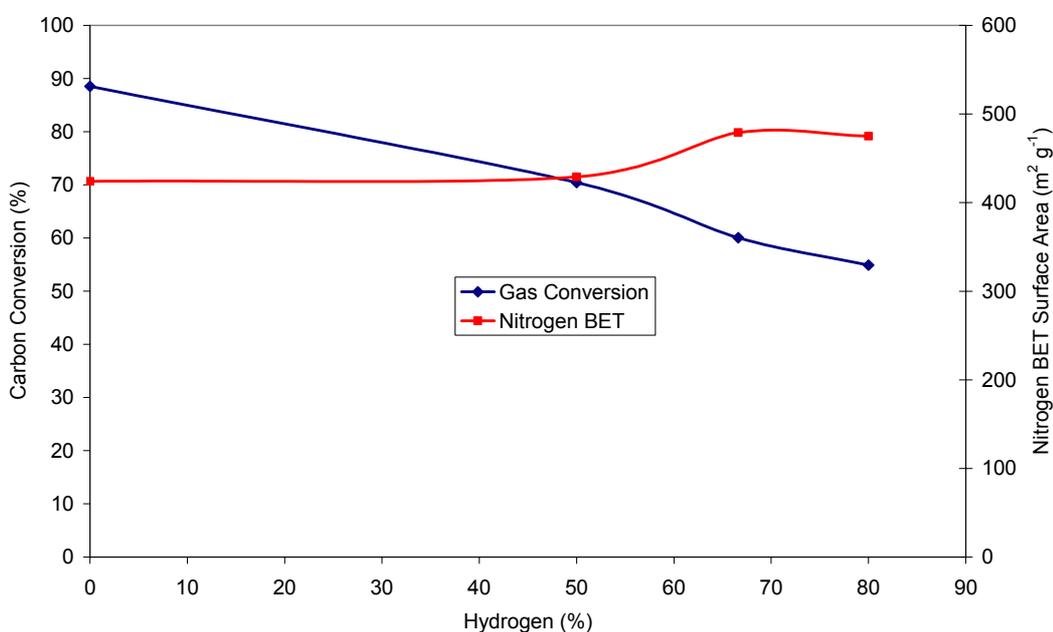
Figure 7-34   The effect of gas composition on the preparation of CNF using Cu$_{20}$Ni$_{80}$ and ethylene-hydrogen-argon gas mixtures at a total flow of 300 ml min^{-1} and 600 $^{\bullet}$C for 3 hours

The hydrogen storage capacity of a CNF sample prepared from ethylene-argon (60-240 ml min^{-1}) was analysed and found to have a reduced uptake relative to the CNF prepared using ethylene-hydrogen (60-240 ml min^{-1}) (Figure 7-35).
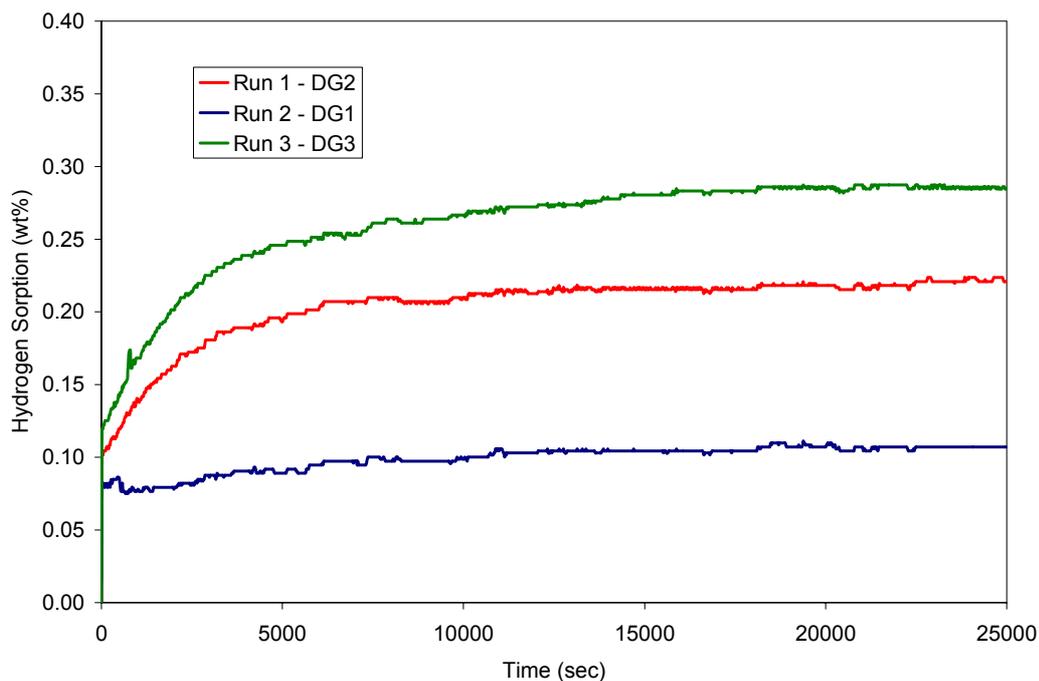
Figure 7-35   **The hydrogen adsorption profile of CNF grown from $Cu_{20}Ni_{80}$ catalyst using ethylene-argon (60-240 ml min^{-1}) at 600 $^{\bullet}$C, recorded at 100 bar and 30 $^{\bullet}$C**

The CNF sample prepared from ethylene-argon (60-240 ml min^{-1}) was analysed by TEM. The CNF were found to be of heterogeneous form with widths of approximately 150-250 nm (Figure 7-36). The CNF studied possess a mixture of platelet and herringbone crystal structures (Figure 7-36 (b) and (c)), which suggests that the CNF grown in the absence of hydrogen are not as well controlled as those which are.

(a)   (b)

(c)
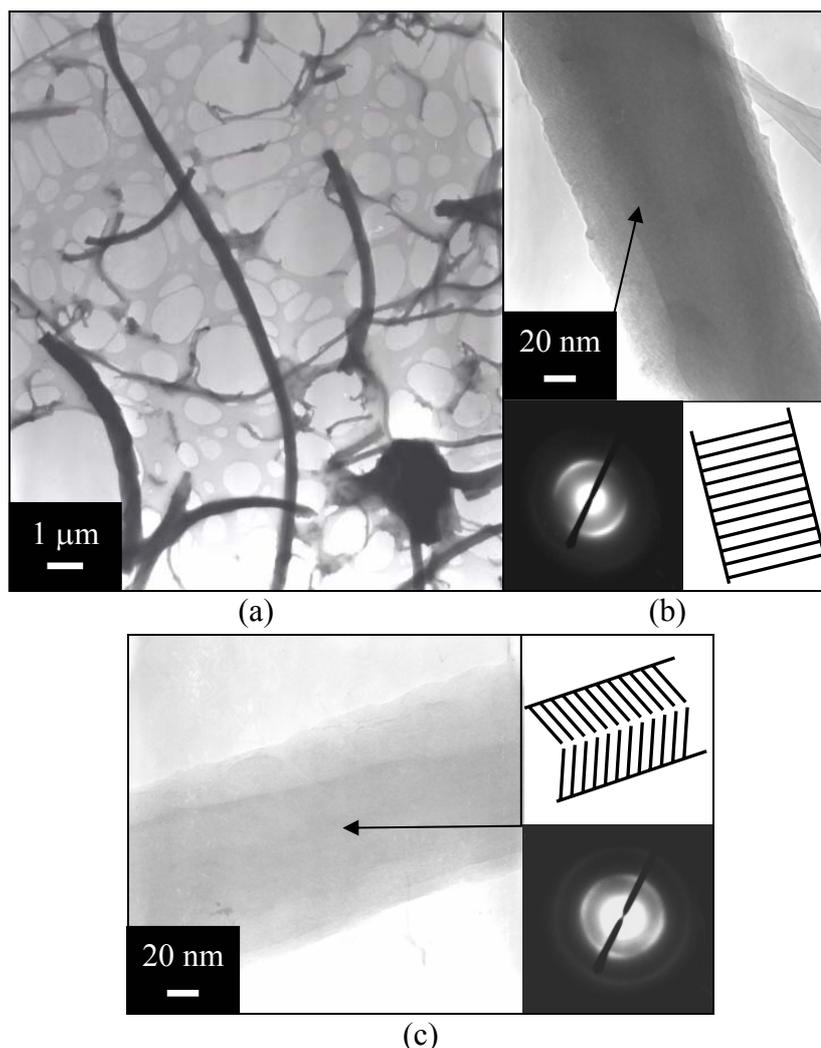
Figure 7-36   TEM images of CNF from ethylene (60 ml min^{-1}) using argon (240 ml min^{-1}) to maintain the flow rate, over Cu$_{20}$Ni$_{80}$ catalyst grown in a quartz reaction vessel at 600 ˚C; (a) low magnification image (b) and (c) high magnification image of a CNF, with a diffraction pattern up of a CNF

7.3.5.3 Monitoring the outlet gas during CVD

The CVD system using a mono component reactant gas (Section 7.3.5.2) allows the study of the reaction using GC-TCD to monitor the hydrogen content and GC-FID to monitor the hydrocarbon gas content. The reaction of Cu$_{20}$Ni$_{80}$ with ethylene was monitored in order to follow its progress (Figure 7-37). The reaction was observed to quickly initiate with over 70 % of the outlet gas found to be hydrogen. After *ca* 100 minutes the reaction began to slow, this is thought to be caused by catalyst deactivation through encapsulation. After 180 minutes the outlet gas was still over 60 % hydrogen, indicating that the reaction was a long way from terminating. The experiment was repeated with excellent reproducibility.
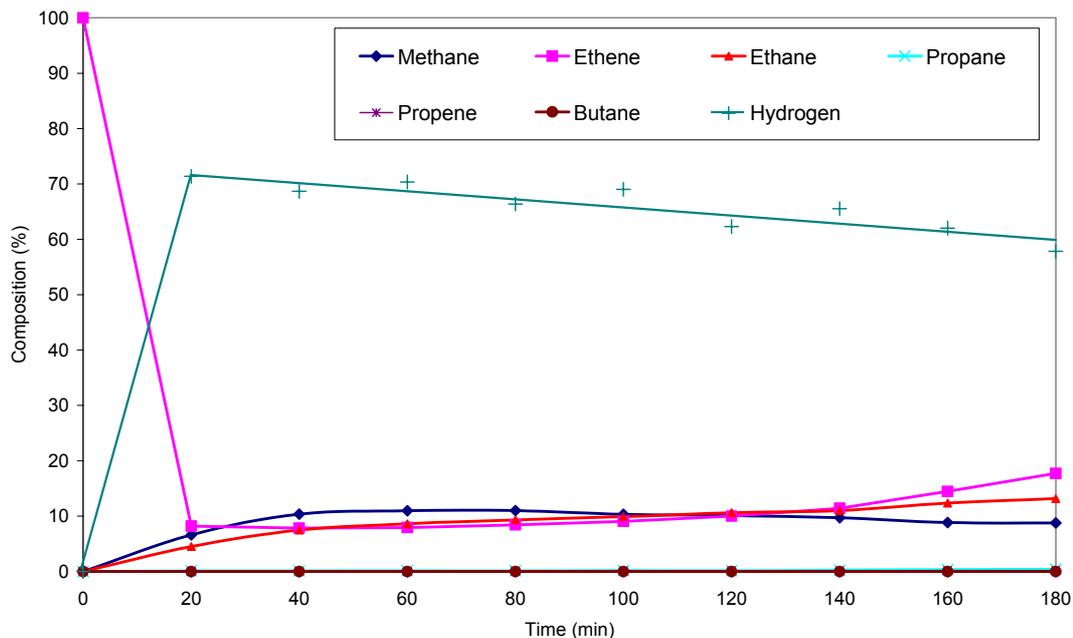
Figure 7-37   Composition of outlet gas from the CVD preparation of CNF from Cu$_{20}$Ni$_{80}$ and ethylene at 600 $^\bullet$C

For comparison, the experiment was repeated with a pure nickel catalyst (Figure 7-38). This reaction was observed to initially produce 60 % hydrogen, but was found begin to slow after 60 minutes and by 140 minutes the reaction had almost completely terminated, with over 90 % of the outlet gas being ethylene.
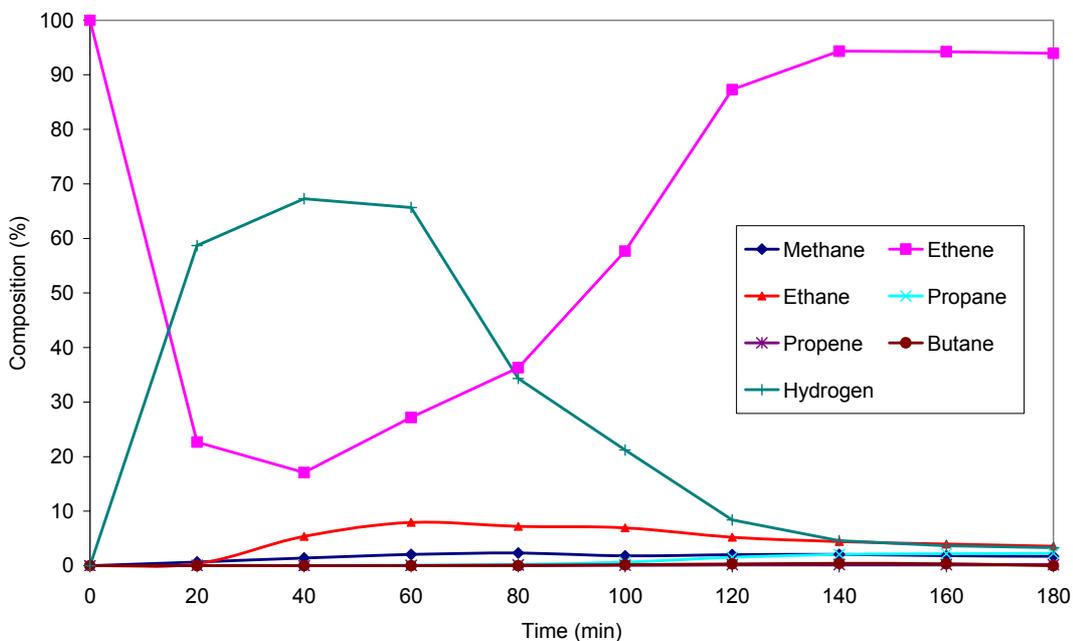
Figure 7-38   Composition of outlet gas from the CVD preparation of CNF from Ni and ethylene at 600 $^\bullet$C

This study highlighted that CVD preparation of CNF from ethylene to be a possible method of producing hydrogen without a carbon dioxide bi-product. Hydrogen production using CVD is beyond the scope of this thesis, but will be studied further in a continuation project investigating different catalysts, flows and gases.

7.4 Pure transition metal catalyst systems

In order to try to explain the trends observed with the bi-metallic catalytic systems, pure metal systems were investigated (Figure 7-39). The copper catalyst was found to have no activity with the ethylene-hydrogen reactant at temperatures from 500-900 ˚C. This was the expected result, as copper is known not to adsorb ethylene thus will not act as catalyst for CNF formation (Smith *et al.*, 2003). Conversely, the nickel catalyst was found to have the greatest activity, with the highest gas conversion being achieved at 600 ˚C. This compared well with both the copper-nickel and iron-nickel catalyst systems, as in both systems the nickel-rich catalysts exhibits the greatest activity. The iron catalyst system was found to require a higher temperature than the nickel system to produce CNF, and the maximum conversion rate was found to less than 25 % of that achieved by the nickel system.

The nickel and iron catalyst systems both exhibited the same soot and gasification onset points, 650 and 800 ˚C respectively. Crystals produced from the gasification over nickel and iron at 800 ˚C were analysed by GC-MS and found to be predominately naphthalene, with a trace presence of a few higher PAHs. The oil from both reactions was also analysed and found to predominately contain anthracene, phenanthrene, fluoranthene and pyrene. The onset temperatures and the PAHs produced are the same as those observed for the $Cu_{20}Ni_{80}$ catalyst system, discussed earlier in this chapter (Section 7.3.5.1). The copper system exhibited the onset of soot formation at 650 ˚C, but no gasification was observed at 800 ˚C and above, this indicates that the soot formation is a non-catalytic process. This was proved by carrying out a run 650 ˚C with no catalyst present, which resulted in only limited soot formation.
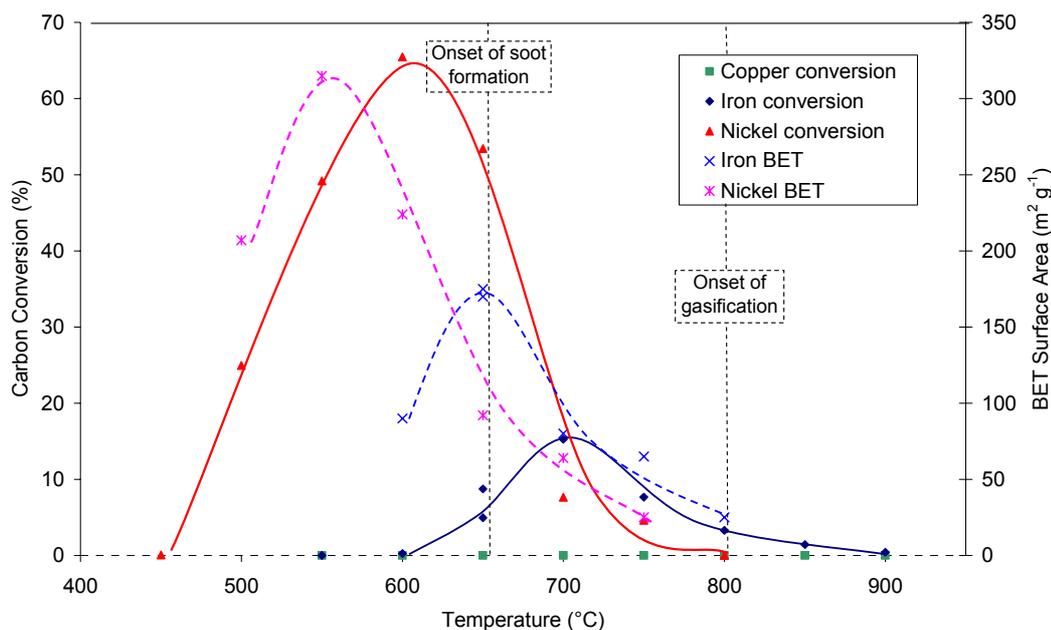
Figure 7-39   Using ethylene-hydrogen (60-240 ml min^{-1}) varying the temperature over a pure copper, iron and nickel catalyst

The hydrogen sorption capacities of a selection of the CNF produced by pure metals were determined (Table 7-8). The hydrogen sorption capacities of the CNF grown using iron were found to be very low which is comparable with bi-metallic systems containing iron.   The CNF grown using nickel exhibits much higher hydrogen storage capacities, which was comparable with the nickel rich bimetallic systems.

Catalyst	CVD Temperature ($^\bullet$C)	BET surface area (m^2 g^{-1})	Hydrogen Sorption (wt%)
Fe	650	172	<0.04
Fe	700	80	<0.04
Ni	500	207	0.16
Ni	550	315	0.17
Ni	600	224	0.30
Ni	700	64	0.12

Table 7-8   Hydrogen sorption capacities and BET surface areas of a selection of CNF samples prepared from pure iron and nickel catalysts from ethylene-hydrogen (60-240 ml min^{-1}) recorded at 100 bar and 30 $^\bullet$C after DG2

The CNF grown using nickel produced at 600 °C possess a hydrogen sorption profile very similar to that of the CNF prepared over $Cu_{20}Ni_{80}$ (Figure 7-40). The instantaneous sorption was less than that observed for the CNF prepared using $Cu_{20}Ni_{80}$, which would be expected, as the BET surface area is 200 m^2 g^{-1} less than

the latter. This corresponds to the hydrogen sorption capacity after DG2 and DG3 being 0.05 wt% less than the equivalent capacities for the nickel grown CNF.
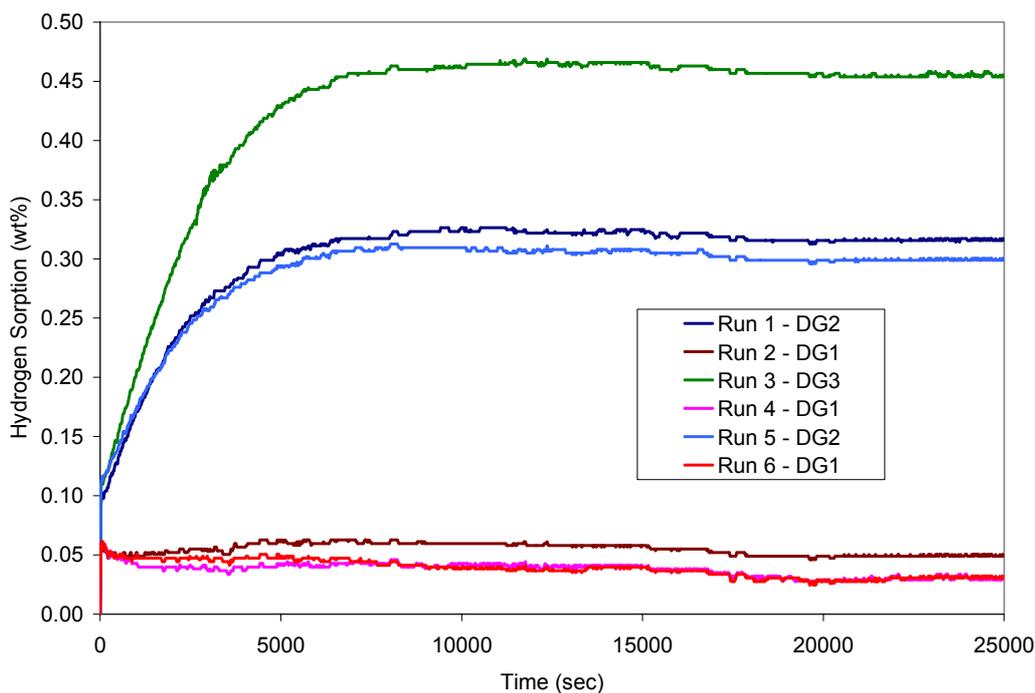
Figure 7-40 The hydrogen adsorption profile of CNF grown from a nickel catalyst using ethylene-argon (60-240 ml min^{-1}) at 600 ˙C recorded at 100 bar and 30 ˙C

7.5 Activation

Activation has been reported to have a beneficial effect on the hydrogen storage capacity of CNT (Yoon *et al.*, 2004).   Thus, it was decided to carry out an explorative investigation into the activation of CNF and the effect on hydrogen sorption capacity. Two CNF systems were selected for the study. Firstly, CNF produced from $Cu_{20}Ni_{80}$ grown at 600 ˙C from a mixture of ethylene-hydrogen (60:240 ml min^{-1}), as this had been proven to the highest hydrogen sorption capacity and BET surface area of the CNF studied, and could be repeatably prepared in high yield with an *ca* 50 % carbon conversion rate (Section 7.3.3). The second CNF system selected was that produced from $Fe_{20}Ni_{80}$, prepared under the same conditions in order to allow comparison. This CNF was selected, as it could also be repeatably prepared in high yield with *ca* 50 % carbon conversion rate, but paradoxically had one of the lowest hydrogen sorption capacities of the those studied (Section 7.3.2.1). Two activation systems were selected for this study in

order to give a comparison of the methods success with CNF systems; physical activation using carbon dioxide and chemical activation using potassium hydroxide.

7.5.1 Initial comparison of the activation methods

The potential performance of the carbon dioxide and potassium hydroxide activation processes were compared by using TGA simulations (Figure 7-41). The two CNF samples and a control sample of graphite were heated to 1000 ˚C under carbon dioxide. The CNF samples were found to possess similar reactivity with carbon dioxide as graphite, with the onset burn off not being observed until 800 ˚C. This implies that the CNF have a graphitised structure, which is in agreement with the previous XRD and TEM work described earlier in this chapter. The lack of extensive burn off indicated that the CNF are unlikely candidates for carbon dioxide activation. However, even limited burn off may result in the opening of pores accessible to hydrogen. Small samples of both of the CNF mixed with potassium hydroxide were heated in the TGA to 1000 ˚C under nitrogen in order to simulate potassium hydroxide activation. The onset of activity was found to be ca 700 ˚C, with a large burn off being observed. This indicated that the CNF were good candidate for potassium hydroxide activation.
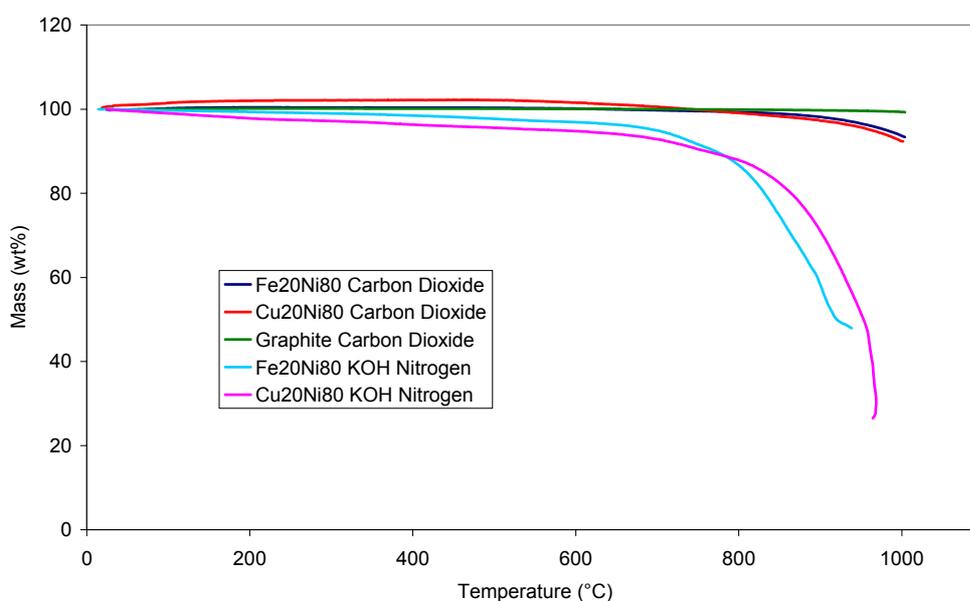
Figure 7-41   Simulation of carbon dioxide and potassium hydroxide activation of CNF prepared using Fe$_{20}$Ni$_{80}$ and Cu$_{20}$ Ni$_{80}$ by TGA

7.5.2 Physical activation

The physical activation of CNF from $Cu_{20}Ni_{80}$ at 900 ˚C was found to be difficult to achieve with good results (Figure 7-42). The carbon displayed the expected pattern of approximately linear increasing burn off with time. However, the surface area was found to decrease linearly with time implying the porous structure of the CNF was being destroyed.
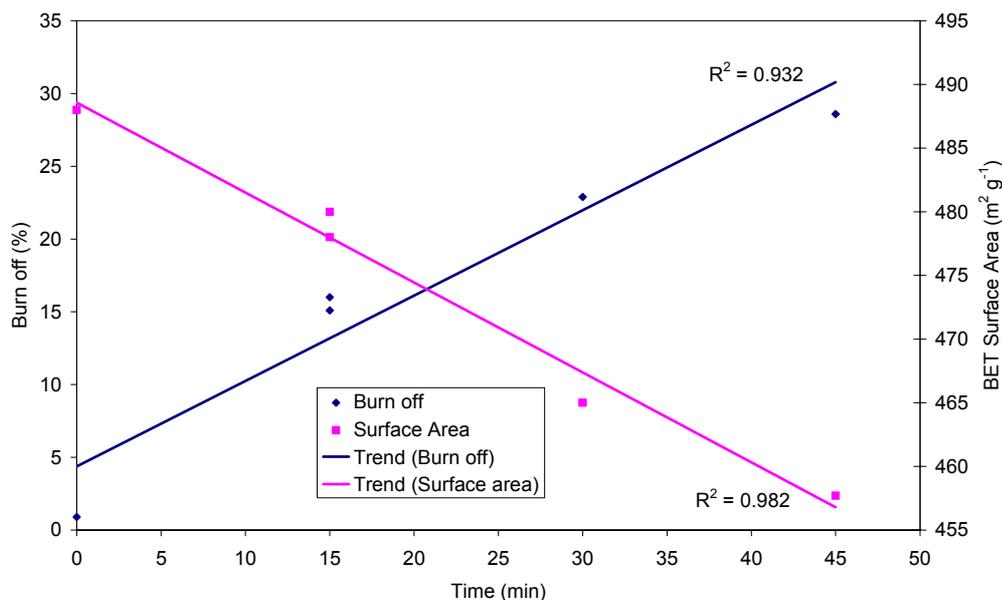
Figure 7-42   The effect of physical activation at 900 ˚C of CNF from $Cu_{20}Ni_{80}$ using carbon dioxide (100 ml min^{-1})

To achieve better activation, longer reaction periods were investigated. To reduce the increased burn off caused by extended activation times, lower activation temperatures were used (Table 7-9). The surface area was observed to increase with duration and with increasing temperature. However, the cost of this is a large increase in the carbon burn off. To determine if the surface area would continue to increase with time, one activation was allowed to run for 8 hours at 825 ˚C, as this was the lowest temperature where an appreciable surface area increase was observed after two hours. The 8 hour activation did result in the highest surface area increase for CNF from $Cu_{20}Ni_{80}$ but the burn off required to achieve this was 73.4 %.

Temperature ($^{\circ}$C)	Time (min)	Burn off (%)	BET ($m^2\ g^{-1}$)
800	30	9.9	476
800	120	21.8	488
825	30	10.8	478
825	120	44.2	517
825	480	73.4	678
850	30	16.7	482
850	120	54.3	521
875	30	17.5	477
875	120	63.0	542

Table 7-9 The BET surface area and burn off results from the activation of CNF from $Cu_{20}Ni_{80}$ using carbon dioxide (100 ml min^{-1}) for extend durations and temperature 800-875 $^{\bullet}$C

The carbon dioxide activation at 900 $^{\circ}$C of CNF from $Fe_{20}Ni_{80}$ was found to be marginally more successful than the CNF from the $Cu_{20}Ni_{80}$ system. Again, the approximately linear carbon burn off relationship was observed. However, the surface area increased slightly with activation, peaking at *ca* 195 $m^2\ g^{-1}$ at 30 min, an increase of 50 $m^2\ g^{-1}$ from the original material. To determine if this could be improved by increased temperature the activations were repeated at 1000 $^{\circ}$C. A similar pattern was observed. However, the surface areas achieved were lower than that of the 900 $^{\circ}$C runs.
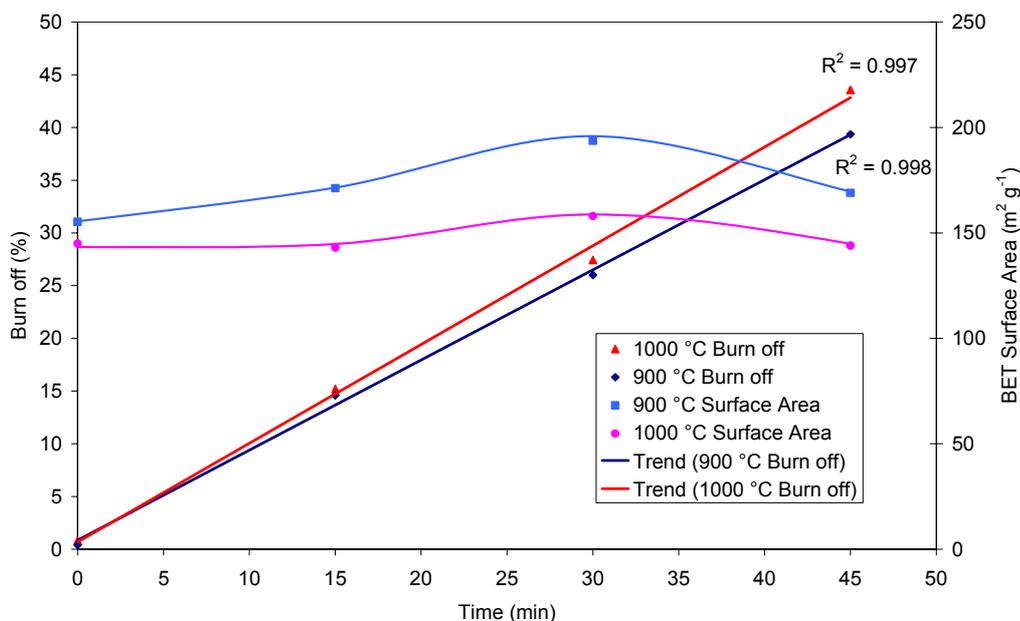
Figure 7-43   The effect of physical activation of CNF from $Fe_{20}Ni_{80}$ using carbon dioxide (100 ml min^{-1}) on nitrogen BET surface area

The precursor CNF and 900 ˚C carbon dioxide activated CNF were examined by SEM to determine the structural effects of the activation (Figure 7-44 and Figure 7-45). There are no major structural changes between the activated and non-activated CNF. The only discernable difference can be seen at high magnification where the surfaces of CNF appear less well defined. Thus, with no large structural observations being made and with the reduced mass recorded by burn off, it was concluded that at 900 ˚C the CNF were being evenly oxidised with no preferential oxidation occurring.
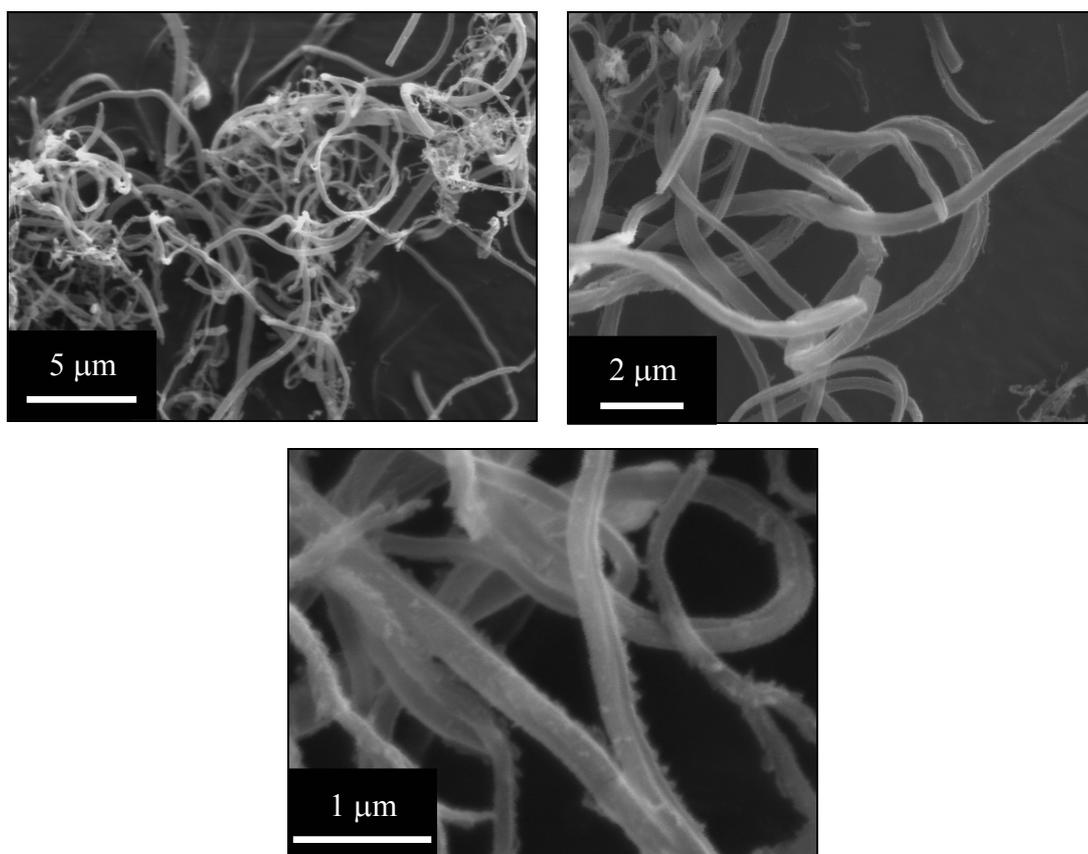
Figure 7-44   **SEM images of CNF from $Cu_{20}Ni_{80}$, after CO_2 activation at 900 ˚C for 30 minutes**
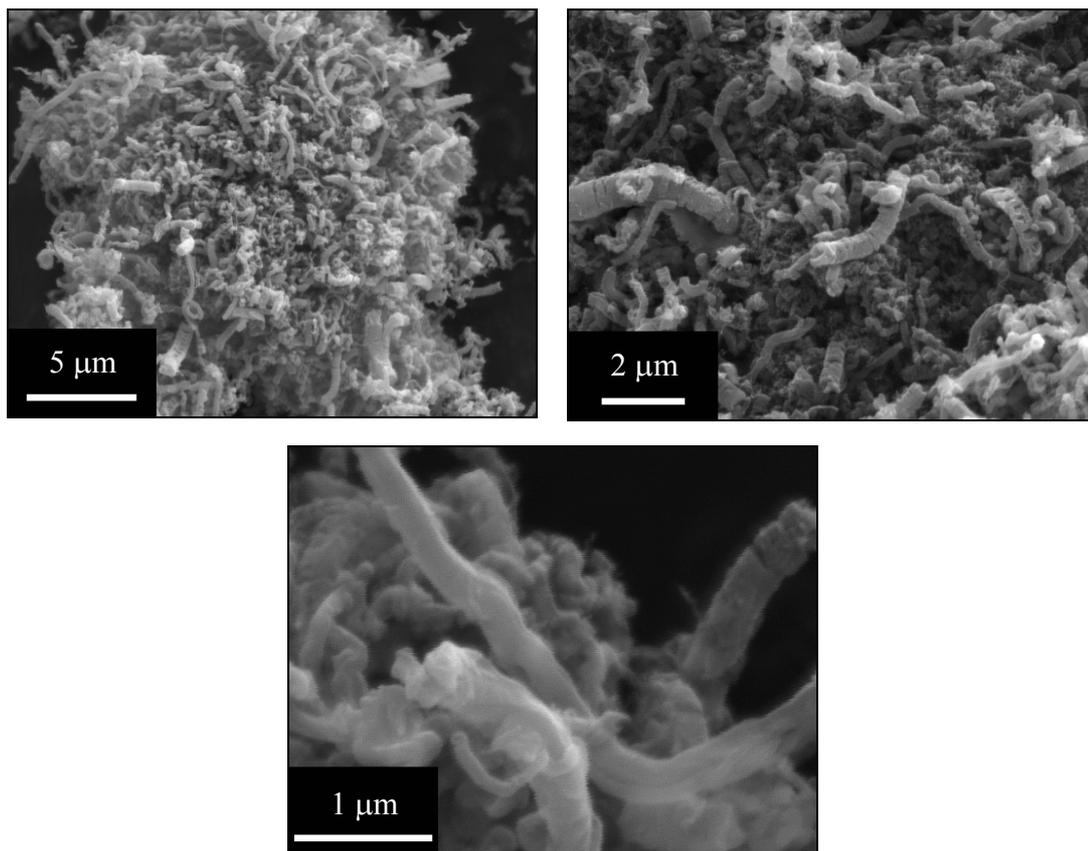
Figure 7-45   SEM images of CNF from Fe$_{20}$Ni$_{80}$, after CO2 activation at 900 ˚C for 30 minutes

The XRD patterns of the precursor CNF and attempted 900 ˚C carbon dioxide activated CNF were recorded in order to determine if any changes in the crystal structure of the materials had occurred (Figure 7-46). The 002 peaks of both the activated samples were reduced, relative to their precursor CNF. This implies that there had been a slight reduction in the crystallinity of the samples. Overall, the patterns of the pre and post activated samples are very similar, which suggests that the structure of the bulk material was largely unchanged by carbon dioxide activation. This was consistent with the observed lack of increased surface area after the activation.
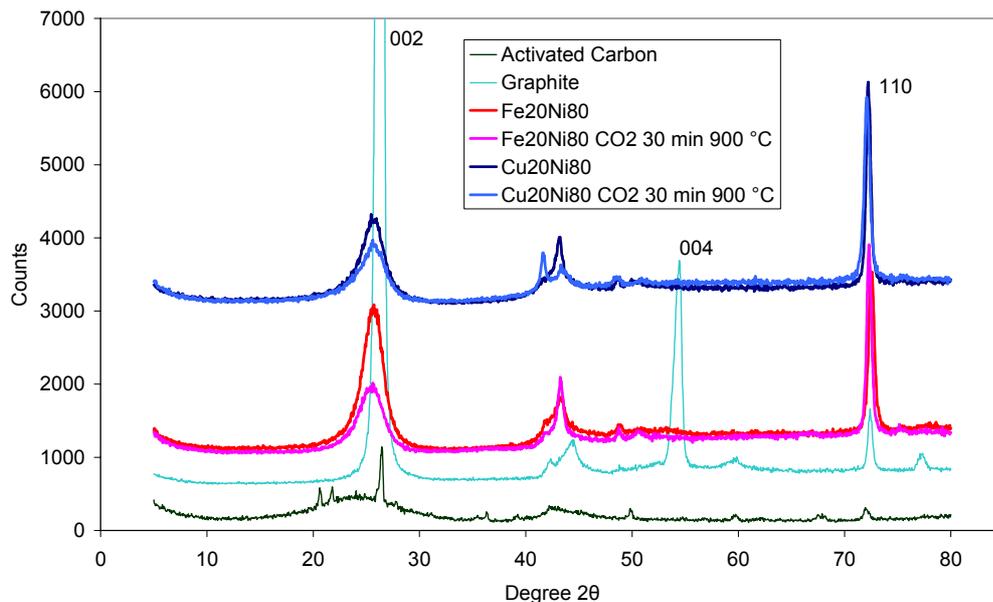
Figure 7-46   XRD patterns of CNF activated by carbon dioxide

The hydrogen sorption capacity of a selection of the CNF prepared using $Cu_{20}Ni_{80}$ and $Fe_{20}Ni_{80}$ activated by carbon dioxide were determined to investigate the effect of carbon dioxide activation on hydrogen sorption capacity. Not all the samples could be analysed because not enough sample was left after activation burn-off for hydrogen sorption determination. The BET surface area increased marginally with increasing time and the hydrogen sorption capacity mostly unchanged (Table 7-10). The extended period actions, although having more success with increased surface area, also failed to display any significant increase in hydrogen storage capacity.

Activation Conditions	H₂ Sorption (wt%)	BET (m² g⁻¹)
As prepared	0.35	475
900 ˚C 15 min	-	472
900 ˚C 30 min	0.26	465
900 ˚C 45 min	0.22	458
800 ˚C 30 min	0.28	476
800 ˚C 120 min	-	488
825 ˚C 30 min	0.31	478
825 ˚C 120 min	0.30	517
825 ˚C 480 min	-	678
850 ˚C 30 min	0.33	482
850 ˚C 120 min	-	521
875 ˚C 30 min	0.27	477
875 ˚C 120 min	-	542

Table 7-10 Hydrogen sorption capacity and BET surface area of $Cu_{20}Ni_{80}$ CNF activated by carbon dioxide at 900 ˚C

The CNF prepared using a $Fe_{20}Ni_{80}$ catalyst and activated by carbon dioxide possessed a much lower surface area than the CNF prepared using $Cu_{20}Ni_{80}$. The hydrogen sorption capacity of the CNF followed a consistent pattern, with sorption observed to be very low, with no increase on activation (Table 7-11).

Activation Conditions	H_2 Sorption (wt%)	BET ($m^2 g^{-1}$)
As prepared	0.07	150
900 °C 15 min	-	171
900 °C 30 min	0.05	194
900 °C 45 min	<0.04	169
1000 °C 15 min	-	143
1000 °C 30 min	0.06	158
1000 °C 45 min	<0.04	144

Table 7-11 Hydrogen sorption capacity, and BET surface area of $Fe_{20}Ni_{80}$ CNF activated by carbon dioxide

7.5.3 Chemical activation

Chemical activation of both CNF produced using $Cu_{20}Ni_{80}$ and $Fe_{20}Ni_{80}$ was found to be successful (Figure 7-47). For CNF from $Cu_{20}Ni_{80}$ activation peaked at 900 °C, at a nitrogen BET surface area of 1000 $m^2 g^{-1}$, which was more than double the original surface area of 475 $m^2 g^{-1}$ and compared well with work reported by Yoon *et al.* (Hwang *et al.*, 2002). Activation of CNF from $Fe_{20}Ni_{80}$ was less successful, achieving a maximum of 230 $m^2 g^{-1}$ between 700 °C and 900 °C, which was an increase of *ca* 80 $m^2 g^{-1}$ compared with the original material.
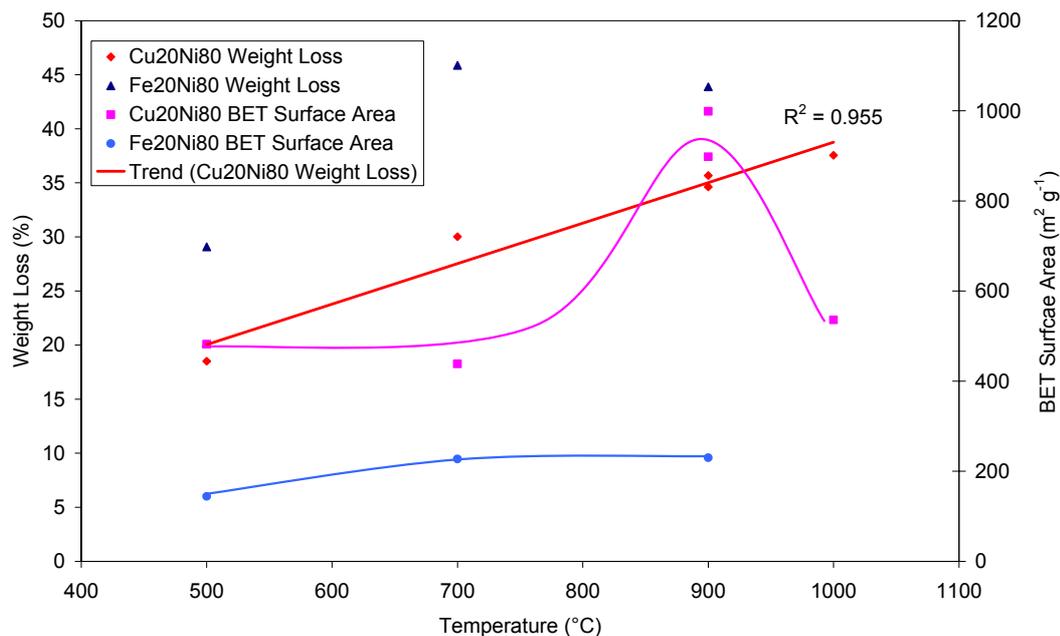
Figure 7-47   The effect of chemical activation of CNF from Cu$_{20}$Ni$_{80}$ and Fe$_{20}$Ni$_{80}$ using potassium hydroxide on nitrogen BET surface area when varying temperature for 30 minutes

In order to optimise the chemical activation process of CNF from Cu$_{20}$Ni$_{80}$ a series of activations were carried out over different time periods (Figure 7-48).   As expected, the weight loss continued to increase with time, as the potassium hydroxide had longer to react with the carbon. However, the nitrogen BET surface area was observed to decrease with longer activation periods, with the original thirty minute period being optimal.
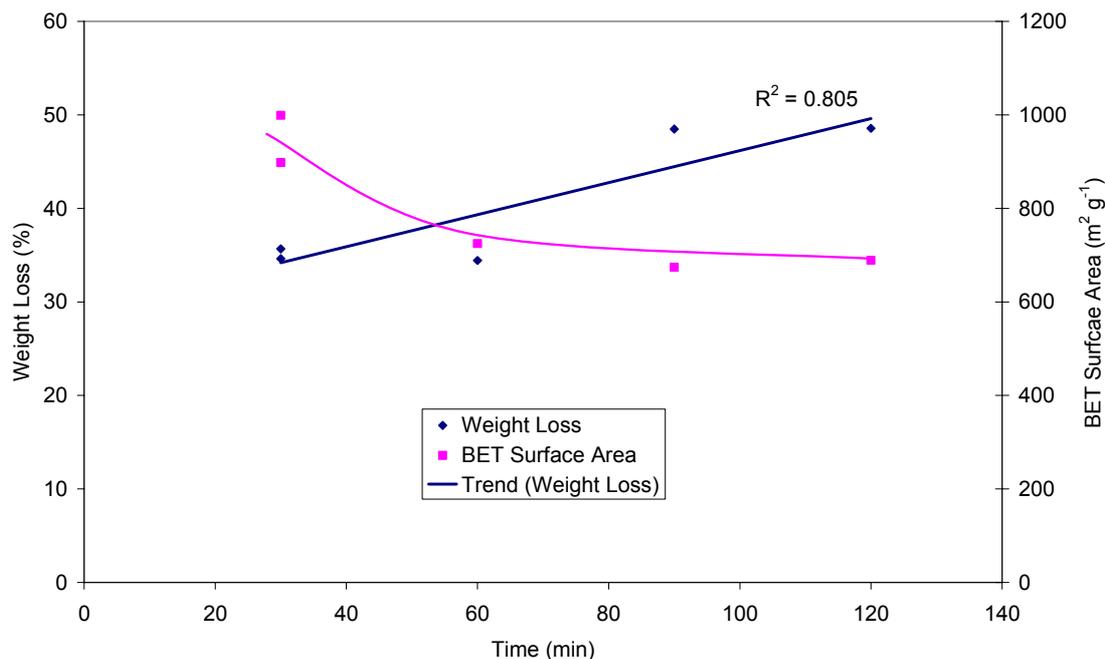
Figure 7-48   **The effect on nitrogen BET surface area of chemical activation of CNF from $Cu_{20}Ni_{80}$ using potassium hydroxide when varying activation time**

The precursor CNF and the potassium hydroxide activated CNF prepared using $Cu_{20}Ni_{80,}$ were examined by SEM to determine the structural effects of the activation (Figure 7-49). After activation the CNF had been heavily eroded with the average length severely reduced and the surfaces heavily etched. This can clearly be seen by comparing the SEM images of the precursor CNF (Figure 7-25) and the potassium hydroxide activated CNF (Figure 7-49). This is consistent with the increased surface area and successful activation.

The precursor CNF and potassium hydroxide activated CNF from $Fe_{20}Ni_{80}$ were examined by SEM to determine the structural effects of the activation (Figure 7-50). A comparison of SEM images of the precursor CNF (Figure 7-20) and the potassium hydroxide activated CNF (Figure 7-50) illustrates that the CNF, after activation, had been so heavily eroded that the original fibrous appearance of the material had been lost. As with the CNF from $Cu_{20}Ni_{80}$, this was consistent with the increased surface area and successful activation.
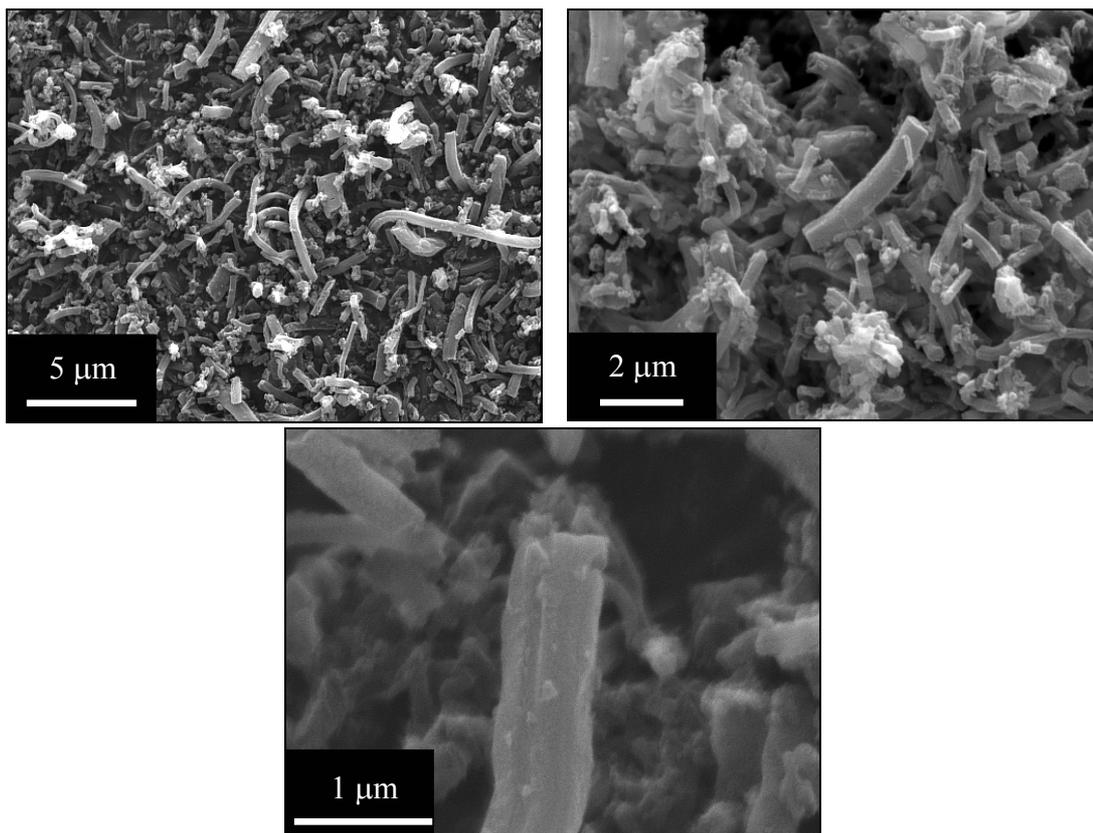
Figure 7-49   SEM images of CNF from Cu$_{20}$Ni$_{80}$ after potassium hydroxide activation
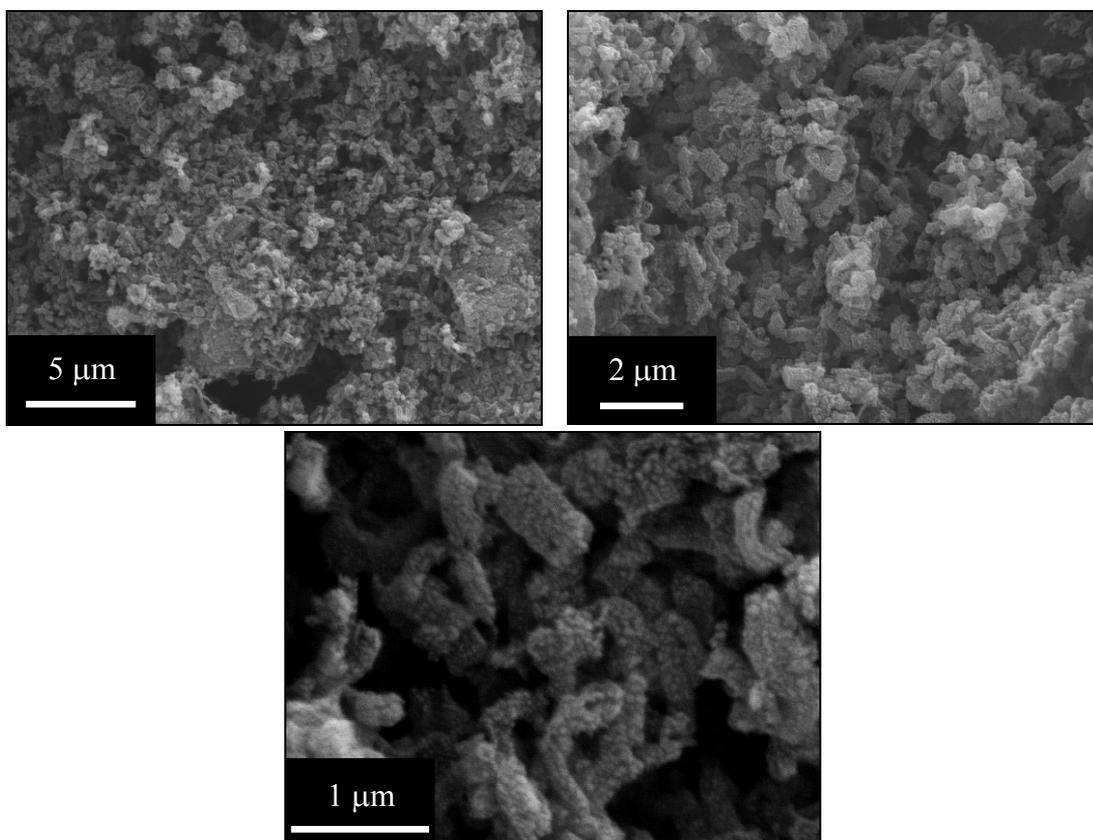
Figure 7-50   SEM images of CNF from Fe$_{20}$Ni$_{80}$ after potassium hydroxide activation

The XRD patterns of the precursor CNF and potassium hydroxide activated CNF were recorded in order to determine if any changes in the crystal structure of the materials had occurred (Figure 7-46). All peaks observed from both the activated samples were greatly diminished relative to those recorded from their precursor CNF, indicative of substantial loss of long range order within the samples.
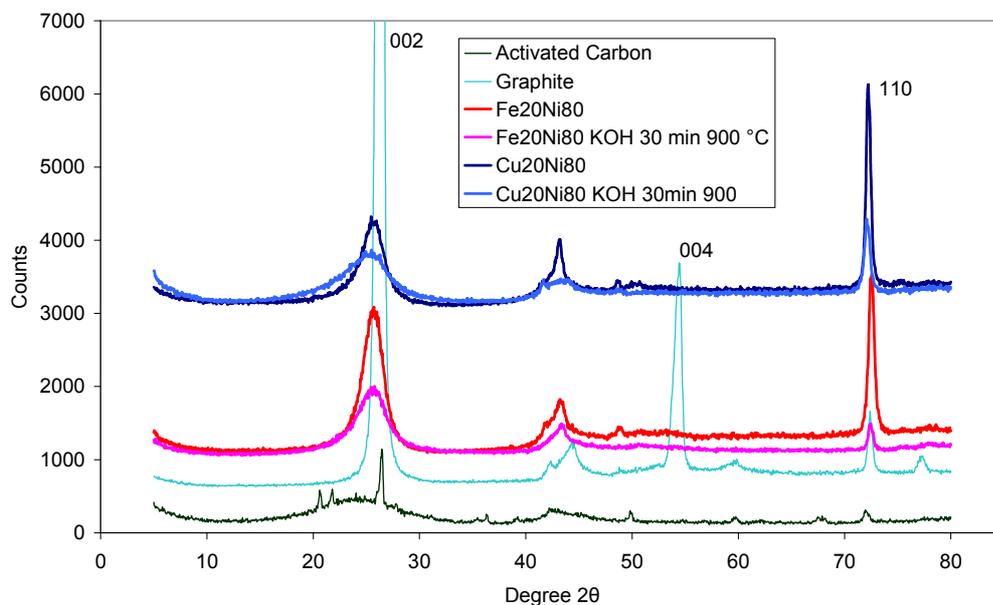
Figure 7-51 XRD patterns of CNF activated by KOH

The hydrogen sorption capacity of the CNF prepared from $Cu_{20}Ni_{80}$ and $Fe_{20}Ni_{80}$ activated by potassium hydroxide at 900 ˚C for 30 min, were determined in order to investigate the effect of chemical activation on hydrogen sorption capacity (Table 7-12). The hydrogen adsorption capacity reduced for CNF produced by $Fe_{20}Ni_{80}$. However, the hydrogen adsorption capacity of CNF prepared from $Cu_{20}Ni_{80}$ increased marginally relative to the original material, but on using the DG3 procedure no further increase in activity was observed. This was a marked difference from the original material, which observed a 0.15 wt% increase.

	Degas	**KOH Activated**	**Original**
$Cu_{20}Ni_{80}$ **CNF**	DG2	0.42	0.35
	DG3	0.40	0.50
$Fe_{20}Ni_{80}$ **CNF**	DG2	<0.05	0.07

Table 7-12 Hydrogen sorption capacities of CNF activated by potassium hydroxide at 900 ˚C for 30 minutes recorded at 100 bar and 30 ˚C after DG2

7.6 Other carbon nanofibre systems

In order to achieve increased hydrogen storage capacities, the use of CNF-metal hydride hybrid systems has been proposed (Hwang *et al.*, 2002). Magnesium hydride has one of the highest hydrogen sorption capacities of the metal hydrides, and, by using a magnesium-nickel catalyst, CNF incorporating magnesium may be grown (Chapter 2). Using this system, and a volumetric adsorption determination method, hydrogen storage capacities of up to 1.4 wt% have been reported.

7.6.1 Magnesium-nickel catalyst prepared carbon nanofibres

Gas conversion was found to be very low for the Mg-Ni catalyst system, with the maximum observed to be 14 % (Figure 7-52). An increase in nickel content of the catalyst was contrasted by a reduction in surface area of the CNF produced.
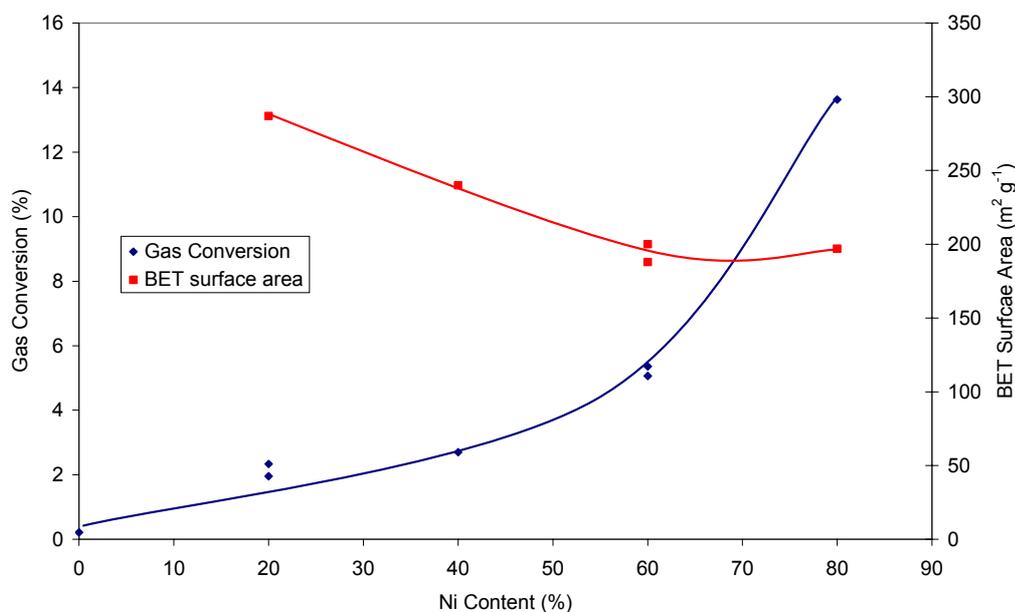
Figure 7-52   Comparison of carbon conversion and BET surface areas of CNF prepared from Mg-Ni catalysts from ethylene-hydrogen (60-240 ml min^{-1}) at 600 $^{\bullet}$C

In order to determine if the gas conversion could be increased by changing the preparation temperature of the CNF, the catalyst $Mg_{40}Ni_{60}$ was used to prepare CNF over a range of temperatures (Figure 7-53). This catalyst was selected, as it achieved the second largest gas conversion, but still possessed a significant percentage of magnesium. The preparation temperature of the CNF was found to have little effect on the level of gas conversion achieved. The BET surface area,

however, of the CNF was affected by temperature of preparation, 500 ˚C producing the CNF with the highest surface area.
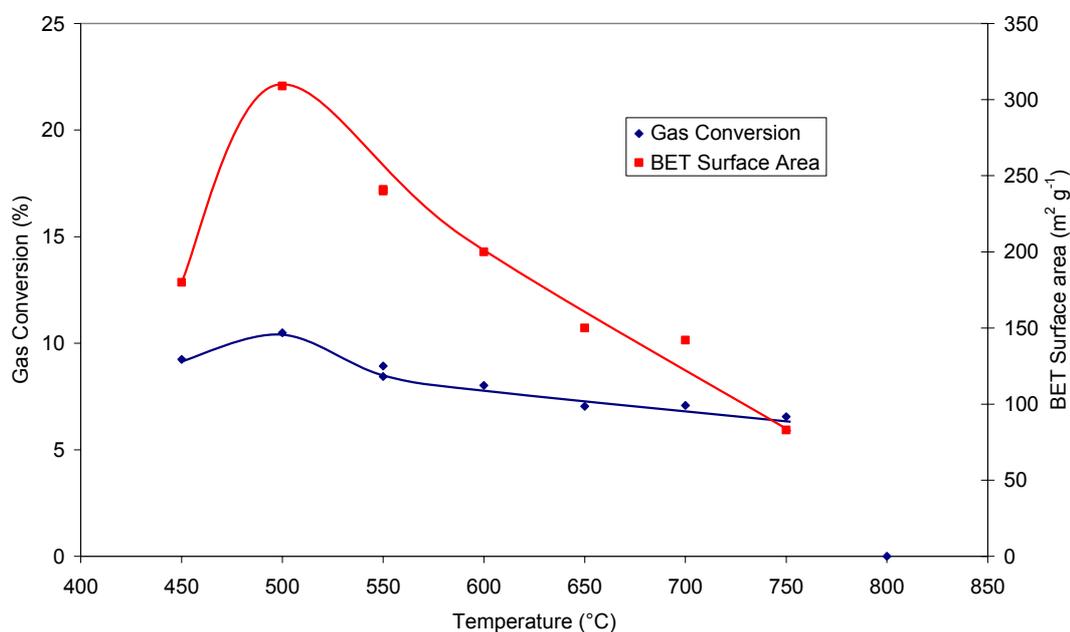
Figure 7-53   **Variation of gas conversion and BET surface area with temperature using a $Mg_{40}Ni_{60}$ catalyst using ethylene-hydrogen (60-240 ml min^{-1})**

The CNF sample prepared over a $Mg_{40}Ni_{60}$ catalyst using ethylene-hydrogen (60-240 ml min^{-1}) was analysed by TEM. The CNF were found to be of heterogeneous form with widths of *ca* 200 nm, (Figure 7-54). The CNF studied had a mixture of platelet and herringbone crystal structures (Figure 7-54 (b)).

(a)   (b)
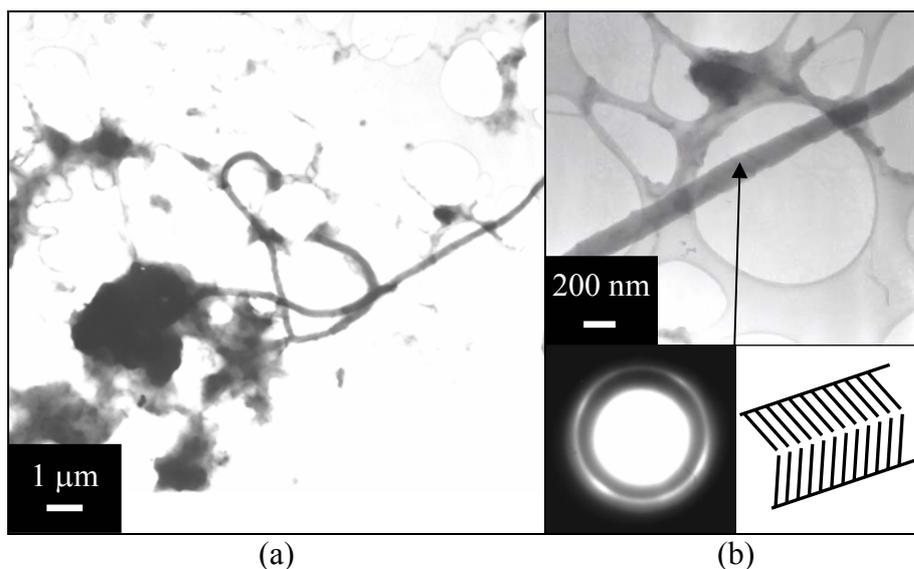
Figure 7-54   **TEM images of CNF from ethylene-hydrogen (60-240 ml min^{-1}), over $Mg_{40}Ni_{60}$ catalyst grown in a quartz reaction vessel at 600 ˚C; (a) low magnification image (b) high magnification image of a CNF, with a diffraction pattern up of a CNF**

The hydrogen storage capacity of two CNF samples, prepared from ethylene-argon (60-240 ml min^{-1}) over $Mg_{20}Ni_{80}$ and $Mg_{40}Ni_{60}$ at 600 ˚C, were analysed (Figure 7-55). The samples were found to fit the profiles of other CNF investigated earlier in this chapter such as $Cu_{20}Ni_{80}$ prepared CNF. Their hydrogen sorption capacities, however, were found to be much lower. Magnesium was present in the $Mg_{20}Ni_{80}$ and $Mg_{40}Ni_{60}$ CNF in concentrations of 0.030 and 0.032 g g^{-1} (catalyst / carbon) respectively. The presence of magnesium in the CNF, however, was observed to have no obvious effect on their hydrogen sorption capacities.
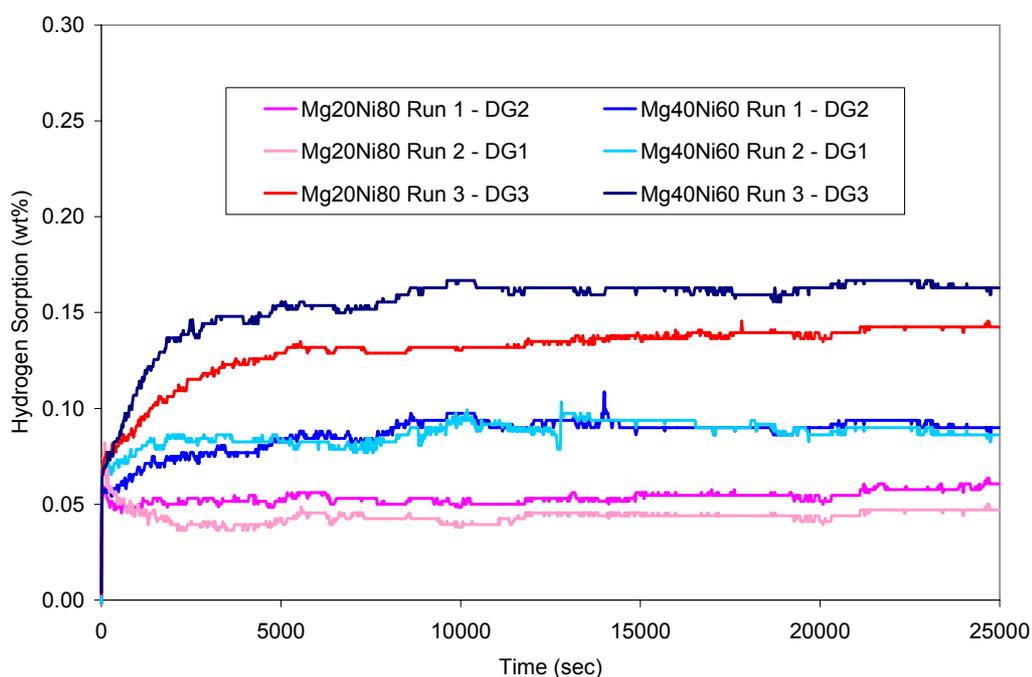
Figure 7-55   The hydrogen adsorption profile of CNF grown from two Mg-Ni catalysts using ethylene-hydrogen (60-240 ml min^{-1}) at 600 ˙C measured at 100 bar and 30 ˙C

7.7 Carbon nanotubes systems

Two samples of commercially prepared CNT were acquired for an explorative study into the hydrogen sorption properties of these materials. MWNT prepared by CVD (1 g; York Point New Energy, China) and SWNT prepared by CVD (1 g; Nanostructured & Amorphous Materials, USA).

7.7.1 Study of Multi-walled nanotubes

The quoted distribution of diameters for the MWNT was 10-40 nm, with a nanotube abundance of 95 %. In order to confirm the quoted properties of the MWNT, a sample was analysed by TEM (Figure 7-56), and observed to contain tubes of diameter *ca* 10 nm.

(a)   (b)
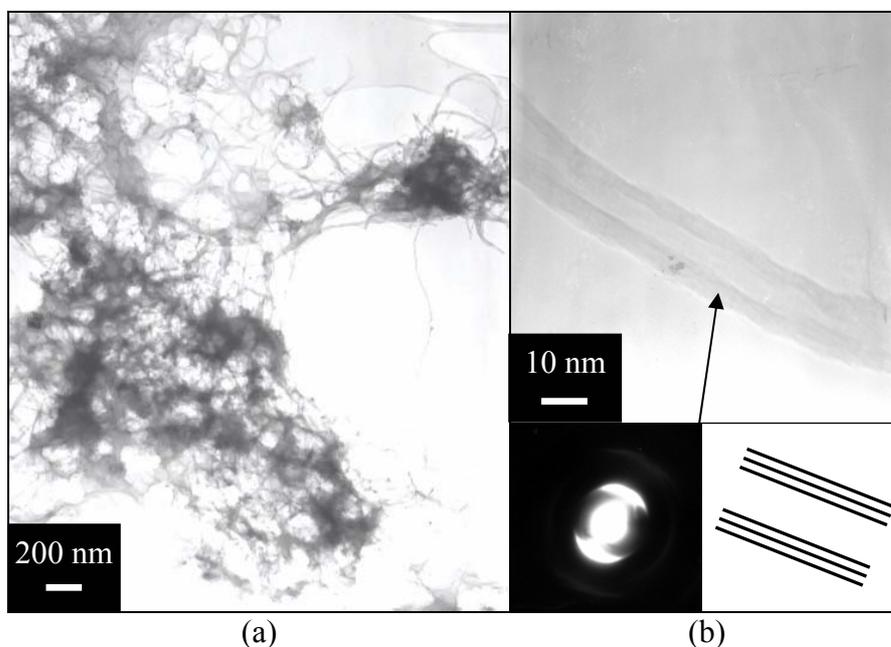
Figure 7-56   TEM images of MWNT; (a) low magnification image (b) high magnification image of a MWNT, with a diffraction pattern of a MWNT

The XRD pattern of the MWNT was recorded, in order to allow comparison with the CNF crystal structure (Figure 7-57). The MWNT were found to have a very similar XRD pattern with the $Cu_{20}Ni_{80}$ CNF and $Fe_{20}Ni_{80}$ CNF, implying that the samples have comparable levels of graphitic character.
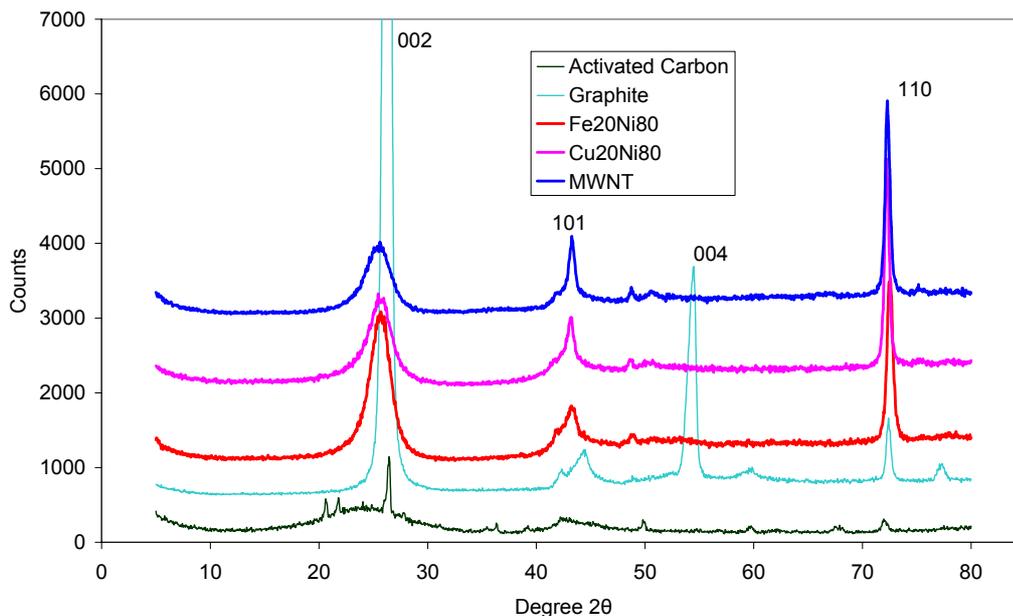
Figure 7-57   XRD patterns of selected CNF and MWNT

The hydrogen storage capacity of MWNT was analysed (Figure 7-58) and was observed to achieve a maximum of 0.3 wt% hydrogen uptake. On cycling, however, the hydrogen storage capacity was found to reduce, independent of the degas method used. The measurement was repeated using a fresh sample of MWNT, and the maximum hydrogen storage capacity observed was 0.26 wt%, again with a reduction of capacity on cycling.
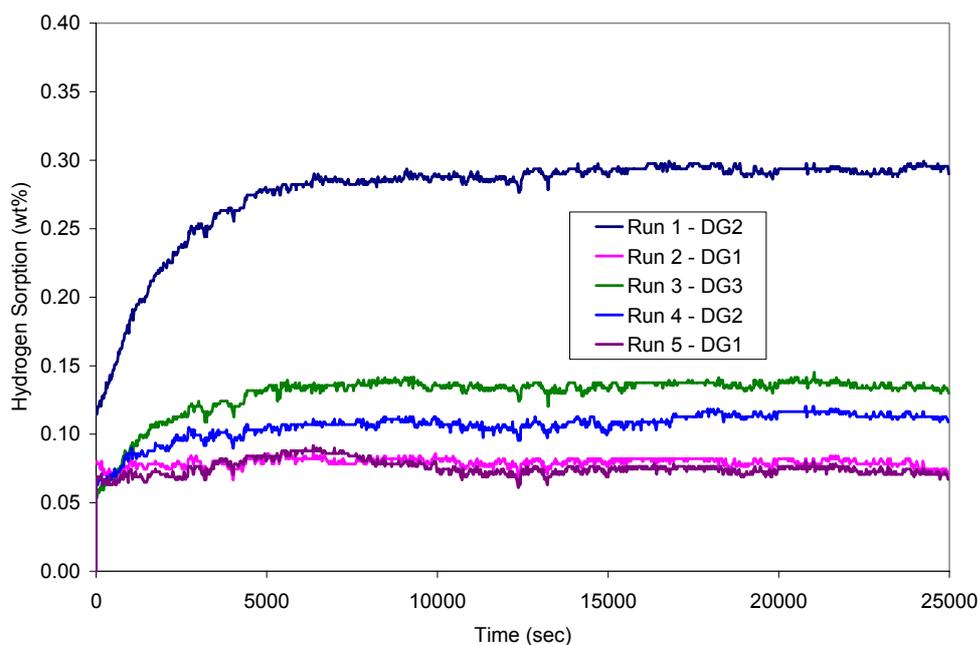
Figure 7-58   The hydrogen adsorption profile of MWNT, recorded at 100 bar and 30 ˚C

7.7.2 Study of single-walled nanotubes

Here the SWNT were quoted to have an abundance purity of *ca* 90 % nanotubes with *ca* 50 % SWNT present in bundles, with a quoted tube diameter of 1-2 nm from HRTEM and lengths of 0.5-100 µm. The SWNT were analysed using HRTEM, which confirmed these characteristics (Figure 7-59).
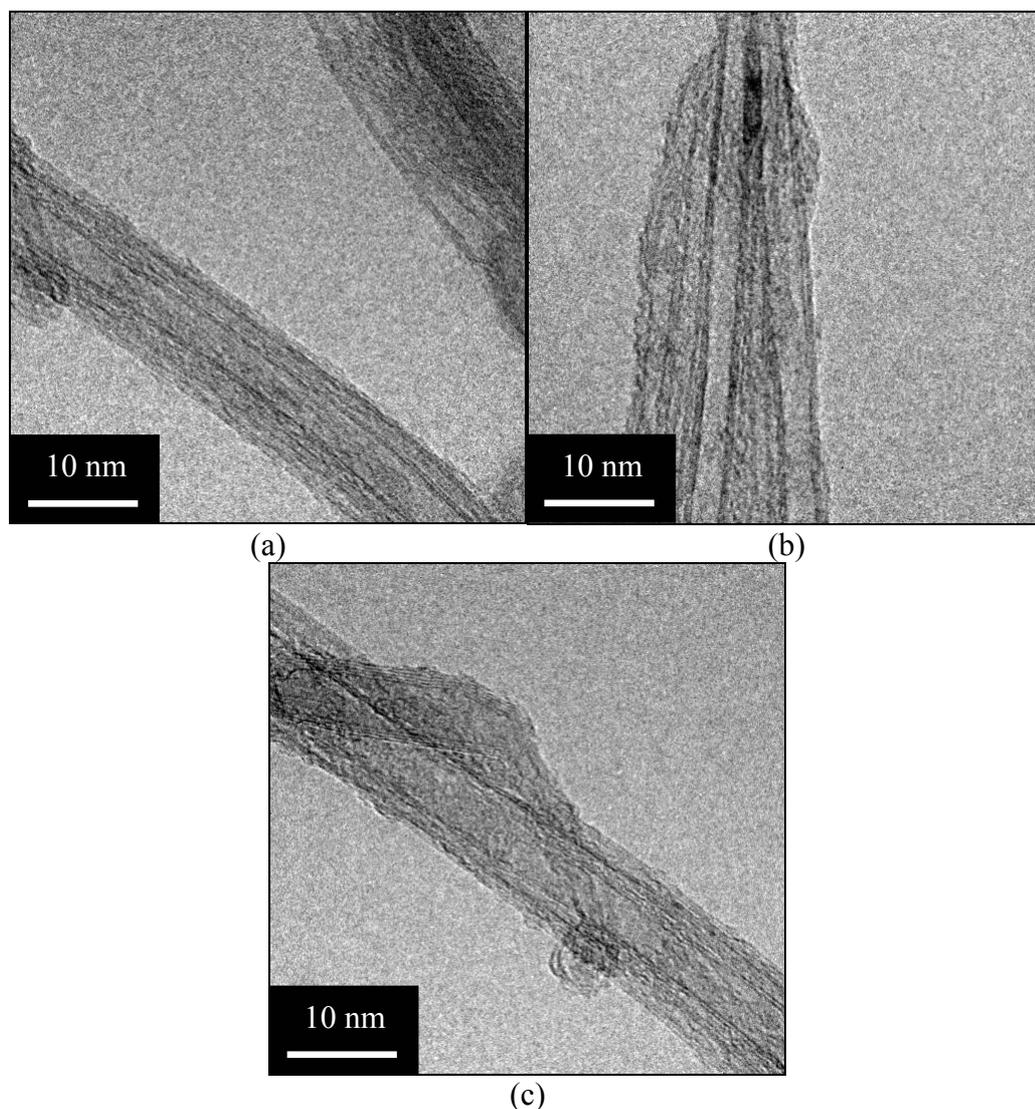
Figure 7-59   HRTEM images of SWNT; (a) & (c) body of tubes (b) tip of a tube

The SWNT were analysed by nitrogen BET and found to possess a surface area of 641 m^2 g^{-1}, which is larger than for any of the other carbon nanomaterials discussed in this thesis. The adsorption-desorption profile suggests the presence of mesopores and macropores in the sample, indicated by the desorption hysteresis loop and significant tail at the end of the adsorption profile, respectively (Figure 7-60).
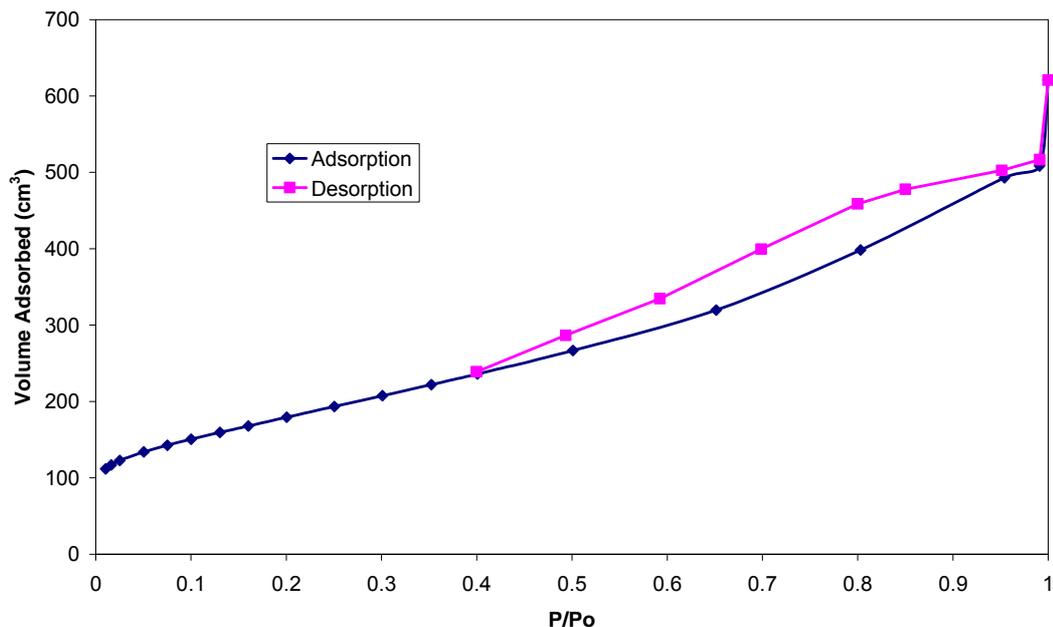
Figure 7-60   **Nitrogen adsorption-desorption profile of SWNT at -196 ˙C**

Further identical samples were analysed for hydrogen sorption capacity (Figure 7-61) and utilised for carbon dioxide activation at low temperature, as this has been reported to significantly enhance CNT uptake characteristics (Andresen *et al.*, 2003). The initial run, after DG2, was observed to achieve a maximum of 0.2 wt%, on repeating, however, an increase to 0.6 wt% was observed, and on further cycling, plateaued at 0.9 wt%. It was hypothesised that this behaviour was caused by the removal of water during each cycle, allowing increased hydrogen sorption each run. The degas temperature was then increased to 300 ˙C, in order to determine whether higher temperature would facilitate improved sorption. A marginal increase was observed, indicating that additional degas was possible, but that the majority of additional adsorbed species had been desorbed. As observed with CNF earlier in this chapter, instantaneous sorption was observed, repeatable using a vacuum degas at ambient temperature, which is believed to correspond to the surface area of the material. The slower adsorption observed for SWNT, after degas at temperature, was significantly larger than for CNF. This additional sorption in CNF was ascribed to hydrogen diffusion between the graphite layers. In SWNT an analogous phenomenon could be hydrogen penetration of the nanotubes through defects in the structure.
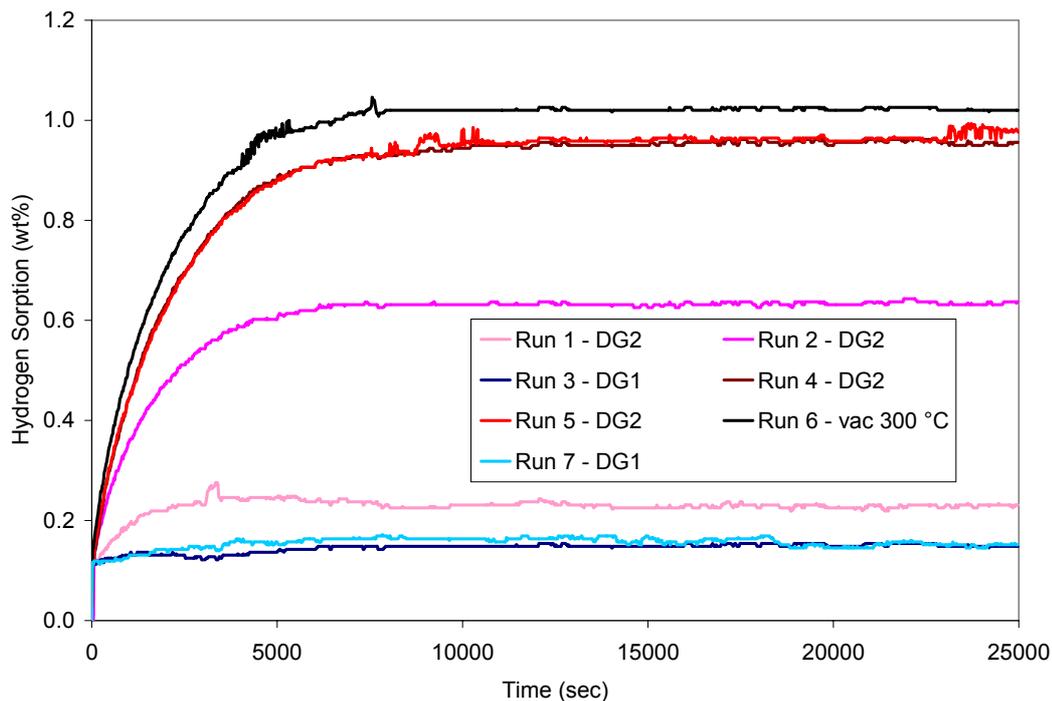
Figure 7-61   **The hydrogen adsorption profile of SWNT recorded at 100 bar and 30 ˚C**

In order to try to improve the hydrogen sorption characteristic of the SWNT, two samples were activated at 550 ˚C for 4 and 16 hours. The surface area, determined by nitrogen BET, was found to increase after 4 hours, but an increase in hydrogen sorption capacity was only observed with the 16 hour activated sample (**Table 7-13**).

Sample	BET Surface Area $(m^2\ g^{-1})$	Hydrogen Sorption (wt%)
Untreated SWNT	641	1.0
SWNT activated at 550 ˚C for 4 hours	758	0.9
SWNT activated at 550 ˚C for 16 hours	780	1.6

Table 7-13   **Nitrogen BET surface area and hydrogen sorption capacities, recorded at 100 bar and 30 ˚C after degassing under vacuum at 300 ˚C, of SWNT activated by carbon dioxide**

The hydrogen sorption capacity of the SWNT, 16 hour carbon dioxide activated, was found to be 1.6 wt%, repeatable through an adsorption-desorption cycle utilising a 300 ˚C degas at vacuum (Figure 7-62). This profile exhibits the same characteristics as the original SWNT, with a period of instantaneous uptake followed by slower sorption of hydrogen. The sample was analysed at a series of

pressures at 20 bar intervals, in order to determine the effect of pressure on hydrogen sorption capacity. The equilibrium time was observed to remain approximately constant with increasing pressure.
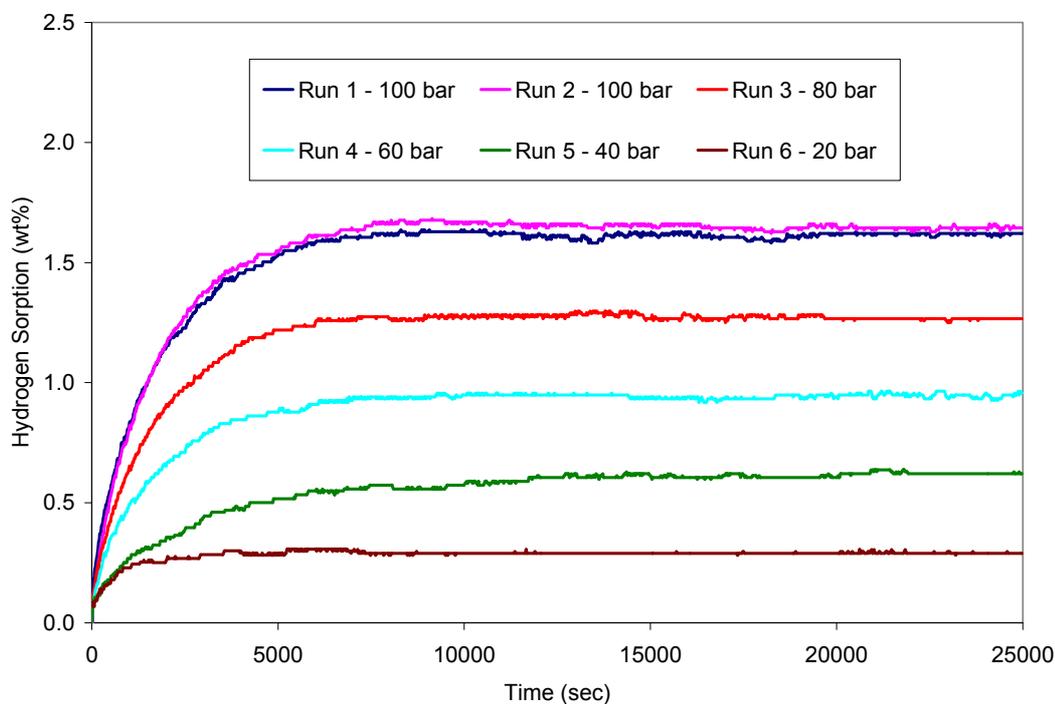
Figure 7-62　The hydrogen adsorption profile of SWNT carbon dioxide activated for 16 hours at 30 ˙C

The isotherm of the hydrogen sorption capacity of the SWNT, activated for 16 hours, displays an approximately linear increase in hydrogen sorption with pressure, with no indication of a plateau (Figure 7-63). From these results it was evident that the isotherm was not complete and analysis at higher pressures was required. However, 100 bar was the upper limit of the operational pressure range of HPAA. If continued above 100 bar, the expected result would be for a knee to be observed in the isotherm, followed by an equilibrium plateau. In addition to this, it was hypothesised that the knee of the isotherm would occur at a significantly higher pressure than 100 bar.
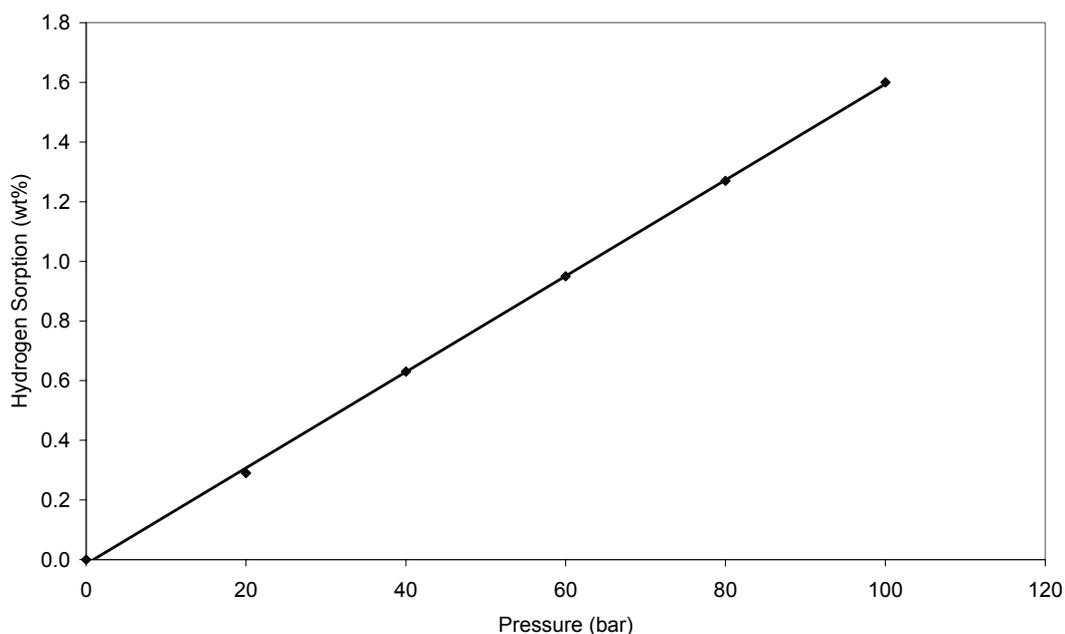
Figure 7-63   The hydrogen adsorption isotherm of SWNT carbon dioxide activated for 16 hours at 30 ˚C

The SWNT sample, activated for 16 hours, was analysed by HRTEM for comparison with the precursor material (Figure 7-64). No obvious changes were observed in the morphology, crystal structure or dimensions of the SWNT after activation. This suggests that the activation causes only subtle changes in the structure of material. It has been hypothesised that activation causes the opening of defects already present in the structure, facilitating the enhanced hydrogen sorption observed relative to the precursor SWNT.

(a)   (b)

(c)   (d)
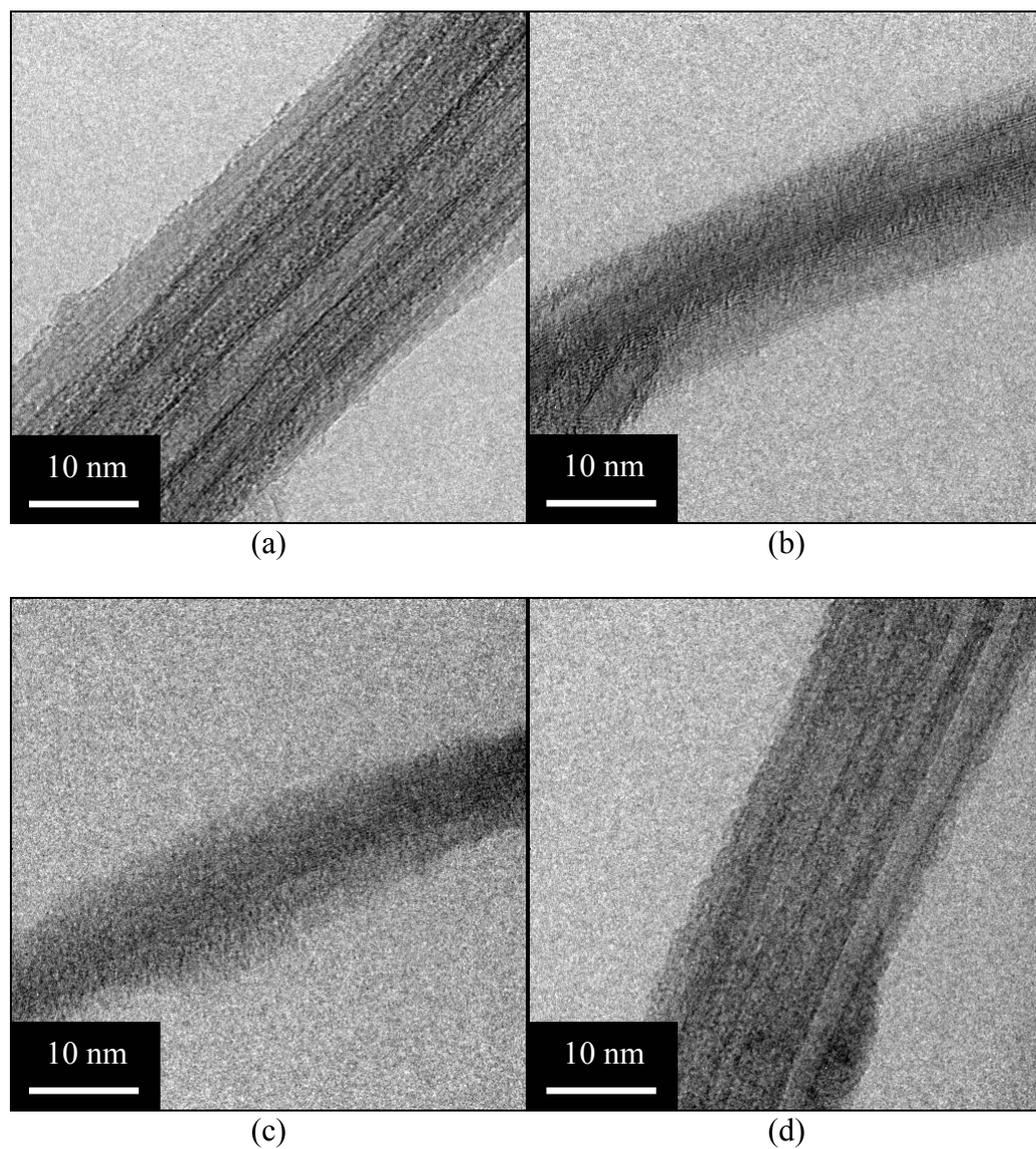
Figure 7-64   HRTEM images of SWNT activated for 16 hours at 550 ˙C

7.8 Comparison of adsorptive properties

The nitrogen BET surface area recorded at -196 ˚C, carbon dioxide DA surface area recorded at 0 ˚C and the hydrogen storage capacity recorded at 30 ˚C of a selection of carbon nanomaterials were determined for comparison (Figure 7-65). A general, increasing, trend of BET surface area with hydrogen sorption capacity was observed. The DA surface area was studied as it was hypothesised that activated diffusion (Chapter 3) would facilitate a stronger correlation between surface area and hydrogen sorption capacity. However, like the BET surface area vs hydrogen sorption relationship, the pattern can only be described as a general trend. This is probably due to the carbon dioxide being considerably larger and more polar than hydrogen, so being attracted to different bonding sites.

Comparison of the DA and BET surface areas of the materials provides insight into their porosity (Chapter 3). For instance, if a material has an ultra-microporous structure, the DA surface area would be expected to be substantially higher than the BET surface area. However, for the materials studied the opposite result is observed. This is indicative of materials with wide micropores, which result in the condensation and pooling of nitrogen when analysed at -196 ˚C, resulting in an erroneous determination of BET surface area.
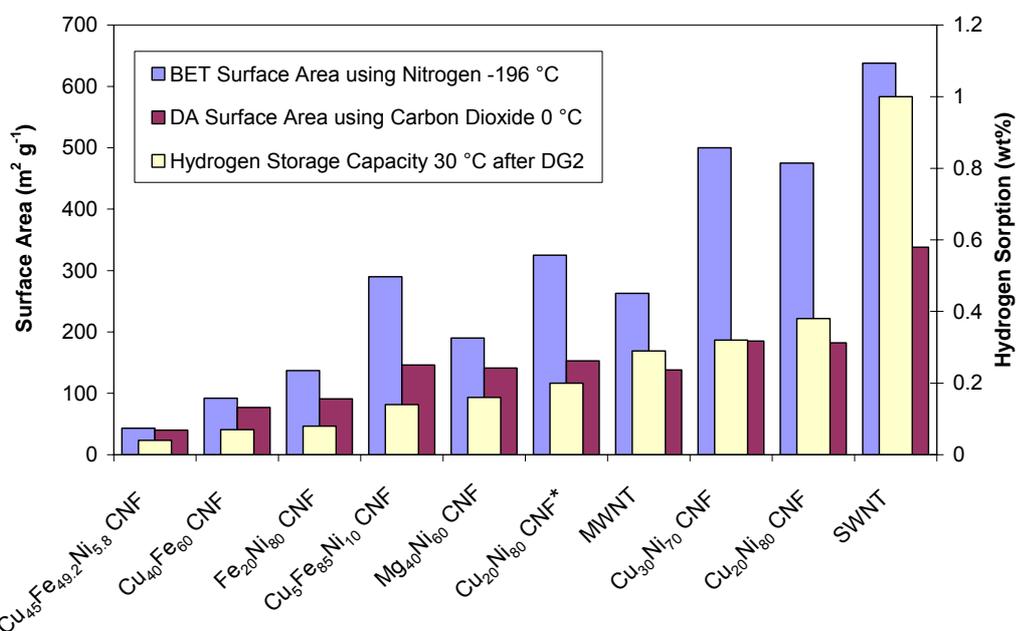
*CNF prepared from ethylene-argon (60-240 ml min^{-1})

Figure 7-65   Comparison of adsorptive properties of a selection of the carbon nanomaterials studied. Unless otherwise stated, the all CNF samples were prepared from ethylene-hydrogen

The trend obtained for data derived from the analysis of hydrogen sorption and surface area of the powdered activated carbons in Chapter 6 was compared with the analysis of the selection of carbon nanomaterials (Figure 7-66). Only one of the materials studied was observed to break the trend by a significant amount, the SWNT sample achieving *ca* 1 wt% sorption. This additional uptake resulted from the slower hydrogen sorption via an unconfirmed mechanism, which occurs after the instantaneous adsorption thought to result from physisorption. This slow uptake is also observed, but to a lesser extent, in many of the CNF. The additional sorption is thought to result from hydrogen slowly diffusing into the SWNT through defects in the structure and between the graphite planes in the CNF.
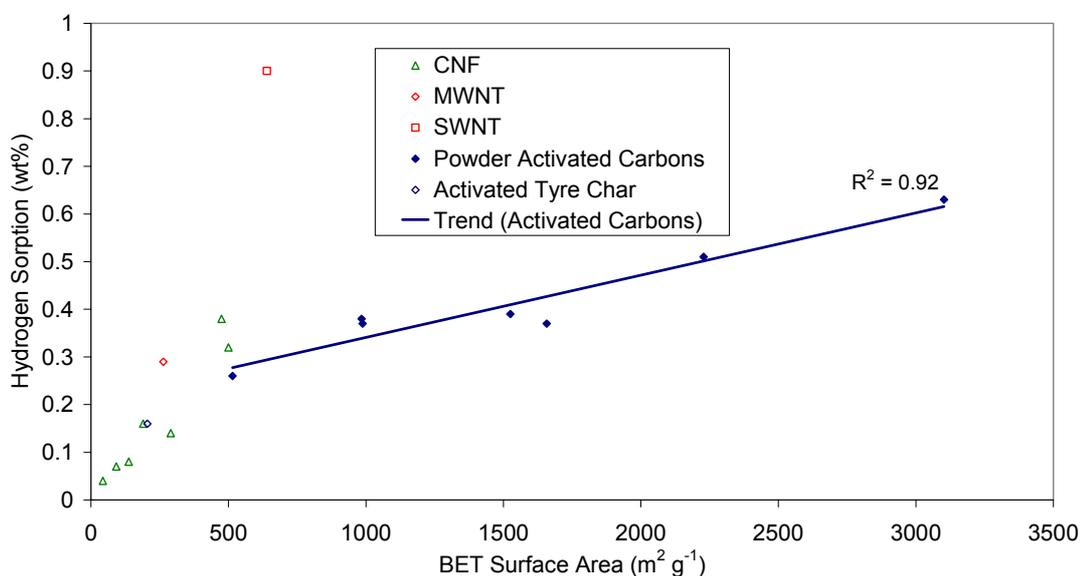
Figure 7-66   Hydrogen sorption properties after DG2 recorded at 30 ˚C and BET nitrogen surface area of the selection of the carbon nanomaterials presented in Figure 7-65 compared with the trend observed for powdered activated carbons described in Chapter 6

7.9 Summary

The preparation of CNF, grown from ethylene over copper, iron and nickel catalysts has been investigated. The catalyst preparation has been tailored to facilitate the production with well-controlled ratios of the three transition metals. The CNF preparation has also be adapted to produce a uniform product, facilitated by the use of hydrogen as an additive gas and the use of a quartz reactor tube.

The Cu-Fe catalyst system was found to afford poor repeatability of CNF preparation with low yields of product. The CNF were found to possess the herringbone structure, the structure favoured in the literature for hydrogen adsorption. However, the hydrogen sorption capacity was found to be very low, less than 0.1 wt%. The Fe-Ni catalyst was found to produce high yields of platelet CNF with good repeatability, and possessing a hydrogen sorption capacity of 0.15 wt%. The Cu-Ni catalyst system produced CNF which possessed the highest surface area of *ca* 500 m^2 g^{-1} and hydrogen storage capacity of 0.5 wt%.

In order, to try to improve the hydrogen storage capacity of the CNF, annealing at high temperature, physical activation and chemical activation were all used, with no significant improvement being observed. However, chemical activation of CNF resulted in a significant increase in BET surface (100 %), with a maximum of *ca* 1000 m^2 g^{-1} being achieved.

Investigations carried out with SWNT yielded the largest uptake of hydrogen for any material discussed in this thesis; the pristine material was observed to have a sorption capacity of *ca* 1 wt%, which increased to 1.6 wt% after carbon dioxide activation at 550 ˚C for 16 hours. This high level of uptake has been hypothesised to result from hydrogen diffusing into the SWNT through defects in structure, which are opened further via the carbon dioxide activation, facilitating additional sorption.

CHAPTER 8
Conclusion and Future Work

8.1 Overview

Overall, this study has provided insight into the field of hydrogen sorption on carbon materials at high pressure and ambient temperature. In addition, this thesis has explored a selection of variables for controlling CNF formation. Chapter 5 details the development of the differential pressure apparatus, whereas Chapter 6 and 7 provide understanding on the sorption of hydrogen on carbon materials.

8.2 Differential pressure method development

The differential pressure method has been developed for the determination of hydrogen sorption capacity of a material at high pressure and ambient temperature. The apparatus has been rigorously tested and evaluated using lanthanide nickel. This evaluation was essential to prove this apparatus as an accurate method of hydrogen sorption determination, free from the ambiguities that have plagued previous results (Darkrim *et al.*, 2002). In order to achieve an accurate, and repeatable, result a helium baseline correction has been proved to be vital. The differential pressure system has also been shown to greatly reduce the effect of small temperature fluctuations of the system on the result.

The apparatus has been proven a versatile piece of apparatus, operating at pressure between 10 and 100 bar. In addition to this, a method has been developed for the analysis of materials at elevated temperatures, demonstrated using lithium nitride as the adsorbent as discussed in Chapter 5.

8.3 Hydrogen sorption on activated carbons

The activated carbons all displayed similar hydrogen sorption properties with uptakes ranging from 0.3 to 0.6 wt%, showing a strong correlation with increasing surface area. The method of degas prior to hydrogen sorption was found to be independent to the hydrogen sorption capacity, which allows adsorption-desorption cycles to be achieved solely by the action of pressure, and indicates that the hydrogen is physisorbed on the carbon. This was supported by the observation that the majority of the hydrogen sorption was almost instantaneous.

8.4 Carbon nanofibre preparation

The preparation of CNF grown from ethylene over copper, iron and nickel catalysts has been extensively investigated. The CNF preparation has also be adapted to produce a uniform product, facilitated by the use of hydrogen as an additive gas and the use of a quartz reactor tube. Close control of the preparation parameters has allowed the controlled formation of CNF, with gas conversions of 0-90 %, surface areas of 10 - 500 m^2 g^{-1}, diameters of 100 - 1000 nm, lengths of 1-10s μm and the formation of herringbone and platelet CNF structures.

8.5 Hydrogen sorption on carbon nanomaterials

The CNF studied were observed to have hydrogen sorption capacities ranging from 0.04-0.5 wt%. The SWNT displayed significantly better uptake, achieving 1 wt%. The amount of hydrogen adsorbed was found to be dependent on the degas method used, indicating that a process other than physisorption may be contributing to the sorption capacity. This process was thought to be due to the diffusion of hydrogen between the graphene layers in CNF or into the SWNT through defects in the structure. However, even with this additional effect, the CNF studied did not achieve the same level of sorption as the activated carbons and a long way removed from the 6.5 to 65 wt% reported in previous studies (Browning *et al.*, 2002; Chambers *et al.*, 1998).

8.6 Final conclusion

High surface area activated carbons displayed ideal characteristics as potential hydrogen adsorbents at ambient temperature cycling by the application and removal of pressure. However, the largest sorption observed, for activated carbons, was still almost an order of magnitude below the commercially viable target set by the US Department of Energy.

The extensive investigation with CNF indicated that comparable levels of hydrogen sorption were achieved with those of activated carbons if the sample was degassed at ambient temperature. However, at higher degas temperature additional slower uptake was observed. The exploratory study with CNT indicated that significantly greater levels of hydrogen sorption could be achieved with SWNT than predicted by the surface area *vs* hydrogen sorption capacity trend observed for activated carbons. Nevertheless, the maximum amount of uptake observed, 1.6 wt% for carbon dioxide activated SWNT, was only a third of the required target of 6.5 wt%. Thus, this study, and concurrent research, are in agreement and indicate that for further research into hydrogen storage on carbons to progress, a radically different approach will be needed if commercial targets are to be reached (Conte *et al.*, 2004; Zhou, 2005).

8.7 Future work

There are several areas that are worthy of additional research in the field of hydrogen storage that have been investigated in this project. In addition to future work on hydrogen storage systems, several possible applications of CNF should be highlighted as avenues for future research.

8.7.1 Hydrogen storage systems

- Dope CNF with lithium using electrolysis
- CNF with high nitrogen content
- Further investigations with Li_3N systems in order to optimise the kinetics of the adsorption and desorption cycle
- Additional research into the activation and enhancement of SWNT
- Further utilisation of HPAA in order to determine the hydrogen storage capacities of solid materials at ambient temperatures and above
- The automation of HPAA for the determination of hydrogen sorption isotherms

8.7.2 Carbon nanofibre applications

- CNF with high nitrogen content for carbon dioxide sequestration
- Study of CNF porosity distribution using DFT
- High surface area CNF as a general cheap adsorbent
- The preparation of CNF as a methane sink, with the extra benefits of being a cheap method of hydrogen production
- CNF as part of a polymer matrix for flame retardant plastics

Bibliography

Aceves, S. M., Martinez-Frias, J., Garcia-Villazana, O. (2000) Analytical and experimental evaluation of insulated pressure vessels for cryogenic hydrogen storage. *International Journal of Hydrogen Energy*, 25, 1075-1085.

Adhyapak, P. V., Maddanimath, T., Pethkar, S., Chandwadkar, A. J., Negi, Y. S., Vijayamohanan, K. (2002) Application of electrochemically prepared carbon nanofibers in supercapacitors. *Journal of Power Sources*, 109, 105-110.

Ahn, C. C., Ye, Y., Ratnakumar, B. V., Witham, C., Bowman, R. C., Fultz, B. (1998) Hydrogen desorption and adsorption measurements on graphite nanofibers. *Applied Physics Letters*, 73, 3378-3380.

Alstrup, I. (1988) A new model explaining carbon-filament growth on Ni, Fe, and Ni-Cu alloy catalysts. *Journal of Catalysis*, 109, 241-251.

Andresen, J. M., Chastain, E. K. (2003) Physical activation of multi-walled carbon nanotubes for hydrogen storage. *Abstracts Of Papers Of The American Chemical Society, Division Fuel Chemistry*, Philadelphia.

Arai, M., Ishikawa, T., Nakayama, T., Nishiyama, Y. (1984) Effects of Metal Support Interaction and Temperature on the Sintering of Pt-Particles and Ag-Particles Supported on Inorganic Solids. *Journal of Colloid and Interface Science*, 97, 254-265.

Atkins, P. W. (1998) *Physical Chemistry*, New York, Freeman.

Attard, G., Barnes, C. (1998) *Surfaces*, Oxford; New York, Oxford University Press.

Audier, M., Guinot, J., Coulon, M., Bonnetain, L. (1981) Formation and characterization of catalytic carbons obtained from co-disproportionation over an iron-nickel catalyst 2-characterization. *Carbon*, 19, 99-105.

Awasthi, K., Kamalakaran, R., Singh, A. K., Srivastava, O. N. (2002) Ball-milled carbon and hydrogen storage. *International Journal of Hydrogen Energy*, 27, 425-432.

Bacsa, R., Laurent, C., Morishima, R., Suzuki, H., Le Lay, M. (2004) Hydrogen storage in high surface area carbon nanotubes produced by catalytic chemical vapor deposition. *Journal of Physical Chemistry B*, 108, 12718-12723.

Badzian, A., Badzian, T., Breval, E., Piotrowski, A. (2001) Nanostructured, nitrogen-doped carbon materials for hydrogen storage. *Thin Solid Films*, 398, 170-174.

Bai, X. D., Zhong, D. Y., Zhang, G. Y., Ma, X. C., Liu, S., Wang, E. G., Chen, Y., Shaw, D. T. (2001) Hydrogen storage in carbon nitride nanobells. *Applied Physics Letters*, 79, 1552-1554.

Baker, R. T. K., Barber, M. A., Harris, P. S., Feates, F. S., Waite, R. J. (1972) Nucleation and growth of carbon deposits from the nickel catalyzed decomposition of acetylene. *Journal of Catalysis*, 28, 51.

Baker, R. T. K., Chludzinski, J. J. (1980) Filamentous carbon growth on nickel-iron surfaces: the effect of various oxide additives. *Journal of Catalysis*, 64, 464.

Baker, R. T. K., Harris, P. S., Thomas, R. B., Waite, R. J. (1973) Formation of filamentous carbon from iron, cobalt and chromium catalyzed decomposition of acetylene. *Journal of Catalysis*, 30, 86-95.

Baker, R. T. K., Waite, R. J. (1975) Formation of carbonaceous deposits from the platinum-iron catalyzed decomposition of acetylene. *Journal of Catalysis*, 37, 101-105.

Bartholomew, C. H. (1982) Carbon Deposition in Steam Reforming and Methanation. *Catalysis Reviews-Science and Engineering*, 24, 67-112.

Benissad, F., Gadelle, P., Coulon, M., Bonnetain, L. (1989) Carbon-fibers from methane 3-impact of catalyst precursors. *Carbon*, 27, 585-592.

Bentzen, J. J., Pedersen, A. S., Kjoller, J. (2001) Screening of hydrogen storage media applying high pressure thermogravimetry. *Journal of Thermal Analysis and Calorimetry*, 64, 859-866.

Bessel, C. A., Laubernds, K., Rodriguez, N. M., Baker, R. T. K. (2001) Graphite nanofibers as an electrode for fuel cell applications. *Journal of Physical Chemistry B*, 105, 1115-1118.

Best, R. J., Walker Russell, W. (1954) Nickel, copper, and some of their alloys as catalysts for ethylene hydrogenation. *Journal of the American Chemical Society*, 76, 838-842.

Bethune, D. S., Kiang, C. H., Devries, M. S., Gorman, G., Savoy, R., Vazquez, J., Beyers, R. (1993) Cobalt-catalyzed growth of carbon nanotubes with single-atomic-layer walls. *Nature*, 363, 605-607.

Boehm, H. P. (1973) Carbon from carbon monoxide disproportionation on nickel and iron catalysts: Morphological studies and possible growth mechanisms. *Carbon*, 11, 583-590.

Boellaard, E., Debokx, P. K., Kock, A., Geus, J. W. (1985) The formation of filamentous carbon on iron and nickel-catalysts 3-morphology. *Journal of Catalysis*, 96, 481-490.

Bogdanovi, B., Schwickardi, M. (1997) Ti-doped alkali metal aluminium hydrides as potential novel reversible hydrogen storage materials. *Journal of Alloys and Compounds*, 253-254, 1-9.

Bonzel, H. P., Ku, R. (1972) Mechanisms of the catalytic carbon monoxide oxidation on Pt (110). *Surface Science*, 33, 91-106.

Bowman, R. C., Witham, C., Fultz, B., Ratnakumar, B. V., Ellis, T. W., Anderson, I. E. (1997) Hydriding behavior of gas-atomized AB(5) alloys. *Journal of Alloys and Compounds*, 253, 613-616.

Browning, D., Jones, P., Packer, K. (1997) An investigation of hydrogen storage methods for fuel cell operation with man-portable equipment. *Journal of Power Sources*, 65, 187-195.

Browning, D. J., Gerrard, M. L., Lakeman, J. B., Mellor, I. M., Mortimer, R. J., Turpin, M. C. (2002) Studies into the storage of hydrogen in carbon nanofibers: Proposal of a possible reaction mechanism. *Nano Letters*, 2, 201-205.

Bruch, L. W., Cole, M. W., Zaremba, E. (1997) *Physical Adsorption: Forces and Phenomena*, Oxford, Clarendon Press.

Brunauer, S., Deming, L. S., Deming, W. E., Teller, E. (1940) On a theory of the van der Waal adsorption of gases. *Journal of the American Chemical Society*, 62, 1723-1732.

Brunauer, S., Teller, E., Emmett, P. H. (1938) Adsorption of Gases multi-molecular layers. *Journal of the American Chemical Society*, 60, 309-319.

Byrne, H. J., Marsh, H. (1995) Origins and structure of porosity. *In* Patrick, J. W. (Ed.) *Porosity in carbons: characterization and applications.* London, Edward Arnold.

Cao, A., Ci, L., Wu, G., Wei, B., Xu, C., Liang, J., Wu, D. (2001a) An effective way to lower catalyst content in well-aligned carbon nanotube films. *Carbon*, 39, 152-155.

Cao, A. Y., Zhu, H. W., Zhang, X. F., Li, X. S., Ruan, D. B., Xu, C. L., Wei, B. Q., Liang, J., Wu, D. H. (2001b) Hydrogen storage of dense-aligned carbon nanotubes. *Chemical Physics Letters*, 342, 510-514.

Chahine, R., Bose, T. K. (1994) Low-pressure adsorption storage of hydrogen. *International Journal of Hydrogen Energy*, 19, 161-164.

Chambers, A., Baker, R. T. K. (1996a) Influence of the nature of the catalyst precursor on the carbon deposition characteristics during ethylene decomposition over copper-cobalt. *Journal of Catalysis*, 158, 356-360.

Chambers, A., Park, C., Baker, R. T. K., Rodriguez, N. M. (1998) Hydrogen storage in graphite nanofibers. *Journal of Physical Chemistry B*, 102, 4253-4256.

Chambers, A., Rodriguez, N. M., Baker, R. T. K. (1996b) Influence of copper on the structural characteristics of carbon nanofibers produced from the cobalt-catalyzed decomposition of ethylene. *Journal of Materials Research*, 11, 430-438.

Chambers, A., Rodriguez, N. M., Baker, R. T. K. (1996c) Influence of silver addition on the catalytic behavior of cobalt. *Journal of Physical Chemistry*, 100, 4229-4236.

Chang, T. S., Rodriguez, N. M., Baker, R. T. K. (1990) Carbon deposition on supported platinum particles. *Journal of Catalysis*, 123, 486-495.

Che, G. L., Lakshmi, B. B., Fisher, E. R., Martin, C. R. (1998) Carbon nanotubule membranes for electrochemical energy storage and production. *Nature*, 393, 346-349.

Che, G. L., Lakshmi, B. B., Martin, C. R., Fisher, E. R. (1999) Metal-nanocluster-filled carbon nanotubes: Catalytic properties and possible applications in electrochemical energy storage and production. *Langmuir*, 15, 750-758.

Chen, P., Wu, X., Lin, J., Tan, K. L. (1999) High hydrogen uptake by alkali-doped carbon nanotubes under ambient pressure and moderate temperatures. *Science*, 285, 91-93.

Chen, P., Xiong, Z. T., Luo, J. Z., Lin, J. Y., Tan, K. L. (2002) Interaction of hydrogen with metal nitrides and imides. *Nature*, 420, 302-304.

Chen, P., Zhang, H. B., Lin, G. D., Hong, Q., Tsai, K. R. (1997) Growth of carbon nanotubes by catalytic decomposition of methane or carbon dioxide on a Ni-MgO catalyst. *Carbon*, 35, 1495-1501.

Chen, Y., Shaw, D. T., Bai, X. D., Wang, E. G., Lund, C., Lu, W. M., Chung, D. D. L. (2001) Hydrogen storage in aligned carbon nanotubes. *Applied Physics Letters*, 78, 2128-2130.

Cheng, H. M., Liu, C., Fan, Y. Y., Li, F., Su, G., Cong, H. T., He, L. L., Liu, M. (2000) Synthesis and hydrogen storage of carbon nanofibers and single-walled carbon nanotubes. *Zeitschrift Fur Metallkunde*, 91, 306-310.

Chitrapu, P., Lund, C. R. F., Tsamopoulos, J. A. (1992) A model for the catalytic growth of carbon filaments. *Carbon*, 30, 285-293.

Ci, L. J., Li, Y. H., Wei, B. Q., Liang, J., Xu, C. L., Wu, D. H. (2000a) Preparation of carbon nanofibers by the floating catalyst method. *Carbon*, 38, 1933-1937.

Ci, L. J., Wei, J. Q., Wei, B. Q., Liang, J., Xu, C. L., Wu, D. H. (2001) Carbon nanofibers and single-walled carbon nanotubes prepared by the floating catalyst method. *Carbon*, 39, 329-335.

Ci, L. J., Zhu, H. W., Wei, B. Q., Xu, C. L., Liang, J., Wu, D. H. (2000b) Graphitization behavior of carbon nanofibers prepared by the floating catalyst method. *Materials Letters*, 43, 291-294.

Ci, L. J., Zhu, H. W., Wei, B. Q., Xu, C. L., Wu, D. H. (2003) Annealing amorphous carbon nanotubes for their application in hydrogen storage. *Applied Surface Science*, 205, 39-43.

Collins, P. G., Zettl, A., Bando, H., Thess, A., Smalley, R. E. (1997) Nanotube nano-device. *Science*, 278, 100-102.

Conte, M., Prosini, P., Passerini, S. (2004) Overview of energy/hydrogen storage: state-of-the-art of the technologies and prospects for nanomaterials. *Materials Science And Engineering B-Solid State Materials For Advanced Technology*, 108, 2-8.

Controls, C. (2003) *www.cal-controls.com* [Accessed 22nd September 2003].

Cracknell, R. F. (2001) Molecular simulation of hydrogen adsorption in graphitic nanofibres. *Physical Chemistry Chemical Physics*, 3, 2091-2097.

Cracknell, R. F. (2002) Simulation of hydrogen adsorption in carbon nanotubes. *Molecular Physics*, 100, 2079-2086.

Cullity, B. D., Stock, S. R. (2001) *Elements of X-ray Diffraction*, Upper Saddle River, NJ, Prentice Hall.

Dagani, R. (2002) Tempest in a tiny tube. *Chemical & Engineering News*, 80, 25-28.

Dai, G. P., Liu, C., Liu, M., Wang, M. Z., Cheng, H. M. (2002) Electrochemical hydrogen storage behavior of ropes of aligned single-walled carbon nanotubes. *Nano Letters*, 2, 503-506.

Darkrim, F., Levesque, D. (1998) Monte Carlo simulations of hydrogen adsorption in single-walled carbon nanotubes. *Journal of Chemical Physics*, 109, 4981-4984.

Darkrim, F., Levesque, D. (2000) High adsorptive property of opened carbon nanotubes at 77 K. *Journal of Physical Chemistry B*, 104, 6773-6776.

Darkrim, F. L., Malbrunot, P., Tartaglia, G. P. (2002) Review of hydrogen storage by adsorption in carbon nanotubes. *International Journal of Hydrogen Energy*, 27, 193-202.

De Jong, K. P., Geus, J. W. (2000) Carbon nanofibers: Catalytic synthesis and applications. *Catalysis Reviews-Science and Engineering*, 42, 481-510.

de la Casa-Lillo, M. A., Lamari-Darkrim, F., Cazorla-Amoros, D., Linares-Solano, A. (2002) Hydrogen storage in activated carbons and activated carbon fibers. *Journal of Physical Chemistry B*, 106, 10930-10934.

Dean, J. R., Metcalfe, E., Ando, D. J., Acol (1997) *Atomic Absorption and Plasma Spectroscopy*, Chichester; New York, Published on behalf of ACOL (University of Greenwich) by John Wiley c1997.

Derbyshire, F., Jagtoyen, M., Thwaites, M. (1995) Activated Carbons - Production and Applications. *In* Patrick, J. W. (Ed.) *Porosity in Carbons: Characterization and Applications.* London, Edward Arnold.

Dillon, A. C., Heben, M. J. (2001) Hydrogen storage using carbon adsorbents: past, present and future. *Applied Physics A-Materials Science & Processing*, 72, 133-142.

Dillon, A. C., Jones, K. M., Bekkedahl, T. A., Kiang, C. H., Bethune, D. S., Heben, M. J. (1997) Storage of hydrogen in single-walled carbon nanotubes. *Nature*, 386, 377-379.

Druck (2004) *www.druck.co.uk* [Accessed 2nd February 2004].

Dubinin, M. M., Radushkevich, L. V. (1947) Equation of the characteristic curve of activated charcoal. *Academy of Sciences*, USSR.

Dynetek (2003) *www.dynetek.com* [Accessed 23rd June 2003].

Ebdon, L., Evans, E. H. (1998) *An Introduction to Analytical Atomic Spectrometry*, Chichester, Wiley.

Edwards, I. A. S. (1989) Structure in Carbons and Carbon Forms. *In* Marsh, H. (Ed.) *Introduction to Carbon Science.* London, Butterworths.

Endo, M., Kim, Y. A., Hayashi, T., Fukai, Y., Oshida, K., Terrones, M., Yanagisawa, T., Higaki, S., Dresselhaus, M. S. (2002) Structural characterization of cup-stacked-type nanofibers with an entirely hollow core. *Applied Physics Letters*, 80, 1267-1269.

Endo, M., Kim, Y. A., Takeda, T., Hong, S. H., Matusita, T., Hayashi, T., Dresselhaus, M. S. (2001) Structural characterization of carbon nanofibers obtained by hydrocarbon pyrolysis. *Carbon*, 39, 2003-2010.

Espinola, A., Miguel, P. M., Salles, M. R., Pinto, A. R. (1986) Electrical-properties of carbons - resistance of powder materials. *Carbon*, 24, 337-341.

Ewe, H., Selbach, H. (1987) *The Storage of Hydrogen*, United Kingdom, Plenum Press.

Fan, Y. Y., Cheng, H. M., Wei, Y. L., Su, G., Shen, Z. H. (2000) Tailoring the diameters of vapor-grown carbon nanofibers. *Carbon*, 38, 921-927.

Fan, Y. Y., Li, F., Cheng, H. M., Su, G., Yu, Y. D., Shen, Z. H. (1998) Preparation, morphology, and microstructure of diameter- controllable vapor-grown carbon nanofibers. *Journal of Materials Research*, 13, 2342-2346.

Fan, Y. Y., Liao, B., Liu, M., Wei, Y. L., Lu, M. Q., Cheng, H. M. (1999) Hydrogen uptake in vapor-grown carbon nanofibers. *Carbon*, 37, 1649-1652.

Flegler, S. L., Heckman, J. W., Klomparens, K. L. (1993) *Scanning and Transmission Electron Microscopy: an Introduction*, New York, W.H. Freeman.

Frackowiak, E., Beguin, F. (2002) Electrochemical storage of energy in carbon nanotubes and nanostructured carbons. *Carbon*, 40, 1775-1787.

Froudakis, G. E. (2001) Hydrogen interaction with single-walled carbon nanotubes: A combined quantum-mechanics/molecular-mechanics study. *Nano Letters*, 1, 179-182.

Froudakis, G. E. (2002) Hydrogen interaction with carbon nanotubes: a review of ab initio studies. *Journal of Physics-Condensed Matter*, 14, R453-R465.

Gadd, G. E., Blackford, M., Moricca, S., Webb, N., Evans, P. J., Smith, A. N., Jacobsen, G., Leung, S., Day, A., Hua, Q. (1997) The world's smallest gas cylinders? *Science*, 277, 933-936.

Gao, B., Kleinhammes, A., Tang, X. P., Bower, C., Fleming, L., Wu, Y., Zhou, O. (1999) Electrochemical intercalation of single-walled carbon nanotubes with lithium. *Chemical Physics Letters*, 307, 153-157.

Gordon, P. A., Saeger, P. B. (1999) Molecular modeling of adsorptive energy storage: Hydrogen storage in single-walled carbon nanotubes. *Industrial & Engineering Chemistry Research*, 38, 4647-4655.

Greenwood, N. N., Earnshaw, A. (1997) *Chemistry of the Elements*, Oxford; Boston, Butterworth-Heinemann.

Gregg, S. J., Sing, K. S. W. (1982) *Adsorption, Surface Area and Porosity*, London; New York, Academic Press.

Gross, K. J., Thomas, G. J., Jensen, C. M. (2002) Catalyzed alanates for hydrogen storage. *Journal of Alloys and Compounds*, 330, 683-690.

Gu, C., Gao, G. H., Yu, Y. X., Mao, Z. Q. (2001) Simulation study of hydrogen storage in single walled carbon nanotubes. *International Journal of Hydrogen Energy*, 26, 691-696.

Guinot, J., Audier, M., Coulon, M., Bonnetain, L. (1981) Formation and characterization of catalytic carbons obtained from co-disproportionation over an iron-nickel catalyst 1-fragmentation and rates of carbon deposition. *Carbon*, 19, 95-98.

Gundiah, G., Govindaraj, A., Rajalakshmi, N., Dhathathreyan, K. S., Rao, C. N. R. (2003) Hydrogen storage in carbon nanotubes and related materials. *Journal of Materials Chemistry*, 13, 209-213.

Gupta, B. K., Srivastava, O. N. (2000) Synthesis and hydrogenation behaviour of graphitic nanofibres. *International Journal of Hydrogen Energy*, 25, 825-830.

Gupta, B. K., Srivastava, O. N. (2001) Further studies on microstructural characterization and hydrogenation behaviour of graphitic nanofibres. *International Journal of Hydrogen Energy*, 26, 857-862.

Higuchi, K., Yamamoto, K., Kajioka, H., Toiyama, K., Honda, M., Orimo, S., Fujii, H. (2002) Remarkable hydrogen storage properties in three-layered Pd/Mg/Pd thin films. *Journal of Alloys and Compounds*, 330, 526-530.

Hirscher, M., Becher, M., Haluska, M., Quintel, A., Skakalova, V., Choi, Y. M., Dettlaff-Weglikowska, U., Roth, S., Stepanek, I., Bernier, P., Leonhardt, A., Fink, J. (2002) Hydrogen storage in carbon nanostructures. *Journal of Alloys and Compounds*, 330, 654-658.

Honda, S., Lee, K. Y., Fujimoto, K., Tsuji, K., Ohkura, S., Katayama, M., Hirao, T., Oura, K. (2002) Formation of carbon nanofiber films by RF magnetron sputtering method. *Physica B-Condensed Matter*, 323, 347-349.

Hou, P. X., Xu, S. T., Ying, Z., Yang, Q. H., Liu, C., Cheng, H. M. (2003) Hydrogen adsorption/desorption behavior of multi-walled carbon nanotubes with different diameters. *Carbon*, 41, 2471-2476.

Hou, P. X., Yang, Q. H., Bai, S., Xu, S. T., Liu, M., Cheng, H. M. (2002) Bulk storage capacity of hydrogen in purified multiwalled carbon nanotubes. *Journal of Physical Chemistry B*, 106, 963-966.

Hu, Y. H., Ruckenstein, E. (2003) Ultrafast reaction between LiH and NH3 during H-2 storage in Li3N. *Journal of Physical Chemistry A*, 107, 9737-9739.

Huang, W. Z., Zhang, X. B., Tu, J. P., Kong, F. Z., Ma, J. X., Liu, F., Lu, H. M., Chen, C. P. (2002) The effect of pretreatments on hydrogen adsorption of multi- walled carbon nanotubes. *Materials Chemistry and Physics*, 78, 144-148.

Huczko, A., Lange, H., Sioda, M., Zhu, Y. Q., Hsu, W. K., Kroto, H. W., Walton, D. R. M. (2002) Hollow cathode plasma synthesis of carbon nanofiber arrays at low temperature. *Journal of Physical Chemistry B*, 106, 1534-1536.

Author (1889) Manufacture of carbon filaments.*212199* UK Patent.

Hwang, J. Y., Lee, S. H., Sim, K. S., Kim, J. W. (2002) Synthesis and hydrogen storage of carbon nanofibers. *Synthetic Metals*, 126, 81-85.

Hynek, S., Fuller, W., Bentley, J. (1997) Hydrogen storage by carbon sorption. *International Journal of Hydrogen Energy*, 22, 601-610.

Ichikawa, T., Isobe, S., Hanada, N., Fujii, H. (2004) Lithium nitride for reversible hydrogen storage. *Journal of Alloys and Compounds*, 365, 271-276.

IEA (1996) *www.eren.doe.gov/hydrogen* [Accessed 25th June 2003].

Iijima, S. (1991) Helical microtubules of graphitic carbon. *Nature*, 354, 56-58.

Iijima, S., Ichihashi, T. (1993) Single-shell carbon nanotubes of 1-nm diameter. *Nature*, 363, 603-605.

Ikuno, T., Ryu, J. T., Oyama, T., Ohkura, S., Baek, Y. G., Honda, S., Katayama, M., Hirao, T., Oura, K. (2002) Characterization of low temperature growth carbon nanofibers synthesized by using plasma enhanced chemical vapor deposition. *Vacuum*, 66, 341-345.

Jacoby, M. (1998) Hydrogen supersponges. *Chemical & Engineering News.*

Jia, Z., Wang, Z., Liang, J., Wei, B., Wu, D. (1999) Production of short multi-walled carbon nanotubes. *Carbon*, 37, 903-906.

Jin, Y. W., Jung, J. E., Park, Y. J., Choi, J. H., Jung, D. S., Lee, H. W., Park, S. H., Lee, N. S., Kim, J. M., Ko, T. Y., Lee, S. J., Hwang, S. Y., You, J. H., Yoo, J. B., Park, C. Y. (2002) Triode-type field emission array using carbon nanotubes and a conducting polymer composite prepared by electrochemical polymerization. *Journal of Applied Physics*, 92, 1065-1068.

Jones, M. D. (2003) *wwwww.bp.com.au/news_information/press_releases* [Accessed 23rd June 2003].

Journet, C., Maser, W. K., Bernier, P., Loiseau, A., delaChapelle, M. L., Lefrant, S., Deniard, P., Lee, R., Fischer, J. E. (1997) Large-scale production of single-walled carbon nanotubes by the electric-arc technique. *Nature*, 388, 756-758.

Kaneko, K. (1989) Effect of temperature on micropore filling of supercritical nitrogen monoxide on iron oxide dispersed activated carbonfibers. *Colloids and Surfaces*, 37, 115-124.

Kibria, A., Mo, Y. H., Park, K. S., Nahm, K. S., Yun, M. H. (2001) Electrochemical hydrogen storage behaviors of CVD, AD and LA grown carbon nanotubes in KOH medium. *International Journal of Hydrogen Energy*, 26, 823-829.

Kim, M. S., Rodriguez, N. M., Baker, R. T. K. (1991) The interaction of hydrocarbons with copper-nickel and nickel in the formation of carbon filaments. *Journal of Catalysis*, 131, 60-73.

Kim, M. S., Rodriguez, N. M., Baker, R. T. K. (1992) The role of interfacial phenomena in the structure of carbon deposits. *Journal of Catalysis*, 134, 253-268.

Kiyobayashi, T., Takeshita, H. T., Tanaka, H., Takeichi, N., Zuttel, A., Schlapbach, L., Kuriyama, N. (2002) Hydrogen adsorption in carbonaceous materials - How to determine the storage capacity accurately. *Journal of Alloys and Compounds*, 330, 666-669.

Koestner, R. J., Frost, J. C., Stair, P. C., Vanhove, M. A., Somorjai, G. A. (1982) Evidence for the formation of stable alkylidyne structures from C3 and C4 unsaturated-hydrocarbons adsorbed on the Pt(111) single-crystal surface. *Surface Science*, 116, 85-103.

Koyama, T. (1972) Formation of carbon fibers from benzene. *Carbon*, 10, 757-758.

Krishnankutty, N., Park, C., Rodriguez, N. M., Baker, R. T. K. (1997) The effect of copper on the structural characteristics of carbon filaments produced from iron catalyzed decomposition of ethylene. *Catalysis Today*, 37, 295-307.

Krishnankutty, N., Rodriguez, N. M., Baker, R. T. K. (1996) Effect of copper on the decomposition of ethylene over an iron catalyst. *Journal of Catalysis*, 158, 217-227.

Kroto, H. W., Heath, J. R., Obrien, S. C., Curl, R. F., Smalley, R. E. (1985) C-60 - Buckminsterfullerene. *Nature*, 318, 162-163.

Laby, T. H., Kaye, G. W. C. (1973) *Tables of Physical and Chemical Constants*, London, Longman.

Lamber, R., Jaeger, N., Schulzekloff, G. (1988) Electron-microscopy study of the interaction of Ni, Pd and Pt with carbon 1-nickel catalyzed graphitization of amorphous carbon. *Surface Science*, 197, 402-414.

Langmuir, I. (1916) The constitution and fundamental properties of solids and liquids. *Journal of the American Chemical Society*, 38, 2221-2295.

Langmuir, I. (1918) The adsorption of gases on plane surfaces of glass, mica and platinum. *Journal of the American Chemical Society*, 40, 1361-1405.

Lee, C. J., Lee, T. J., Park, J. (2001a) Carbon nanofibers grown on sodalime glass at 500 degrees C using thermal chemical vapor deposition. *Chemical Physics Letters*, 340, 413-418.

Lee, C. J., Lyu, S. C., Kim, H. W., Park, C. Y., Yang, C. W. (2002a) Large-scale production of aligned carbon nanotubes by the vapor phase growth method. *Chemical Physics Letters*, 359, 109-114.

Lee, E. C., Kim, Y. S., Jin, Y. G., Chang, K. J. (2002b) First-principles study of hydrogen adsorption on carbon nanotube surfaces. *Physical Review B*, 66, art. no.-073415.

Lee, S. M., An, K. H., Kim, W. S., Lee, Y. H., Park, Y. S., Seifert, G., Frauenheim, T. (2001b) Hydrogen storage in carbon nanotubes. *Synthetic Metals*, 121, 1189-1190.

Lee, S. M., An, K. H., Lee, Y. H., Seifert, G., Frauenheim, T. (2001c) A hydrogen storage mechanism in single-walled carbon nanotubes. *Journal of the American Chemical Society*, 123, 5059-5063.

Lee, S. M., Lee, Y. H. (2000a) Hydrogen storage in single-walled carbon nanotubes. *Applied Physics Letters*, 76, 2877-2879.

Lee, S. M., Park, K. S., Choi, Y. C., Park, Y. S., Bok, J. M., Bae, D. J., Nahm, K. S., Choi, Y. G., Yu, S. C., Kim, N. G., Frauenheim, T., Lee, Y. H. (2000b) Hydrogen adsorption and storage in carbon nanotubes. *Synthetic Metals*, 113, 209-216.

Levesque, D., Gicquel, A., Darkrim, F. L., Kayiran, S. B. (2002) Monte Carlo simulations of hydrogen storage in carbon nanotubes. *Journal of Physics-Condensed Matter*, 14, 9285-9293.

Li, X. S., Zhu, H. W., Ci, L. J., Xu, C. L., Mao, Z. Q., Wei, B. Q., Liang, J., Wu, D. H. (2001) Hydrogen uptake by graphitized multi-walled carbon nanotubes under moderate pressure and at room temperature. *Carbon*, 39, 2077-2079.

Lide, D. R. (2003) *CRC Handbook of Chemistry and Physics*, Boca Raton, CRC Press.

Liu, C., Fan, Y. Y., Liu, M., Cong, H. T., Cheng, H. M., Dresselhaus, M. S. (1999) Hydrogen storage in single-walled carbon nanotubes at room temperature. *Science*, 286, 1127-1129.

Lueking, A., Yang, R. T. (2002) Hydrogen spillover from a metal oxide catalyst onto carbon nanotubes - Implications for hydrogen storage. *Journal of Catalysis*, 206, 165-168.

Lueking, A., Yang, R. T. (2003) Hydrogen storage in carbon nanotubes: Residual metal content and pretreatment temperature. *AIChE Journal*, 49, 1556-1568.

Lueking, A. D., Yang, R. T., Rodriguez, N. M., Baker, R. T. K. (2004) Hydrogen storage in graphite nanofibers: Effect of synthesis catalyst and pretreatment conditions. *Langmuir*, 20, 714-721.

Luo, S., Clewley, J. D., Flanagan, T. B., Bowman, R. C., Wade, L. A. (1998) Further studies of the isotherms of LaNi$_5$-xSn$_x$-H for x=0-0.5. *Journal of Alloys and Compounds*, 267, 171-181.

Lupu, D., Biris, A. R., Misan, I., Lupsa, N., Biris, A. S., Buzatu, D. A., Kleeve, M. (2002) Growth of nanoscale carbon structures and their corresponding hydrogen uptake properties. *Particulate Science and Technology*, 20, 225-234.

Luxembourg, D., Flamant, G., Guillot, A., Laplaze, D. (2004) Hydrogen storage in solar produced single-walled carbon nanotubes. *Materials Science And Engineering B-Solid State Materials For Advanced Technology*, 108, 114-119.

Ma, Y. C., Xia, Y. Y., Zhao, M. W., Wang, R. J., Mei, L. M. (2001) Effective hydrogen storage in single-wall carbon nanotubes. *Physical Review B*, 6311, art. no.-115422.

Ma, Y. C., Xia, Y. Y., Zhao, M. W., Ying, M. J. (2002) Hydrogen storage capacity in single-walled carbon nanotubes. *Physical Review B*, 65, art. no.-155430.

Maddox, M. W., Gubbins, K. E. (1994) Molecular simulation of fluid adsorption in buckytubes and MCM- 41. *International Journal of Thermophysics*, 15, 1115-1123.

Maddox, M. W., Gubbins, K. E. (1995) Molecular simulation of fluid adsorption in buckytubes. *Langmuir*, 11, 3988-3996.

Marksberry, A. (2004) *www.caer.uky.edu/carbon/history/carbonhistory.shtml* [28th February 2004].

McAlister, R. (1999) Solar hydrogen: powering the new millennium. *Natural Science*, 164-172.

McEnaney, B. (2002) Properties of activated carbons. *In* Schüth, F., Sing, K. S. W., Weitkamp, J. (Eds.) *Handbook of porous solids.* Weinheim, Wiley-VCH.

McEnaney, B. (2003) Go further with H_2. *Chemistry in Britain*, 39, 24-26.

McNicol, D. M. (1913) *American telegraph practice; a complete technical course in modern telegraphy, including simultaneous telegraphy and telephony*, New York, McGraw-Hill Book Company.

Meguro, T., Torikai, N., Watanabe, N., Tomizuka, I. (1985) Application of the Dubinin-Radushkevich equation to iodine adsorption by activated carbons from aqueous solution. *Carbon*, 23, 137-140.

Melechko, A. V., Merkulov, V. I., Lowndes, D. H., Guillorn, M. A., Simpson, M. L. (2002) Transition between 'base' and 'tip' carbon nanofiber growth modes. *Chemical Physics Letters*, 356, 527-533.

Mellor, I. (2003) *Blackman, J. M.* [Personal Communication Received 11th March 2003].

Meregalli, V., Parrinello, M. (2001) Review of theoretical calculations of hydrogen storage in carbon-based materials. *Applied Physics A-Materials Science & Processing*, 72, 143-146.

Merkulov, V., Melechko, A. V., Guillorn, M. A., Lowndes, D. H., Simpson, M. L. (2002a) Growth rate of plasma-synthesized vertically aligned carbon nanofibers. *Chemical Physics Letters*, 361, 492-498.

Merkulov, V. I., Hensley, D. K., Melechko, A. V., Guillorn, M. A., Lowndes, D. H., Simpson, M. L. (2002b) Control mechanisms for the growth of isolated vertically aligned carbon nanofibers. *Journal of Physical Chemistry B*, 106, 10570-10577.

Merkulov, V. I., Melechko, A. V., Guillorn, M. A., Lowndes, D. H., Simpson, M. L. (2001) Alignment mechanism of carbon nanofibers produced by plasma-enhanced chemical-vapor deposition. *Applied Physics Letters*, 79, 2970-2972.

Merkulov, V. I., Melechko, A. V., Guillorn, M. A., Lowndes, D. H., Simpson, M. L. (2002c) Effects of spatial separation on the growth of vertically aligned carbon nanofibers produced by plasma-enhanced chemical vapor deposition. *Applied Physics Letters*, 80, 476-478.

Merkulov, V. I., Melechko, A. V., Guillorn, M. A., Simpson, M. L., Lowndes, D. H., Whealton, J. H., Raridon, R. J. (2002d) Controlled alignment of carbon nanofibers in a large-scale synthesis process. *Applied Physics Letters*, 80, 4816-4818.

Motojima, S., Kawaguchi, M., Nozaki, K., Iwanaga, H. (1991) Preparation of coiled carbon-fibers by catalytic pyrolysis of acetylene, and its morphology and extension characteristics. *Carbon*, 29, 379-385.

Nikolaev, P., Bronikowski, M. J., Bradley, R. K., Rohmund, F., Colbert, D. T., Smith, K. A., Smalley, R. E. (1999) Gas-phase catalytic growth of single-walled carbon nanotubes from carbon monoxide. *Chemical Physics Letters*, 313, 91-97.

Niu, C. M., Sichel, E. K., Hoch, R., Moy, D., Tennent, H. (1997) High power electrochemical capacitors based on carbon nanotube electrodes. *Applied Physics Letters*, 70, 1480-1482.

Oberlin, A., Endo, M., Koyama, T. (1976) Filamentous growth of carbon through benzene decomposition. *Journal of Crystal Growth*, 32, 335-349.

Oh, S. G., Baker, R. T. K. (1991) Insitu electron-microscopy investigation of the behavior of supported cobalt particles. *Journal of Catalysis*, 128, 137-147.

Ohkawara, Y., Ohshio, S., Suzuki, T., Yatsui, K., Ito, H., Saitoh, H. (2002) Hydrogen storage in amorphous phase of hydrogenated carbon nitride. *Japanese Journal of Applied Physics Part 1-Regular Papers Short Notes & Review Papers*, 41, 7508-7509.

Orimo, S., Matsushima, T., Fujii, H., Fukunaga, T., Majer, G. (2001) Hydrogen desorption property of mechanically prepared nanostructured graphite. *Journal of Applied Physics*, 90, 1545-1549.

Owens, W. T., Rodriguez, N. M., Baker, R. T. K. (1992) Carbon-filament growth on platinum catalysts. *Journal of Physical Chemistry*, 96, 5048-5053.

Park, C., Anderson, P. E., Chambers, A., Tan, C. D., Hidalgo, R., Rodriguez, N. M. (1999) Further studies of the interaction of hydrogen with graphite nanofibers. *Journal of Physical Chemistry B*, 103, 10572-10581.

Park, C., Baker, R. T. K. (1998) Carbon deposition on iron-nickel during interaction with ethylene-hydrogen mixtures. *Journal of Catalysis*, 179, 361-374.

Park, C., Keane, M. A. (2001) Controlled growth of highly ordered carbon nanofibers from Y zeolite supported nickel catalysts. *Langmuir*, 17, 8386-8396.

Pattabiraman, P., Rodriguez, N. M., Jang, B. Z., Baker, R. T. K. (1990) A study of the interaction of atomic oxygen with various carbonaceous materials. *Carbon*, 28, 867-878.

Perry, R. H., Green, D. W., Maloney, J. O. (1997) *Perry's Chemical Engineers' handbook*, New York, McGraw-Hill.

Peschka, W. (1992) *Liquid hydrogen Fuel For the Future*, New York, Springer-Verlag.

Peschka, W. (1998) Hydrogen: The future cryofuel in internal combustion engines. *International Journal of Hydrogen Energy*, 23, 27-43.

Pham-Huu, C., Keller, N., Roddatis, V. V., Mestl, G., Schlogl, R., Ledoux, M. J. (2002) Large scale synthesis of carbon nanofibers by catalytic decomposition

of ethane on nickel nanoclusters decorating carbon nanotubes. *Physical Chemistry Chemical Physics*, 4, 514-521.

Pico (2004) *www.picotech.com* [Accessed 28th January 2004].

Pinkerton, F. E., Wicke, B. G., Olk, C. H., Tibbetts, G. G., Meisner, G. P., Meyer, M. S., Herbst, J. F. (2000) Thermogravimetric measurement of hydrogen absorption in alkali- modified carbon materials. *Journal of Physical Chemistry B*, 104, 9460-9467.

Poirier, E., Chahine, R., Bose, T. K. (2001) Hydrogen adsorption in carbon nanostructures. *International Journal of Hydrogen Energy*, 26, 831-835.

Pradhan, B. K., Harutyunyan, A., Eklund, P. (2002) Hydrogen storage in carbon nanomaterials at low temperature. *Abstracts of Papers of the American Chemical Society*, 224, 024.

Quantum (2003) *www.qtww.com* [Accessed 23rd June 2003].

Ren, Z. F., Huang, Z. P., Xu, J. W., Wang, J. H., Bush, P., Siegal, M. P., Provencio, P. N. (1998) Synthesis of large arrays of well-aligned carbon nanotubes on glass. *Science*, 282, 1105-1107.

Rinzler, A. G., Liu, J., Dai, H., Nikolaev, P., Huffman, C. B., Rodriguez-Macias, F. J., Boul, P. J., Lu, A. H., Heymann, D., Colbert, D. T., Lee, R. S., Fischer, J. E., Rao, A. M., Eklund, P. C., Smalley, R. E. (1998) Large-scale purification of single-wall carbon nanotubes: process, product, and characterization. *Applied Physics A-Materials Science & Processing*, 67, 29-37.

Ritschel, M., Uhlemann, M., Gutfleisch, O., Leonhardt, A., Graff, A., Taschner, C., Fink, J. (2002) Hydrogen storage in different carbon nanostructures. *Applied Physics Letters*, 80, 2985-2987.

Rodriguez-Reinoso, F. (2002) Production and Applications of Activated Carbons. *In* Schüth, F., Sing, K. S. W., Weitkamp, J. (Eds.) *Handbook of porous solids*. Weinheim, Wiley-VCH.

Rodriguez, N., Yokono, T., Takahashi, N., Sanada, Y., Marsh, H. (1987) Electron-spin-resonance study of the interactions between a rank range of coals, fresh and oxidized, with iodine. *Fuel*, 66, 1743-1745.

Rodriguez, N. M. (1993) A review of catalytically grown carbon nanofibers. *Journal of Materials Research*, 8, 3233-3250.

Rodriguez, N. M., Chambers, A., Baker, R. T. K. (1995) Catalytic engineering of carbon nanostructures. *Langmuir*, 11, 3862-3866.

Rodriguez, N. M., Kim, M. S., Baker, R. T. K. (1993a) Deactivation of copper nickel-catalysts due to changes in surface-composition. *Journal of Catalysis*, 140, 16-29.

Rodriguez, N. M., Kim, M. S., Baker, R. T. K. (1993b) Promotional effect of carbon-monoxide on the decomposition of ethylene over an iron catalyst. *Journal of Catalysis*, 144, 93-108.

Rodriguez, N. M., Kim, M. S., Baker, R. T. K. (1994) Carbon nanofibers - a unique catalyst support medium. *Journal of Physical Chemistry*, 98, 13108-13111.

Rosi, N. L., Eckert, J., Eddaoudi, M., Vodak, D. T., Kim, J., O'Keeffe, M., Yaghi, O. M. (2003) Hydrogen storage in microporous metal-organic frameworks. *Science*, 300, 1127-1129.

Ruthven, D. M. (1984) *Principles of Adsorption and Adsorption Processes*, New York, Wiley.

Rzepka, M., Lamp, P., de la Casa-Lillo, M. A. (1998) Physisorption of hydrogen on microporous carbon and carbon nanotubes. *Journal of Physical Chemistry B*, 102, 10894-10898.

Sacco, A., Thacker, P., Chang, T. N., Chiang, A. T. S. (1984) The initiation and growth of filamentous carbon from alpha-Iron in hydrogen, methane, water, carbon dioxide, and carbon monoxide gas-mixtures. *Journal of Catalysis*, 85, 224-236.

Sandrock, G., Gross, K., Thomas, G. (2002) Effect of Ti-catalyst content on the reversible hydrogen storage properties of the sodium alanates. *Journal of Alloys and Compounds*, 339, 299-308.

Sandrock, G. D., Huston, E. L. (1981) How metals store hydrogen. *Chemtech*, 11, 754-762.

Sen, R., Govindaraj, A., Rao, C. N. R. (1997) Carbon nanotubes by the metallocene route. *Chemical Physics Letters*, 267, 276-280.

Sherif, S. A., Zeytinoglu, N., Veziroglu, T. N. (1997) Liquid hydrogen: Potential, problems, and a proposed research program. *International Journal of Hydrogen Energy*, 22, 683-688.

Shi, Z. J., Lian, Y. F., Liao, F. H., Zhou, X. H., Gu, Z. N., Zhang, Y., Iijima, S., Li, H. D., Yue, K. T., Zhang, S. L. (2000) Large scale synthesis of single-wall carbon nanotubes by arc- discharge method. *Journal of Physics and Chemistry of Solids*, 61, 1031-1036.

Shiraishi, M., Takenobu, T., Yamada, A., Ata, M., Kataura, H. (2002) Hydrogen storage in single-walled carbon nanotube bundles and peapods. *Chemical Physics Letters*, 358, 213-218.

Shriver, D. F., Atkins, P. W. (1999) *Inorganic Chemistry*, New York, W.H. Freeman and Co.

Simonyan, J., Vahan, V., Johnson, J. K. (2002) Hydrogen storage in carbon nanotubes and graphitic nanofibers. *Journal of Alloys and Compounds*, 330, 659-665.

Simonyan, V. V., Diep, P., Johnson, J. K. (1999) Molecular simulation of hydrogen adsorption in charged single- walled carbon nanotubes. *Journal of Chemical Physics*, 111, 9778-9783.

Sinfelt, J. H., Carter, J. L., Yates, D. J. C. (1972) Catalytic hydrogenolysis and dehydrogenation over copper-nickel alloys. *Journal of Catalysis*, 24, 283-296.

Singh, C., Quested, T., Boothroyd, C. B., Thomas, P., Kinloch, I. A., Abou-Kandil, A. I., Windle, A. H. (2002) Synthesis and characterization of carbon nanofibers produced by the floating catalyst method. *Journal of Physical Chemistry B*, 106, 10915-10922.

Sivakumar, R., Ramaprabhu, S., Rama Rao, K. V. S., Anton, H., Schmidt, P. C. (1999) Hydrogen absorption characteristics in the $Tb_{1-x}Zr_xFe_3$ (x=0.1, 0.2, 0.3) system. *Journal of Alloys and Compounds*, 285, 143-149.

Skoog, D. A. (2000) *Analytical Chemistry: An Introduction*, Fort Worth; London, Saunders College.

Smith, M. R., Bittner, E. W., Shi, W., Johnson, J. K., Bockrath, B. C. (2003) Chemical activation of single-walled carbon nanotubes for hydrogen adsorption. *Journal of Physical Chemistry B*, 107, 3752-3760.

Steigerwalt, E. S., Deluga, G. A., Cliffel, D. E., Lukehart, C. M. (2001) A Pt-Ru/graphitic carbon nanofiber nanocomposite exhibiting high relative performance as a direct-methanol fuel cell anode catalyst. *Journal of Physical Chemistry B*, 105, 8097-8101.

Steigerwalt, E. S., Deluga, G. A., Lukehart, C. M. (2002) Pt-Ru/carbon fiber nanocomposites: Synthesis, characterization, and performance as anode

catalysts of direct methanol fuel cells. A search for exceptional performance. *Journal of Physical Chemistry B*, 106, 760-766.

Strobel, R., Jorissen, L., Schliermann, T., Trapp, V., Schutz, W., Bohmhammel, K., Wolf, G., Garche, J. (1999) Hydrogen adsorption on carbon materials. *Journal of Power Sources*, 84, 221-224.

Swagelok (2004) *www.swagelok.com* [Accessed 26th January 2004].

Systemtechnik (2003) *wwwwww.l-b-systemtechnik.com* [Accessed 24th June 2003].

Thess, A., Lee, R., Nikolaev, P., Dai, H. J., Petit, P., Robert, J., Xu, C. H., Lee, Y. H., Kim, S. G., Rinzler, A. G., Colbert, D. T., Scuseria, G. E., Tomanek, D., Fischer, J. E., Smalley, R. E. (1996) Crystalline ropes of metallic carbon nanotubes. *Science*, 273, 483-487.

Thostenson, E. T., Ren, Z. F., Chou, T. W. (2001) Advances in the science and technology of carbon nanotubes and their composites: a review. *Composites Science and Technology*, 61, 1899-1912.

Tibbetts, G. G., Finegan, I. C., Kwag, C. (2002) Mechanical and electrical properties of vapor-grown carbon fiber thermoplastic composites. *Molecular Crystals and Liquid Crystals*, 387, 353-357.

Tibbetts, G. G., Meisner, G. P., Olk, C. H. (2001) Hydrogen storage capacity of carbon nanotubes, filaments, and vapor-grown fibers. *Carbon*, 39, 2291-2301.

Toebes, M. L., Bitter, J. H., van Dillen, A. J., de Jong, K. P. (2002a) Impact of the structure and reactivity of nickel particles on the catalytic growth of carbon nanofibers. *Catalysis Today*, 76, 33-42.

Toebes, M. L., Prinsloo, F. F., Bitter, J. H., van Dillen, A. J., de Jong, K. P. (2002b) Synthesis and characterization of carbon nanofiber supported ruthenium catalysts. *Scientific Bases for the Preparation of Heterogeneous Catalysts*.

United-Nations (1997) *wwwwww.unep.org/* [Accessed 24th June 2003].

van der Waals, J. D. (1873) Over de continuiteit van den gas- en vloeistoftoestand (on the continuity of the gas and liquid state). *Physics.* Leyden, Leyden University.

Vander Wal, R. L., Ticich, T. M., Curtis, V. E. (2000) Directed synthesis of metal-catalyzed carbon nanofibers and graphite encapsulated metal nanoparticles. *Journal of Physical Chemistry B*, 104, 11606-11611.

Vander Wal, R. L., Ticich, T. M., Curtis, V. E. (2001) Substrate-support interactions in metal-catalyzed carbon nanofiber growth. *Carbon*, 39, 2277-2289.

Verbetsky, V. N., Malyshenko, S. P., Mitrokhin, S. V., Solovei, V. V., Shmal'ko, Y. F. (1998) Metal hydrides: Properties and practical applications. Review of the works in CIS-countries. *International Journal of Hydrogen Energy*, 23, 1165-1177.

Wang, Q. K., Zhu, C. C., Liu, W. H., Wu, T. (2002) Hydrogen storage by carbon nanotube and their films under ambient pressure. *International Journal of Hydrogen Energy*, 27, 497-500.

Wang, Q. Y., Johnson, J. K. (1999a) Computer simulations of hydrogen adsorption on graphite nanofibers. *Journal of Physical Chemistry B*, 103, 277-281.

Wang, Q. Y., Johnson, J. K. (1999b) Molecular simulation of hydrogen adsorption in single-walled carbon nanotubes and idealized carbon slit pores. *Journal of Chemical Physics*, 110, 577-586.

Wang, Q. Y., Johnson, J. K. (1999c) Optimization of carbon nanotube arrays for hydrogen adsorption. *Journal of Physical Chemistry B*, 103, 4809-4813.

Wang, X. K., Lin, X. W., Dravid, V. P., Ketterson, J. B., Chang, R. P. H. (1995) Carbon nanotubes synthesized in a hydrogen arc-discharge. *Applied Physics Letters*, 66, 2430-2432.

Warren, B. E. (1990) *X-ray Diffraction*, New York, Dover.

Webb, P. A., Clyde, O. (1997) *Analytical Methods in Fine Particle Technology*, Norcross, Micrometrics.

Wei, C. Y., Srivastava, D., Cho, K. J. (2002) Thermal expansion and diffusion coefficients of carbon nanotube-polymer composites. *Nano Letters*, 2, 647-650.

Welz, B., Sperling, M. R. (1999) *Atomic Absorption Spectrometry*, Chichester, Wiley-VCH.

Williams, D. H., Fleming, I. (1995) *Spectroscopic Methods in Organic Chemistry*, London, McGraw-Hill.

Williams, K. A., Eklund, P. C. (2000) Monte Carlo simulations of H_2 physisorption in finite-diameter carbon nanotube ropes. *Chemical Physics Letters*, 320, 352-358.

Witham, C., Bowman, R. C., Fultz, B. (1997) Gas-phase H_2 absorption and microstructural properties of $LaNi_5-xGe_x$ alloys. *Journal of Alloys and Compounds*, 253, 574-578.

Wolf, J. (2002) Liquid-hydrogen technology for vehicles. *Mrs Bulletin*, 27, 684-687.

Wu, X. B., Chen, P., Lin, J., Tan, K. L. (2000) Hydrogen uptake by carbon nanotubes. *International Journal of Hydrogen Energy*, 25, 261-265.

Yamamoto, K., Orimo, S., Fujii, H., Kitano, Y. (1999) Hydriding properties of the heat-treated MgNi alloys with nanostructural designed multiphase. *Journal of Alloys and Compounds*, 295, 546-551.

Yang, R. T. (2000) Hydrogen storage by alkali-doped carbon nanotubes-revisited. *Carbon*, 38, 623-626.

Yang, R. T., Yang, K. L. (1985) Evidence for temperature-driven carbon diffusion mechanism of coke deposition on catalysts. *Journal of Catalysis*, 93, 182-185.

Yasutake, M., Shirakawabe, Y., Okawa, T., Mizooka, S., Nakayama, Y. (2002) Performance of the carbon nano-tube assembled tip for surface shape characterization. *Ultramicroscopy*, 91, 57-62.

Yin, Y. F., Mays, T., McEnaney, B. (2000) Molecular simulations of hydrogen storage in carbon nanotube arrays. *Langmuir*, 16, 10521-10527.

Yoon, S. H., Lim, S., Song, Y., Ota, Y., Qiao, W. M., Tanaka, A., Mochida, I. (2004) KOH activation of carbon nanofibers. *Carbon*, 42, 1723-1729.

Yoon, Y. J., Baik, H. K. (2001) Catalytic growth mechanism of carbon nanofibers through chemical vapor deposition. *Diamond and Related Materials*, 10, 1214-1217.

Zaluska, A., Zaluski, L., Strom-Olsen, J. O. (1999a) Nanocrystalline magnesium for hydrogen storage. *Journal of Alloys and Compounds*, 288, 217-225.

Zaluska, A., Zaluski, L., Strom-Olsen, J. O. (1999b) Synergy of hydrogen sorption in ball-milled hydrides of Mg and Mg_2Ni. *Journal of Alloys and Compounds*, 289, 197-206.

Zaluska, A., Zaluski, L., Strom-Olsen, J. O. (2000) Sodium alanates for reversible hydrogen storage. *Journal of Alloys and Compounds*, 298, 125-134.

Zhang, Y., Iijima, S. (1999) Formation of single-wall carbon nanotubes by laser ablation of fullerenes at low temperature. *Applied Physics Letters*, 75, 3087-3089.

Zhou, L. (2005) Progress and problems in hydrogen storage methods. *Renewable and Sustainable Energy Reviews*, 9, 395.

Zhou, L., Zhou, Y., Sun, Y. (2004) A comparative study of hydrogen adsorption on superactivated carbon versus carbon nanotubes. *International Journal of Hydrogen Energy*, 29, 475.

Zhu, H. W., Cao, A. Y., Li, X. S., Xu, C. L., Mao, Z. Q., Ruan, D. B., Liang, J., Wu, D. H. (2001) Hydrogen adsorption in bundles of well-aligned carbon nano tubes at room temperature. *Applied Surface Science*, 178, 50-55.

Zhu, H. W., Li, C. H., Li, X. S., Xu, C. L., Mao, Z. Q., Liang, J., Wu, D. H. (2002) Hydrogen storage by platelet-carbon fibers at room temperature. *Materials Letters*, 57, 32-35.

Zhu, H. W., Li, X. S., Ci, L. J., Xu, C. L., Wu, D. H., Mao, Z. Q. (2003) Hydrogen storage in heat-treated carbon nanofibers prepared by the vertical floating catalyst method. *Materials Chemistry and Physics*, 78, 670-675.

Zhu, X. Y., White, J. M. (1989) Interaction of ethylene and acetylene with Ni(111) - a Sims study. *Surface Science*, 214, 240-256.

Appendix 1 - **Hydrogen adsorption procedure**

Full schematic of HPAA
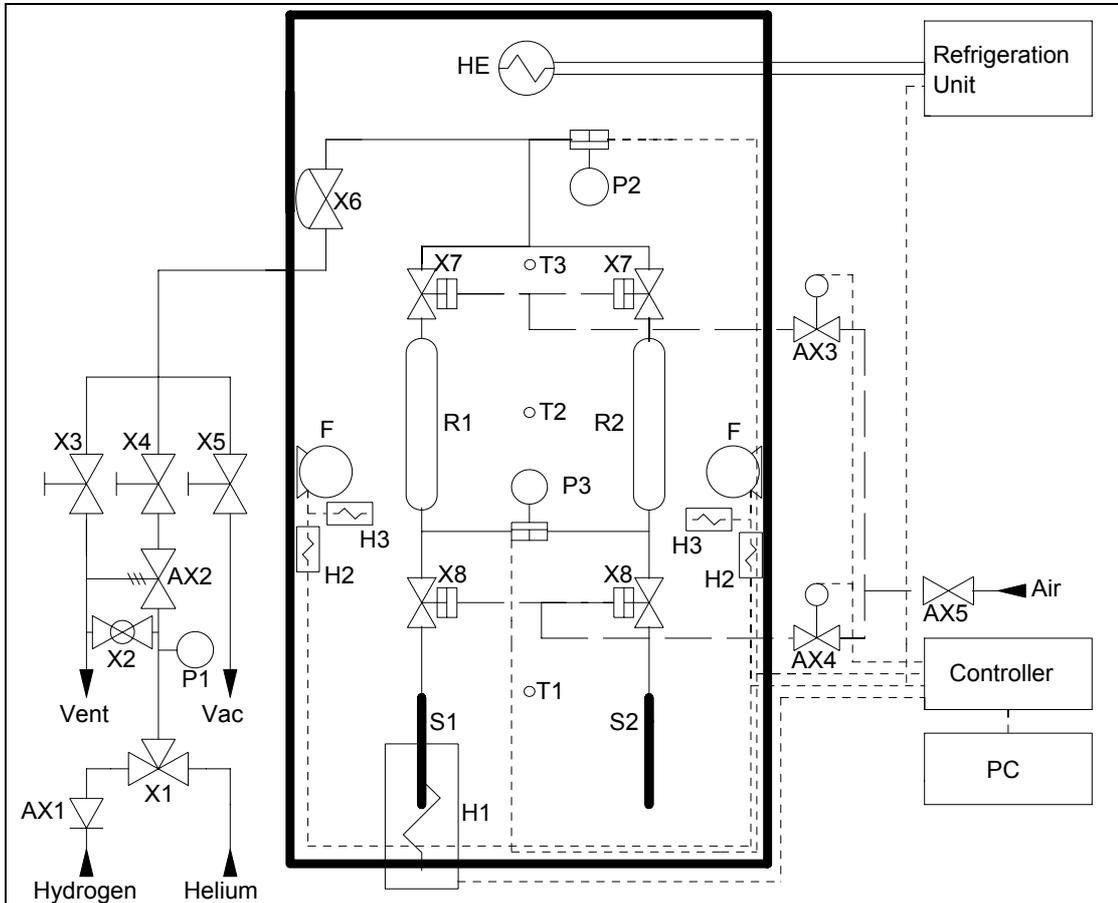
X1	Three way valve	P1	Analogue pressure gauge (0-200 bar)
X2	Ball valve	P2	Pressure transducer (0-160 bar)
X3	Needle valve	P3	Differential pressure transducer (± 5 bar)
X4	Needle valve		
X5	Needle valve	R1	Gas reservoir 1
X6	Diaphragm Valve	R2	Gas reservoir 2
X7	Remotely controlled inter-linked Bellows valves (normally closed)	S1	Sample cell 1
		S2	Sample cell 2
X8	Remotely controlled inter-linked Bellows valves (normally open)	T1	Lower logged thermistor
		T2	Middle logged thermistor
		T3	Top logged thermistor
AX1	Non-return valve	H1	Furnace PID controlled
AX2	Relief Valve (180 bar)	H2	Electric strip heaters*
AX3	Solenoid (control box operated)	H3	Electric strip heaters with fins*
AX4	Solenoid (wall switch operated)	F	Fans
AX5	Needle valve	He	Heat exchanger

* H2, H3 and the refrigeration unit are controlled by PID on a heat-cool cycle

Basic schematic of high pressure adsorption apparatus control box

	PID2	PID controller for temperature enclosure
	PID1	PID controller for H1
	IT1	Independent apparatus temperature indicator
	IP3	P3 indicator
	IP2	P2 indicator
	SP	Main power switch
	SH1	H1 isolator switch
	SX7	X7 actuator switch
	STE	Temperature enclosure control power switch
	SH3	Switch to isolate part of temperature control system
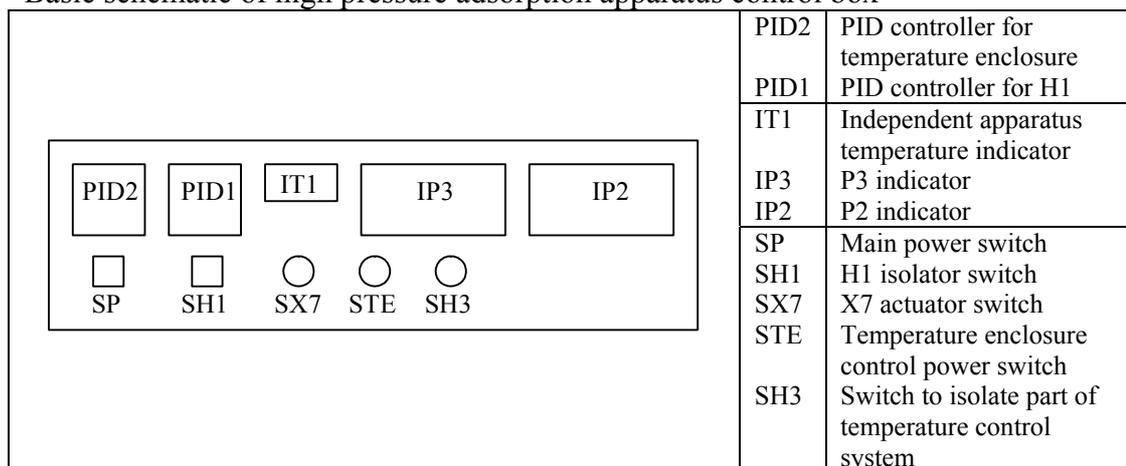
The Helium and hydrogen are further purified by a liquid nitrogen trap for all procedures on the high pressure adsorption apparatus.

Pre-measurement Procedure

Sample loading

1. Weigh sample cell
2. Fill sample cell with the material to be studied for hydrogen storage capacity
3. Weigh sample cell
4. Fit glass wool plug above sample (*ca* 0.5 g)
5. Weigh sample cell
6. Fit o-ring to sample cell and attach to the high pressure adsorption apparatus

Free space analysis

NB interlinked valves X7 are separated for this procedure
1. Ensure all valves labelled X1 – X7 are closed
2. Turn on power to adsorption rig control box and computer
3. Turn on compressed air
4. Open X6 and both X7 valves (SX7)
5. Switch on the vacuum pump
6. Bleed gas out of system using needle valve X5
7. Leave system at vacuum for ten minutes then close the X7 valve of the limb that is not to have free space analysis
8. Close interlinked valves X8 (wall switch marked X8)
9. Close X5
10. Set helium regulator to 5 bar
11. Start data logger
12. Open X1 to helium
13. Allow helium into the apparatus using X4
14. Close X4, X6 and X7 (SX7)
15. Equilibrate for 30 seconds
16. Open X8 (wall switch marked X8)
17. Equilibrate for 30 seconds
18. Turn off data logger

19. Open X6 and X7 (SX7)
20. Bleed helium to vent through X3 helium through then close X3
21. Close all valves

DG1

1. Ensure all valves labelled X1 –X7 are closed
2. Turn on power to adsorption rig control box and computer
3. Turn on compressed air
4. Open V6 and linked bellows valves X7 (SX7)
5. Switch on the vacuum pump
6. Bleed gas out of system using needle valve X5
7. Leave system at vacuum for ten minutes then close X5
8. Set helium regulator to 5 bar
9. Open X1 to helium
10. Allow helium into the apparatus using X4 then close X4
11. Bleed helium to vent through X3 helium through then close X3
12. Repeat steps 6 to 11 three times
13. Bleed gas out of system using needle valve X5
14. Degas achieved when vacuum reaches 10^{-3} torr

DG2

15. Ensure all valves labelled X1 – X7 are closed
16. Turn on power to adsorption rig control box and computer
17. Turn on compressed air
18. Open X6 and linked bellows valves X7 (SX7)
19. Switch on the vacuum pump
20. Bleed gas out of system using needle valve X5
21. Leave system at vacuum for ten minutes then close X5
22. Set helium regulator to 5 bar
23. Open X1 to helium
24. Allow helium into the apparatus using X4 then close X4
25. Bleed helium to vent through X3 helium through then close X3
26. Repeat steps 6 to 11 three times
27. Bleed gas out of system using needle valve X5
28. Raise H1 into position around the sample cell (S1 or S2) and place heat guards around the top of the furnace.
29. Switch on H1 (SH1) and ramp the temperature to 150 °C (4 °C min^{-1}) controlled by PID1.
30. Degas complete when vacuum reaches 10^{-3} torr
31. At end of this period switch off H1 (SH1)
32. Lower H1 from enclosure

DG3

1. Carry out Basic procedure outlined above
2. While heating at 150 °C, close X5
3. Set hydrogen regulator to 10 bar
4. Slowly bleed hydrogen into the apparatus through valve X4 then close X4
5. Switch off H1 (SH1)

6. Lower H1 from enclosure
7. Bleed hydrogen slowly to vent through X3
8. Repeat steps 1 to 7 three times
9. Carry out DG2 procedure

Single Temperature Hydrogen Measurement Operating Procedure

NB system remains at vacuum from degas procedure
1. Close and bolt shut the temperature controlled enclosurer
2. Set PID2 to 30 °C
3. Turn on temperature control system using switches STE and SH3
4. Allow enclosure 1 hour to equilibrate to 30 °C (as monitored using data logger)
5. Close X5 and linked valves X8 (wall switch marked X8)
6. Switch off the vacuum pump.
7. Watching the hydrogen regulator cylinder gauge open the cylinder value slowly until pressure is registered on the gauge.
8. Open X1,X6 and X7 (SX7)
9. Watching both the regulator and P1 open the regulator to the desired pressure slowly
10. Open X4 very slowly to admit hydrogen into the hydrogen reservoirs inside the enclosure watching the absolute pressure indicator (IP2)
11. Close X4, X6 and linked bellows valves X7 (SX7)
12. Close regulator and the cylinder valve
13. Open X2 to vent the hydrogen supply line

NB The rig is now isolated from the cylinder. At any time during the test, should the registered differential pressure at PI-2 exceed ±5 bar, the computer will open the air-actuated bellows valves X7 in order to equalise pressure on both sides of the DP cell in order to protect the latter from over-pressure damage. In this event, the test will be null and void, and an alarm will be raised in a dialogue box on the computer screen.

14. Initiate computer data logger (The computer starts to log output from the gauge and differential pressure indicators IP2 and IP3 and the three thermistor temperatures)
15. Open linked valves X8 to begin test (X8)
16. At the end of the test turn off the data logger
17. open linked valves X7 (SX7) and valve X6
18. Slowly open X3 to bleed the hydrogen from the system
19. Close X3, X6 and X7 (SX7)
20. Turn off computer and controller and turn off at wall switches

Single Temperature Helium Blank Measurement Operating Procedure

As hydrogen measurement operating procedure except using helium

Split Temperature Hydrogen Measurement Operating Procedure

NB system remains at vacuum from degas procedure
1. Carry out steps 1-14 of the single temperature hydrogen measurement Operating Procedure
2. Maintain until equilibrium is achieved
3. Open the temperature controlled enclosurer
4. Raise H1 into position around the sample cell (S1 or S2) and place heat guards around the top of the furnace.
5. Switch on H1 (SH1) and ramp the temperature to desired adsorbent temperature (4 °C min^{-1}) controlled by PID1.
6. Close and bolt shut the temperature controlled enclosurer
7. Set PID2 to 35 °C
8. Monitor process until equilibrium is achieved
9. Switch off H1 (SH1)
10. Lower H1 from enclosure
11. Set PID2 to 30 °C
12. Maintain until equilibrium is achieved
13. Turn off the data logger
14. open linked valves X7 (SX7) and valve X6
15. Slowly open X3 to bleed the hydrogen from the system
16. Close X3, X6 and X7 (SX7)
17. Turn off computer and controller and turn off at wall switches

Appendix 2 - **Summary of materials purchased**

Substance	Supplier	Purity	CAS no	Code
Citric acid	Fisher Chemicals	99.5%	[5949-29-1]	12491
Copper nitrate trihydrate	Lancaster	99 %	[10031-43-3]	14121
Hydrochloric acid	Lancaster	36 % w/w	[7647-01-0]	13091
Iron nitrate nonahydrate	Lancaster	98 %	[7782-61-8]	14454
Magnesium nitrate hexahydrate	Lancaster	98 %	[13446-18-9]	13250
Nickel nitrate hexahydrate	Lancaster	98 %	[13478-00-7]	13674
Nitric acid	Fisher Chemicals	58 % w/w	[7697-37-2]	13362
Sodium hydroxide	Fisher Chemicals	98.6 %	[1310-73-2]	20606
Potassium hydroxide	Fisher Chemicals	98 %	[1310-58-3]	13406
Carbon FGD	Fisher Chemicals			
Carbon FGA	Fisher Chemicals			
Carbon graphite	Fisher Chemicals			
Carbon Norit FGD	Norit			
Picazine	Pica			
MWNT	York Point	95 %		
SWNT	Nanoamor	90 %		

Gas	Supplier	Purity
Argon	Air products	99.9 %
Carbon dioxide	Air products	99.9 %
Ethylene	Air products	99.5 %
Helium	Air products	99.9 %
Hydrogen	Air products	99.9 %
Nitrogen	Air products	99.9 %

Appendix 3 - Derivation of differential pressure calculation

This derivation is required to prove that the hydrogen adsorption uptake, determined via the differential pressure method calculation, is independent of the measurement made by the direct pressure gauge (p_a) (Chapter 5).

Pre-adsorption

$$p_a V = n_y RT$$

$$n_y = \frac{p_a V}{RT}$$

Post-adsorption

$$(p_a - \Delta p)V = n_z RT$$

$$n_z = \frac{(p_a - \Delta p)V}{RT}$$

Amount of gas adsorbed

$$\Delta n = n_y - n_z$$

$$\Delta n = \frac{p_a V}{RT} - \frac{(p_a - \Delta p)V}{RT}$$

$$\Delta n = \frac{p_a V - (p_a - \Delta p)V}{RT}$$

$$\Delta n = \frac{p_a V - p_a V + \Delta p V}{RT}$$

$$\Delta n = \frac{\Delta p V}{RT}$$

Key	
n_y	= Initial amount of gas
n_z	= Final amount of gas
Δn	= Amount of gas adsorbed
p_a	= Pressure pre-adsorption
Δp	= Differential pressure
R	= Gas constant
T	= System temperature
V	= Volume pre expansion

Appendix 4 - **Derivation of volume calibration**
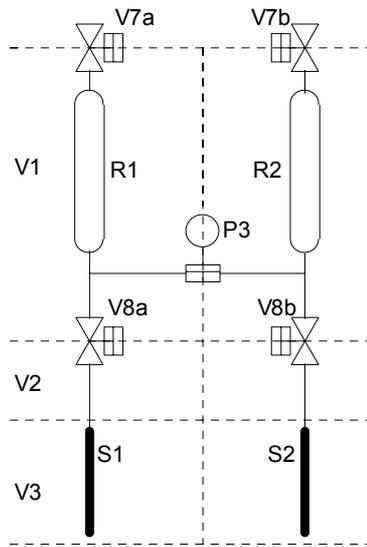
	V1	V2	V3
Left Limb (1)	Reservoir (R1)	Connecting pipe	Sample Cell (S1)
Right Limb (2)	Reservoir (R2)	Connecting pipe	Sample Cell (S2)

Key
P_1 Pre-expansion pressure
P_2 Post expansion pressure

If the temperature is kept constant

$$p_1 V_1 = p_2 (V_1 + V_2 + V_3)$$

$$\frac{p_1}{p_2} = \frac{V_1 + V_2 + V_3}{V_1}$$

$$\frac{p_1}{p_2} = \frac{V_1}{V_1} + \frac{V_2 + V_3}{V_1}$$

$$\frac{p_1}{p_2} - 1 = \frac{V_2 + V_3}{V_1}$$

Appendix 5 - **Standard GC-FID trace**

Component	Quantity
Methane	10 %
Ethylene	10 %
Ethane	10 %
Propylene	10 %
Propane	10 %
n-Butane	10 %
Helium	Balance
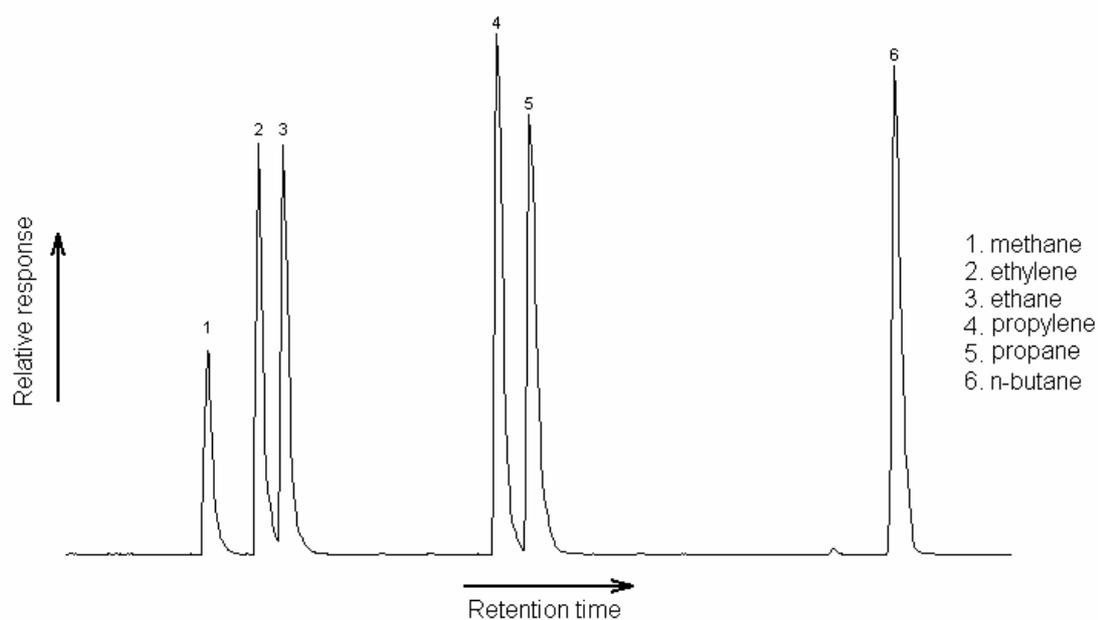
Appendix 6 - PAH characteristics
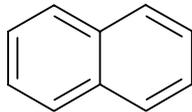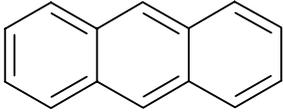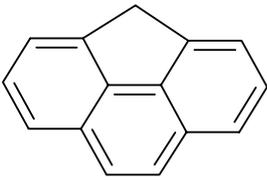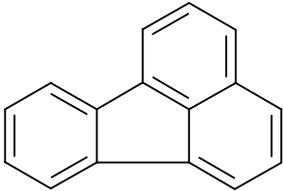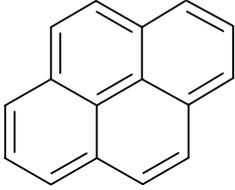
Structure and IUPAC Name	Formula	Molecular Mass (g mol^{-1})	Melting Point (°C)	Boiling Point (°C)
Naphthalene	$C_{10}H_8$	128.16	81	218
Anthracene	$C_{14}H_{10}$	178.24	101	340
Cyclopentaphenanthrene	$C_{15}H_{10}$	190.24	116	353
Fluoranthene	$C_{16}H_{10}$	202.26	111	375
Pyrene	$C_{16}H_{10}$	202.66	156	404